Understanding the mechanism of peptide self-assembly

Samuel John Bunce

Submitted in accordance with the requirements for the degree of
Doctor of Philosophy

The University of Leeds
Faculty of Biological Sciences

September 2018

Intellectual Property and Publication Statement

The candidate confirms that the work submitted is his own, except where work which has formed part of jointly-authored publications has been included. The contribution of the candidate and the other authors to this work has been explicitly indicated below. The candidate confirms that appropriate credit has been given within the thesis where reference has been made to the work of others.

Some of the work described in Chapter 2 formed the basis of a research article that has been submitted and is currently under review (Wang, Y.; Bunce, S. J.; Radford, S. E.; Wilson, A. J.; Auer, S.; Hall, C. K; *Proc. Natl. Acad. Sci. U.S.A;* **2018**). The contributions were as follows: SJB (i.e. the candidate) synthesised the reagents and performed the experiments; YW performed the simulations; YW, SA and CKH designed the simulations and any models used within the simulation; YW, SJB, SER, AJW, SA, CKH designed the research; YW and SJB wrote the manuscript that was edited into its present form prior to submission by all the authors. The appropriate parts of the work were then rewritten by SJB to be incorporated into Chapter 2.

Some of the work in Chapter 2 and the majority of the work in Chapter 3 formed the basis of a research article that has been submitted and is currently under review (Bunce, S. J; Wang, Y; Stewart, K. L.; Ashcroft, A. E.; Radford, S. E.; Hall, C. K. Hall; Wilson, A. J.; *Sci. Adv.*; **2018**). The contributions were as follows: SJB (i.e. the candidate) performed the experiments and synthesised some of the reagents; YW performed the simulations; KLS performed recombinant protein synthesis and purification; YW and CKH designed the simulation and any models used within the simulations; SJB, YW, AEA, SER, CKH and AJW designed the research; SJB, YW, SER, CKH and AJW wrote the manuscript that was then edited into its present form prior to submission by all the authors. The work was then rewritten by SJB and incorporated into the relevant sections of Chapter 2 and the entirety of Chapter 3.

Acknowledgements

Firstly, I would like to thank my supervisors (Prof. Andy Wilson, Prof. Sheena Radford FRS and Prof. Alison Ashcroft) for providing me with the opportunity to work on an engaging and intellectually challenging project. Your support, encouragement and guidance was invaluable throughout my PhD studies. In particular, my primary supervisor, Prof. Andy Wilson, who has supervised me for a full five years, has consistently aided me and always been available when needed.

I would also particularly like to thank both Yiming Wang and Prof. Carol Hall (North Carolina State University) for being excellent collaborators, whose contribution has significantly enhanced the work I have performed throughout my PhD, both intellectually and materially. A special thank you also goes to Dr. Katie Stewart, who synthesised all of the $A\beta_{40}$ used in this work, and introduced me to the weird world of amyloid kinetics. I would also like to thank Professor Nik Kapur and Mark Levenstein (University of Leeds) for building the cross-linking lamp that has made much of this work possible, as well as the technical staff in both the School of Chemistry and Faculty of Biological Sciences for their support.

Both the Radford and Ashcroft groups have been friendly and welcoming labs in which to work. Particular mentions go to Dr. Matt Iadanza for all his help with EM, Dr's Anton Calabrese and Patrick Knight for help with MS and Jim Horne for helping to set-up and problem shoot the fluorescence quenching assays. Dr. Matt Jackson, Hugh, Atenas and Jess have also been particularly kind, especially in finding the way to the pub.

The Wilson group (both past and present) has been the perfect place in which to do a PhD and I could not have asked for a nicer group of people with which to spend the past five years. Emma and Dr. Martin Walko have been always been there to help share the amyloid pain, whilst Kris, Heather, Tom, Zsofia, Som and Sonia are fantastic co-workers. I would like to apologise for any time I have been slightly less than happy in the office…

Three groups of friends have made this time highly enjoyable. In Leeds, Bobby, Ryan, Rob, Aisling, Lewis, Aaron and Lauren have been there throughout this time whilst numerous others, both past and present have made Chemistry a great place to work. In London, Nathan, Luke, Will, Tom, Jacob, Gabby, Ali, Elena and Chloe have provided the perfect weekend escape and one of the most comfortable sofas I have ever slept

on. Family/friends, including the Seddons, Havards, Coopers, Fieldings, Pymans and Reeses, have been there to enjoy many holidays away from the lab.

My family, David, Rachel, Meg, Nee and Ted have given love and support that I cannot begin to quantify. Without you, I would never have started a PhD, let alone finish one. Finally, I would like to dedicate this thesis to Hester, who turned the most difficult years of my life into the best.

Abstract

Understanding the molecular mechanism of peptide self-assembly is vital; both as a fundamental biological process but also to combat the pathological disease state known as amyloid. A wide range of techniques, including computer simulations and biophysical assays, will need to be employed to answer this question. The development of experimental techniques that can capture and isolate the fleeting states that occur during peptide self-assembly is thus essential in order to elucidate the underlying mechanism. In order to meet this need, Chapter 1 outlines key concepts that relate to peptide self-assembly by examining two key examples (diphenylalanine and the amyloid-β peptide). In Chapter 2, a combination of experiments (including photo-induced cross-linking and fluorescence quenching) and discontinuous molecular dynamics simulations were used to understand the self-assembly process of a small amyloid peptide, $A\beta_{16-22}$, at the molecular level. In Chapter 3, both the experimental methods that have been developed and the understanding of the mechanism of $A\beta_{16-22}$ self-assembly were extended to understand the mechanism by which $A\beta_{16-22}$ interacts with, and influences the aggregation rate of, a related sequence, $A\beta_{40.}$ Together, the work presented here describes how it is possible to explore complex self-assembling systems, with temporal resolution, at the molecular level.

Table of Contents

Abbreviations and Symbols

Aβ	Amyloid-β
AcOH	Acetic acid
AD	Alzheimer's Disease
AFM	Atomic Force Microscopy
Ahx	6-Aminohexanoic acid
ANS	1-Anillinonapthalene-8-sulfonic acid
APP	Amyloid Precursor Protein
Ar	Aromatic
β_2M	β_2-microglobulin
BACE	β-site APP cleavage enzyme
Boc	*tert*-Butyloxycarbonyl
CCS	Collision Cross-Section
CD	Circular Dichroism
CID	Collision-induced dissociation
$CHCl_3$	Chloroform
δ_C	Carbon Chemical Shift
δ_H	Hydrogen Chemical Shift
Δm	Difference in Mass
d	Doublet
DIC	*N,N*-Di*iso*propylcarbodiimide
DIPEA	*N,N*-Di*iso*propylethylyamine
DCM	Dichloromethane
DLS	Dynamic Light Scattering
DMD	Discontinuous Molecular Dynamics
DMF	Dimethylformamide
DMSO	Dimethylsulfoxide
EGCG	Epigallocatechin gallate
EM	Electron Microscopy
EPR	Electron Paramagnetic Resonance
ESI	Electrospray Ionisation
ESI-IMS-MS	Electrospray ionisation-ion mobility spectrometry-mass spectrometry
Et_2O	Diethylether
EtOAc	Ethyl acetate

EtOH	Ethanol
FLIM	Fluorescence Lifetime Imaging
Fmoc	Fluorenylmethyloxycarbonyl
FTIR	Fourier-Transform Infra-Red
HDX	Hydrogen Deuterium Exchange
HFIP	1, 1, 1, 3, 3, 3-Hexafluoroisopropanol
HPLC	High Performance Liquid Chromatography
HRMS	High Resolution Mass Spectrometry
IAPP	Islet Amyloid Polypeptide
IMS	Ion Mobility Spectrometry
ITC	Isothermal Calorimetry
J	Coupling constant
J_{app}	Apparent coupling constant
λ_{max}	Wavelength of maximum absorption
LCMS	Liquid Chromatography
LED	Light Emitting Diode
m	Multiplet
m/z	Mass-to-charge ratio
MALDI	Matrix-assisted Laser Desportion Ionisation
MD	Molecular Dynamics
MeCN	Acetonitrile
MeOH	Methanol
MS	Mass Spectrometry
NaOH	Sodium Hydroxide
nESI	Nanospray-Electrospray Ionisation
NIAD-4	2-[[5'-(4-hydroxyphenyl)[2,2'-bithiophen]-5-yl]-methylene]-propanedinitrile
NMR	Nuclear Magnetic Resonance
PCA-AD	Posterior Cortical Atrophy-AD
PD	Parkinson’s Disease
PDB	Protein Data Bank
pE	Pryoglutamate
PIC	Photo-induced Cross-linking
ppm	Parts-per-million
PRIME20	Protein Intermediate-Resolution Model
PrD	Prion-determining Region

r-AD	Rapid-AD
REMD	Rapid Exchange Molecular Dynamics
R_f	Retention Factor
s	Singlet
SANS	Small-angle Neutron Scattering
SAXS	Small-angle X-ray Scattering
SEM	Scanning Electron Microscopy
SPPS	Solid Phase Peptide Synthesis
t	Triplet
t-AD	Typical-AD
TAMRA	Tetramethylrhodamine
TBDPS	Tetrabutyldiphenylsilane
t_D	Drift time
TEM	Transmission Electron Microscopy
TFA	Trifluoroacetic acid
TFMD	Trifluoromethyldiazirine
THF	Tetrahydrofuran
TIPS	Tri*iso*propylsilane
Ts	Toluenesulphonyl
UV	Ultraviolet
WT	Wild type

Table of amino acid residues

Amino Acid	Three letter code	Single three code
Alanine	Ala	A
Arginine	Arg	R
Asparagine	Asn	N
Aspartic Acid	Asp	D
Cysteine	Cys	C
Glutamic Acid	Glu	E
Glutamine	Gln	Q
Glycine	Gly	G
Histidine	His	H
Isoleucine	Ile	I
Leucine	Leu	L
Lysine	Lys	K
Methionine	Met	M
Phenylalanine	Phe	F
Proline	Pro	P
Serine	Ser	S
Threonine	Thr	T
Tryptophan	Trp	W
Tyrosine	Tyr	Y
Valine	Val	V

Chapter 1:
Introduction

1.1 General comments on self-assembly

The following chapter will introduce important concepts that relate to peptide self-assembly, including the underlying molecular organisation of the supramolecular structures formed, the mechanism by which these structures are created and the kinetic and thermodynamic parameters that dominate peptide self-assembly. These concepts will initially be illustrated using a simple dipeptide (diphenylalanine). The diphenylalanine motif is a core region in longer amyloidogenic sequences and offers a convenient starting point to explore peptide self-assembly. Following this, the discussion will then be expanded to include the pathological state known as amyloid, including a description of the underlying fibril structure associated with amyloid and the kinetic mechanisms of amyloid self-assembly. The amyloid-β (Aβ) sequence, implicated in Alzheimer's Disease (AD), will be used as an example to explore amyloidogenic peptides. The literature surveyed in this chapter will thus provide a sound description of the key concepts that underlie the experimental work found in Chapter's 2 and 3.

The spontaneous formation of monomeric units into highly ordered and functional macroscale structures is fundamental to all cellular life.[1–3] Understanding this process, termed molecular self-assembly, is necessary to rationally design functional materials and also help to combat some of the most prevalent and debilitating diseases.[3–6] Although a wide range of building blocks can be used to design self-assembling systems (such as heterocycles **1** and **2**, which spontaneously self-assemble to form macrocycle **3**, Figure 1) those based on peptides have emerged as a significant area of scientific research.[7,8] The easy availability, cost effectiveness, biological origin and modular nature of the amino acid sequence offers a unique opportunity for the design of materials, with self-assembled peptides being amongst the most mechanically strong biological structures currently known.[9–11] Furthermore, understanding how peptides self-assemble into the pathological disease state, known as amyloid, is central to developing strategies for conditions such as Alzheimer's and Parkinson's Disease (AD and PD respectively).[6,12,13]

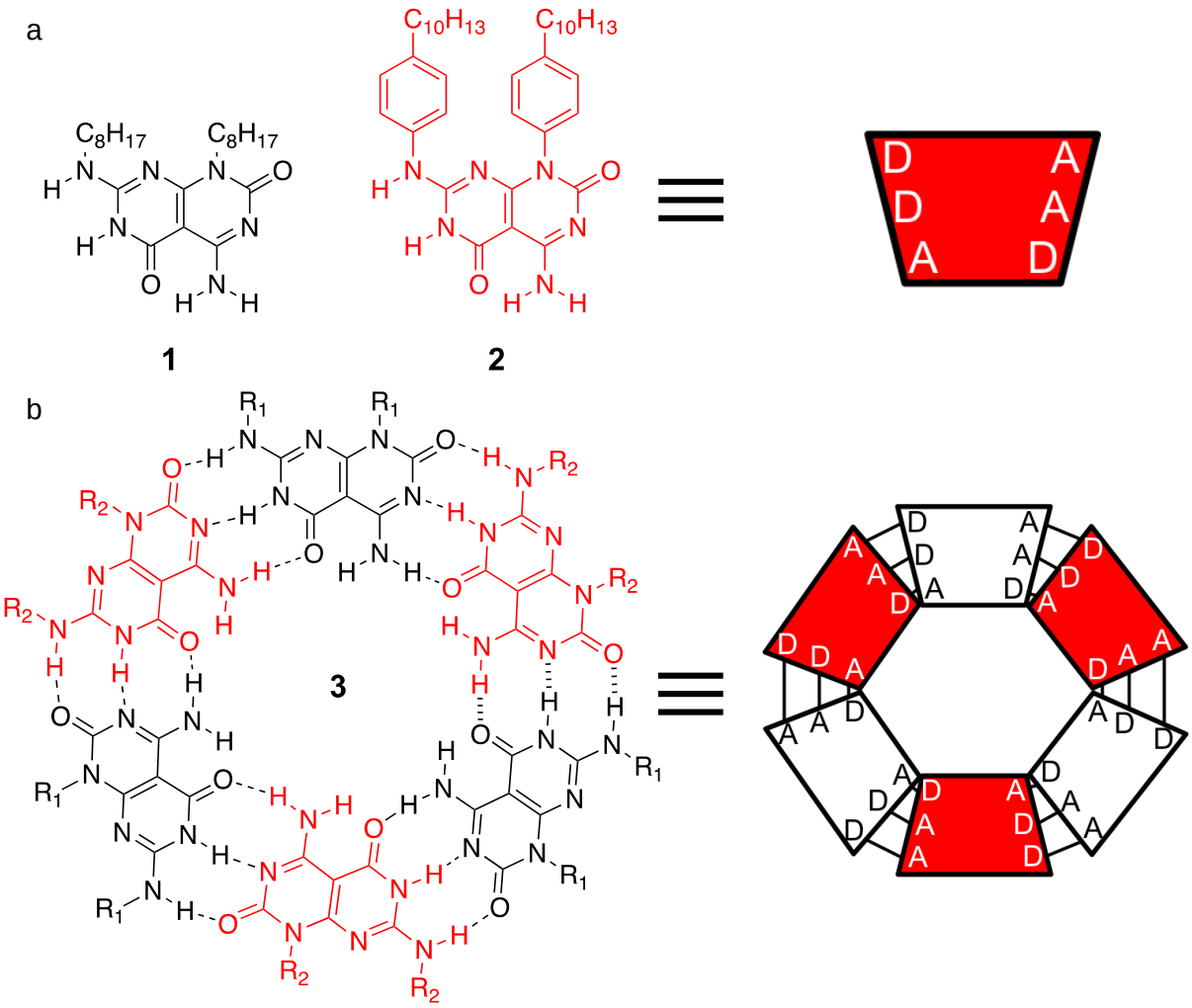

Figure 1. The principle of molecular self-assembly. Small molecules (such as **1** and **2**, a) can come together to form larger supramolecular structures (such as macrocycle **3**) through spontaneous self-assembly. When dissolved in toluene, **1** and **2** form hydrogen bonds with each other (as there are no hydrogen bonding opportunities with the solvent), eventually leading to the supramolecular organisation outlined above. The white and red blocks represent heterocycles **1** and **2** respectively, whilst D and A represent hydrogen bond donors or acceptors.

1.2 Peptide self-assembly: nanotubes

In biological systems, it has long been known that peptides can self-assemble into highly ordered fibrillar structures, e.g. actin polymerisation.[14] The rational design of self-assembling peptides was first theoretically proposed by De Santis in 1974, however, it took until 1993 for Ghadiri and co-workers to demonstrate experimentally the formation of peptide based nanotubes.[15,16] In this elegant work, an eight residue cyclic peptide containing alternating D- and L-amino acids (sequence: cyclo-[D-Ala-Glu-D-Ala-Gln]$_2$,

4, Figure 2a) was shown to form hollow nanotubes with a diameter of 7 - 8 Å and length of 100 nm (Figure 2b). This sequence samples a flat, ring-like structure in which the amino acid side chains face out into solution, with the amides participating in an antiparallel hydrogen bonding arrangement down the long axis of the nanotube (Figure 2c). Self-assembly was trigged by a decrease in pH that protonated the glutamic acid side chain and reduced the solubility of the peptide, such that the formation of the nanotubes was more favourable than the individual units remaining in solution. This work was extended by Ghadiri and co-workers when they explored the impact of side chain hydrophobicity on nanotube morphology.[17] In aqueous acidic conditions, all of the sequences formed nanotubes that were resistant to disassembly in a number of organic solvents such as dimethylsulfoxide (DMSO), 1, 1, 1, 3, 3, 3-hexafluoroisopropanol (HFIP) and dimethylformamide (DMF), at pH's between 1 – 14 and displayed good mechanical stability.[17] Taken together, these results clearly demonstrated that the rational design of peptide nanotubes was not only possible, but could also be used to form materials with remarkable properties, such as those developed by Gazit and co-workers, from diphenylalanine (**5**, see next section).[18]

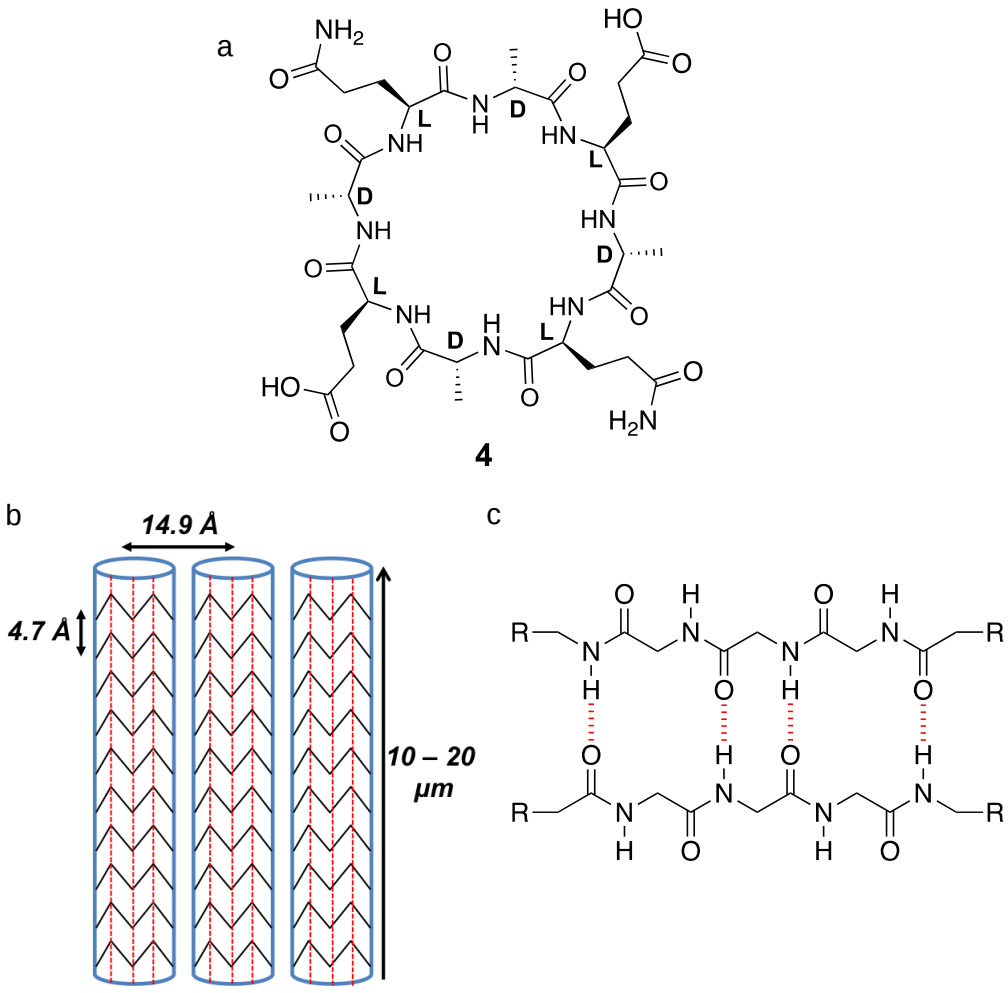

Figure 2. The formation of peptide nanotubes from cyclic peptides. The cyclo-peptide [D-Ala-Glu-D-Ala-Gln]$_2$ (a, **4**) forms long unbranched nanotubes (b) when placed in acidic solution through a flat ring conformation (black) with an antiparallel hydrogen bonding arrangement (red dashed lines). The hydrogen bonding arrangement (c, the side chains and back of the ring have been omitted for clarity) runs down the long axis of the nanotubes.

1.3 The self-assembly of a short peptide sequence: diphenylalanine (FF)

By the early 2000's it had been established that short peptide fragments taken from the full-length sequences of amyloidogenic peptides, such as amyloid-β (Aβ), human calcitonin and the islet-amyloid polypeptide (IAPP), could also form amyloid fibrils.[19–23] Given these results, and the knowledge that aromatic interactions can play a key role in self-assembled systems, Gazit and co-workers started to explore the formation of nanotubes by small dipeptides, namely diphenylalanine (**5**, FF, Figure 3a).[18,24,25] The FF motif, located in the central fibril forming core region of the full-length Aβ peptide (residues 19 and 20), has been shown to be key for the aggregation propensity of Aβ.[26–28] When FF was diluted out of a HFIP stock solution, it quickly formed well-ordered, hollow nanotubes (diameter: 100 – 150 nm, length: >1000 nm).[18] When

studied using Fourier-Transform Infra-Red (FTIR) spectroscopy, the nanotubes displayed the characteristic peaks of a β-sheet in the amide 1 region and also produced green-gold birefringence when incubated with Congo-Red (considered to be a hallmark of amyloid fibrils).[29] Further demonstrating the applicability of self-assembled peptides to materials science, these nanotubes were used to cast silver nanowires (removal of the peptide template was easily achieved using proteinase K, Figure 3b). The properties of the FF nanotubes were assessed in later studies, demonstrating that they were stable in solvents such as ethanol, methanol and acetonitrile, temperatures of 150 °C (dry heat) and also displayed remarkable stiffness for a biologically based material.[30,31]

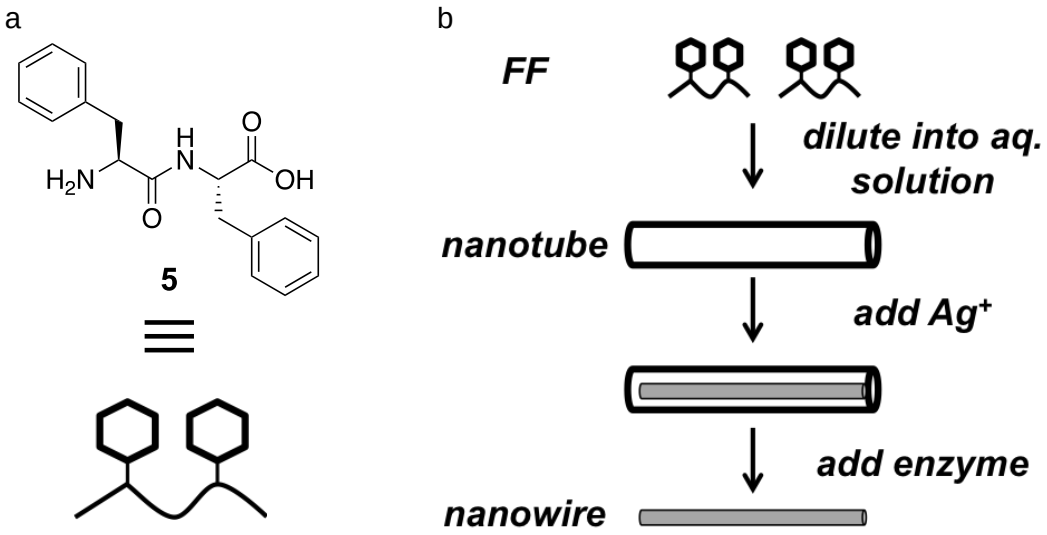

Figure 3. The molecular structure of FF and the casting of nanowires. The diphenylalanine peptide, FF (**5**, a), represented throughout this chapter by the cartoon schematic shown above, can be used to form highly ordered nanotubes that can in turn be used to cast silver nanowires (b).

Originally, Gazit and co-workers proposed a different underlying molecular structure for the nanotubes than the structure observed by Görbitz for a single crystal of FF (formed by rapid evaporation of the aqueous solvent at 80 °C).[18,32] In this study, FF formed hollow, solvent filled tubular structures (diameter ~10 Å) with six FF dipeptides arranged in a hexagon (Figure 4a).[32] The FF side chains were arranged such that they face away from the interior of the nanotube (in a similar manner to the nanotubes observed by Ghadiri and co-workers) and the amino/amide groups engaging in head-to-tail hydrogen bonding with both the other dipeptides and the water filled cavity (Figure 4b).[16,32] The protruding aromatic side chains of each hexagonal unit interact with the side chains of multiple other hexagonal units, with four nanotubes found in the

unit cell. This extended aromatic stacking interaction stabilises the formation of the nanotubes and provides directionality for nanotube growth.[5,33,34] Further investigations, performed using X-ray diffraction and the same self-assembly protocol (i.e. dilution of FF from a HFIP stock) confirmed that the FF nanotubes observed by Gazit were in fact consistent with the single crystal structure.[35]

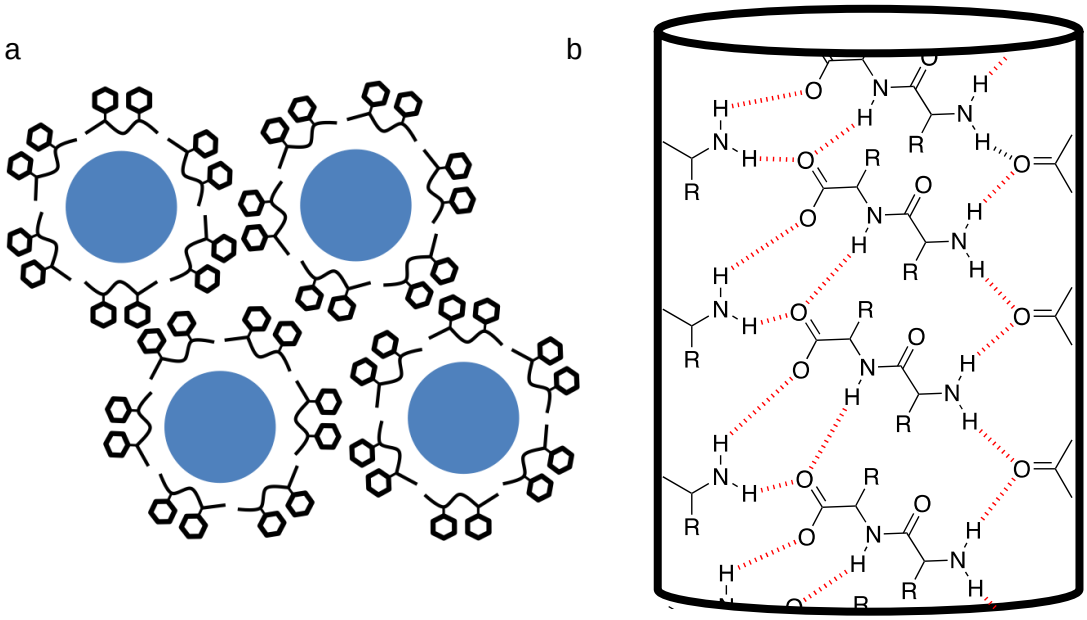

Figure 4. The organisation of FF within the nanotubes. FF forms hexagonal structures (a) that contain a solvent filled core, with stabilisation between different tubes coming through side chain-side chain interactions. The head-to-tail hydrogen bonding arrangement (b, for clarity the extra H^+ on the amino group that faces into the channel has been omitted, as has the charge on the carboxy group) runs down the long axis of the nanotube.

The simple nature of the FF dipeptide has allowed the synthesis of numerous analogues, including fluorenylmethyloxycarbonyl (Fmoc)-FF (**6**), *tert*-butyloxycarbonyl (Boc)-FF (**7**) and cationic $^{+}H_3N$-FF-$CONH_2$ (**8**, Figure 5) .[4,5,36–40] These analogues have been used to form a wide variety of functional materials, including hydrogels, scaffolds for cell culture and drug delivery vehicles.[37–39] Interestingly, these analogues can form different supramolecular structures than the nanotubes observed for H_2N-FF-COOH. Both cationic-FF and Boc-FF have an underlying α-helical structure but form fibrils and tubes respectively.[39,41] The cationic-FF analogue can transition from the nanotubular structure into spherical vesicles (via dilution), behaviour that has also been observed for H_2N-FF-COOH.[39,42] Boc-FF has also been shown to form partially crystalline vesicles when diluted from a HFIP stock into a 50:50 (v:v) solution of water and

ethanol.[43] Fmoc-FF forms nanofibrils, rather than nanotubes, that have an underlying β-sheet structure.[38,41] As FF is a small dipeptide, it is relatively simple to substantially change the overall properties of the peptide, allowing the relationship between non-

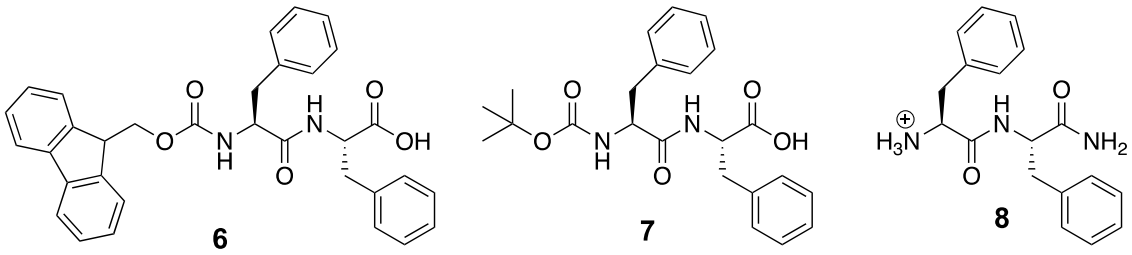

Figure 5. The molecular structures of Fmoc-FF (**6**), Boc-FF (**7**) and cationic-FF (**8**).

covalent interactions and molecular structure and its influence self-assembly to be probed.[41]

1.4 The mechanism of FF self-assembly

A number of studies have tried to establish the mechanism of FF self-assembly, both experimentally and through molecular dynamics (MD) simulations.[34,40,44–47] An implicit solvent MD simulation of FF demonstrated that the peptide spontaneously forms either open or ring-like aggregates, with the charged termini involved in head-to-tail hydrogen bonding interactions.[44] The peptide also formed “t-shaped” side chain interactions in agreement with the hexagonal crystal structure solved by Görbitz.[32,35] Another study performed a number of MD simulations (explicit solvent) to explore oligomer formation by FF, indicating oligomer formation principally proceeds through a dimer, stabilised through their hydrophobic side chains.[46] A head-to-tail arrangement of the termini was also observed in this simulation, with two hydrogens of the protonated amino group interacting with another peptide and the third with the water in the solvent filled cavity. In order to try and experimentally unpick the difference between these two models (i.e. dimer formation stabilised through a head-to-tail termini interaction prior to forming the hexagonal unit or stabilisation through side chain interactions), Bowers and co-workers assessed oligomerisation process of capped FF through ion mobility spectrometry-mass spectrometry (IMS-MS) in different solvents (water, methanol and acetonitrile, Figure 6).[45] The only stable non-covalent interaction between FF and a solvent was with water, highlighting its importance in the early stages of FF self-assembly. The collision cross-section (CCS) estimates indicated that capped FF dimers existed as two conformers: one composed of two monomers that could go on to form the hexagonal

unit (in a complex with a large water cluster) and one in which the peptides interacted primarily through their side chains.[45]

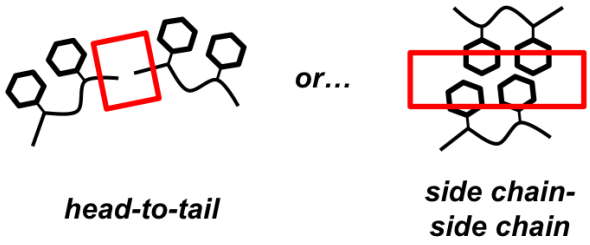

Figure 6. The proposed dimer conformations that FF can initially form during self-assembly. The dimers are stabilised by either head-to-tail hydrogen bonding (left) or side chain-side chain aromatic interactions (right).

In their investigation on the effect of substrate, pH and temperature on the morphology of FF nanotubes, Krishnan and co-workers proposed the following mechanism for FF self-assembly (Figure 7).[34] In this study, a solution containing FF was placed on to the substrate and placed in a vacuum (in order to remove the solvent). As the solvent evaporates, FF monomers start to form intermolecular hydrogen bonds, with the strong electrostatic interactions between the charged termini providing some directionality (i.e. directing the monomers into a head-to-tail configuration). Once these initial interactions have occurred, aromatic interactions between the side chains start to template the formation of β-sheet structure within the nanotubes, causing them to lengthen (lateral association is also possible). At some point, these peptide sheets may "roll over", forming the hollow nanotubes observed via electron microscopy (EM). The hydrophobic side chains face out into the bulk solution, thus avoiding any steric hindrance that may be present if they were located within the tubes. The kinetics of FF self-assembly have been shown to occur in two-steps, with self-assembly reliant on a nucleation step, which did not occur immediately upon solvation, demonstrating that the FF monomers were required to orientate themselves correctly prior to nanotube formation.[47]

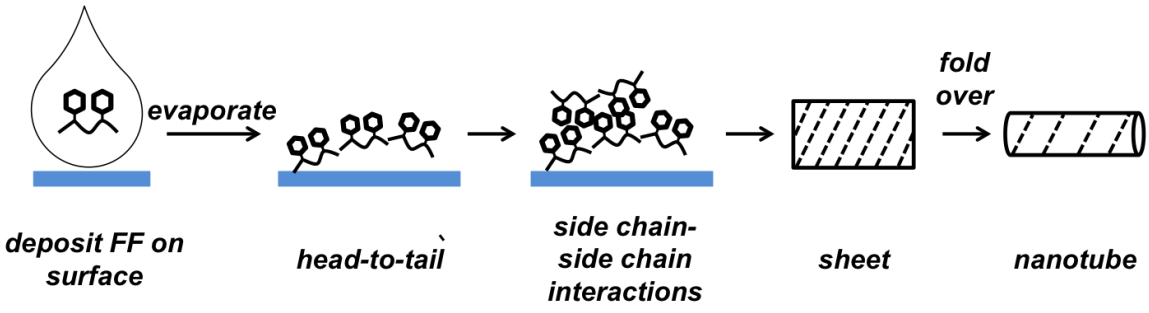

Figure 7. The mechanism of FF self-assembly proposed by Krishnan and co-workers. After deposition on the surface (and solvent evaporation), FF first orientates into a head-to-tail manner. β-sheet structure is then templated by side chain interaction, followed by the formation of sheet-like structures that fold over to form nanotubes.

An in-depth study into the mechanism of FF self-assembly was undertaken by Gazit and co-workers, who explored the self-assembly behaviour of Boc-FF.[40] Boc-FF was chosen as previous reports had demonstrated that introducing ethanol into the solvent mixture could promote vesicle, rather than nanotube, formation.[40] Prior to initiating self-assembly, Boc-FF was held in a supersaturated solution followed by dilution into solvent mixtures with different water/ethanol ratios (the concentration of Boc-FF was also varied). At the lowest concentration of Boc-FF and the highest water/ethanol ratio tested, Boc-FF formed nanotubes, however, as the concentration of Boc-FF was increased two distinct populations (spheres and nanotubes) were observed.[40] To fully characterise the sphere-nanotube transition, a scanning electron microscopy (SEM) time course was performed. After dilution of Boc-FF into the water/ethanol mixture, spherical aggregates were initially visible (t = 20 min), followed by dissolution of these aggregates and the formation of fibrils (t = 30 min) and then nanotubes (t = 45 mins). Placing the self-assembly reaction in a small volume capillary supressed tube formation, indicating that this is a nucleation dependent process (in agreement with previous studies).[47] Further examination of the spherical aggregates demonstrated that they changed size progressively over a period of time, and given that the monomer concentration did not change during this process, the author's likened this to Ostwald ripening.[40] Ostwald ripening is the processes by which smaller particles dissolve to preferentially form larger particles.[48] In this system, during the spheres rearrangement, monomers preferentially desolvate from small spheres (where the fraction of solvent exposed peptides is higher) in order to join larger spheres (where the fraction of solvent exposed peptides is lower). Given the highly charged nature of the spheres, tube formation via coalescence of these aggregates was deemed unlikely. The nanofibrils were observed to undergo disassembly prior to the formation of the nanotubes, with nucleation of the nanotubes occurring close to the site of fibril disassembly. A significant drop in free monomer concentration was observed during the period of tube growth. Taken together, the authors proposed the mechanism outlined in Figure 8, in which the tubes are the most thermodynamically stable structure and are formed in a nucleation dependent process, sequestering monomeric FF that is available in solution (and monomers lost from the spherical aggregates during the Ostwald ripening process). The author's noted that these results were agreement with Ostwald's rule of stages (in which the least energetically stable structure is formed first).

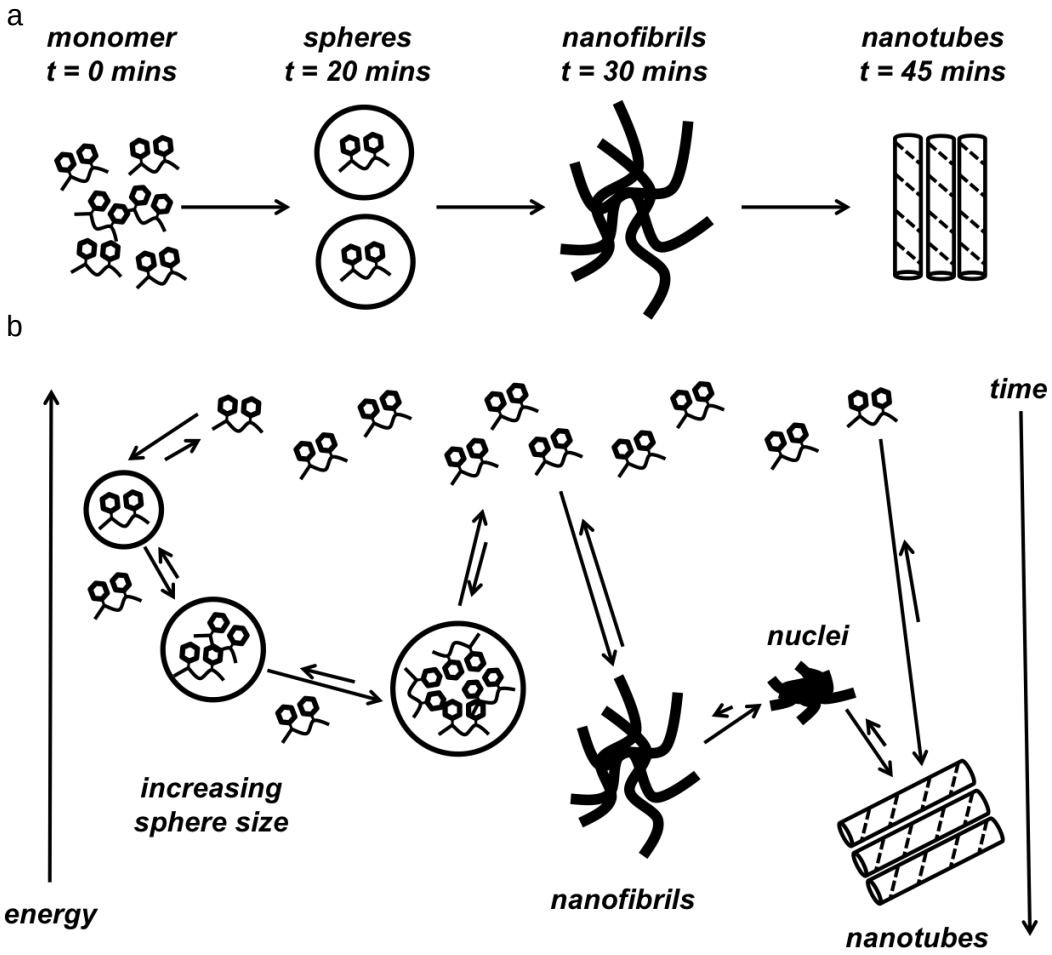

Figure 8. The mechanism of Boc-FF self-assembly proposed by Gazit and co-workers. Boc-FF forms three major species during the self-assembly process (a), with the spheres and nanofibrils being metastable species that disassemble, prior to nucleation and nanotube formation (b).

1.5 The kinetics and thermodynamics of peptide self-assembly: FF as a model peptide

As the study above elegantly demonstrates, peptide self-assembly exists on a complex energy landscape in which multiple species can occupy low energy minima.[3] Although the products of peptide self-assembly (i.e. nanotubes and fibrils) may form thermodynamic minima on the energy landscape, the significant effect that temperature, pH and solvent conditions can exert on these systems emphasises the importance of kinetic factors in peptide self-assembly.[9] The formation of FF into spherical structures, via a change in solvent conditions, highlights that, despite the nanotube structure being the lowest energy structure, tuning of the kinetic parameters can trap otherwise metastable structures.[9,40,42] FF is thus an interesting model with

which to explore the fundamental kinetic and thermodynamic factors involved in peptide self-assembly.

Gazit and co-workers extended their work on FF by establishing the thermodynamic parameters of self-assembly.[49] To do this, the critical concentration (i.e. the concentration below which no aggregation occurs) of FF in pure water was determined. The total peptide concentration was then assessed against the peptide concentration left in solution. A linear relationship was discovered (however deviation did occur upon reaching the critical concentration), indicating that FF has a large barrier to primary nucleation. Assessing the variation in critical concentration over a range of temperatures allowed the calculation of the enthalpy, entropy and free energy of activation. This analysis demonstrated that FF self-assembly closely follows the expected energy profile of a hydrophobic peptide undergoing desolvation, with the overall change in the free energy of activation dominated by entropy at low temperatures and enthalpy at high temperatures.[49] These results highlight that the hydrophobic and aromatic character of FF is largely responsible for its thermodynamic signature. Interestingly, this balance of thermodynamic components at different temperatures was also found for amyloidogenic peptides with longer amino acid sequences.[50,51]

The above sections demonstrate that using small peptide models, such as FF, can allow the thorough exploration of the thermodynamic and kinetic components of molecular self-assembly. Understanding these principles has allowed the rational design of a number of remarkable materials with unique properties, emphasising the advance in this area that the scientific community has made in the last 30 years. Taking these insights and applying them to longer, more biologically relevant sequences will be key in combating an increasing number of devastating diseases in which self-assembling peptides, referred to as amyloid, are implicated. The rest of this chapter will focus on this pathological state and will outline the molecular fibril structure, structural mechanism and kinetic model of amyloid self-assembly. This will be done by focusing on the Aβ peptide, the sequence implicated in the progression of AD, a widely studied and still not fully understood self-assembling peptide.

1.6 Amyloid: Definition and general comments

Amyloid was first observed and named by Rudolf Virchow in 1854, who noted that a substance in brain tissue stained blue when treated with iodine, a common test for the presence of starch, hence the name amyloid (from the Greek amylon and Latin amylum for starch).[52] Since the identification of neurofibrillary tangles, by Alois Alzheimer in 1906, in the brain of a patient suffering dementia, the study of amyloid has emerged as major area for scientific enquiry.[6,12,13,53] As a wide variety of proteins with diverse functions and sequences have been shown to form amyloid, the identification of a structure as amyloid has historically relied on certain characteristics: rigid unbranched fibrils that have a cross-β X-ray diffraction pattern that are deposited extracellularly *in vivo* and display green-gold birefringence when bound to Congo Red.[29,53] Using this definition, there are 36 positively identified proteins that can be classed as amyloid.[29] However, the identification of a number of proteins/peptides that do not exhibit all of these requirements, but go on to form highly ordered fibril structures *in vitro* has led to a structural definition being employed by biophysicists, based on the cross-β X-ray diffraction pattern.[53] Using this definition, there may be over 50 disorders that are related to the deposition of amyloid fibrils.[12] Prevalent diseases such as type II diabetes, AD, PD and systemic amyloidoses have all been linked to the deposition of amyloid proteins/peptides, whether extraceullarly (AD) or intracellularly (PD).[6] Furthermore, the acknowledgement that amyloid may represent a global energy minimum available to all polypeptide chains, and that the native state of a protein may only be a metastable state that is prevented from forming amyloid by high kinetic energy barriers, only serves to highlight the need to understand the amyloid self-assembly process at the molecular level (Figure 9).[6,12]

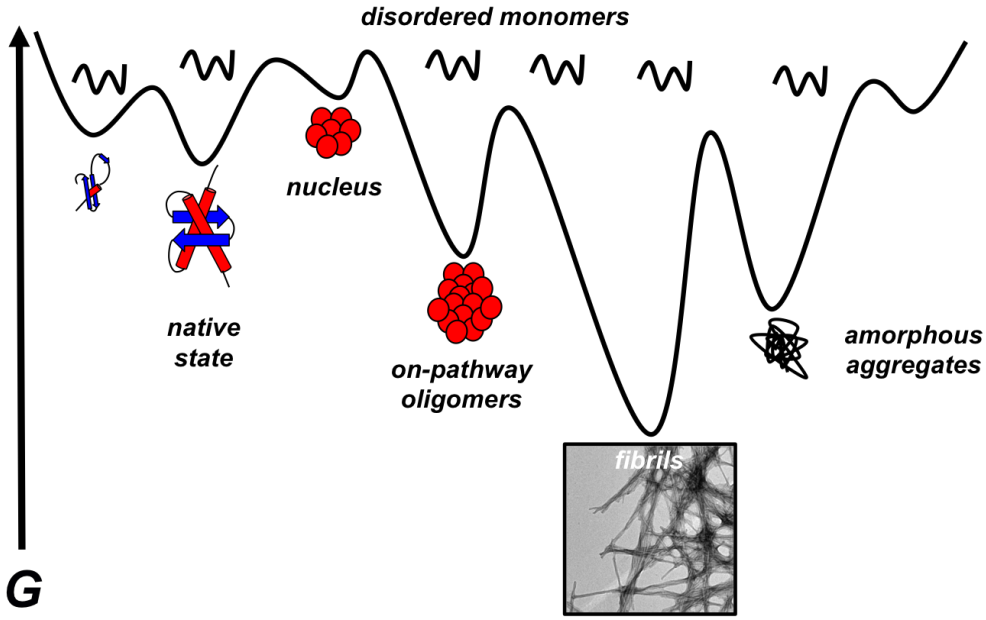

Figure 9. The energy landscape for amyloid assembly. Peptides/proteins can begin as random coil monomers (black) that spontaneously fold into a functional, native state. The native state (or an intrinsically disordered protein) may then aggregate, eventually forming a stable nucleus. This nucleus can in turn go on to form on-pathway oligomers, which will eventually form amyloid fibrils. The fibrils occupy a low-energy minima on the energy landscape.

1.7 The structure of an amyloid fibril

As described above, the unifying factor that connects amyloid peptides is the underlying molecular fibril structures. The fibrils are highly ordered supramolecular structures that are formed of β-strands, arranged perpendicular to the long axis of the fibril with an intersheet distance of 9 – 10 Å and intrastrand distance of ~4.8 Å (as deduced from X-ray diffraction studies).[53–56] The diameter of the fibrils can vary, depending on the number of individual protofilaments that twist together to form the observed "rope–like" fibrils, although they are typically 50 – 100 Å in diameter (Figure 10a).[55,56] Due to the highly extended nature of a β-strand (the dihedral angle around the C_α bond is φ = ~-120° and ψ = ~+120°), the hydrogen bonds between each β-strand are approximately planar.[57] The underlying β-strands can either be orientated in parallel (i.e. all the C_α-C_β bond vectors point in the same direction, Figure 10b) or antiparallel fashion (i.e. the C_α-C_β bond vectors alternate, Figure 10c). Each β-strand can also be considered to have two faces (unless each side chain is identical) and the side chain packing arrangement has been shown to form a dry interface from which water is excluded, referred to as a "steric zipper".[58–61]

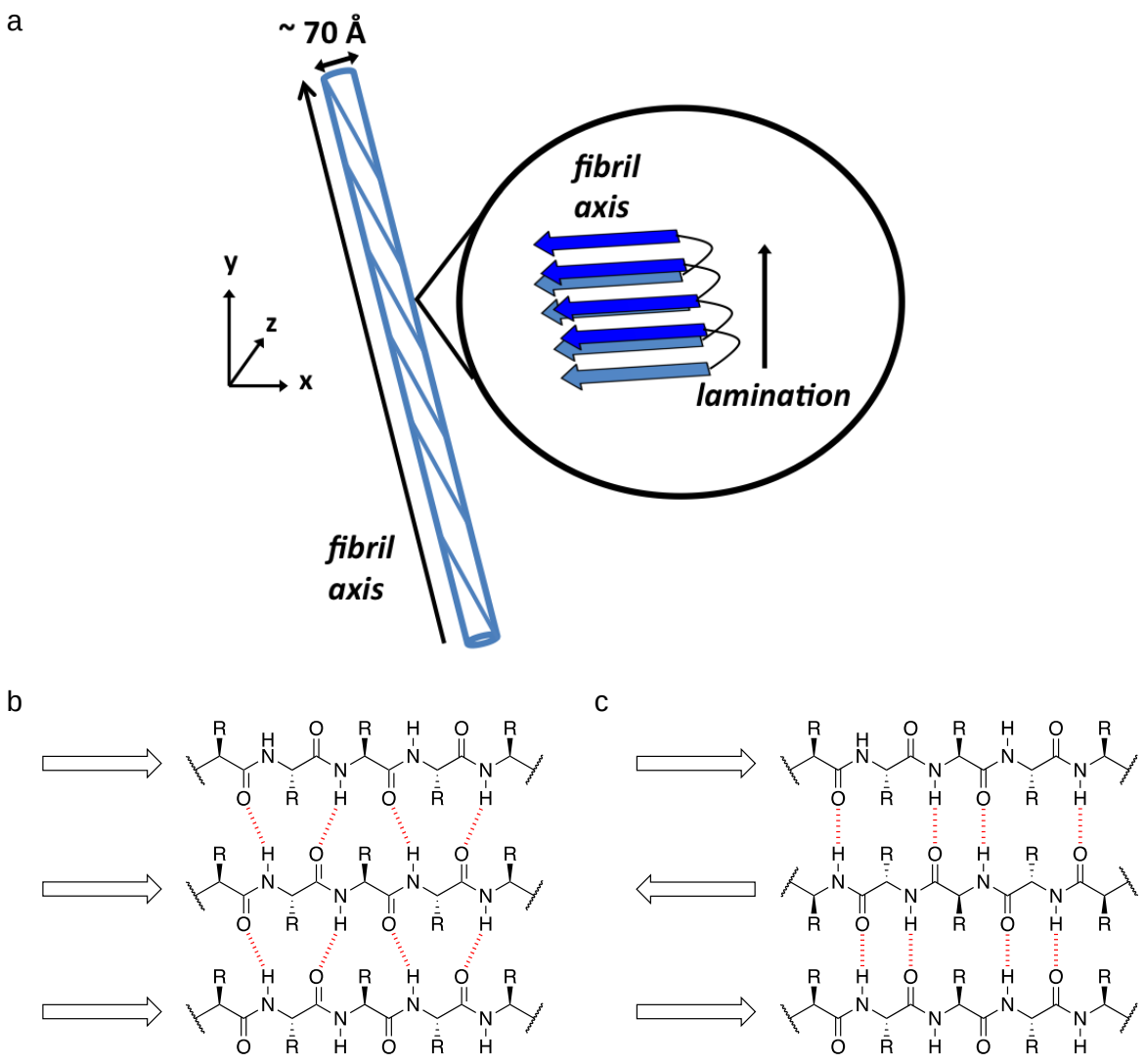

Figure 10. The underlying molecular structure of an amyloid fibril. Individual β-strands are orientated perpendicular to the long axis of the fibril (a). Different hydrogen bonding patterns are available within β-sheets, which can either be in parallel (b) or antiparallel (c) orientations.

1.8 The amyloid-β (Aβ) peptide

A widely studied and clinically important amyloidogenic sequence is the Aβ peptide, a major component of the extracellular plaques observed in AD.[62,63] Aβ is generated by the sequential proteolytic cleavage of the Amyloid Precursor Protein (APP), a transmembrane protein with a large extracellular domain.[64,65] APP is processed by the concerted action of BACE (β-site APP cleavage enzyme) secretase in the ectodomain and the γ-secretase in the transmembrane domain. The Aβ sequence is located between these two sites and a variety of peptides can be generated depending on the

site of cleavage (Table 1).[66–68] The most abundant of these peptides is 40 residues long ($A\beta_{40}$), although the more hydrophobic 42 residue variant ($A\beta_{42}$) may be more important clinically as it has been shown to have a much greater propensity for aggregation and is more neurotoxic.[69–72] Interestingly, some research indicates that $A\beta_{40}$ may play a protective role in AD and it is the ratio of the two peptides that is important.[73,74] The exact role of the Aβ peptide in the progression of AD is still not fully understood, however, a body of evidence now implicates the soluble, oligomeric intermediates that are formed during self-assembly as the neurotoxic species.[75–81]

Peptide	Amino Acid Sequence								
$A\beta_{1-37}$	DAEFR	HDSGY	EVHHQ	KLVFF	AEDVG	SNKGA	IIGLM	VG	
$A\beta_{1-38}$	DAEFR	HDSGY	EVHHQ	KLVFF	AEDVG	SNKGA	IIGLM	VGG	
$A\beta_{1-39}$	DAEFR	HDSGY	EVHHQ	KLVFF	AEDVG	SNKGA	IIGLM	VGGV	
$A\beta_{1-40}$	DAEFR	HDSGY	EVHHQ	KLVFF	AEDVG	SNKGA	IIGLM	VGGVV	
$A\beta_{1-42}$	DAEFR	HDSGY	EVHHQ	KLVFF	AEDVG	SNKGA	IIGLM	VGGVV	IA
$A\beta_{1-43}$	DAEFR	HDSGY	EVHHQ	KLVFF	AEDVG	SNKGA	IIGLM	VGGVV	IAT
$A\beta_{3-40}$	EFR	HDSGY	EVHHQ	KLVFF	AEDVG	SNKGA	IIGLM	VGGVV	
$A\beta_{3-42}$	EFR	HDSGY	EVHHQ	KLVFF	AEDVG	SNKGA	IIGLM	VGGVV	IA
$A\beta_{3-43}$	EFR	HDSGY	EVHHQ	KLVFF	AEDVG	SNKGA	IIGLM	VGGVV	IAT
$A\beta_{3(pE)-42}$	pEFR	HDSGY	EVHHQ	KLVFF	AEDVG	SNKGA	IIGLM	VGGVV	IA
Residue N.	1	6	11	16	21	26	31	36	41

Table 1. The amino acid sequence of Aβ variants that have been identified *in vivo*.

1.9 The structure of $A\beta_{40}$ fibrils grown *in vitro*

The inherent heterogeneity of $A\beta_{40}$ fibrils made elucidating the underlying β-sheet structure difficult for many years.[82] Some constraints could be placed on the fibril structure based on the diameter of fibrils (as measured by EM and atomic force microscopy (AFM)) and, given that it was amyloid, it was known that some, or all, of the backbone amides must be engaged in hydrogen bonding.[82–84] Studies undertaken by Wetzel and co-workers, using proteolytic digestion and hydrogen-deuterium exchange (HDX) mass spectrometry demonstrated that not all of the residues were engaged in hydrogen bonding, with the N-terminal residues (up to K16) prone to both exchange and proteolytic degradation.[83,84] The use of solid-state nuclear magnetic resonance (ssNMR) spectroscopy by Tycko and co-workers has allowed a model of $A\beta_{40}$ fibrils to

be established (when incubated under agitated conditions).[85–87] In this model, the N-terminal region (residues 1 – 10) is flexible, with two parallel, in-register β-sheets (12 – 24 and 30 – 40) connected by a flexible turn region (25 – 29) and a salt bridge between D23 and K28 (Figure 11a).[86,87] Two cross-β units (i.e. two $A\beta_{40}$ peptides) form the observed diameter for $A\beta_{40}$ fibrils. One notable feature of $A\beta_{40}$ is the polymorphism displayed by the fibrils when incubated under different conditions.[88,89] In the second model, formed when $A\beta_{40}$ is grown under quiescent conditions has three $A\beta_{40}$ peptides making up the monomeric unit, with the same in-register parallel β-sheet structure observed when incubated under quiescent conditions (Figure 11b).[90] When viewed by EM, the fibrils grown under quiescent conditions appear as twisted helical structures. Another model has been proposed by Bertini and co-workers, closely resembling the underlying fibril structure that $A\beta_{40}$ forms under agitated conditions, however, the β-sheets now constitute residues 11 – 23 and 31 – 40.[91]

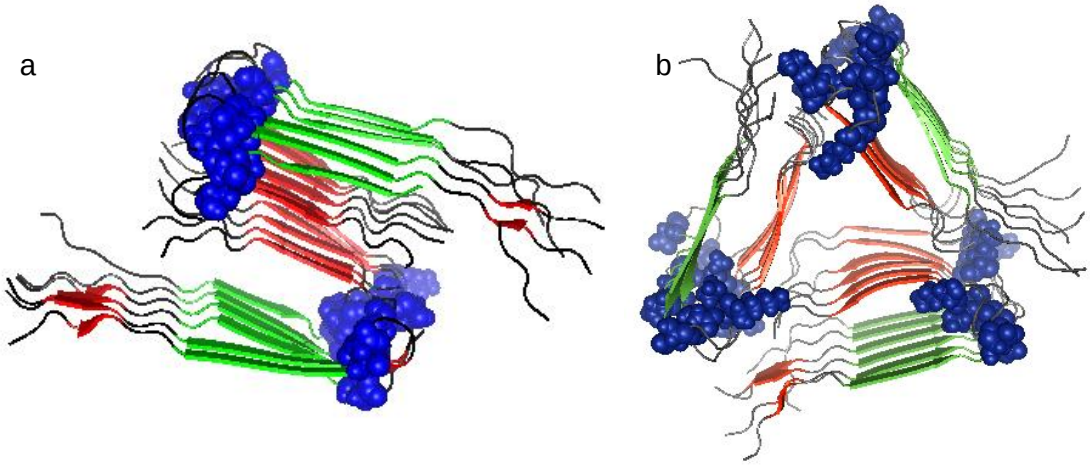

Figure 11. The underlying fibril structures of $A\beta_{40}$ grown *in vitro* under either agitated (a, "striated ribbon", PDB: 2LMN, adapted from reference 90) or quiescent conditions (b, "twisted helical", PDB: 2LMP, adapted from reference 90). The β-sheets are coloured in red, any residues involved salt bridge interactions are highlighted in blue and the central region $A\beta_{16\text{-}22}$ is highlighted in green. Images were created with Pymol, 2018.

1.10 The structure of $A\beta_{42}$ fibrils grown *in vitro*

Although $A\beta_{40}$ forms at least three fibril polymorphs, the underlying β-sheet arrangement stays relatively consistent (Figure 11).[90–92] This is not the case for $A\beta_{42}$, in which a number of different underlying structures have been proposed, using both ssNMR and cryo-EM.[93–96] The ssNMR structure of $A\beta_{42}$, proposed by Ishii and co-workers, contained three parallel, in-register β-sheets (residues V12 – F20, N27 – I32

and V36 – I41) connected by two loop regions (A21 – S26 and G33 – M35) with a salt bridge between K28 and the C-termini of A42 (Figure 12a).[93] In contrast, Riek and co-workers proposed a structure in which each $A\beta_{42}$ has five in-register, parallel β-sheets that wind around two hydrophobic cores in a double horseshoe arrangement, with significant stabilisation coming from ladders of N and Q residues running down the axis of the fibril (Figure 12b).[94] Two other proposed fibril structures can be seen in Figures 12c and d.[95,96] Despite these differences, all of these structures bury the hydrophobic C-termini residues within the core of the fibril, confirming the importance of these

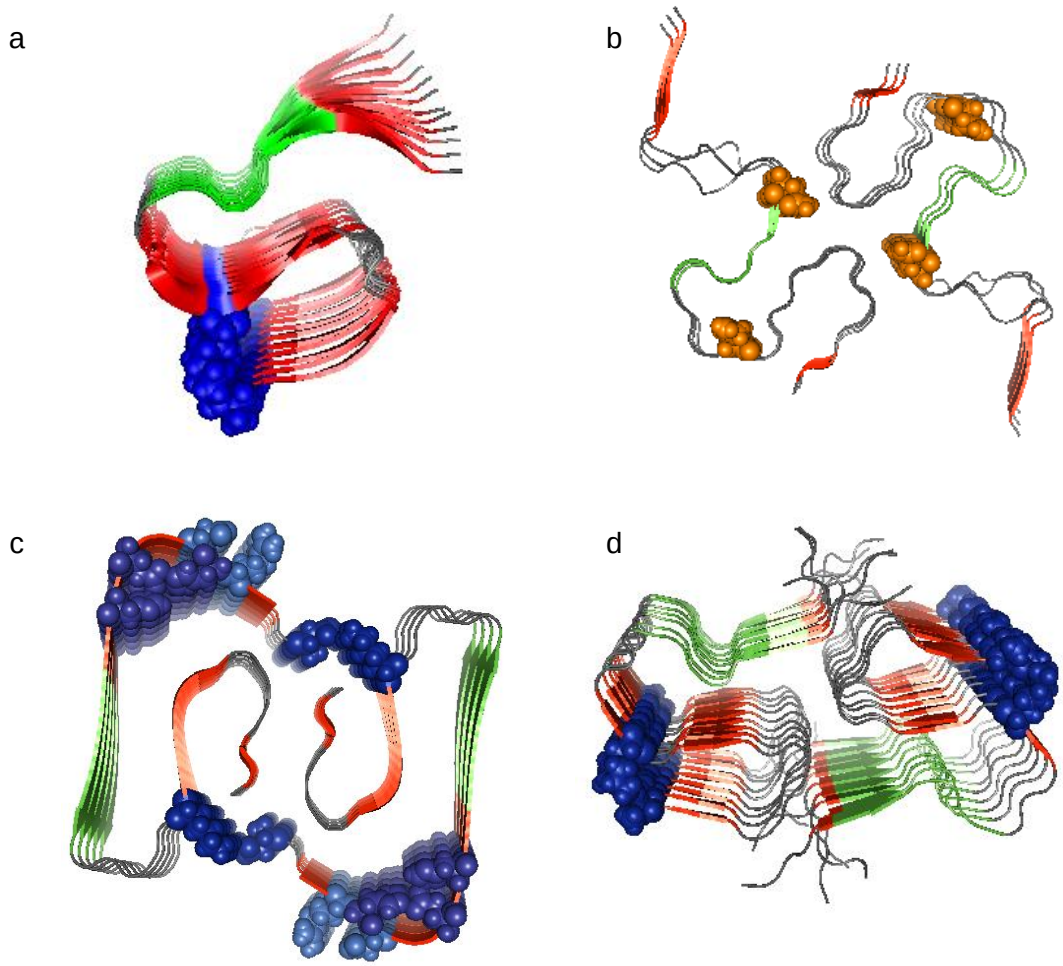

Figure 12. The different models of $A\beta_{42}$ fibrils grown *in vitro*. (a) PDB: 2MXU; adapted from reference 93, (b) PDB: 2NAO; adapted from reference 94, (c) PDB: 5OQV; adapted from reference 95, the different shades of blue indicate that multiple salt bridge interactions are formed in this structure and (d) PDB: 5KK3; adapted from reference 96. Red indicates β-sheet structure, blue indicates residues that are involved in salt bridge interactions, orange indicates the N and Q ladders and green represents $A\beta_{16-22}$. Images were created with Pymol, 2018.

residues for the aggregation propensity of $A\beta_{42}$.[69]

1.11 The structure of Aβ fibrils *in vivo*

Understanding the underlying fibril structures formed by $A\beta_{40/42}$ *in vitro* is important in order to build up a molecular picture of the self-assembly process, however, they may differ significantly from the structures formed *in vivo*. As such, studies that can extract and isolate Aβ from tissue samples and elucidate structural information are highly valuable. Tycko and co-workers developed an approach whereby they can seed ^{15}N and ^{13}C labelled $A\beta_{40/42}$ with extracts from patients with AD followed by structural characterisation by ssNMR.[97,98] Using this method, they demonstrated that, when seeding labelled $A\beta_{40}$ with tissue from two different AD patients, a single predominant $A\beta_{40}$ polymorph was present in each case.[97] The fibrils formed from each patient had different structures, with both of these structures being different to those seen *in vitro (*Section 1.10). One of these fibril polymorphs was analysed further and was shown to have parallel, in-register β-sheets with three-fold symmetry down the long axis of the fibril (stabilised by a salt bridge between D23 and K28, Figure 13). Novel features of this structure included a twist in residues 19 – 23 (such that F10 and E22 are buried into the fibril core) and a kink at G33, allowing the side chains of I32 and L34 to point in different directions. This work was extended by taking thirty-seven tissue samples from eighteen patients with different types of AD: rapidly progressing (r-AD), posterior cortical atrophy (PCA-AD) and typical prolonged-duration (t-AD).[98] In this work, the authors found that a single predominant form of $A\beta_{40}$ was the most abundant in patients with PCA-AD and t-AD, whereas those with r-AD had $A\beta_{40}$ with significantly higher proportion of additional structures. $A\beta_{42}$ also demonstrated much more heterogeneity, with at least two prevalent structures being observed in the tissues.

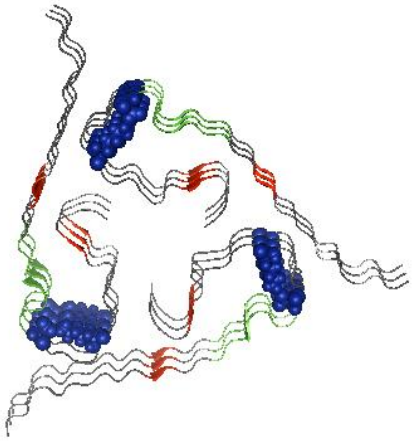

Figure 13. The ssNMR structure of $A\beta_{40}$ fibrils that have been seeded from AD brain tissue (PDB: 2M4J; adapted from reference 97). Red indicates β-sheet structure and green indicates $A\beta_{16\text{-}22}$. Image created using Pymol, 2018.

1.12 Amyloid aggregation kinetics

A characteristic of amyloid self-assembly is the sigmoidal growth curve observed using dyes, such as Thioflavin-T (ThT), that bind quantitatively to amyloid fibrils.[99–103] In these assays, Aβ displays a sigmoidal growth curve with three distinct phases: a lag phase, exponential growth phase and (if in a system with a defined monomer concentration) a plateau (Figure 14a).[100,104,105] This curve shape is associated with a nucleated growth mechanism.[104–106] Aβ is an intrinsically disordered peptide that initially starts in solution as a monomer. If the peptide is below the critical concentration for self-assembly, Aβ will stay as a homogenous monomeric solution indefinitely, due to the high kinetic barriers associated with oligomer formation.[106,107] The spontaneous coalescence of these peptide monomers is highly unlikely and, as such, growth must occur via the formation of critical nuclei (when the total peptide concentration is above the critical concentration, Figure 14b). A nucleus can be defined as the smallest aggregate that is stable enough such that it would rather grow than dissociate back into its constituent monomers. Small aggregates that have not reached this size are likely to dissociate, due to the high interfacial energy between the aggregate and the aqueous environment.[106]. This process, in which monomeric peptide units come together to form a nucleus is termed primary nucleation.[105,106] Primary nucleation can be homogeneous (i.e. occurs in bulk solution) or heterogeneous (i.e. occurs at a foreign surface) and its rate is solely dependent on the initial monomer concentration. The formation of nuclei is an obligatory step on the reaction pathway and nuclei occupy the highest point on the free energy landscape. It should be noted that the lag phase does not correlate

with the formation of nuclei, as this process occurs throughout the course of the reaction. Once the nuclei have gone on to form oligomers and then fibrils a variety of secondary pathways can occur: elongation, fragmentation and secondary nucleation.[105,106] It should be noted that these secondary processes can occur after the formation of a nucleus, however, as ThT measures fibrillar content, for clarity, the discussion around secondary pathways will refer to either monomers or fibrils as the dominant species contributing to the kinetic mechanism.

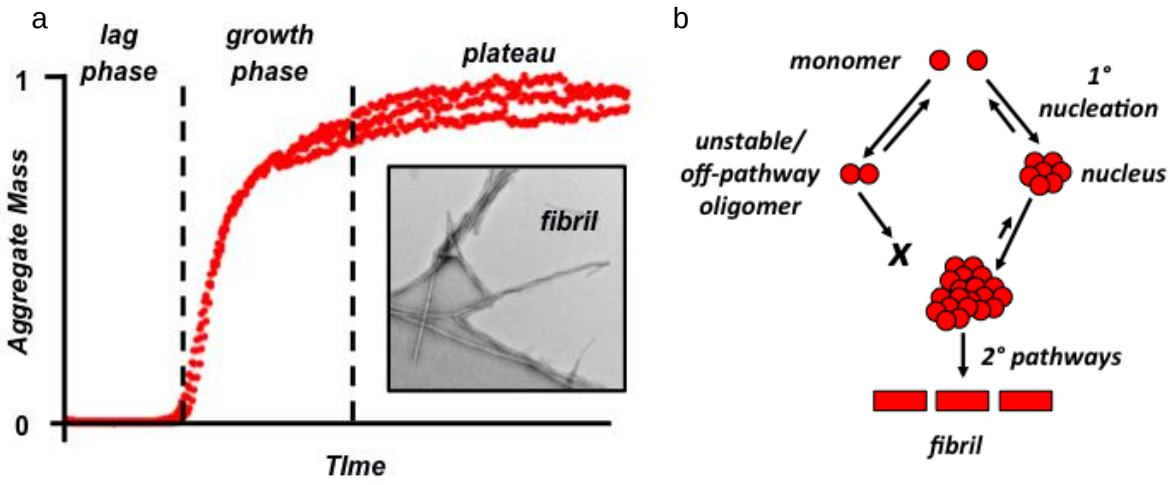

Figure 14. The sigmoidal growth curve of amyloid peptides such as Aβ (a) and a simplified reaction network of the microscopic processes involved in aggregation (b). Inset shows negative stain TEM image of $A\beta_{16-22}$ (unpublished data).

1.12.1 Elongation

Elongation, whereby soluble peptides add onto fibril ends, is the primary mechanism for the growth of amyloid fibrils (Figure 15a).[108] If the soluble peptide is monomeric, this process has been shown to have first order kinetics with respect to the concentration of both monomers and fibrils and, as such, is generally thought to proceed through a two-step mechanism.[109] In this mechanism, the soluble peptide initially docks on the end of the fibril, prior to undergoing a rearrangement step and being fully incorporated into the fibril structure. This mechanism is supported by the experimental observation that elongation can become saturated at high monomer concentrations as well as MD simulations exploring this process (Figure 15b).[108,110]

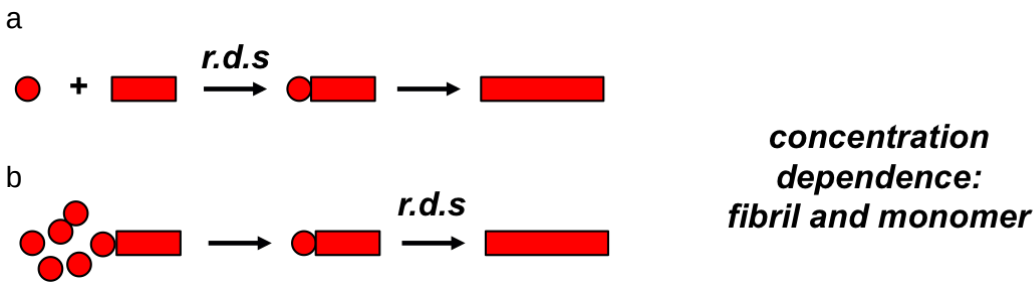

Figure 15. Simplified schematic of fibril elongation (a). Under high monomer concentrations, this process can become saturated, causing the rearrangement step to become rate determining (r.d.s., b). Red circles = monomer, red block = fibrils/oligomers.

1.12.2 Surface catalysed secondary nucleation

Secondary nucleation is defined as a process whereby monomers form a nucleus on the surface of a preformed aggregate that consists of the same monomeric building blocks (distinguishing it from heterogeneous primary nucleation).[106] Secondary nucleation can be thought of as having three steps: monomer attachment (the rate of which is monomer dependent), formation of nuclei on the fibril surface followed by the loss of the nuclei from the fibril surface (the rate of both steps in monomer independent, Figure 16a). As with elongation, this process is sensitive to both monomer and fibril concentration and can become saturated at high monomer concentrations.[102,106] If the concentration of monomers is such that the fibril surface is consistently filled then the rate-determining step will be the detachment of the nuclei from the fibril surface (Figure 16b). Although noted as a key driver of amyloid kinetics, the underlying molecular mechanism of this process is still not fully understood.[106] For example, it is not known whether, after binding to the surface, the monomers form oligomers that can go on and catalyse reactions (i.e. formation of nuclei on the surface) or whether they exit the surface as disordered oligomers that then undergo a rearrangement step (i.e. formation of nuclei in solution). Furthermore, it is not known whether secondary nucleation occurs as a diffuse process (i.e. all over the fibril surface) or whether it occurs at specific sites. Experimental observations would seem to indicate a high degree of structural similarity is needed for secondary nucleation (i.e. $A\beta_{40}$ fibrils cannot seed $A\beta_{42}$ growth) and may therefore occur at specific sites on the fibril surface.[106,111]

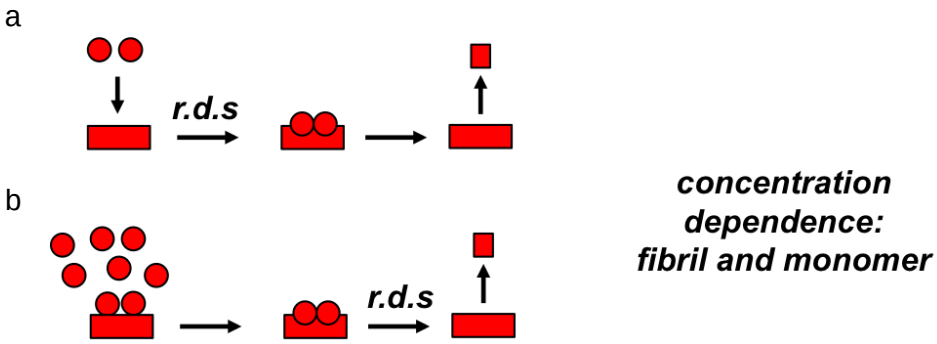

Figure 16. Simplified schematic of surface catalysed secondary nucleation (a). Under high monomer conditions, this process can become saturated, causing the rearrangement step to become rate determining (r.d.s., b). Red circles = monomer, red block = fibrils/oligomers.

1.12.3 Fragmentation

Fragmentation is the process by which a single fibril breaks down into fibrils of shorter length, increasing the aggregate mass exponentially (Figure 17).[108,112] As a single fibril has two ends (by which it can potentially grow through elongation, see above, and a surface on which other monomers can then nucleate) however, when it breaks down into two smaller fibrils there are now potentially four ends on which new monomers can add. As fragmentation is solely based on the concentration of fibrils, this process can be considered to be monomer independent.[100,108] For Aβ, fragmentation has been shown to be negligible under quiescent conditions, whereas for prion proteins fragmentation is key, even impacting on whether or not a strain is infectious.[102,113,114]

Figure 17. Simplified schematic of fibril fragmentation.

1.12.4 The role of seeding in understanding amyloid assembly mechanisms

Given the complex nature of amyloid self-assembly reactions (in which there are multiple molecular processes all contributing to aggregate growth) strategies are needed that can help to isolate certain pathways. A powerful method with which to do this is by taking preformed fibrils (referred to as “seeds”) and introducing them into the pool of monomers (Figure 18a).[100,105] Seeding a reaction with preformed fibrils bypasses the slow primary nucleation step (effectively lowering the kinetic barrier to aggregation), allowing the reaction to proceed through secondary processes (described above). At high seed concentrations the overall rate of aggregation has been shown to be dominated by elongation (as there are now a significant number of fibril ends introduced into the reaction, Figure 18b).[100] At low seed concentrations however, the rate is dominated by surface catalysed nucleation (as there is now a lower end to surface area ratio, Figure 18b).[100]

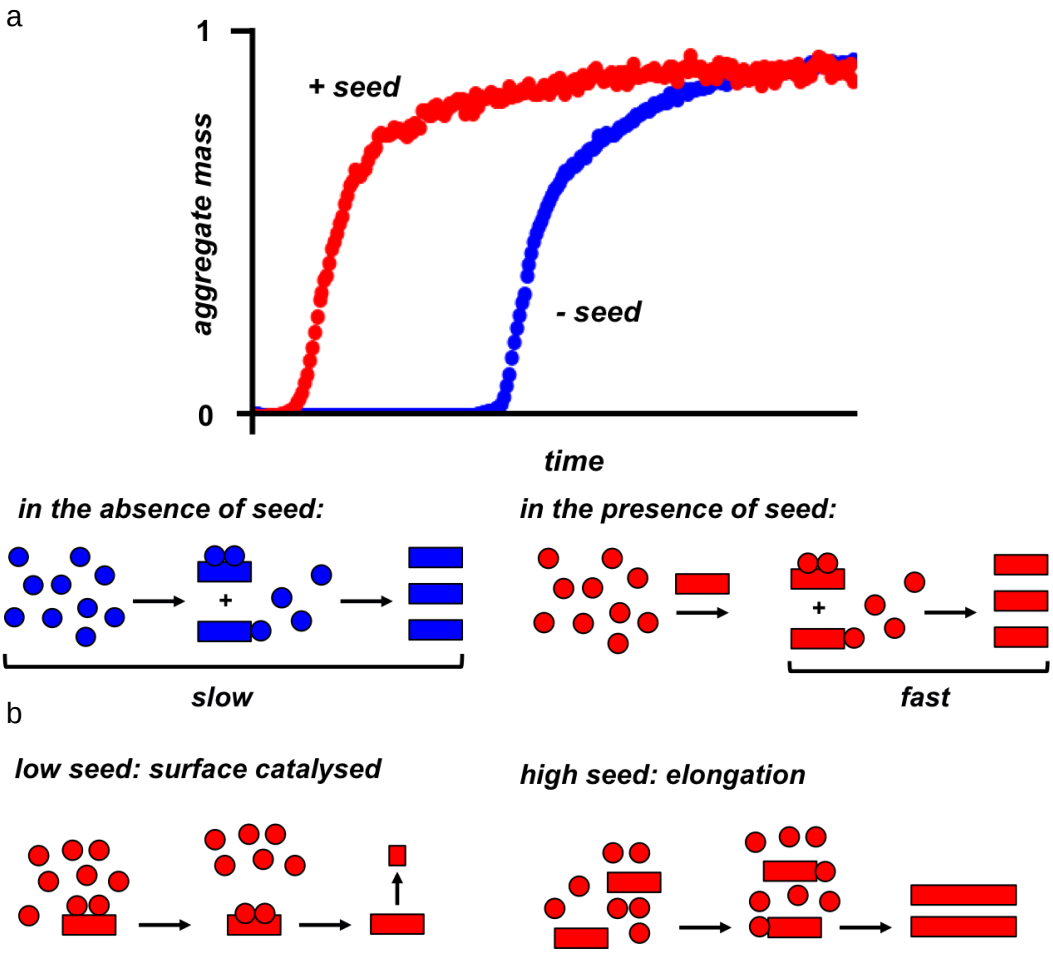

Figure 18. The effect of seeding on an amyloid self-assembly reaction. By introducing preformed fibrils (i.e. seeds, red) the rate of aggregation can be dramatically increased compared to when a seed is absent (blue, a). Under low seed concentrations (<5%) surface catalysed mechanism dominates, whereas at high seed concentration (>20%) elongation dominates (b).

1.13 The underlying kinetic mechanism of $A\beta_{40/42}$ amyloid formation

The microscopic processes important for the self-assembly of $A\beta_{42}$ were uncovered in a series of elegant studies performed by Linse, Dobson and Knowles in which they established that $A\beta_{42}$ aggregation is dominated by secondary nucleation.[102] Three lines of evidence supported this conclusion: global kinetic analysis of $A\beta_{42}$ aggregation under a variety of regimes, the influence of seeding on $A\beta_{42}$ aggregation, and assays using radiolabelled peptides. The global kinetic analysis demonstrated that no models for fragmentation/primary nucleation would fit the observed rate of fibril formation, however, a model that included primary nucleation, secondary nucleation and fibril growth did fit the kinetic analysis. This was confirmed via seeding experiments with the addition of preformed $A\beta_{42}$ seeds having a dramatic effect on the rate of aggregation. Experiments in which preformed $A\beta_{42}$ seeds were added to a pool of radiolabelled $A\beta_{42}$ monomers demonstrated that the aggregates formed were solely formed from monomers that had nucleated on the fibril surface, rather than an elongation based mechanism (where a mixture of unlabelled and labelled would be expected). These authors extended this work by comparing the fibril formation kinetics of $A\beta_{40}$ and $A\beta_{42}$, demonstrating that although the dominant mechanism was still secondary nucleation, the rate constants for all processes were smaller for $A\beta_{40}$ relative to $A\beta_{42}$.[115] In particular, the contribution of primary nucleation to $A\beta_{40}$ aggregation was reduced by an order of magnitude, indicating a much higher kinetic barrier to $A\beta_{40}$ aggregation. After establishing the mechanism of Aβ aggregation, including a mathematical description of the microscopic processes, the authors then moved on to characterise the thermodynamic parameters for each process.[116] Surprisingly, this analysis demonstrated that secondary nucleation has a different thermodynamic signature, namely that it has a favourable enthalpy of activation and unfavourable entropy. In contrast, primary nucleation and elongation demonstrated the reverse, with a favourable entropy of activation and unfavourable enthalpy.

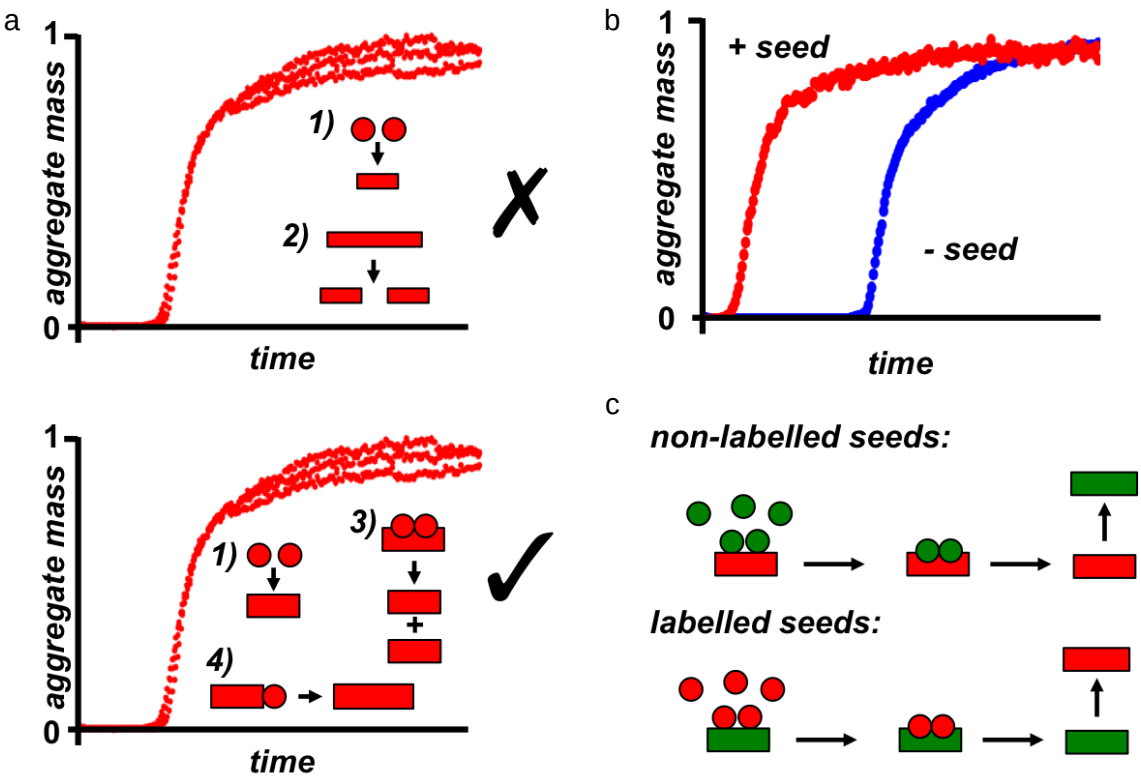

Figure 19. The evidence for surface catalysed secondary nucleation being the driver of $A\beta_{42}$ aggregation. Using a global kinetic analysis, Knowles, Dobson, Linse and co-workers demonstrated that a primary nucleation (1) and fragmentation (2) mechanism did not fit with the observed rate of $A\beta_{42}$ aggregation (top), whereas a model with primary nucleation (1), surface catalysed secondary nucleation (3) and elongation (4) does fit (bottom). The dramatic effect of self-seeding also supported the role of secondary processes in the aggregation rate of $A\beta_{42}$ (b). When introducing $A\beta_{42}$ fibrils into a pool of radiolabelled monomers, the aggregates that are formed are solely formed from the radiolabelled monomers, indicating that surface catalysed surface nucleation is the dominant driver of $A\beta_{42}$ aggregation (c).

1.14 Understanding the structural changes that occur during amyloid assembly

The above sections have described the extensive work performed in order to understand the overall kinetics, thermodynamics and structural end-points of amyloid self-assembly. Despite this work, a significant gap still exists in our knowledge: characterisation in molecular detail of the structural transitions that occur during the early stages of aggregation. This task represents a challenge to the standard techniques used in the biological sciences, such as NMR, CD and IR, as these techniques all give population average data. It is well known that fleeting structural intermediates, such as the intermediary I_T state in β_2-microglobulin, can have a

significant impact of the overall aggregation of the system. As such, techniques that can trap and analyse these structural intermediates, particularly techniques that can then relate these changes to time will be important in fully understanding this complex biological process.

In Chapter 2, the aggregation of model peptide ($A\beta_{16-22}$) that incorporates the FF motif and forms the central hydrophobic core region of the Aβ sequence, was studied. The kinetic mechanism was established using fluorescence quenching experiments and an EM time course, allowing the use of photo-induced cross-linking (PIC) and electrospray ionisation-ion mobility spectrometry-mass spectrometry (ESI-IMS-MS) to capture the structural transitions that occur during the early stages of aggregation. These experimental insights were compared with a discontinuous molecular dynamics (DMD) simulation that visualised the entire process. By combining the experimental data and the simulations, the early stages of aggregation can be studied at the molecular level.

Using model peptides, such as $A\beta_{16-22}$, allows techniques and methodologies to be developed that can in turn be used to explore larger, or more complex, aggregating systems. As $A\beta_{16-22}$ represents the core region of the full length sequence, in Chapter 3, the aggregation behaviour of $A\beta_{40}$ was assessed is the presence of $A\beta_{16-22}$, extended the experimental and *in silico* approaches in Chapter 2. The effect of $A\beta_{16-22}$ on $A\beta_{40}$ aggregation was explored using Thioflavin-T (ThT) experiments, demonstrating that the aggregation rate of $A\beta_{40}$ is increased in the presence of $A\beta_{16-22}$. Fluorescence quenching experiments were then performed highlighting that under these conditions $A\beta_{16-22}$ aggregates quickly and is unaffected by the presence of $A\beta_{40}$. The use of seeding experiments identified that it was the fibrillar form of $A\beta_{16-22}$ that had the most impact on the rate of aggregation, despite the identification of heteromolecular oligomers (observed using ESI-IMS-MS). Finally, a combination of PIC experiments and EM experiments confirmed that majority homomolecular fibrils are formed at the end of the self-assembly reaction, confirming that $A\beta_{16-22}$ increases the aggregation rate of $A\beta_{40}$ via a surface catalysed secondary nucleation mechanism. The combined experimental and DMD approach used in Chapter 2 was then applied to the mixed aggregation system, allowing the proposed mechanism to be understood at the molecular level, with particular focus on understanding the structural changes that occur during surface catalysed nucleation.

References:

1 G. M. Whitesides and B. Grzybowski, *Science*, 2002, **295**, 2418–21.

2 B. A. Grzybowski, C. E. Wilmer, J. Kim, K. P. Browne and K. J. M. Bishop, *Soft Matter*, 2009, **5**, 1110.

3 C. M. Dobson, *Nature*, 2003, **426**, 884–890.

4 L. Adler-Abramovich and E. Gazit, *Chem. Soc. Rev.*, 2014, **43**, 6881–6893.

5 X. Yan, P. Zhu and J. Li, *Chem. Soc. Rev.*, 2010, **39**, 1877.

6 F. Chiti and C. M. Dobson, *Annu. Rev. Biochem.*, 2006, **75**, 333–366.

7 A. Marsh, M. Silvestri and J. M. Lehn, *Chem. Commun.*, 1996, 1527–1528.

8 E. Gazit, *Chem. Soc. Rev.*, 2007, **36**, 1263–1269.

9 J. Wang, K. Liu, R. Xing and X. Yan, *Chem. Soc. Rev.*, 2016, **45**, 5589–5604.

10 T. P. J. Knowles and M. J. Buehler, *Nat. Nanotechnol.*, 2011, **6**, 469–479.

11 C. J. C. Edwards-Gayle and I. W. Hamley, *Org. Biomol. Chem.*, 2017, **15**, 5867–5876.

12 T. P. J. Knowles, M. Vendruscolo and C. M. Dobson, *Nat. Rev. Mol. Cell Biol.*, 2014, **15**, 384–96.

13 D. J. Selkoe and J. Hardy, *EMBO Mol. Med.*, 2016, **8**, 1–14.

14 M. W. Kirschner and T. J. Mitchison, *Cell*, 1986, **45**, 329–342.

15 P. De Santis, S. Morosetti and R. Rizzo, *Macromolecules*, 1974, **7**, 52–58.

16 Ghadiri, M. R., Granja, J. R., Milligan, R. A., McRee, D. E., Khazanovich, N., *Nature*, 1993, **366**, 324–327.

17 J. D. Hartgerink, J. R. Granja, R. A. Milligan and M. R. Ghadiri, *J. Am. Chem. Soc.*, 1996, **118**, 43–50.

18 M. Reches and E. Gazit, *Science.*, 2003, **300**, 625–627.

19 J. J. Balbach, Y. Ishii, O. N. Antzutkin, R. D. Leapman, N. W. Rizzo, F. Dyda, J. Reed and R. Tycko, *Biochemistry*, 2000, **39**, 13748–13759.

20 R. Azriel and E. Gazit, *J. Biol. Chem.*, 2001, **276**, 34156–34161.

21 M. Reches, Y. Porat and E. Gazit, *J. Biol. Chem.*, 2002, **277**, 35475–35480.

22 Y. Mazor, S. Gilead, I. Benhar and E. Gazit, *J. Mol. Biol.*, 2002, **322**, 1013–1024.

23 D. G. Lynn and S. C. Meredith, *J. Struct. Biol.*, 2000, **173**, 153–173.

24 C. G. Claessens and J. F. Stoddart, *J. Phys. Org. Chem.*, 1997, **10**, 254–272.

25 M. L. Waters, *Curr. Opin. Chem. Biol.*, 2002, 736–741.

26 C. Hilbich, B. Kisters-woike, J. Reed, C. L. Masters and K. Beyreuther, *J. Mol. Biol.*, 1992, **228**, 460–473.

27 L. O. Tjernberg, D. J. E. Callaway, A. Tjernberg, S. Hahne, C. Lilliehöök, L. Terenius, J. Thyberg and C. Nordstedt, *J. Biol. Chem.*, 1999, **274**, 12619–

12625.

28 C. Wurth, N. K. Guimard and M. H. Hecht, *J. Mol. Biol.*, 2002, **319**, 1279–1290.

29 J. D. Sipe, M. D. Benson, J. N. Buxbaum, S. Ikeda, G. Merlini, M. J. M. Saraiva and P. Westermark, *Amyloid*, 2016, **23**, 209–213.

30 N. Kol, L. Adler-Abramovich, D. Barlam, R. Z. Shneck, E. Gazit and I. Rousso, *Nano Lett.*, 2005, **5**, 1343–1346.

31 L. Adler-Abramovich, M. Reches, V. L. Sedman, S. Allen, S. J. B. Tendler and E. Gazit, *Langmuir*, 2006, **22**, 1313–1320.

32 C. H. Görbitz, *Chem. - A Eur. J.*, 2001, **7**, 5153–5159.

33 Z. A. Arnon, A. Vitalis, A. Levin, T. C. T. Michaels, A. Caflisch, T. P. J. Knowles, L. Adler-Abramovich and E. Gazit, *Nat. Commun.*, 2016, **7**, 1–7.

34 P. Kumaraswamy, R. Lakshmanan, S. Sethuraman and U. M. Krishnan, *Soft Matter*, 2011, **7**, 2744–2754.

35 C. H. Görbitz, *Chem. Commun.*, 2006, 2332–2334.

36 A. Mahler, M. Reches, M. Rechter, S. Cohen and E. Gazit, *Adv. Mater.*, 2006, **18**, 1365–1370.

37 V. Jayawarna, M. Ali, T. A. Jowitt, A. F. Miller, A. Saiani, J. E. Gough and R. V. Ulijn, *Adv. Mater.*, 2006, **18**, 611–614.

38 A. M. Smith, R. J. Williams, C. Tang, P. Coppo, R. F. Collins, M. L. Turner, A. Saiani and R. V. Ulijn, *Adv. Mater.*, 2008, **20**, 37–41.

39 X. Yan, Q. He, K. Wang, L. Duan, Y. Cui and J. Li, *Angew. Chemie - Int. Ed.*, 2007, **46**, 2431–2434.

40 A. Levin, T. O. Mason, L. Adler-Abramovich, A. K. Buell, G. Meisl, C. Galvagnion, Y. Bram, S. A. Stratford, C. M. Dobson, T. P. J. Knowles and E. Gazit, *Nat. Commun.*, 2014, **5**, 1–8.

41 M. Reches and E. Gazit, *Isr. J. Chem.*, 2005, **45**, 363–371.

42 Y. Song, S. R. Challa, C. J. Medforth, Y. Qiu, R. K. Watt, D. Pena, J. E. Miller, F. V. Swol and J. A. Shelnutt, *Chem. Commun*., 2004, 1044–1045.

43 L. Adler-Abramovich, N. Kol, I. Yanai, D. Barlam, R. Z. Shneck, E. Gazit and I. Rousso, *Angew. Chemie - Int. Ed.*, 2010, **49**, 9939–9942.

44 P. Tamamis, L. Adler-Abramovich, M. Reches, K. Marshall, P. Sikorski, L. Serpell, E. Gazit and G. Archontis, *Biophys. J.*, 2009, **96**, 5020–5029.

45 T. D. Do and M. T. Bowers, *Anal. Chem.*, 2015, **87**, 4245–4252.

46 J. Jeon, C. E. Mills and M. S. Shell, *J. Phys. Chem. B*, 2013, **117**, 3935–3943.

47 M. S. Ishikawa, C. Busch, M. Motzkus, H. Martinho and T. Buckup, *Phys. Chem. Chem. Phys.*, 2017, **19**, 31647–31654.

48 A. Kabalnov, *J. Dispers. Sci. Technol.*, 2001, **22**, 1–12.

49 T. O. Mason, T. C. T. Michaels, A. Levin, C. M. Dobson, E. Gazit, T. P. J. Knowles and A. K. Buell, *J. Am. Chem. Soc.*, 2017, **139**, 16134–16142.

50 A. J. Baldwin, T. P. J. Knowles, G. G. Tartaglia, A. W. Fitzpatrick, G. L. Devlin, S. L. Shammas, C. A. Waudby, M. F. Mossuto, S. Meehan, S. L. Gras, J. Christodoulou, S. J. Anthony-Cahill, P. D. Barker, M. Vendruscolo and C. M. Dobson, *J. Am. Chem. Soc.*, 2011, **133**, 14160–14163.

51 A. K. Buell, A. Dhulesia, D. A. White, T. P. J. Knowles, C. M. Dobson and M. E. Welland, *Angew. Chemie Int. Ed.*, 2012, **51**, 5247–5251.

52 J. D. Sipe and A. S. Cohen, *J. Struct. Biol.*, 2000, **130**, 88–98.

53 D. Eisenberg and M. Jucker, *Cell*, 2012, 148, 1188–1203.

54 H. Inouye, P. E. Fraser and D. A. Kirschner, *Biophys. J.*, 1993, **64**, 502–519.

55 S. B. Malinchik, H. Inouye, K. E. Szumowski and D. A> Kirschner, *Biophys. J.*, 1998, **74**, 537–545.

56 L. C. Serpell, *Biochim. Biophys. Acta*, 2000, **1502**, 16–30.

57 C. M. Dobson, A. J. Gerrard and A. J. Pratt, *Foundations of Chemical Biology*, Oxford Univeristy Press, Oxford, 2001.

58 M. Balbirnie, R. Grothe and D. S. Eisenberg, *Proc. Natl. Acad. Sci. U.S. A.*, 2001, **98**, 2375–2380.

59 M. R. Sawaya, S. Sambashivan, R. Nelson, M. I. Ivanova, S. A. Sievers, M. I. Apostol, M. J. Thompson, M. Balbirnie, J. J. W. W. Wiltzius, H. T. McFarlane, A. Ø. Madsen, C. Riekel and D. Eisenberg, *Nature*, 2007, **447**, 453–457.

60 R. Diaz-Avalos, C. Long, E. Fontano, M. Balbirnie, R. Grothe, D. Eisenberg and D. L. D. Caspar, *J. Mol. Biol.*, 2003, **330**, 1165–1175.

61 R. Nelson, M. R. Sawaya, M. Balbirnie, A. Madsen, C. Riekel, R. Grothe and D. Eisenberg, *Nature*, 2005, **435**, 773–778.

62 G. G. Glenner and C. W. Wong, *Biochem. Biophys. Res. Commun.*, 1984, **120**, 885–890.

63 C. L. Masters, G. Multhaup, G. Simms, J. Pottgiesser, R. N. Martins and K. Beyreuther, *EMBO J.*, 1985, **4**, 2757–2763.

64 R. J. O'Brien and P. C. Wong, *Annu. Rev. Neurosci.*, 2011, **34**, 185–204.

65 R. Vassar, B. D. Bennett, S. Babu-Khan, S. Kahn, E. A. Mendiaz, P. Denis, D. B. Teplow, S. Ross, P. Amarante, R. Loeloff, Y. Luo, S. Fisher, J. Fuller, S. Edenson, J. Lile, M. A. Jarosinski, A. L. Biere, E. Curran, T. Burgess, J. C. Louis, F. Collins, J. Treanor, G. Rogers and M. Citron, *Science*, 1999, **286**, 735–741.

66 H. Mori, K. Takio, M. Ogawara and D. J. Selkoe, *J. Biol. Chem.*, 1992, **267**, 17082–17086.

67 J. Wiltfang, H. Esselmann, M. Bibl, A. Smirnov, M. Otto, S. Paul, B. Schmidt, H. Klafki, M. Maler, T. Dyrks, M. Bienert, M. Beyermann and E. Ru, *J. Neurochem.*, 2002, **81**, 481–496.

68 D. Scheuner, C. Eckman, M. Jensen, X. Song, M. Citron, N. Suzuki, T. D. Bird, J. Hardy, M. Hutton, W. Kukull, E. Larson, E. Levy-Lahad, M. Viitanen, E. Peskind, P. Poorkaj, G. Schellenberg, R. Tanzi, W. Wasco, L. Lannfelt, D. Selkoe and S. Younkin, *Nature*, 1996, **2**, 874–870.

69 J. T. Jarrett, E. P. Berger and P. T. Lansbury, *Biochemistry.*, 1993, **695**, 144–148.

70 K. Irie, K. Murakami, Y. Masuda, A. Morimoto, H. Ohigashi, R. Ohashi, K. Takegoshi, M. Nagao, T. Shimizu and T. Shirasawa, *J. Biosci. Bioeng.*, 2005, **99**, 437–447.

71 K. Pauwels, T. L. Williams, K. L. Morris, W. Jonckheere, A. Vandersteen, G. Kelly, J. Schymkowitz, F. Rousseau, A. Pastore, L. C. Serpell and K. Broersen, *J. Biol. Chem.*, 2012, **287**, 5650–5660.

72 J. Hardy and D. J. Selkoe, *Science*, 2002, **297**, 353–356.

73 J. Kim, L. Onstead, S. Randle, R. Price, L. Smithson, C. Zwizinski, D. W. Dickson, T. Golde and E. McGowan, *J. Neurosci.*, 2007, **27**, 627–633.

74 Y. Yan and C. Wang, *J. Mol. Biol.*, 2007, **369**, 909–916.

75 C. Haass and D. J. Selkoe, *Nat. Rev. Mol. Cell Biol.*, 2007, **8**, 101–12.

76 B. De Strooper and E. Karran, *Cell*, 2016, **164**, 603–615.

77 R. Kayed, E. Head, J. L. Thompson, T. M. McIntire, S. C. Milton, C. W. Cotman and C. G. Glabe, *Science*, 2003, **300**, 486–489.

78 S. Lesné, M. T. Koh, L. Kotilinek, R. Kayed, C. G. Glabe, A. Yang, M. Gallagher and K. H. Ashe, *Nature*, 2006, **440**, 352–357.

79 J. C. Stroud, C. Liu, P. K. Teng and D. Eisenberg, *Proc. Natl. Acad. Sci. U. S. A.*, 2012, **109**, 7717–7722.

80 M. Necula, R. Kayed, S. Milton and C. G. Glabe, *J. Biol. Chem.*, 2007, **282**, 10311–10324.

81 C. G. Glabe, *J. Biol. Chem.*, 2008, **283**, 29639–29643.

82 R. Tycko, *Cold Spring Harb. Perspect. Med.*, 2016, **6**, a024083.

83 I. Kheterpal, S. Zhou, K. D. Cook and R. Wetzel, *Proc. Natl. Acad. Sci. U. S. A.*, 2000, **97**, 13597–13601.

84 I. Kheterpal, A. Williams, C. Murphy, B. Bledsoe and R. Wetzel, *Biochemistry*, 2001, **40**, 11757–11767.

85 J. J. Balbach, A. T. Petkova, N. A. Oyler, O. N. Antzutkin, D. J. Gordon, S. C. Meredith and R. Tycko, *Biophys. J.*, 2002, **83**, 1205–1216.

86 A. T. Petkova, Y. Ishii, J. J. Balbach, O. N. Antzutkin, D. Leapman, F. Delaglio, R. Tycko, A. T. Petkova, Y. Ishii, J. J. Balbach, N. A. Oleg, R. D. Leapman and F. Delaglio, *Proc. Natl. Acad. Sci. U. S. A.*, 2002, **99**, 16742–16747.

87 O. N. Antzutkin, J. J. Balbach and R. Tycko, *Biophys. J.*, 2003, **84**, 3326–3335.

88 C. Goldsbury, P. Frey, V. Olivieri, U. Aebi and S. A. Müller, *J. Mol. Biol.*, 2005, **352**, 282–298.

89 A. T. Petkova, W.-M. Yau and R. Tycko, *Biochemistry*, 2006, **45**, 498–512.

90 A. K. Paravastu, R. D. Leapman, W. Yau and R. Tycko, *Proc. Natl. Acad. Sci. U. S. A.*, 2008, **105**.

91 I. Bertini, L. Gonnelli, C. Luchinat, J. Mao and A. Nesi, *J. Am. Chem. Soc.*, 2011, **133**, 16013–16022.

92 A. T. Petkova, R. D. Leapman, Z. Guo, W.-M. Yau, M. P. Mattson and R. Tycko, *Science*, 2005, **307**, 262–265.

93 Y. Xiao, B. Ma, D. McElheny, S. Parthasarathy, F. Long, M. Hoshi, R. Nussinov and Y. Ishii, *Nat. Struct. Mol. Biol.*, 2015, **22**, 499–505.

94 M. A. Wälti, F. Ravotti, H. Arai, C. G. Glabe, J. S. Wall, A. Böckmann, P. Güntert, B. H. Meier and R. Riek, *Proc. Natl. Acad. Sci.*, 2016, **113**, E4976–E4984.

95 L. Gremer, D. Scholzel, C. Schenk, E. Reinartz, J. Labahn, R. B. G. Ravelli, M. Tusche, C. Lopez-Iglesis, W. Hoyer, H. Heise, D. Willbold and G. F. Schroder, *Science.*, 2017.

96 M. T. Colvin, R. Silvers, Q. Z. Ni, T. V. Can, I. Sergeyev, M. Rosay, K. J. Donovan, B. Michael, J. Wall, S. Linse and R. G. Griffin, *J. Am. Chem. Soc.*, 2016, **138**, 9663–9674.

97 J.-X. Lu, W. Qiang, W.-M. Yau, C. D. Schwieters, S. C. Meredith and R. Tycko, *Cell*, 2013, **154**, 1257–68.

98 W. Qiang, W.-M. Yau, J.-X. Lu, J. Collinge and R. Tycko, *Nature*, 2017, **541**, 217–221.

99 M. R. Nilsson, *Methods*, 2004, **34**, 151–160.

100 G. Meisl, J. B. Kirkegaard, P. Arosio, T. C. T. Michaels, M. Vendruscolo, C. M. Dobson, S. Linse and T. P. J. Knowles, *Nat. Protoc.*, 2016, **11**, 252–272.

101 K. P. R. Nilsson, *FEBS Lett.*, 2009, **583**, 2593–2599.

102 S. I. A. Cohen, S. Linse, L. M. Luheshi, E. Hellstrand, D. A. White, L. Rajah, D. E. Otzen, M. Vendruscolo, C. M. Dobson and T. P. J. Knowles, *Proc. Natl. Acad. Sci. U. S. A.*, 2013, **110**, 9758–63.

103 C. Xue, D. Chang, T. Y. Lin and Z. Guo, *R. Soc. Open. Sci.*, 2017, **4**, 160696.

104 E. Hellstrand, B. Boland, D. M. Walsh and S. Linse, *ACS Chem. Neurosci.*,

2010, **1**, 13–18.

105 S. I. A. Cohen, M. Vendruscolo, C. M. Dobson and T. P. J. Knowles, *J. Mol. Biol.*, 2012, **421**, 160–171.

106 M. Tö, T. C. T. Michaels, K. Sanagavarapu, X. Yang, G. Meisl, S. I. A. Cohen, T. P. J. Knowles Bd and S. Linse, *Chem. Commun.*, 2018.

107 T. P. J. Knowles, D. A. White, A. R. Abate, J. J. Agresti, S. I. A. Cohen, R. A. Sperling, E. J. De Genst, C. M. Dobson and D. A. Weitz, *Proc. Natl. Acad. Sci.*, 2011, **108**, 14746–14751.

108 G. Meisl, L. Rajah, S. I. A. Cohen, M. Pfammatter, A. Šarić, E. Hellstrand, A. K. Buell, A. Aguzzi, S. Linse, M. Vendruscolo, C. M. Dobson and T. P. J. Knowles, *Chem. Sci.*, 2017.

109 M. J. Cannon, A. D. Williams, R. Wetzel and D. G. Myszka, *Anal. Biochem.*, 2004, **328**, 67–75.

110 T. Gurry and C. M. Stultz, *Biochemistry*, 2014, **53**, 6981–6991.

111 R. Cukalevski, X. Yang, G. Meisl, U. Weininger, K. Bernfur, B. Frohm, T. P. J. Knowles and S. Linse, *Chem. Sci.*, 2015, **6**, 4215–4233.

112 Knowles, Tuomas P. J, C. A. Waudby, G. L. Devlin, S. I. A. Cohen, A. Aguzzi, M. Vendruscolo, E. M. Terentjev, M. E. Welland and C. M. Dobson, *Science.*, 2009, **326**, 1533–1538.

113 S. R. Collins, A. Douglass, R. D. Vale and J. S. Weissman, *PLoS Biol.*, 2004, **2**.

114 M. Tanaka, S. R. Collins, B. H. Toyama and J. S. Weissman, *Nature*, 2006, **442**, 585–589.

115 G. Meisl, X. Yang, E. Hellstrand, B. Frohm, J. B. Kirkegaard, S. I. A. Cohen, C. M. Dobson, S. Linse and T. P. J. Knowles, *Proc. Natl. Acad. Sci. U. S. A.*, 2014, **111**, 9384–9.

116 S. I. A. Cohen, R. Cukalevski, T. C. T. Michaels, A. Šarić, M. Törnquist, M. Vendruscolo, C. M. Dobson, A. K. Buell, T. P. J. Knowles and S. Linse, *Nat. Chem.*, 2018, 1–9.

Chapter 2:
Using photo cross-linking to understand the self-assembly of $A\beta_{16-22}$

2.1 Using peptide fragments to understand self-assembly

Self-assembling peptides can be difficult to study *in vitro* due to their hydrophobicity and propensity to aggregate spontaneously. Due to this, shorter synthetic peptide fragments from longer amyloidogenic sequences offer convenient model systems with which to explore peptide self-assembly.[1,2] A case in point is the GNNQQNY sequence, taken from the prion-determining domain (PrD) of the 635 residue Sup35 yeast protein.[2–4] Eisenberg and co-workers established in 2001 that, in aqueous conditions, this sequence self-assembled into highly ordered fibril structures that displayed the characteristic cross-β X-ray diffraction pattern of amyloid peptides.[2] The short nature of GNNQQNY made the formation of micro-crystals suitable for electron diffraction possible, demonstrating that the underlying parallel in-register β-sheet structure formed a steric zipper with a dry interface between the inter-digitated side chains.[3] The power of this approach was highlighted further when the atomic structure of micro-crystals from the peptide VQIVYK (from the tau sequence) was solved, informing the structure-based design of full-length tau inhibitors.[4,5] GNNQQNY clearly demonstrates that peptide fragments can be useful models of longer amyloid sequences, revealing atomic level information that may otherwise be unavailable due to the flexibility of longer peptide chains. The short nature of peptide fragments also lends them to the development of new methods to study self-assembling peptides, such as photo-crosslinking and molecular dynamics simulations.[6–8]

2.2 Amyloid-$\beta_{16\text{-}22}$ ($A\beta_{16\text{-}22}$): A model peptide fragment

One the most widely studied amyloidogenic fragments is $A\beta_{16\text{-}22}$ (**9**), a synthetic seven-residue peptide that forms the central fibril-forming region of the Aβ sequence (Figure 20).[1] $A\beta_{16\text{-}22}$ is a small fragments of Aβ that forms fibrils with a cross-β structure and can be readily synthesized readily using solid-phase peptide synthesis (SPPS).[1] Substitutions within this region of full-length Aβ peptide have been shown to affect its aggregation propensity significantly, both *in vitro* and *in vivo*, highlighting the importance of the motif.[9–11] These factors make $A\beta_{16\text{-}22}$ an ideal model with which to explore the properties of this region from the full-length Aβ sequence. The noted ability of $A\beta_{16\text{-}22}$ to form a range of supramolecular structures at different pH values further highlights the value of using $A\beta_{16\text{-}22}$ to understand the fundamental molecular mechanisms of peptide self-assembly.[12,13]

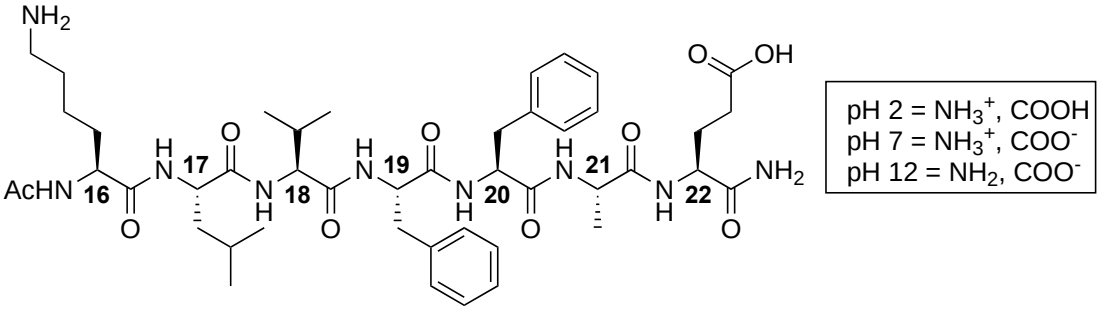

9

Ac – K – L – V – F – F – A – E – $CONH_2$

Figure 20. The amino acid sequence and molecular structure of $A\beta_{16-22}$ (**9**), small numbering refers to the full-length Aβ sequence).

2.2.1 $A\beta_{16-22}$ polymorphism and underlying β-sheet structure

Tycko and co-workers used ssNMR, transmission electron microscopy (TEM) and X-ray diffraction to establish that at neutral pH $A\beta_{16-22}$ forms in-register, antiparallel fibril structures that displayed green birefringence when bound to Congo Red (Figure 21a).[1] In X-ray diffraction experiments the fibrils displayed periodic reflections at 4.9 and 9.9 Å (characteristic of the spacing between β-strands and β-sheet layers respectively). Average fibril lengths were between 300 - >8000 Å and the average diameter of the fibrils was 100 – 200 Å. These fibrils consisted of smaller filaments with an average diameters of 50 Å. Given that a monomeric $A\beta_{16-22}$ peptide in a fully extended β-sheet conformation would be approximately ~25 Å, some form of higher order lamination must occur to account for the observed diameters.

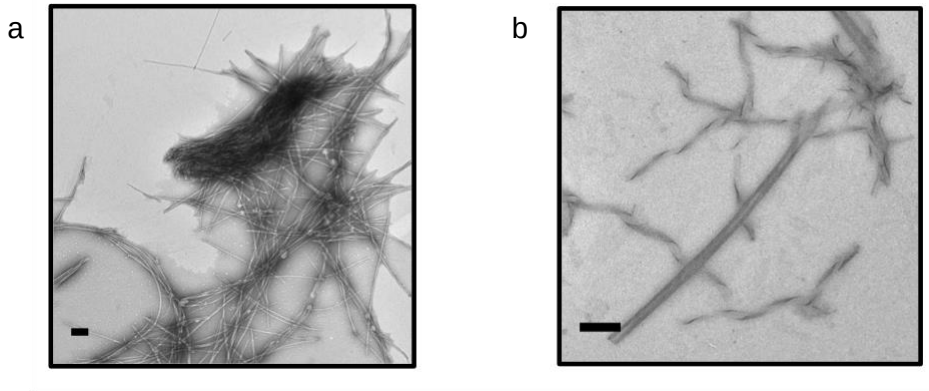

Figure 21. The supramolecular structures formed by $A\beta_{16-22}$ at different pHs. At neutral pH (a), $A\beta_{16-22}$ forms rope-like fibrils whereas at acidic pH (b) $A\beta_{16-22}$ forms hollow nanotubes and helical ribbons. Scale bar = 200 nm. TEM images were taken by the author.

Lowering the pH to acidic conditions (pH 2) neutralises the negative charge on the E residue of $A\beta_{16-22}$, leading to a switch in the supramolecular structure formed by $A\beta_{16-22}$.[12,14] Rather than the fibril structures seen previously, after 20 h incubation wide sheet-like structures can be observed that are 130 nm wide and 4 nm thick.[12] These structures transition into twisted helical ribbons after a further 10 h incubation (width 95 ± 5 nm and average length >10 μm, measured by AFM) that small-angle X-ray scattering (SAXS) and small-angle neutron scattering (SANS) experiments indicate are formed by monodisperse hollow nanotubes collapsing on the surface of the grids (Figure 21b). These experiments indicated that the walls of the nanotube are formed of a $A\beta_{16-22}$ bilayer (4 nm thick) with the radius of the nanotube given as 26 nm.[12,14] Initial data suggested that an antiparallel, in-register β-sheet alignment was present, however, later NMR studies suggested that an out-of-register antiparallel orientation domintated.[14] At basic pH (pH 12) $A\beta_{16-22}$ has been shown to form wide nanotapes that are similar in morphology to those formed at pH 2 but are wider in diameter and much more polydisperse (300 ± 100 nm).[15]

These different underlying β-sheet structures give rise to different driving forces of self-assembly (Figure 22).[14,16,17] In the in-register alignment, $A\beta_{16-22}$ presents one polar face (with all K/E residues on the same face, Figure 22a). This alignment is thus stabilised by the formation of salt bridges at both termini of the peptide dimer. An out-of-register alignment places the same residues on both faces of the peptide (i.e. both faces are symmetrical, Figure 22b). Stabilisation in this alignment now comes from V/A side chain packing and the multiple sheet-sheet stacking interactions available due to the symmetrical nature of the faces. Amino acid substitution experiments elegantly demonstrate this subtle difference. An E22L mutant of $A\beta_{16-22}$ forms nanotubes at neutral pH, highlighting the importance of the salt bridge interaction in driving the fibril structure.[14] The role of the FF motif has been shown to be key to the kinetics of aggregation and thermodynamic stability of peptide assembly, with increasing hydrophobicity and steric volume having a notable effect at position 19.[7,16,17] The nanotube morphology can also be disrupted by the substitution of the FF motif, confirming its important role in stabilising this morphology through cross-strand pairing.[14]

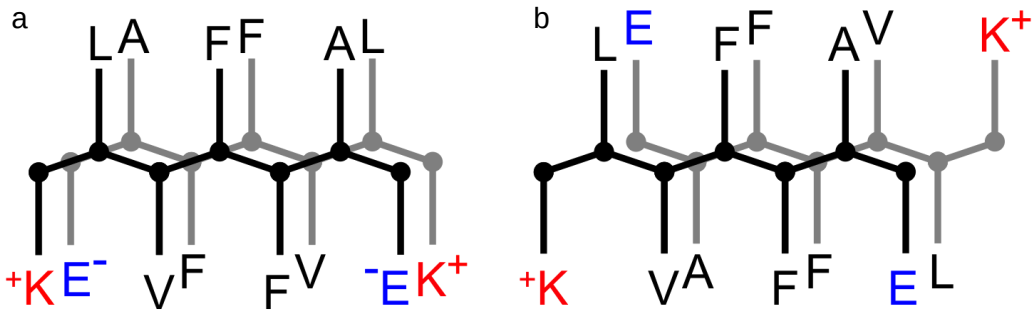

Figure 22. The underlying β-sheet alignment of $A\beta_{16-22}$ at different pHs. At neutral pH (a) $A\beta_{16-22}$ has an in-register, antiparallel alignment whereas at acidic pH (b) $A\beta_{16-22}$ is thought to adopt an out-of-register, antiparallel alignment.

2.2.2 The structural transitions that occur during $A\beta_{16-22}$ self-assembly

Understanding the transitions that occur during $A\beta_{16-22}$ self-assembly is the ultimate goal of studying these systems. Petty and Decatur used isotope-edited IR to establish that at neutral pH, $A\beta_{16-22}$ forms an initial β-strand alignment that is not identical to the final equilibrium alignment, i.e. there is some β-sheet reorganisation during the self-assembly process.[18] Lynn and co-workers demonstrated that, at both acidic and neutral pH, $A\beta_{16-22}$ passes through an intermediary out-of-register ribbon-like structure.[13] The time taken to reach the final fibril alignment (measured by far-UV CD) was different at each pH: at neutral pH $A\beta_{16-22}$ reached a plateau after 5 days whereas at acidic pH a lag phase of 4 days was observed, with the final plateau being reached after 10 days (Figure 23a).[13] Initially $A\beta_{16-22}$ has been shown to form micrometre sized particles with a high concentration of peptides in a liquid-like state.[19,20] These particles are metastable (containing around 20 – 33% β-sheet content) and can transition into nanotubes or fibrils with the correct changes in temperature and pH (Figure 23b). In all cases, it should be noted that changes in temperature, concentration and ionic strength can have a significant impact on the kinetics of $A\beta_{16-22}$ aggregation.[12,13,16,19]

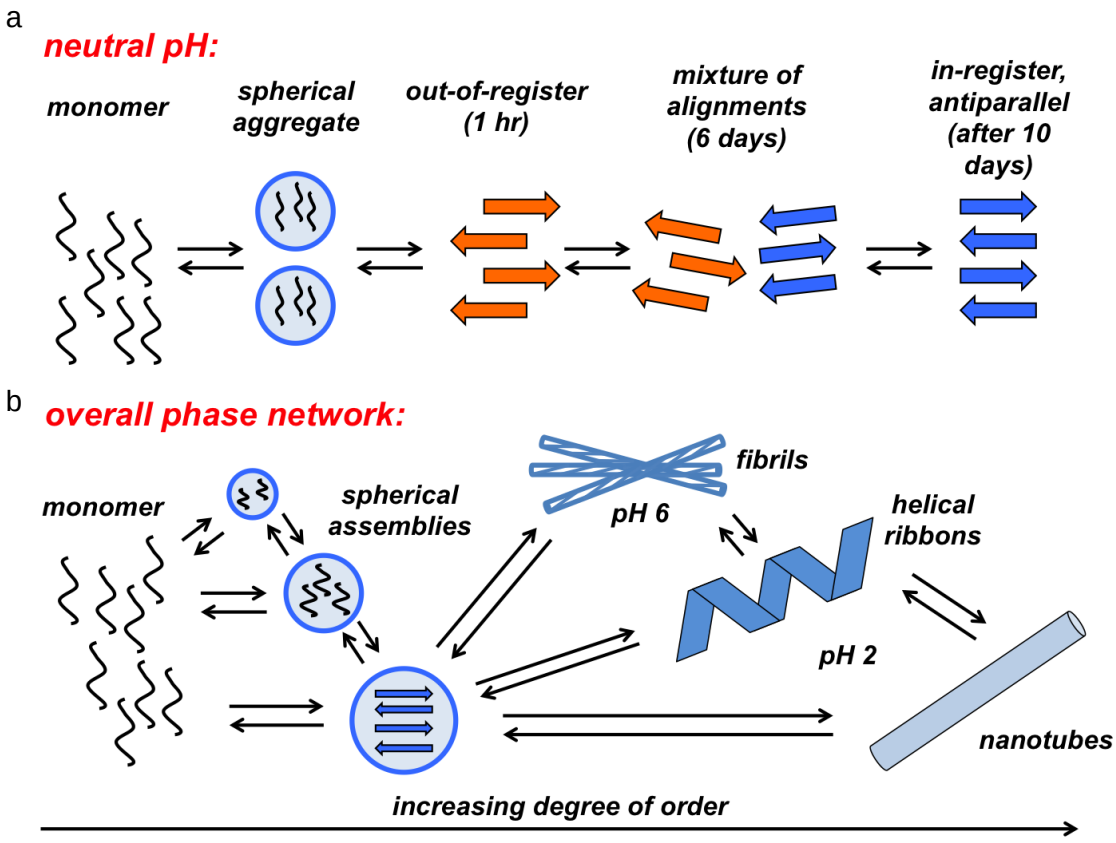

Figure 23. The transitions that $A\beta_{16-22}$ undergoes during aggregation. At neutral pH (a) $A\beta_{16-22}$ passes through an out-of-register intermediate, prior to forming in-register, antiparallel β-sheets. The aggregation of $A\beta_{16-22}$ can be understood to be a hierarchal network of phases (b). Adapted from (20).

2.3 The application of molecular dynamics simulations to $A\beta_{16-22}$

The transient intermediates formed during the early stages of peptide self-assembly can be difficult to characterise experimentally. By contrast this experimental challenge makes these systems well suited to the application of MD simulations.[8,21–23] The first studies, carried out by Klimov and Thirumali, demonstrated that monomeric $A\beta_{16-22}$ preferentially adopts either a random coil or extended β-strand conformation.[21] These structures then progress through an obligatory α-helical intermediate prior to forming stable antiparallel, in-register oligomers. Later studies also observed that $A\beta_{16-22}$ monomers are primarily in random coil conformations, although the presence of an α-helical intermediate was disputed.[22,23] These simulations also highlighted the complex pathways that $A\beta_{16-22}$ accesses during the self-assembly process and that the antiparallel, in-register structure is the preferred structure due to its stability (Section

2.2.1). Hall and co-workers performed the most informative simulations involving $A\beta_{16-22}$, by using their Protein Intermediate-Resolution Model (referred to as PRIME20) in combination with a coarse-grained discontinuous molecular dynamics (DMD) simulation approach (for a detailed description of this study see the next page).[8,24,25]

MD simulations explore dynamic systems by calculating (using Newton's equations of motion) the trajectories of particles within a system.[26,27] Properties of the system in question are then assessed by observing the averages of the particles' trajectories. In DMD, the interactions between the particles are based on hard spheres (i.e. they can collide with each other but not overlap).[27] As stated by Newton's equations of motion, a particle will stay on the same trajectory at constant velocity until another force (e.g. a collision with another particle) acts upon it. In DMD simulations this is referred to as an event, with the simulation progressing on an event-by-event basis (e.g. an event is located, the simulation progresses to that point in time and the dynamics of the system are then recalculated). As the time steps are variable and solely driven by events occurring in the system, the computing power needed to model large systems on long time scales is reduced.[27] The implicit solvent PRIME20 model complements this approach by providing an intermediary description of peptide structure.[25] In the model, each amino acid residue is treated as four solid spheres, one for each NH, $C_\alpha H$ and CO bond and one for the side chain. Each amino acid is then classified into 1 of 14 groups based on size, polarity, hydrophobicity, charge and potential for side chain hydrogen bonding. To ensure that the peptide backbone forms the correct geometry, pseudo-bonds can be imposed around the C_α-C_α vector.[25] In this approach, periodic boundary conditions are also imposed. The suitability of this combined approach has been demonstrated by exploring the self-assembly of polyalanine, tau peptide fragments, the structural conversion of longer peptides such as $A\beta_{17-42}$, and the interaction of a variety of inhibitors with $A\beta_{17-36}$.[24,28–30]

Hall and co-workers demonstrated that 48 $A\beta_{16-22}$ peptide monomers have different self-assembly mechanisms depending on the temperature at which the simulation is performed.[8] At high temperature, $A\beta_{16-22}$ starts as monomeric random coils that then progress to a number of unstable structures (such as disordered aggregates and single β-sheet layers), eventually forming a stable fibril nucleus. This nucleus can then grow through either monomer addition, random attachment followed by structural reorganisation, or the formation of a secondary nucleus that adds on to the pre-existing nucleus. Given the presence of a lag phase followed by growth from a stable nucleus, the authors referred to the mechanism as "nucleation followed by templated growth"

(Figure 24a).[8] At low temperature, however, self-assembly initially starts with a hydrophobic collapse, followed by oligomeric merging of partially ordered protofilament structures before proceeding to the highly ordered antiparallel, in-register β-sheet structure (Figure 24b). It should be noted that the stable structures form the highly interdigitated steric zippers observed by Eisenberg and co-workers, confirming that this approach not only allows the atomistic visualisation of the early events in self-assembly but also returns experimentally valid results.[3]

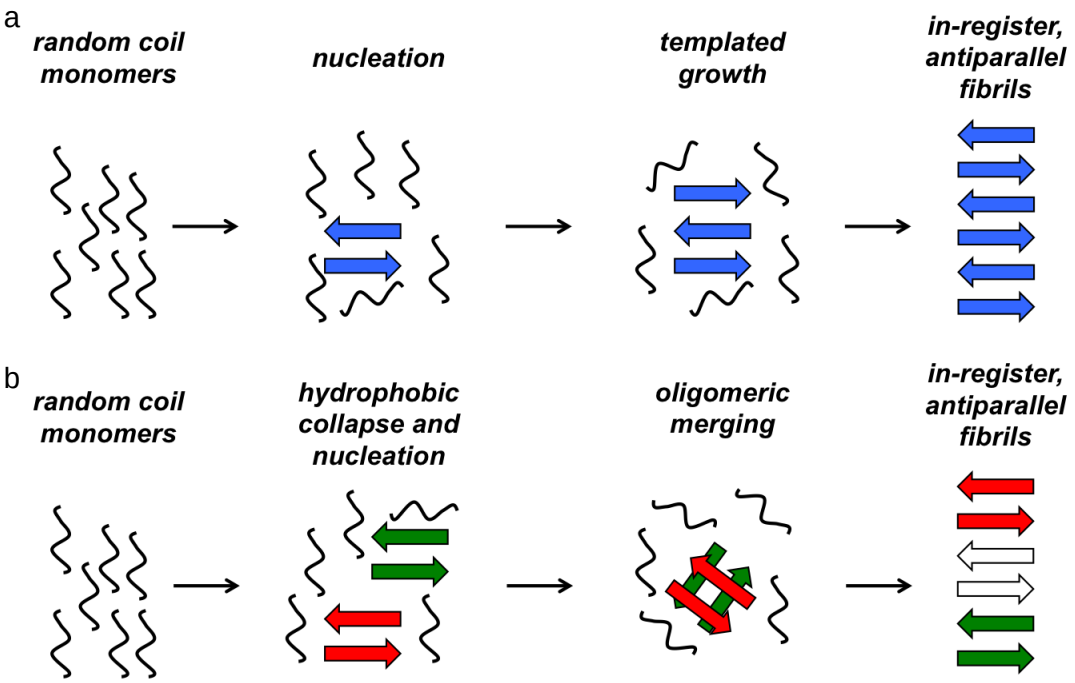

Figure 24. The different $A\beta_{16-22}$ self-assembly pathways observed by Hall and co-workers. At higher temperatures (a) $A\beta_{16-22}$ undergoes a nucleation and template growth mechanism whereas at lower temperatures, $A\beta_{16-22}$ undergoes hydrophobic collapse followed by the formation of multiple nuclei and then oligomeric merging (b). At the end of both pathways, $A\beta_{16-22}$ forms an antiparallel, in-register structure.

2.4. Photo-induced cross-linking (PIC)

Fleeting meta-stable states often play key roles in peptide self-assembly.[31] Techniques that can capture these states as they occur, such as photo-induced cross-linking (PIC), are highly valuable.[32,33] Using photo-reactive groups not only allows non-covalent connectivity to be translated into a stable covalent form, but also allows any structural changes to be related to time. The wide range of cross-linking reagents, from those that generate reactivity in unmodified proteins to functionalised amino acid residues,

can be used to provide structural insights at both the residue and quaternary level both *in vitro* and *in vivo*.[7,34–36] A general schematic of the PIC strategy can be seen in Figure 25. Given the wide range of cross-linking agents available, matching the right cross-linking reagent to the biological system and type of data required is essential. Table 2 compares the properties of some commonly used cross-linking reagents.[33,37]

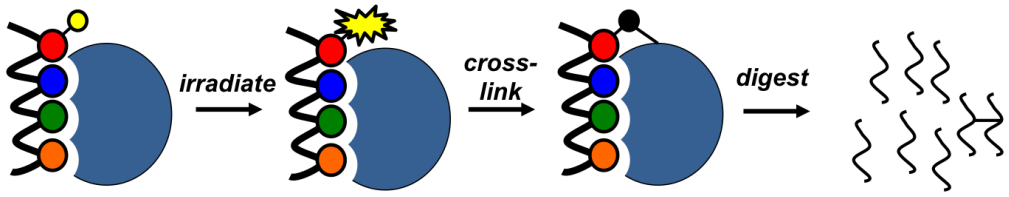

Figure 25. General schematic of a PIC study. Cross-linking experiments can use reagents that have been introduced to a peptide/protein through either solid phase peptide synthesis or other recombinant methods and, upon irradiation, react with proteins/peptides that are in close contact. Digestion and tandem MS/MS sequencing can then locate the cross-links, allowing structural information about the system to be gained.

Reagent and wavelength (λmax)	Reactive intermediate	XL preference	Competing processes after irradiation	Pro	Cons
Aryl azides (~250 nm)	singlet nitrene	preferentially reacts with amines over hydrocarbons in aq. solution, inserts into Nu-H bonds	ring expansion (can be limited by fluorination around the aromatic ring)	good XL yield	competing reactions after irradiation and distinct chemical reactivity
Benzyl ketones (350 – 360 nm)	triplet ketyl biradical	preferentially reacts with the α-C of glycine/C – H bonds	reversible excitation	unreactive to H_2O commercially available	bulky and hydrophobic, long irradiation time, strong preference for C – H
Diazirine (350 – 360 nm)	carbene (singlet dominates in solution)	few obvious inherent preferences, inserts in to X – H bonds (X = C, N, O)	stochastic conversion to linear diazoisomer	ns, indiscriminate reactivity excellent stability (light, pH, temp.)	formation of diazoisomer can bias XL results

Table 2. Summary of some commonly used non-native PIC reagents, including aryl azides, benzyl ketones (such as benzophenone) and diazirines. XL stands for cross-link, Nu stands for nucleophile. Adapted from references (33, 37).

Some of the most commonly used non-native PIC reagents are based on diazirine/diazo moities, due to their favourable photochemical properties and the high reactivity of the associated carbene (Figure 26a).[33,38–40] Diazirines (**10**) are three-membered heterocycles that upon irradiation at 365 nm can either extrude molecular N_2 and generate a carbene (**11**) or interconvert stochastically to the linear diazoisomer (Figure 26b).[41,42] The diazoisomer is much longer lived than the carbene and is prone to form carbocations that react preferentially with nucleophiles, biasing the cross-linked products formed in these reactions.[33,43] The carbene that is formed reacts on a nanosecond timescale and has a triplet ground state, although cross-linking reactions in neat solvents have confirmed that in solution the high energy singlet state dominates (**12**).[33,44,45]

A number of diazirine PIC reagents are available, both aliphatic (**13** and **14**) and aromatic, including functionalised amino acids (**15** – **16**).[35,43,45,46] The substituents on either side of the diazirine can have a significant impact on the photochemistry of reagent, in turn impacting on the cross-linked products. Aliphatic diazirines are often used due to their small size.[43] However, significant drawbacks are associated with their use, including alkene or ring formation and significant diazoisomer formation.[43,45] Richards and co-workers developed 3-trifluoromethyl-3-phenyldiazirine (TFMD), affording a PIC reagent with excellent stability to pH, temperature and ambient light.[45] The triflouromethyl group aids the stability of the diazoisomer, whilst the aromatic group helps to stabilise the singlet carbene.[33,45] Fishwick and co-workers developed a synthesis that combined TFMD and Phe, extending the use of this reagent for biological systems significantly (**17**).[46]

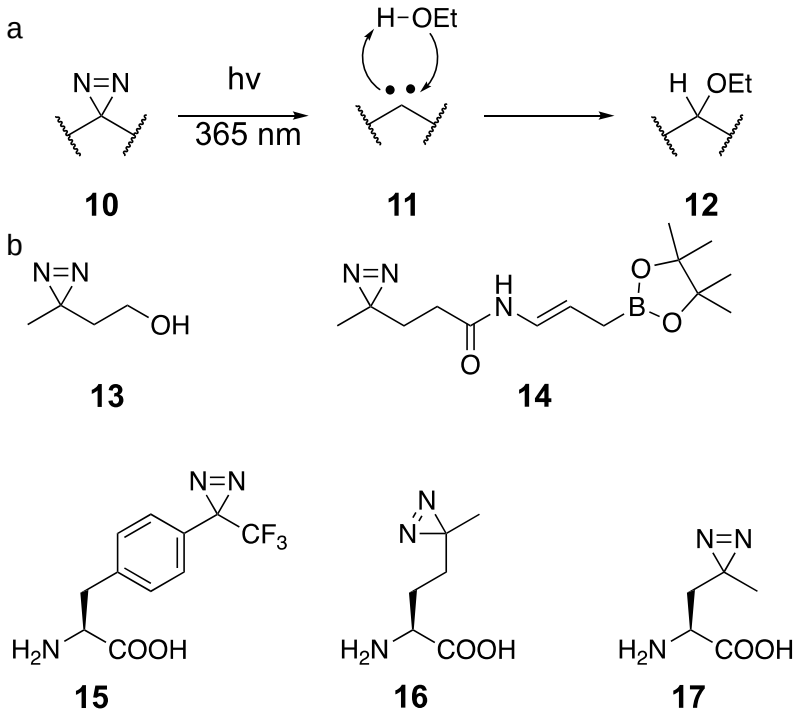

Figure 26. Diazirine reagents and their photochemistry. Upon irradiation at 365 nm, the diazirine ring extrudes molecular N_2 and generates a highly reactive carbene that can react indiscriminately on a nanosecond timescale (a). A wide range of diazirine based reagents, including functionalised amino acids, are synthetically available (b).

2.5 Mass Spectrometry as a tool to explore biological systems

Mass spectrometry is a powerful analytical technique that can identify gas phase ions based on their mass-to-charge (m/z) ratio.[47] The development of soft-ionisation techniques such as electrospray ionisation (ESI) and matrix-assisted laser desorption ionisation (MALDI), has expanded the use of mass spectrometry from the study of small organic molecules to large biological complexes.[48–50] Soft-ionisation techniques are so called as they produce little or no fragmentation in the sample. Mass spectrometry offers many advantages over other analytical techniques (e.g. NMR or ITC) including the low amounts of sample required (pmol vs µmol/mmol), high sensitivity and the ability to analyse complex heterogeneous mixtures without prior separation. Fundamental biophysical values such as binding constants can also be elucidated.[48] When combined with other techniques (e.g. ion mobility spectrometry (IMS) and tandem MS/MS sequencing), mass spectrometry can provide detailed information about biological systems, such as identifying fleeting co-assembled oligomers in islet amyloid polypeptide (IAPP) self-assembly.[36,48,51]

2.6 The mechanism of ESI

In ESI the sample can be taken directly from solution and transferred into the gas phase, preserving non-covalent interactions.[50] This offers an advantage compared with MALDI, as it can take large biomolecules straight from solution into the gas phase (the mechanism is outlined in Figure 27).[49,50,52] The sample is dissolved in a volatile buffer and passed down a capillary with a coaxial nebulising gas. A voltage is passed across the tip of the capillary, causing the sample to be ejected as highly charged droplets. A drying gas (such as N_2) assists the process of solvent evaporation, reducing the size of the droplets until the sample is transferred into the mass spectrometer as a highly charged ion. Nano-ESI (nESI) works on the same principle but with increased sensitivity and a lower flow rate, making it more suitable for larger protein complexes.[48] ESI often produces multiply charged species whereas other techniques, such as MALDI, tend to generate singly charged ions.[49]

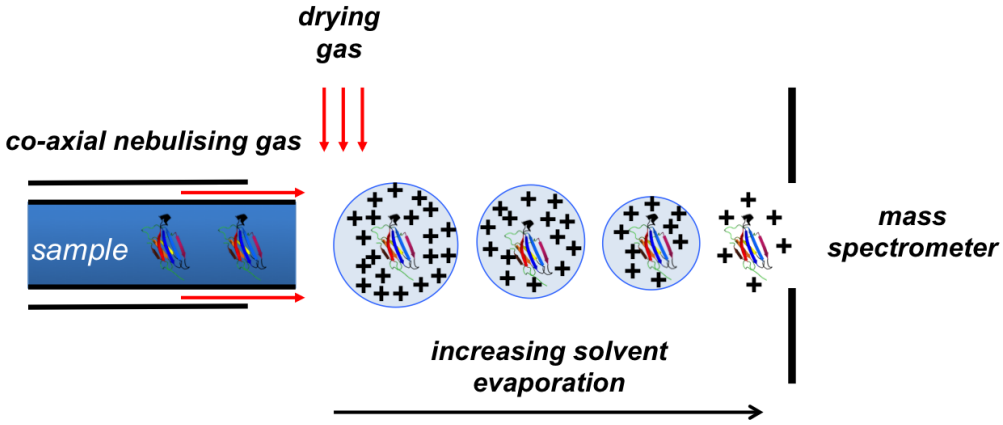

Figure 27. The mechanism of electrospray ionisation. The voltage passed across the tip of the capillary ejects the analyte as highly charged droplets. As the droplets travels towards the mass spectrometer, a drying gas aid the evaporation process. Eventually, the size of the droplet reduces such that the analyte remains as a highly charged ion. Adapted from (50).

2.7 Ion mobility spectrometry (IMS)

In peptide self-assembly reactions there can often be (a) multiple species that have the same mass, and/or m/z ratio or (b) species with multiple conformations.[51] Methods, such as IMS, that separate ions based on their gas phase conformation (i.e. in terms of shape and size) as well as m/z ratio can provide vital information on the underlying mechanism of self-assembly.[53–55] Following ESI, but prior to introduction into the analyser region of the mass spectrometer, the ions are passed through a drift tube filled with an inert buffer gas (N_2 or Ar). As ions pass through the drift tube, collisions with the buffer gas cause them to separate based on their gas phase conformation, giving each ion a unique drift-time (t_D, usually measured in milliseconds, Figure 27). This drift-time can be related to the ion's collision cross-section (CCS) by comparing it with known standards.[56] As such, small changes in transient populations can be identified within complex mixtures, something that may not be possible with other techniques. ESI-IMS-MS has been used to demonstrate that $A\beta_{42}$ forms a dodecameric species in solution (whereas $A\beta_{40}$ does not) and that the tetramers formed by each peptide have different conformations, providing insight into why the peptides have different aggregation propensities, as well as identifying different modes of inhibitor binding to IAPP.[57,58]

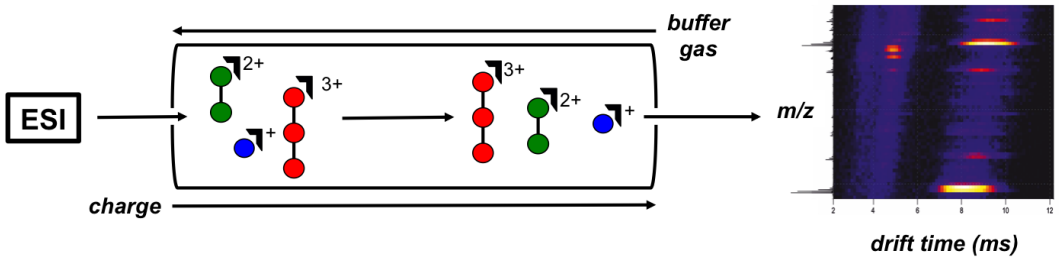

Figure 28. The mechanism by which IMS separates ions as they pass through the drift-tube. The IMS system used in this work makes use of a travelling wave, in which the ions are propelled through the drift tube by an alternating current. A representative drift-scope image is also shown. The drift-scope image was taken by the author.

2.8 Using PIC in combination with ESI-IMS-MS

Combining the ability of PIC to encode supramolecular connectivity into a stable covalent form with the separative power of ESI-IMS-MS affords a technique that is able to explore peptide self-assembly in a unique manner (Figure 29).[6,7] Wilson and co-workers used TFMD-Phe to explore the underlying β-sheet structure of $A\beta_{16-22}$ polymorphs at both pH 2 and pH 7 (after 2 weeks incubation).[7] By placing the PIC reagent within the peptide structure (using SPPS), the cross-linking reaction is not limited by diffusion. The structural heterogeneity of the cross-linked products should also be reduced, allowing more facile identification by tandem MS/MS sequencing.[33] Tandem MS/MS sequencing is a technique that can be used to identify modifications to individual amino acids via sequential cleavage along the peptide backbone (if using collision induced dissociation, CID) and is often used to identify proteins in proteomics studies.[59] Prior to introduction to the IMS drift tube, the ion of interest can be isolated in the quadrupole and then fragmented in either the trap or transfer cell (i.e. before or after the drift cell, depending on the type of separation required). From the fragmentation pattern, the position of the cross-link can be identified and the underlying structure elucidated. In the work performed by Wilson and co-workers, the pattern of cross-links indicated that antiparallel, in-register β-sheets were formed at both pHs, in disagreement with the literature (which saw antiparallel, out-of-register β-sheets at pH 2).[7,14] The authors proposed that the difference in aggregate morphology may be due to higher order packing effects rather than differences in underlying β-sheet structure, a situation that was also observed by Hamley and co-workers when studying the related fragment AAKLVFF.[60]

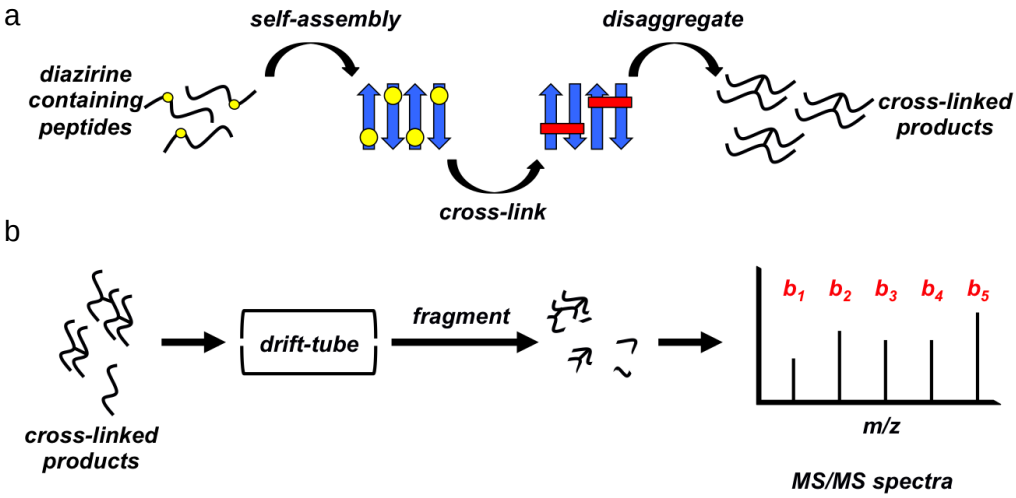

Figure 29. A general schematic outlining the strategy used in PIC experiments. Peptides containing TFMD-Phe (yellow) undergo self-assembly and the system is irradiated at 365 nm, forming covalent cross-links (red) between the β-sheets (a). The structures are then disaggregated with 1, 1, 1, 3, 3, 3-hexafluoroisopropanol (HFIP), introduced into the mass spectrometer, whereby they are separated in the IMS drift tube prior to fragmentation in the transfer cell (b). Analysis of the MS/MS spectra allows the position of the cross-link to be identified and the underlying β-sheet structure elucidated.

Aims and Objectives

In this chapter, experiments were designed to develop a more extensive picture of $A\beta_{16-22}$ aggregation, including an understanding of the kinetic pathway and the thermodynamic phase behaviour the peptide. Characterising, at the molecular level, the transitions that $A\beta_{16-22}$ undergoes as it self-assembles was the ultimate aim of this chapter, as there is a significant need to develop techniques that can capture fleeting structural intermediates and relate them to the overall course of aggregation. Using experimental techniques, in combination with DMD simulations, insights of assembly are derived at an atomistic level, both validating the simulation procedure and allowing the visualisation of these important molecular processes.

In order to meet these aims, an *in silico* prediction (carried out in collaboration with Yiming Wang and Professor Carol Hall of North Carolina State University) of the thermodynamic phase behaviour of $A\beta_{16-22}$ was undertaken. These predictions were then tested experimentally, confirming the predicted phase boundaries. With this knowledge in hand, the kinetics of $A\beta_{16-22}$ assembly (in a suitable buffer for mass spectrometry) needed to be established, as it is well known that buffer conditions have a significant impact on the rate of $A\beta_{16-22}$ aggregation. As described in the introduction to this chapter, it is thought that $A\beta_{16-22}$ passes through an obligatory out-of-register, antiparallel intermediary state irrespective of the pH at which self-assembly occurs. Once the kinetics of $A\beta_{16-22}$ assembly were established, attempts were made to capture and characterise this intermediate using PIC. The same system was then simulated using DMD, with the results in close agreement with experimental data. Given that this technique has never been used to study kinetic intermediates in peptide self-assembly this will represent an important step in developing ESI-IMS-MS/MS with PIC as a technique to explore the self-assembly of larger systems; including more disease relevant peptides.

Results and Discussion

2.9 The thermodynamic phase diagram of $A\beta_{16-22}$ and dye screen against amyloid dyes

$A\beta_{16-22}$ was synthesized using standard SPPS conditions (Scheme 1) and purified using reverse phase HPLC (>95%, see Sections 4.1 - 4 for the procedures). The identity of the product was confirmed by molecular mass analysis using high resolution mass spectrometry (HRMS) and tandem MS/MS sequencing to confirm the sequence identity (Appendices 1 and 2). Due to solubility issues in aqueous buffers, stock solutions of $A\beta_{16-22}$ in DMSO were used. In order to assess the ideal peptide concentration and temperature under which to perform this study, the thermodynamic phase diagram for $A\beta_{16-22}$ was calculated *in silico* (in collaboration with Yiming Wang and Professor Carol Hall) using their discontinuous molecular dynamics (DMD) simulations and the PRIME20 model.[8]

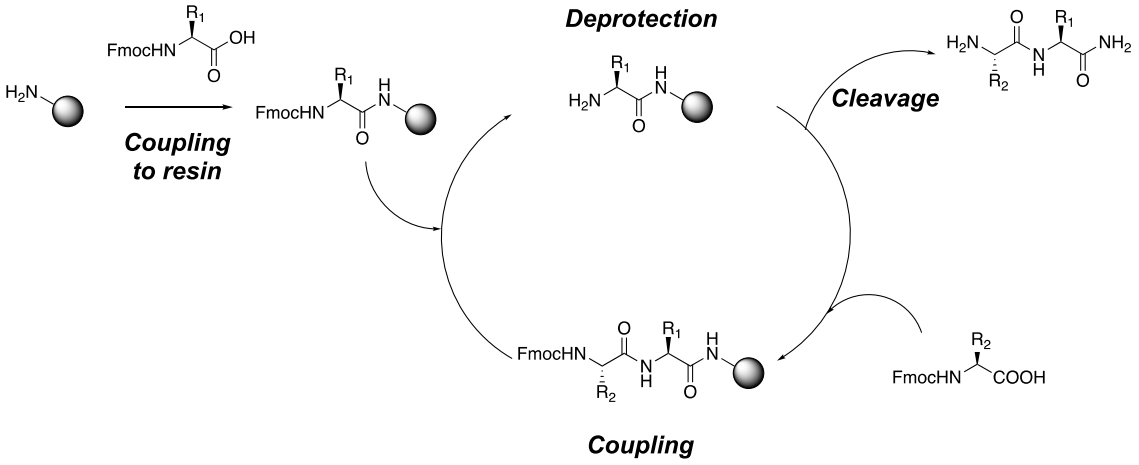

Scheme 1. Outline of SPPS. The growing peptide chain is attached to a resin and goes through iterative cycles of amide coupling and Fmoc deprotection. When the sequence is completed, acid mediated cleavage of the peptide from the resin produces the desired peptide.

The phase diagram was generated using DMD simulations by assessing the solubility of different types of aggregate (e.g metastable oligomers and fibril structures) at different temperatures.[61] In the simulation, each aggregate was placed in a box with periodic boundary conditions and a pool of free monomers. The aggregate was allowed to grow or shrink via monomer addition, but constrained such that no extra β-sheet structure could form. The solution peptide concentration was monitored until this value reached a plateau (i.e. where the aggregate neither grows nor shrinks) and this peptide

concentration was taken to be the solubility of that aggregate.

To confirm the validity of the DMD approach, aggregation experiments were set up at different peptide concentrations and temperatures in 100 mM ammonium bicarbonate buffer (i.e. a mass spectrometry compatible buffer) at pH 7 for at least a week (Section 4.8). The presence of fibrils was confirmed by negative stain TEM and compared with the phase diagram generated *in silico* (Section 4.9). As shown in Figure 30, the experimental data are in excellent agreement with the calculated phase diagram. From these experiments the following conditions were chosen for all the following $A\beta_{16-22}$ aggregation assays; final peptide concentration between 20 - 100 µM (depending on the assay) in 100 mM ammonium bicarbonate, pH 7, with 1% final concentration of DMSO (v/v) and an incubation temperature of 37 °C.

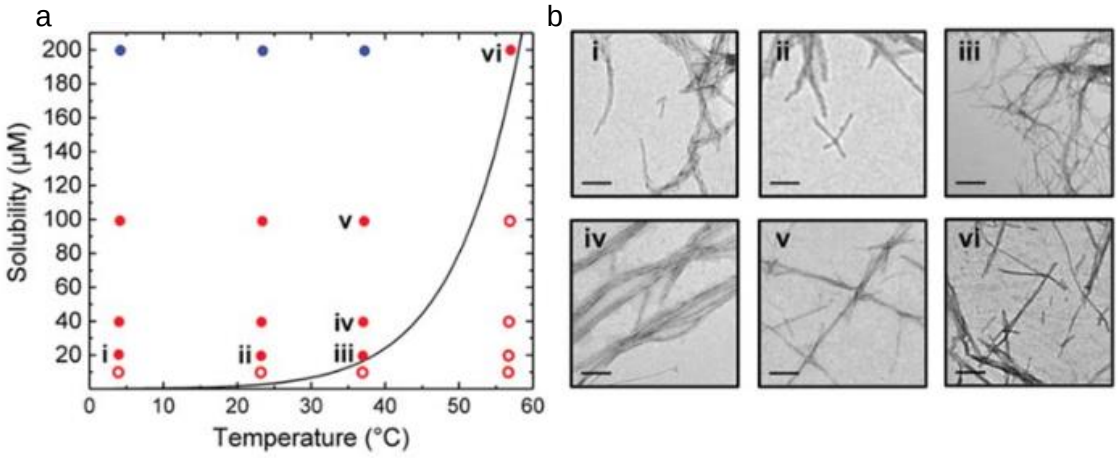

Figure 30. Plot of the temperature-dependent solubility line for $A\beta_{16-22}$ and fibrillation experiments. Red dots and red open circles indicate conditions under which fibrils have been found (via TEM) to form, or not form, respectively (a). Blue dots indicate that fibrils have been reported in the literature to form under these conditions or would be assumed to form given that fibrils have been reported under the same conditions at a lower concentration.[1, 6] Selected TEM images (b, i- vi) showing that $A\beta_{16-22}$ forms fibrils under these conditions, corresponding to the red dots labelled (i – vi) in (a). Scale bar = 200 nm.

Amyloid aggregation is commonly followed by the use of fluorescent dyes, such as ThT.[62–65] ThT is a benzothiazole dye that, upon binding to amyloid fibrils, fluoresces due to restricted rotation around the benzylamine/benzothiazole bond.[66,67] However, under the conditions employed in this study, $A\beta_{16-22}$ fibrils do not cause a significant increase of ThT fluorescence, in agreement with the weak binding affinity reported by

several literature sources.[16,68,69] As there are a significant number of amyloid-binding dyes, a literature search was performed in order to screen appropriate dyes against pre-formed $A\beta_{16-22}$ fibrils. From this literature search Congo-Red, 1-anillinonapthalene-8-sulfonic acid (ANS) and 2-[[5'-(4-hydroxyphenyl)[2,2'-bithiophen]-5-yl]-methylene]-propanedinitrile (NIAD-4) were chosen to screen (Figure 31).[1,69–72] $A\beta_{16-22}$ was incubated for at least 24 h (with the presence of fibrils confirmed by negative stain TEM) and then mixed with the dyes at either a 1:1 or 10:1 molar ratio of dye to fibril (final peptide concentration 50 μM). Only NIAD-4 produced a large enough signal-to-noise ratio in the presence of fibrils to take forward (Figure 31e and f). When incubated with $A\beta_{16-22}$ as a monomer (i.e. taken straight from the DMSO stock), however, no significant difference in the amount of fluorescence could be observed between the initial state and the monomer, demonstrating that NIAD-4 was unsuitable to follow the kinetics of $A\beta_{16-22}$ growth due to the lack of a dynamic range for the measurements (Figure 32).

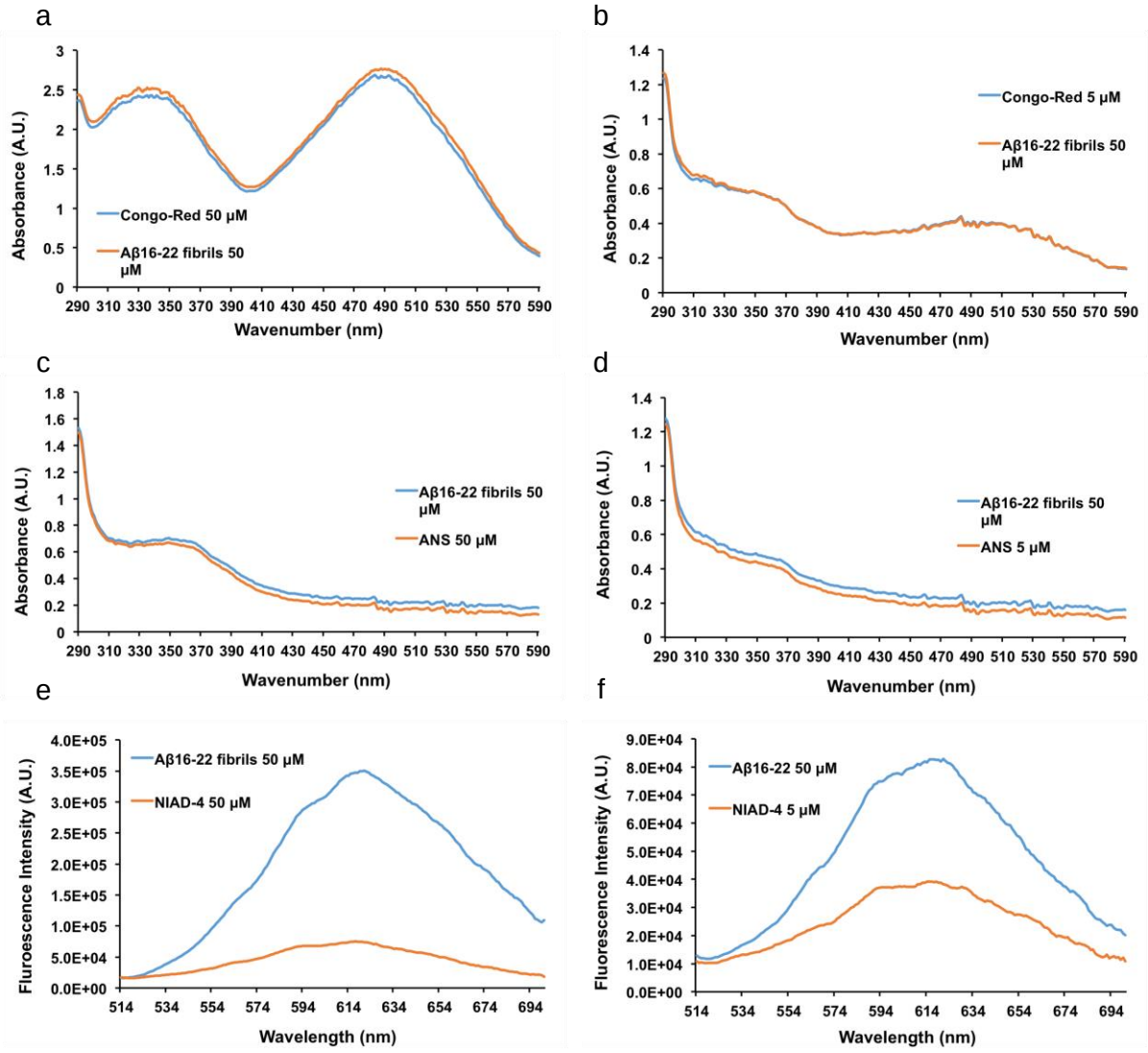

Figure 31. Summary of dye screen against $A\beta_{16-22}$ fibrils. 50 µM $A\beta_{16-22}$ was incubated in 100 mM ammonium bicarbonate, pH 7.4 with a final concentration of 1% (v/v) DMSO overnight and the presence of fibrils confirmed using TEM (data not shown). Either 50 µM (left) or 5 µM (right) of Congo Red (a and b), ANS (c and d) and NIAD-4 (e and f) was then incubated with the fibrils and the absorbance (a – d) or fluorescence (e and f) was measured. In each graph, orange is the dye in isolation and blue is the dye with 50 µM $A\beta_{16-22}$ fibrils added. No dye produced a significant increase in absorbance/fluorescence except for NIAD-4.

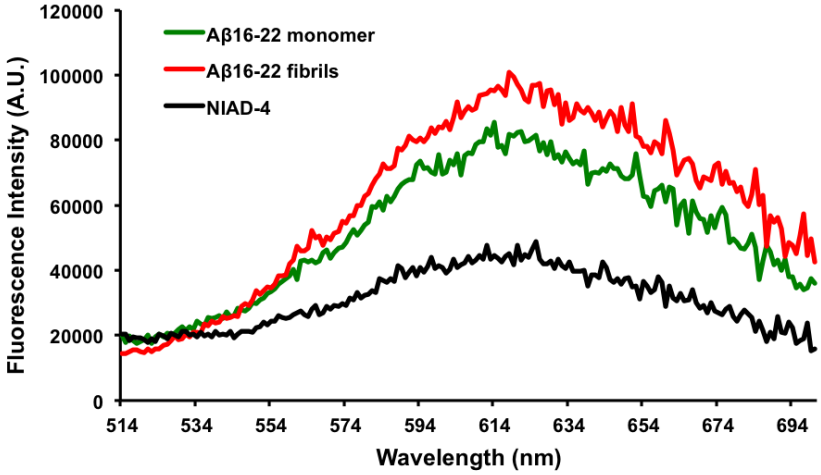

Figure 32. NIAD-4 fluoresces at a similar intensity when bound to either $A\beta_{16-22}$ fibrils or monomers. 50 μM of $A\beta_{16-22}$ monomers (i.e. taken straight from a DMSO stock, dead time 30 s, green) or fibrils (red) was incubated with 5 μM of NIAD-4 (black) and the fluorescence intensity measured.

2.10 Developing a fluorescence quenching assay for $A\beta_{16-22}$

Although extrinsic fluorescence dyes are the most common method with which to follow amyloid aggregation, covalently linking the fluorophore to the peptide in question has also been used to follow self-assembly quantitatively.[73,74] Fluorescence quenching (FQ) has been used to study the folding of single proteins, as well as follow the aggregation of Aβ and α-synuclein *in vitro* and *in vivo*.[74–78] Frieden and co-workers used tetramethylrhodamine (TAMRA) conjugated to the *N*-terminal K residues of both $A\beta_{40/42}$ to identify three distinct phase of aggregate growth: an oligomerisation phase, intermediate lag phase and a final growth phase.[74] Fluorescence quenching is a process whereby the fluorescence intensity of emission is reduced due to the presence of another fluorophore and/or quencher.[79] As the fluorophore labelled monomer is sequestered within the highly ordered β-sheet structure of the fibril, the fluorophores come into close contact, resulting in a time dependent decrease in fluorescence intensity (Figure 33). It should be noted that both unstructured and structured aggregates could both produce time-dependent fluorescence quenching, so other complementary techniques, such as TEM time courses, must be used to confirm aggregation into fibrils. Fluorescence lifetime imaging (FLIM) has been used to explore the environment within aggregates including nucleation events that occur as $A\beta_{16-22}$ self-assembles at pH 2.[20,80] This technique requires high end optical set-ups and so was not appropriate for this study.

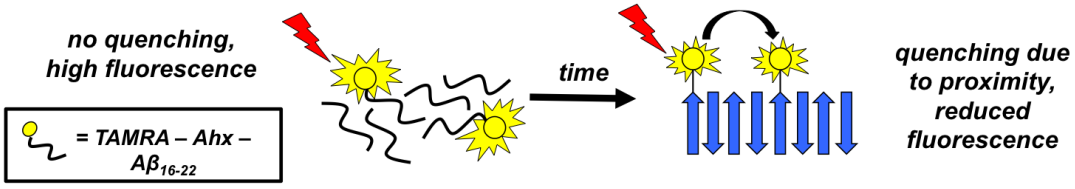

Figure 33. Schematic of the fluorescence quenching assay used in this work. As TAMRA-labelled $A\beta_{16-22}$ is incorporated into the aggregate (dye = yellow), the fluorophores come into closer contact and the fluorescence is quenched. The decreased in fluorescence emission can be used as a measure for self-assembly.

As traditional amyloid dyes could not be used to follow $A\beta_{16-22}$ assembly, a fluorescence quenching assay was developed. In order to perform these experiments an N-terminally TAMRA labelled variant of $A\beta_{16-22}$ (**18**) was synthesised and purified as described above (Figure 34a). Previously a Rhodamine-variant of $A\beta_{16-22}$, in which the N-terminal K had been replaced with Rhodamine, has been used in FLIM experiments, however, given the importance of K to the formation of the fibrils at neutral pH, a 6-aminohexanoic acid (Ahx) linker was also included between the peptide and the fluorophore.[20] Prior to performing the kinetic assay, a number of factors needed to be considered/optimised:

- Is the fluorescence in an aggregate significantly quenched when compared with the monomer, i.e. establish the dynamic range of the experiment
- Establish the correct percentage of TAMRA-Ahx-$A\beta_{16-22}$ to WT $A\beta_{16-22}$ (to prevent any disruption to the supramolecular fibril structure)
- Establish the appropriate concentration range of TAMRA-Ahx-$A\beta_{16-22}$

As a proof-of-principle experiment, a mixture of $A\beta_{16-22}$ with 10% TAMRA-Ahx-$A\beta_{16-22}$ (40 µM total peptide concentration) was left to incubate for 24 h, with the presence of fibrils confirmed by negative stain TEM (Figure 34b). The aggregate was then placed in a temperature controlled fluorimeter and fluorescene excited at 545 nm (with emission collected at 575 nm) and compared with the same concentration of TAMRA-Ahx-$A\beta_{16-22}$ taken straight from a DMSO stock (dead time 30 s, Figure 34c, Section 4.10). The aggregated TAMRA-Ahx-$A\beta_{16-22}$ produced a significantly lower amount of fluorescence than the nascent TAMRA-Ahx-$A\beta_{16-22}$, indicating that the fluorophore is indeed self-quenched in the aggregated form. Different ratios of TAMRA-Ahx-$A\beta_{16-22}$ to WT $A\beta_{16-22}$

(100, 50 and 1% label respectively) were also tested after 24 h aggregation, with all samples demonstrating the same fluorescence quenching when in the aggregate form (Appendix 3).

a

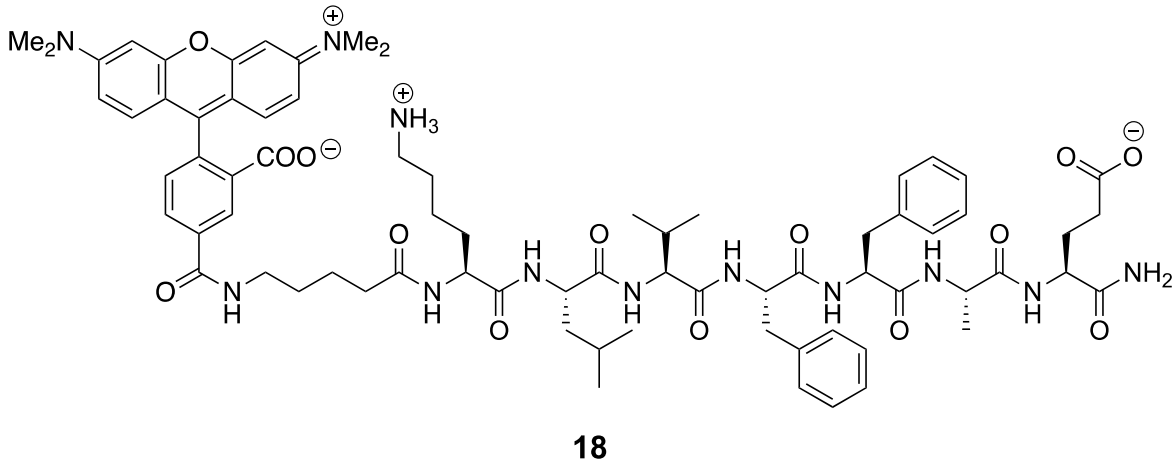

18

b

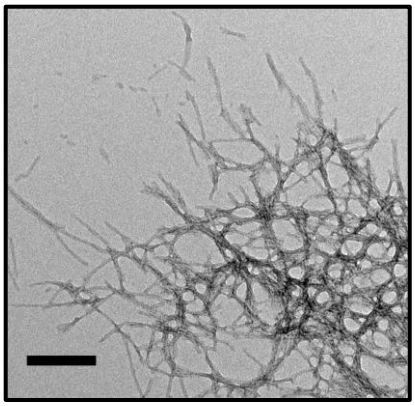

c

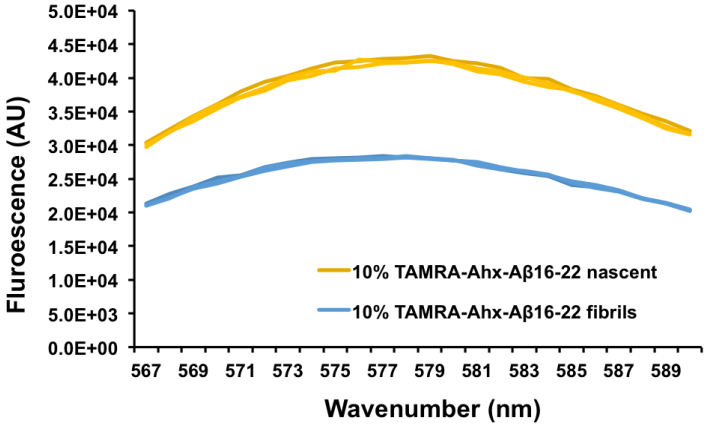

Figure 34. Initial validation of the fluorescence quenching assay. The molecular structure of TAMRA-Ahx-$A\beta_{16-22}$ (a). After 24 h incubation, WT $A\beta_{16-22}$ spiked with 10% TAMRA-Ahx-$A\beta_{16-22}$ forms fibrils that are morphologically similar to WT $A\beta_{16-22}$ (b) and significant quenching of fluorescence is observed when compared with the same mixture taken straight from a DMSO stock (dead time = 30s, c). Scale bar = 200 nm.

One issue with the assay was that the fluorescence intensity of the nascent TAMRA-Ahx-$A\beta_{16-22}$ was displaying significant non-linearity as the concentration of TAMRA-Ahx-$A\beta_{16-22}$ increased. A noted reason for non-linearity in fluorescence studies is the inner filter effect.[74,79] As the concentration of fluorophore increases in solution so does the optical density of that solution. In turn, the absorption of the excitation light by the fluorophore at the “front” of the cuvette can prevent the absorption of light by

fluorophores at the “centre” of the cuvette. As fluorescence intensity is directly proportional to the amount of light absorbed, this reduction in absorption can reduce the total fluorescence emitted, hence producing non-linearity in fluorescence at high molar concentrations. Frieden and co-workers noted that this effect was present at micromolar concentrations of TAMRA and as such used slightly different excitation/emission wavelengths to mitigate the inner filter effect (520 and 600 nm respectively).[74] In order to establish the correct concentration range and wavelength combination, a control experiment was performed. TAMRA-COOH was dissolved in buffer at a range of different concentrations (2 nM to 100 μM) and the fluorescence intensity measured using two different sets of wavelengths (A and B, 545/575 and 520/600 nm respectively, Figure 35a and b). As expected, set up B demonstrated more linear fluorescence intensity over a slightly larger concentration range (2 nM to 10 μM vs 2 nM to 2 μM). Above 10 μM significant deviation away from linearity was observed in both set ups. To fully confirm the assay settings, TAMRA-Ahx-$A\beta_{16-22}$ was dissolved in buffer at concentrations ranging from 200 nM to 2 μM and analysed using set-up B (slit widths of 0.2 and 5 nm to reduce the possibility of photobleaching). These results confirmed that these settings and concentration ranges were suitable for the kinetic assays (Figure 35c). As such, the labelling ratio was set at 5% TAMRA-Ahx-$A\beta_{16-22}$ label in the self-assembly reaction.

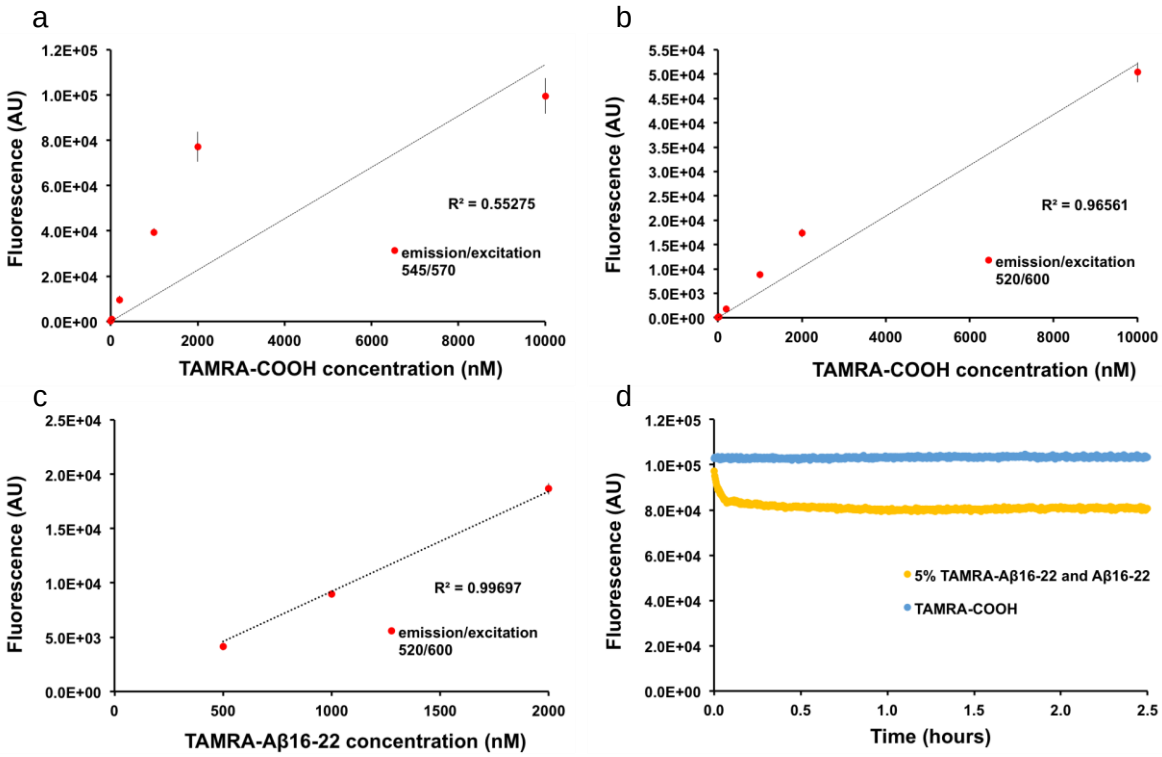

Figure 35. Development of the correct assay conditions for the fluorescence quenching experiments. Due to the inner filter effect, TAMRA-COOH can display non-linearity when at micromolar concentrations (a). By using slightly different emission and excitation wavelengths (520 and 600 nm respectively) this effect can be reduced (b). Using the settings, TAMRA-Ahx-$A\beta_{16-22}$ displays a linear increase in fluorescence with increasing concentration (c). TAMRA-COOH does not display significant fluorescence quenching, whereas 5% TAMRA-Ahx-$A\beta_{16-22}$ in $A\beta_{16-22}$ does, highlighting that quenching is aggregation dependent (d).

2.11 The kinetics of $A\beta_{16-22}$ aggregation

Two different concentrations of $A\beta_{16-22}$ were tested (20 and 40 μM) in 100 mM ammonium bicarbonate buffer, pH 7, with 2% final concentration of DMSO (v:v). Fluorescence emission was scanned every 30 s for 20 h, with TAMRA-COOH included in a separate cuvette as control. As can be seen from Figure 36, both self-assembly reactions proceed with a rapid initial decrease in fluorescence intensity followed by a second slower phase that reaches a plateau after around 1 h. Although the TAMRA-COOH control also shows a small decrease in intensity, the fluorescence recovers quickly and stays constant over the time course of the experiment (Figure 35d). To confirm that the decrease in fluorescence intensity was not due to precipitation of the peptides at the end of the assay (20 h) the cuvettes were shaken and re-tested. No

recovery in fluorescence intensity was observed, indicating that the effect was due to $A\beta_{16-22}$ self-assembly (data not shown).

Although a powerful method with which to measure amyloid formation kinetics, fluorescence quenching is limited in that it does not report on the type of structures formed, only the proximity of the fluorophores. To understand the aggregation process of $A\beta_{16-22}$ further, a negative stain TEM time course was performed with samples taken after 5 mins, 1 h and 24 h (Figure 36c). At 5 mins, fibrils can clearly be observed with a small amount of amorphous aggregates also present. After 1 h incubation at 37 °C, no amorphous aggregates can be seen and a significant amount of fibrils are present on the grids. At these early time points, the fibrils are fairly well dispersed without significant bundling, whereas at later time points (e.g. after 24 h) there is significant bundling of the $A\beta_{16-22}$ fibrils. Attempts to quantify the aggregation process using HPLC sedimentation assays were unsuccessful due to the low concentration (40 μM) of $A\beta_{16-22}$ used in this study and the low molar extinction coefficient of small peptides. Taken together, under the conditions employed in this study, these results show that $A\beta_{16-22}$ forms fibril structures quickly (~5 mins) with these fibrils then continuing to bundle together as the self-assembly reaction proceeds.

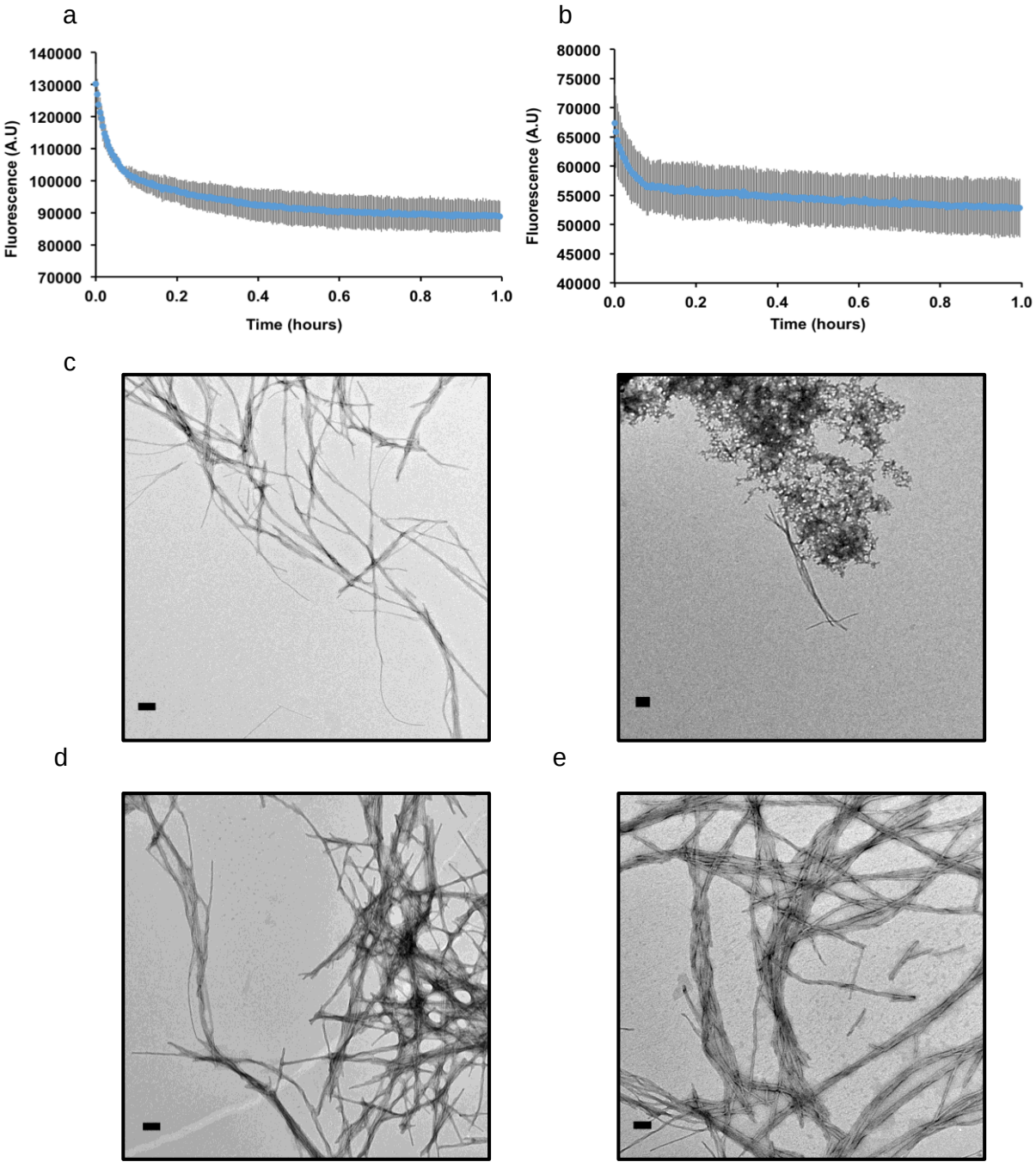

Figure 36. The aggregation kinetics of $A\beta_{16-22}$ as followed by fluorescence quenching. At both 40 and 20 μM (a and b respectively), $A\beta_{16-22}$ displays two-phase aggregation kinetics with the quenching reaching a plateau after around 1 h. In a TEM time course (c), WT $A\beta_{16-22}$ forms highly ordered fibril structures within 5 mins and small amounts of amorphous aggregates(c), which transition into fibrils after 1 h (d) and 24 h (e), confirming the results of the fluorescence quenching assay. Scale bar = 200 nm.

2.12 Large scale DMD simulations of $A\beta_{16-22}$ compare favourably with the experimental results

Given the success of the DMD and PRIME20 approach in predicting the thermodynamic phase boundaries of $A\beta_{16-22}$ in Section 2.9 and the approach pioneered by Hall and co-workers outlined in Section 2.3, the next question was whether these simulations could be extended into visualising the transitions that occur during the self-assembly process and whether these results would compare favourably with the experimental results. To answer this question, a large scale DMD simulation in which 192 $A\beta_{16-22}$ peptides in a random coil conformation were placed in a box with periodic boundary conditions (simulations performed by Yiming Wang and Professor Carol Hall, North Carolina State University, 37a). The simulation was progressed as described in Section 2.3 and a series of simulation snapshots can be seen in Figure 37. After t = 652 ns simulation time, most peptides are still in a random coil conformation with some disordered aggregates and small amounts of ordered oligomers present. As the simulation progresses (t = 1278 ns, Figure 37b), the formation of an antiparallel, in-register oligomer can be seen, as well as a small amount of disordered aggregates. This is in agreement with the structures observed by TEM at early time points (~5 min) where both fibrils and amorphous aggregates are present. At later time points (t = 2159 and 6283 ns, Figure 37d and e), most peptides are now in ordered aggregates with antiparallel, in-register structures dominating, and a single, 4-layered β-sheet structure present at the simulation end point (t = 12661 ns, Figure 37f). Again, these results are in agreement with the experimental data, in which both ordered fibrils and amorphous aggregates were observed at early time points (presumably after a hydrophobic collapse of the peptides upon dissolution), prior to the disappearance of the amorphous aggregates and continued formation of fibrils (Figure 36c).

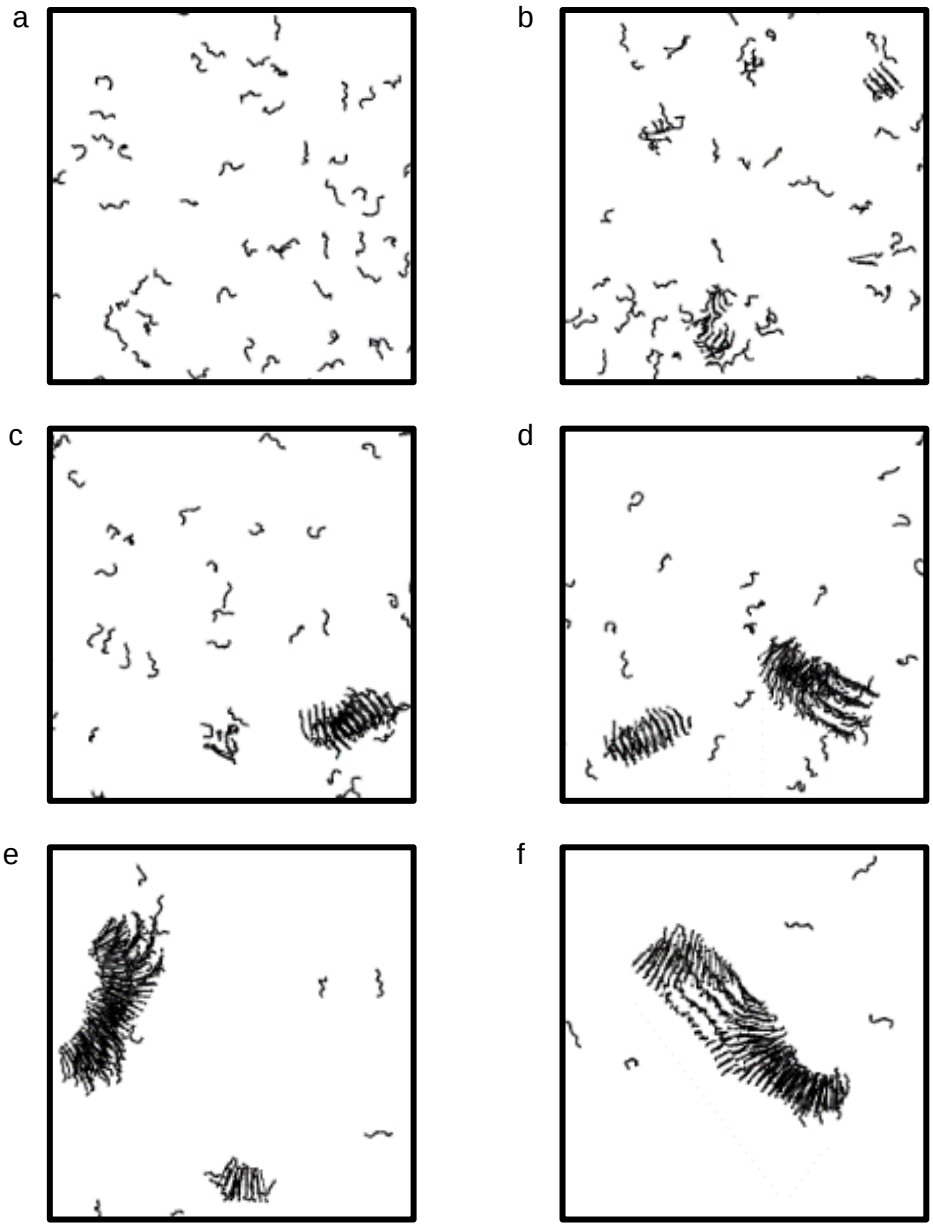

Figure 37. Large scale DMD simulation of 192 $A\beta_{16-22}$ peptides. Simulation snapshots were taken at 0 ns (a), 653 ns (b), 1278 ns (c), 2159 ns (d), 6283 ns (e) and 12661 ns (f) and show the transformation of $A\beta_{16-22}$ from random coils into a highly ordered β-sheet structure.

In the simulations, the kinetics of $A\beta_{16-22}$ aggregation can be measured by calculating the percentage of residues that are in a β-sheet conformation versus time. Figure 38 demonstrates, in agreement with the fluorescence quenching data, that aggregation proceeds with a rapid increase in β-sheet content (from 0 – 50% in the first 4000 ns) followed by a slower second phase (4000 – 12000 ns). The agreement between the TEM time course and the simulation snapshots (i.e. hydrophobic collapse and the presence of small amounts of fibrils at early time points followed by a transition to/continued fibril formation) and the two phase kinetics observed in both the fluorescence quenching (Figure 36 a/b) and simulations, confirms that using

experimental data and simulations in combination represents a powerful approach with which to explore the initial stages of peptide self-assembly.

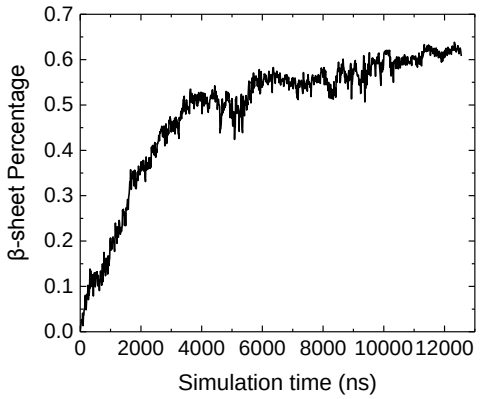

Figure 38. The aggregation kinetics of $A\beta_{16-22}$ as measured by the percentage of residues in a β-sheet of the DMD simulation seen in Figure 37.

2.13 Using ESI-IMS-MS and PIC to follow the structural changes that occur during $A\beta_{16-22}$ aggregation

After establishing the aggregation kinetics of $A\beta_{16-22}$, the next step was to unravel which structures $A\beta_{16-22}$ accesses during its transition from a random coil through to a highly ordered β-sheet lattice, using diazirine labelled $A\beta_{16-22}$ ($A\beta^*_{16-22}$, **19**, Figure 39). Prior to undertaking the PIC experiments, the diazirine containing fluorenylmethyloxycarbonyl-TFMD-phenylalanine (Fmoc-TFMD-Phe, **30**) was synthesized, according to the method developed by Fishwick and co-workers with modifications by Smith and co-workers (Scheme 2 and Section 4.6).[6,46] Fmoc-TFMD-Phe was then installed at position 20 within $A\beta_{16-22}$ using manual SPPS. Position 20 was chosen as previous work by Preston and co-workers demonstrated that placing the diazirine at F19 inhibited the formation of nanotubes at pH 2.[7] $A\beta^*_{16-22}$ was purified by HPLC, with the sequence identity confirmed using tandem MS/MS sequencing (Appendices 1 and 2).

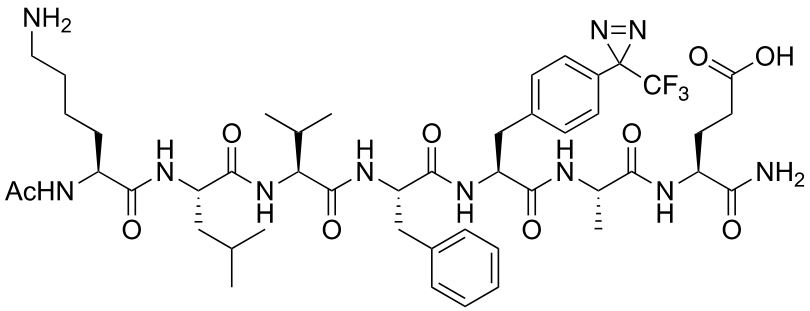

19

Figure 39. The molecular structure of $A\beta^*_{16-22}$ (**19**).

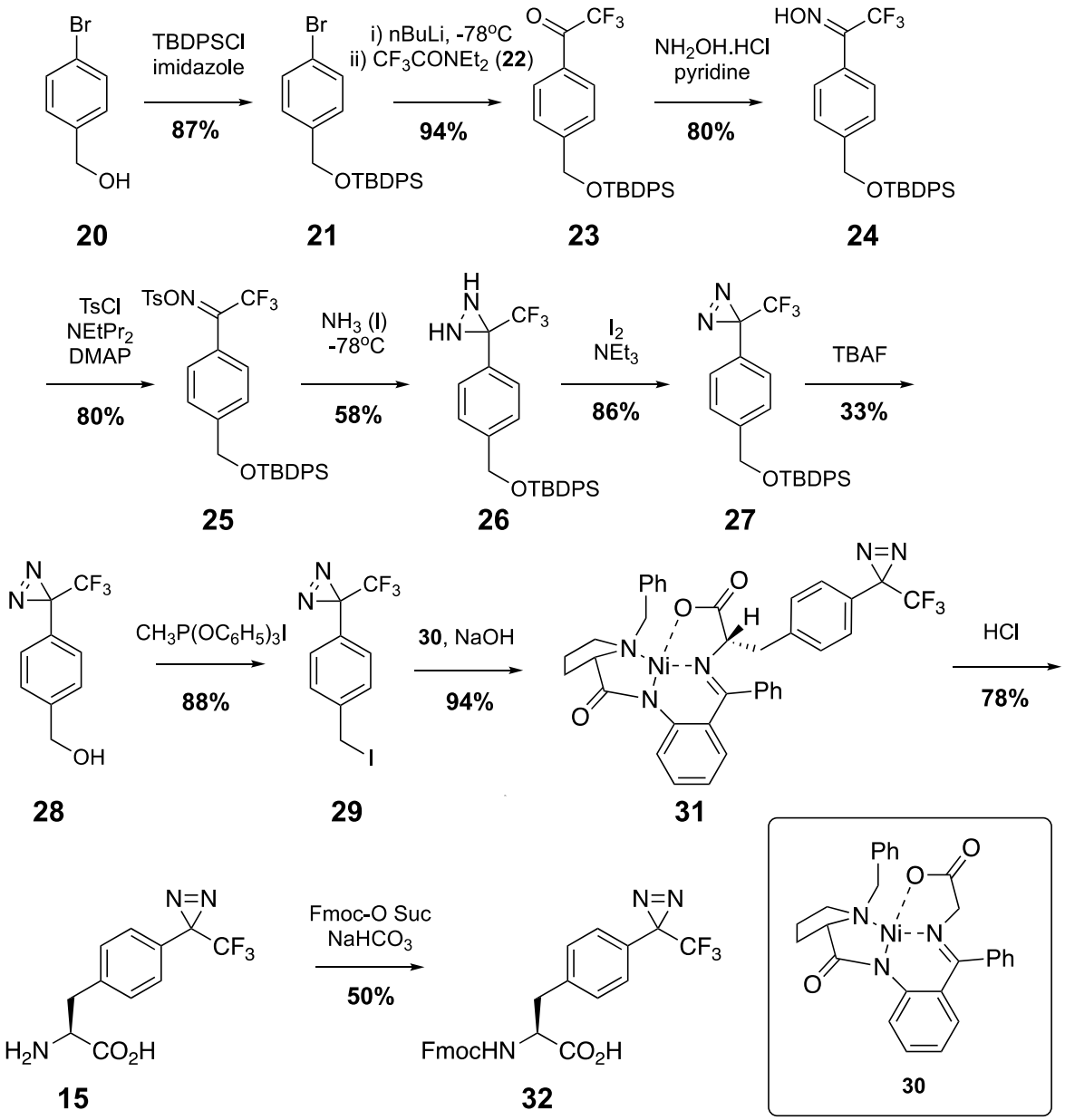

Scheme 2. The synthetic route to Fmoc-TFMD-Phe, adapted from the original synthesis by Fishwick and co-workers with modifications by Smith and co-workers (6, 7).

To confirm that the reagent had been successfully synthesized, a control experiment was performed whereby Aβ*$_{16-22}$ was left to aggregate for 2 weeks at 37 °C in 100 mM ammonium bicarbonate (pH 7, Figure 40a). Previous studies by Preston and co-workers were undertaken after 2 weeks of self-assembly in PBS buffer at room temperature (total peptide concentration of 400 μM). Two systems were used, either Aβ*$_{16-22}$ alone or a 4:1 (mol:mol) ratio of Aβ$_{16-22}$/Aβ*$_{16-22}$. The aim of performing this control experiment was to confirm that at the end of both self-assembly reactions the

same underlying β-sheet structure (in-register, antiparallel) was present in the buffer used in this study. For a more detailed description of the cross-linking protocol and ESI-IMS-MS/MS setting used in the PIC experiments please see Sections 4.11 – 4.14. Briefly, after being allowed to self-assemble for the required time, the sample was irradiated at 365 nm for 1 min using a home built LED lamp (see Appendix 4) and lyophilised, prior to disaggregation using HFIP. The HFIP was removed under a stream of N_2 and the peptide dissolved in water:acetonitrile (50:50) + 0.1 (v/v) formic acid prior to injection into the mass spectrometer.

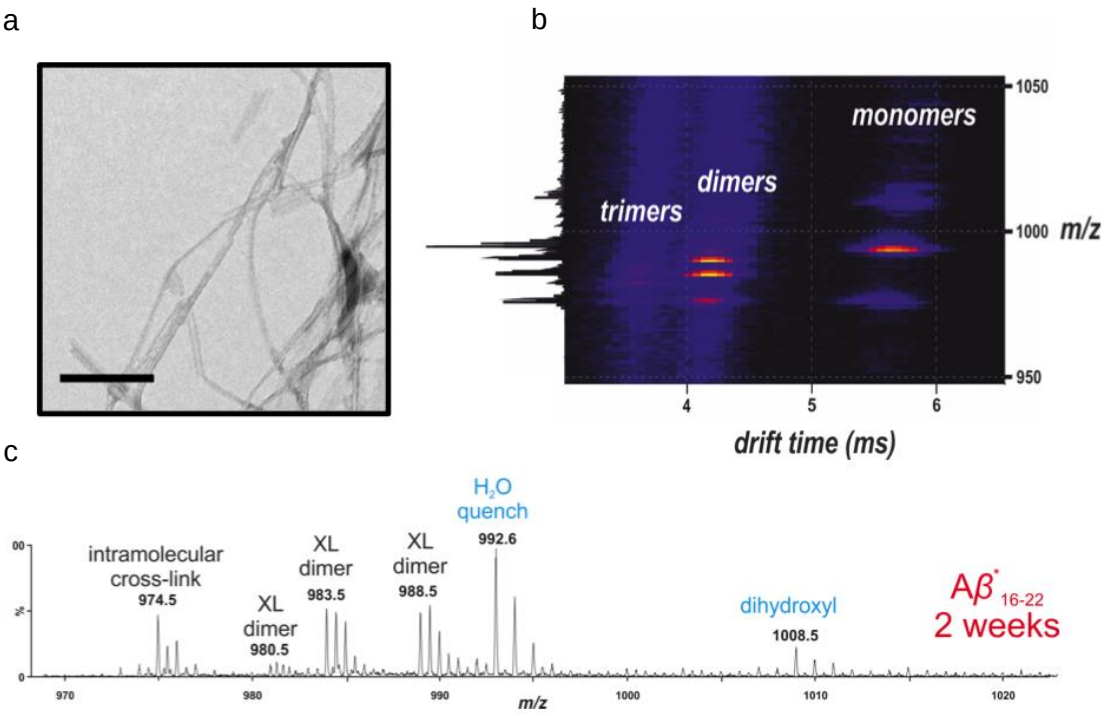

Figure 40. Control PIC experiment for Aβ*$_{16-22}$, under the conditions used in this study. After 2 weeks incubation, Aβ*$_{16-22}$ forms fibrils that are morphologically similar to those formed by WT Aβ$_{16-22}$ (a). After irradiation at 365 nm and disaggregation in HFIP, the drift-scope image (b) demonstrates that IMS can resolve monomers, dimers and trimers prior to ms/ms analysis. In the mass spectrum, 5 major peaks can be observed (c). Scale bar = 200 nm.

2.14 Analysis of cross-linked products after 2 weeks incubation: General comments

The 4:1 w/w ratio of $A\beta_{16-22}/A\beta^*_{16-22}$ did not provide any useful structural cross-linking information due to the low concentration of diazirine labelled peptide within the sample (data not shown). As such, all future cross-linking studies solely focused on $A\beta^*_{16-22}$, i.e. every peptide within the sample has a TFMD group at position F20. Figure 40b and c show the results of the PIC experiment performed after 2 weeks. The IMS function on the mass spectrometer confirmed that cross-linked monomer, dimer and very small amounts of trimer could be observed within the sample, in agreement with the previous work reported by the Group (Figure 40b).[7] The mass spectrum identified five major species (Figure 40c). The following section will focus on the MS/MS sequencing strategy undertaken to identify the species responsible for each peak.

2.15. Identity of the singly charged (i.e. monomeric) peaks (m/z 974.52, 992.60 and 1008.5)

Tandem MS/MS sequencing fragments the isolated peptide along its amide backbone, producing a variety of different fragment ions (see Appendix 5 for explanation of the notation).[47,59,81,82] For larger peptides *b* and *y* ions often dominate the spectra, although for shorter peptides other ions (such as *a* ions) can also be observed.[82] The mass difference (Δm) between individual peaks in the MS/MS spectrum corresponds to individual amino acid residues and any modifications that may have occurred. For example, the MS/MS spectrum of the most abundant peak in the initial mass spectrum at 2 weeks (m/z 992.60, 1^+) can be seen in Figure 41. Sequential cleavage has produced a series of *b* ions, corresponding to the amino acid sequence of $A\beta^*_{16-22}$. Between the b_6 and b_5 ions, the Δm = 245.1 Da; as the mass of the isolated TFMD-Phe having extruded molecular N_2 is = 227.1 Da, the Δm of 18.0 Da would indicate the addition of water. As such, the peak m/z 992.58 can be identified as a monomeric $A\beta^*_{16-22}$ that has reacted with water, forming a hydroxyl on F20 (see Figure 41). This assignment is in agreement with the previous studies performed by the group.[33] The peak at m/z 1008.5 was confirmed to be two hydroxyl groups, which can be formed via a number of different reaction processes.

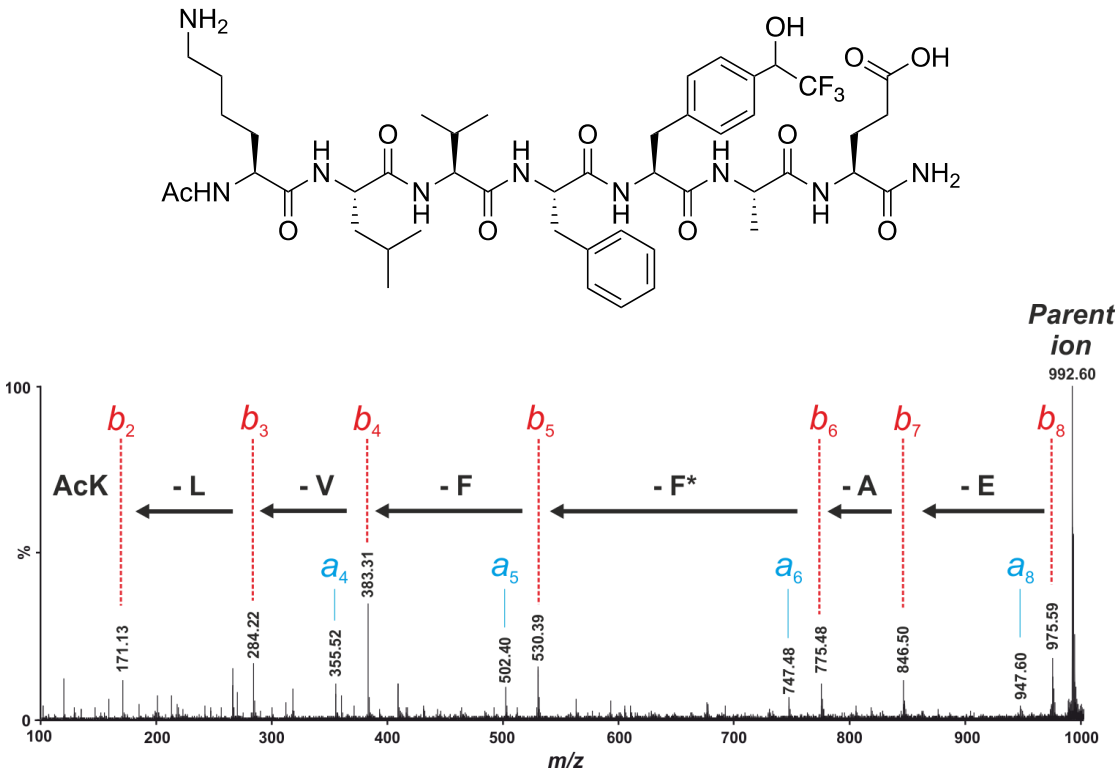

Figure 41. Annotated tandem MS/MS spectrum for the peak with m/z 992.60 (mass 991.60 Da), with the molecular structure of the H_2O quenched cross-linked product shown above.

The MS/MS spectrum of the second major monomeric product (m/z 974.52, 1^+) is shown below (Figure 42). In the spectra, no *b* ions can be observed between b_5 and b_8, indicating that an intramolecuar cross-link may have formed between F20 and E22. The covalent link formed between the side chains forms a stable region that is not fragmented in the same way as the peptide backbone. Preston and co-workers developed a method whereby n-propylamine (NPA) is added to the mixture during the disaggregation step, with NPA reacting with the ester formed between F20 and E22, forming the amide.[7] This in turn could be identified by the disappearance of the peak at m/s 974.52 and the appearance of a new peak at m/z 1034.52 (data not shown). Attempts to confirm this assignment with NPA were unsuccessful as the peak at m/z 974.52 disappeared but the associated amide peak could not be observed. Despite this, given the suppression of the *b* ions and the disappearance of the peak with NPA treatment, this peak was assigned as intramolecular cross-link formed by F20 and E22, again in agreement with the pattern of cross-links seen by Preston and co-workers.[7]

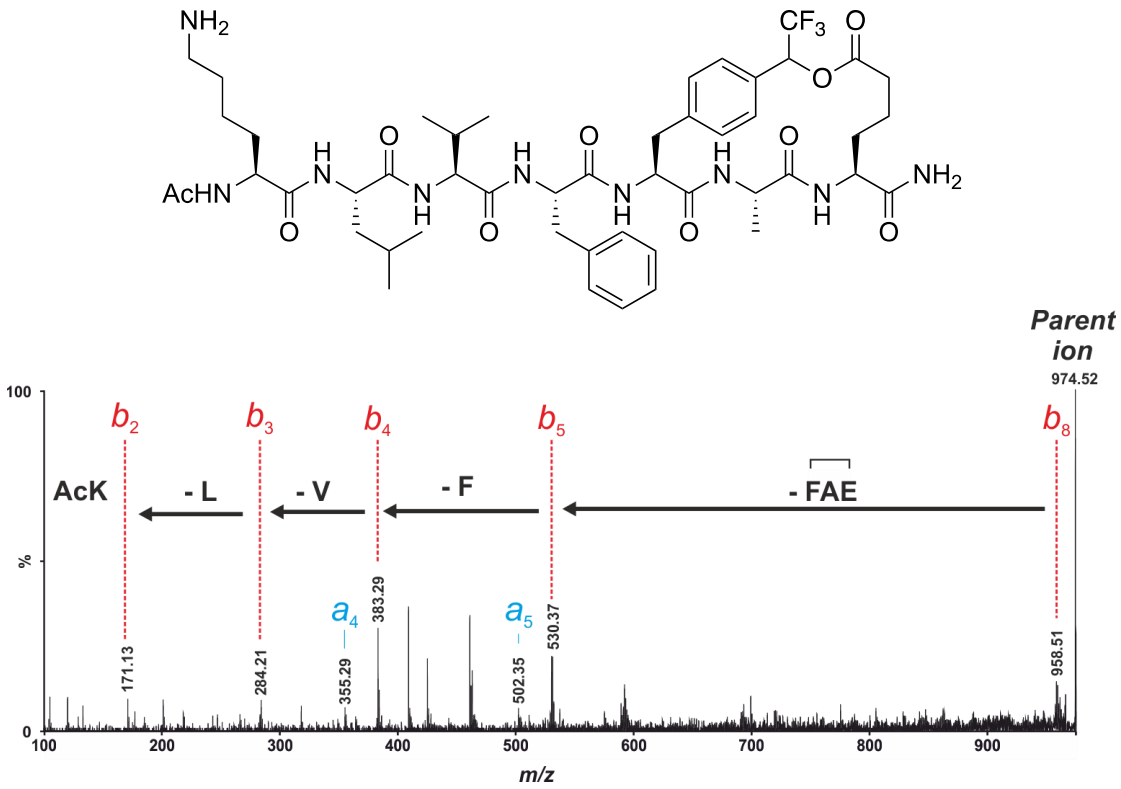

Figure 42. Annotated tandem MS/MS spectrum for the peak with m/z 974.52 (mass 973.52 Da), with the molecular structure of the intramolecular ester cross-linked product shown above.

2.16 Assignment of Aβ*$_{16-22}$ dimers- General comments

To analyse the cross-linked dimers, one peptide chain is considered to be the donor chain (i.e. from where the cross-link originates) and the second peptide chain is considered the acceptor chain (i.e. where the cross-link is going to, Figure 43a). The diazirine containing F20 on the acceptor chain (referred to as F* in Figure 43 and the following sections) can have a number of fates (e.g. conversion to the linear diazoisomer or reaction with H_2O to form a hydroxyl). The nature of the transformation on the acceptor chain will determine the overall m/z of the cross-linked dimer. As such, the first step identifying the position of the cross-link is to establish the fate of the diazirine at F* of the acceptor chain. The m/z ratios of the singly charged species described in Section 2.15 aids the assignment of the cross-linked dimer. For example, if the carbene has been quenched by H_2O, the mass for this species is 992.5 Da. When this value is added to the mass of Aβ*$_{16-22}$ having extruded molecular N_2 and gained a proton (i.e. has formed a cross-link, mass 973.5), the overall mass of the cross-linked dimer is 1965.0 Da. Hence, if a cross-linked dimer with a m/z of 983.5 (2^+) is observed, we can identify this as a cross-linked dimer in which the F20 of the donor chain has formed a cross-link to an acceptor chain, in which F* is a H_2O quenched

species (Figure 43a). The following sections will describe some general principles that need to be applied when analysing cross-linked dimers, then demonstrate the assignment process using the fragmentation pattern of the peak at m/z 988.58, 2^+ (mass 1975.16 Da, cross-linked dimer in which F* in the acceptor chain is a linear diazoisomer).

As described in Section 2.15, tandem MS/MS sequencing fragments peptides sequentially along the amide backbone. The ion series represent sequential fragmentation from either the N or C termini of the peptide (e.g. forming *b* or *y* ions), allowing the identification of any amino acid modifications. In a cross-linked dimer, there are four termini at which fragmentation can occur (i.e. amino acid residues can be lost from either the donor or the acceptor chain). This degeneracy complicates the cross-linking analysis, as for certain m/z ratios there are multiple isomeric products (Figure 43b). In the example outlined in Figure 43b, a peak with a m/z ratio of 1583.5 (1^+) would indicate that residues KLVF (16-19) have been lost form the N terminus of the cross-linked dimer, forming a *y* ion. As both the donor and acceptor chains contain these amino acid residues, there is no possible way of distinguishing where the fragmentation has occurred. Without being able to identify which chain the amino acids have been lost from, it is impossible to correctly locate the position of the cross-link (i.e. the cross-link could have formed between F20 on the donor and any residue in the acceptor chain with the loss of KLVF occurring at the N terminus of the donor chain).

In order to unambiguously assign the location of the cross-link on the acceptor chain, F* must be lost (Figure 43c). As F20 in the donor chain forms the cross-link, in the fragmentation experiments this residue cannot be lost (as it forms a non-labile bond with the acceptor chain). This in turn means that the only residue with a different mass in the acceptor chain is F* (i.e. K16 has the same mass in both the donor and the acceptor chain). Once a fragment containing F* has been lost, the cross-link can be assigned to the acceptor chain. In Figure 43c, the loss of KLVFF* from the acceptor chain produces an ion with m/z 1436.5. As no other fragment ion can have this mass, the cross-link has formed with either A21 or E22 on the acceptor chain. The possibility of double fragmentation (i.e. fragments are lost from both acceptor and donor chains) can complicate the assignment process. In order to help the assignment of such complex spectra the Group has previously developed a calculator that can aid in the assessment of complex MS/MS spectra (see Appendix 7 for a description of how the calculator operates).

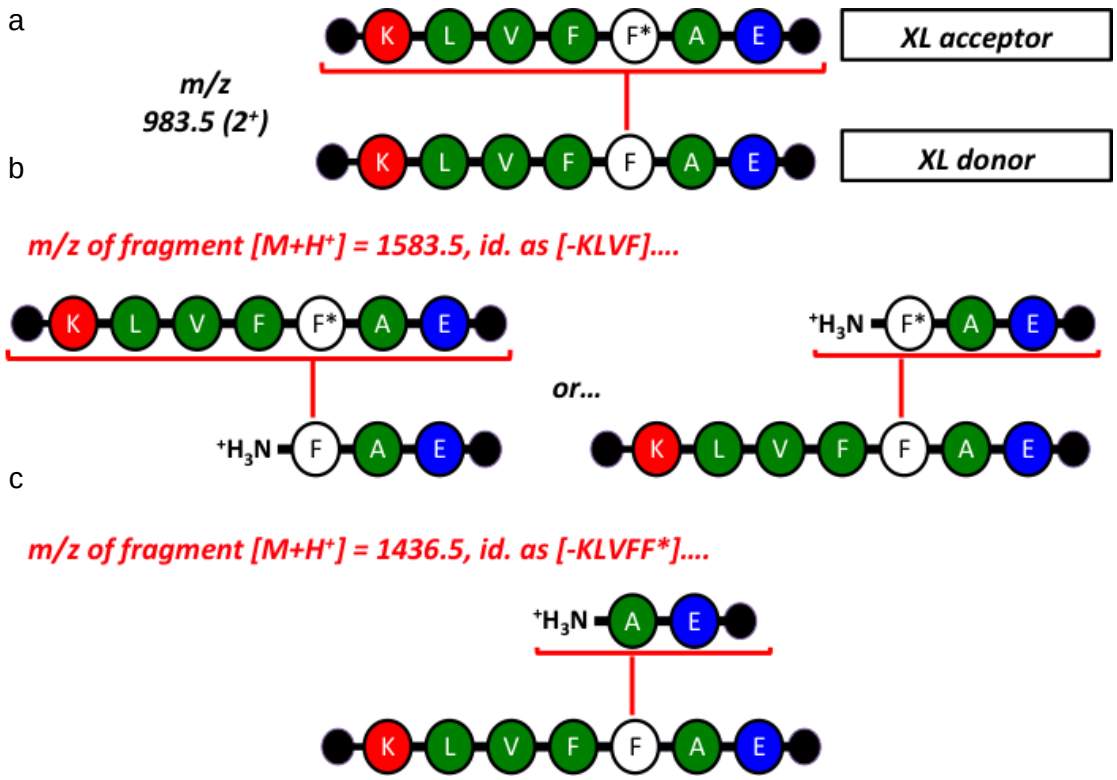

Figure 43. The diazirine labelled F20 of the acceptor chain (F*) is structurally diagnostic when assigning the cross-link position. When analysing the cross-linking data, the peptide chain from which the cross-link originates is referred to as the donor and the chain to which the cross-link goes is referred to as the cross-link acceptor (a). The identity of F* can be elucidated from the overall m/z ratio of the cross-linked dimer. As the two peptide chains are almost identical, certain ions can have multiple isomeric products (b). Once F* has been lost from the acceptor chain, the fragment can be confirmed to have come from the acceptor chain and the position of the cross-link can be identified (c).

Once the identity of F* and the position of the cross-link in the acceptor chain have been identified, this information must be compared with the different possible models (i.e. parallel/antiparallel and in/out-of-register) to identify the underlying β-sheet structure. It should be noted that due to the distance constraint imposed by placing the diazirine in the amino acid sequence, only inter-sheet (vs intra-strand) cross-links are possible. As described in Section 1.7, the inter-sheet distance is ~4.9 Å, whereas as the distance between strands is between 9 – 10 Å and so the diazirine located at F20 will not be able to react with any side chains in a separate strand. Care must be taken with the unambiguous assignment of a cross-link, as there is degeneracy in the possible β-sheet alignments. For example, if a cross-link has formed between F20

(donor) and A21 (acceptor) there are two possible β-sheet alignments that could have allowed this cross-link to form (antiparallel, out-of-register and parallel, out-of-register, Figure 44). In the parallel, out-of-register alignment F20 and A21 are located directly opposite each other whereas in the antiparallel, out-of-register alignment A21 is at a diagonal to F20 (i.e. the side chains are close together in the fibril structure). In comparison, the antiparallel, in-register and antiparallel, out-of-register fibril alignments place the acceptor chains A21 in regions of space that are inaccessible to F20 on the donor chain. In comparison, if a cross-link had formed between the F20 (donor) and K16 (acceptor), this cross-link would confirm that an antiparallel, in-register β-sheet alignment was present as there are no other alignments in which these 2 residues will come into contact. Taken together there are two key factors that allow a cross-link to be positively assigned and the underlying β-sheet identified: that F* has been lost from the acceptor chain and that the cross-link formed is only present in one sheet alignment.

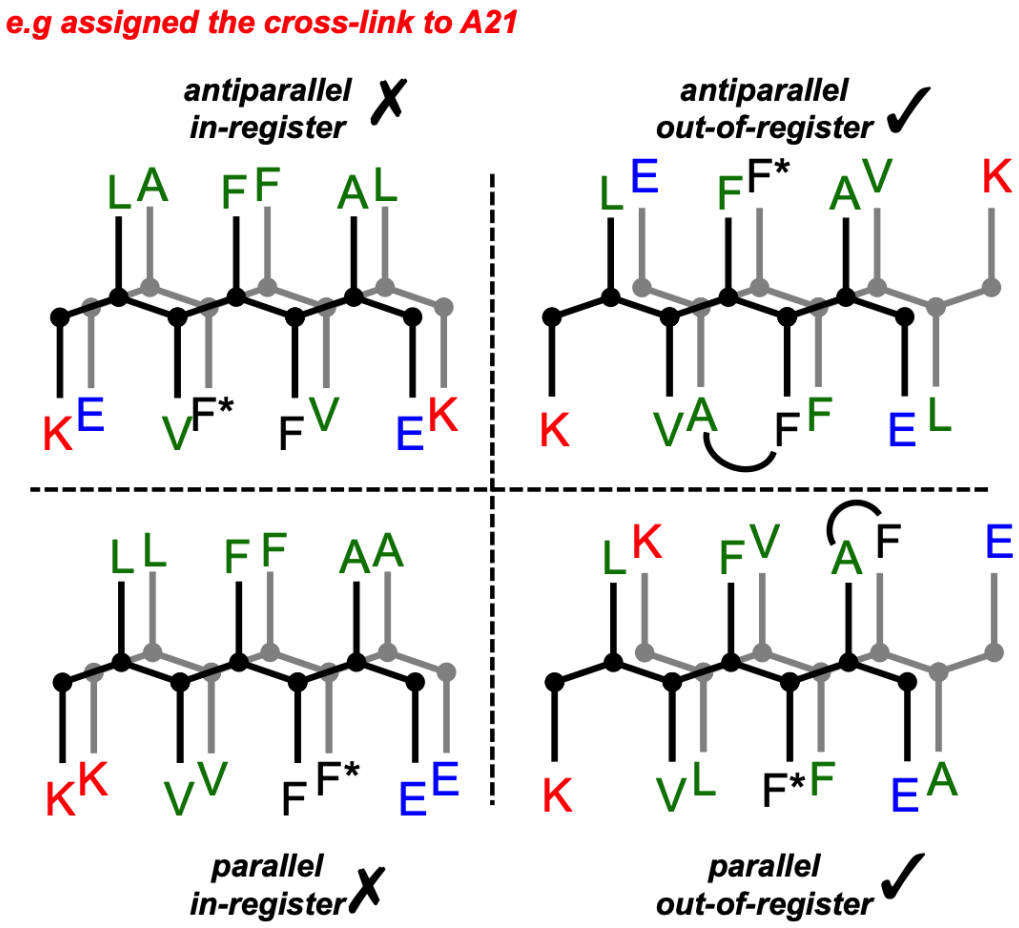

Figure 44. Different underlying β-sheet structures can produce the same cross-links. A cross-link that has been positively identified as being formed from F20 to A21 in the acceptor chain could indicate either a parallel in-register or a parallel out-of-register β-sheet alignment. Ticks indicate that a cross-link between F20 and A21 is consistent with this underlying β-sheet structure and crosses indicate that a cross-link between F20 and A21 would not occur in the alignment. Charged residues are highlighted in blue and red, hydrophobic amino acids are colour in green, F* represents F20 on the acceptor chain and F indicates where the cross-link originates. The cross-link is highlighted in black.

2.17 Assignment of Aβ*$_{16-22}$ dimer at m/z 988.58

The following section will outline how the cross-linked dimer with m/z 988.58 (2^+, mass 1977.16 Da) was assigned and the underlying antiparallel, in-register β-sheet structure identified. This PIC experiment was conducted on Aβ*$_{16-22}$ fibrils (2 weeks, see control experiment in Section 2.13 and Figure 40). As described above, a dimer with a m/z of 988.58 (2^+) indicates that the F* moiety is formed of a linear diazoisomer. The fully assigned MS/MS spectra of m/z 988.58 (2^+, i.e. mass 1977.16 Da) can be seen in Figure 45. In the spectra a number of different fragmentation patterns can be observed

including both double fragmentation products and *a* ions. As discussed in Section 2.16, due to the number of possible isomeric products, these fragmentation products do not contain useful structural information. In addition to these ions, both a series of *b* (b_5 to b_2; LVF*AE) and *y* (y_6 to y_4; KLVF) ions can be seen (Figure 45). The *y* ion series locates the cross-link to residues F*AE on the acceptor chain and, as no other *y* ions are observed (e.g. y_3 or y_2) in the MS/MS spectra, this cross-link is most likely to have formed between F20 on the donor chain and F* on the acceptor chain. In contrast to the *y* ion series, a full *b* ion series can be observed in the spectra (up to b_2), locating the cross-link to K16 on the acceptor chain. The position of both of these cross-links is consistent with an underlying antiparallel, in-register β-sheet structure, in agreement with the previous cross-linking data and literature reports.[1,7] In particular, the formation of cross-link between F20 on the donor chain and K16 on the acceptor chain is strong evidence for an antiparallel, in-register alignment as there is no other alignment in which this cross-link can form (Figure 45). The second dominant dimeric product (m/z 983.50, 2^+; mass 1965.0 Da) also confirms the presence of antiparallel, in-register β-sheets (a full assignment of this peak can been found in Appendix 7).

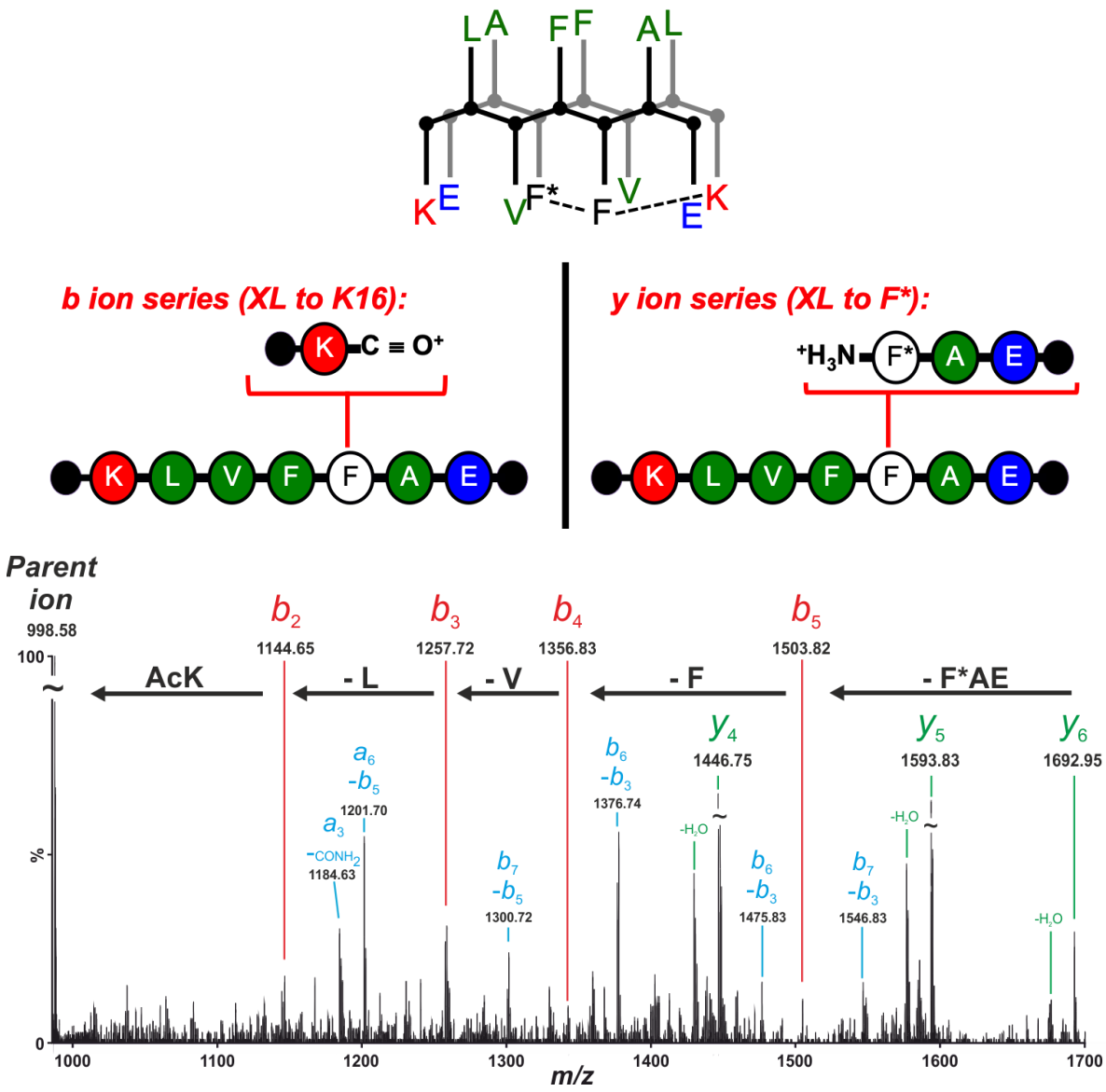

Figure 45. Aβ*$_{16\text{-}22}$ forms antiparallel, in-register β-sheets after 2 weeks incubation. The fully assigned tandem MS/MS spectrum for the peak at m/z 988.58 (2^+; mass 1975.16 Da) contains *b* ions (red), *y* ions (green) and double fragmentation products (blue). The two major fragmentation series (*b* and *y* ion) located the cross-link position to K16 and F* on the acceptor chain respectively. Both of these cross-links are consistent with antiparallel, in-register β-sheet alignment. Charged residues are highlighted in blue and red, hydrophobic amino acids are coloured in green and residues containing diazirines are coloured black, F indicates the residue from which the cross-link originates and F* represents the moiety on the acceptor chain (a linear diazoisomer). The cross-links are represented by dashed lines.

2.18 $A\beta_{16-22}$ forms antiparallel, in-register β-sheets at all time points

The overall mass spectrum from each time point (5 min, 1 h, 24 h and 2 weeks) can be seen in Figure 46. Intermolecular cross-links can be seen at all time points, with the intensity (relative to the water quenched $A\beta_{16-22}$) increasing as time progresses. This can be attributed to the significant bundling of the $A\beta_{16-22}$ fibrils after aggregation is complete, as the bundling of the fibrils creates dry interfaces in which water is excluded. The exclusion of water allows the carbene to react with peptide side chains, rather than being instantly quenched to form a hydroxyl group. These results may also reflect the slower conversion of amorphous aggregates into more ordered fibrils at later time points.

At each time point, both dominant intermolecular cross-link peaks (i.e m/z 998.58, 2^+; mass 1995.16 Da and 983.50, 2^+; 1965.0 Da) were isolated and sequenced using the method described above. The results from sequencing the peak at m/z 988.58 can be seen in Figure 47 (sequencing data can be for peak m/z 983.50 can be seen in Appendix 7). The cross-linking pattern observed at each time point is identical to that observed for $A\beta^*_{16-22}$ that had been incubated for 2 weeks (i.e. $A\beta^*_{16-22}$ is fibrillar, Section 2.17). A series of *y* ions can be observed (y_6 to y_4), locating the cross-link to F* on the acceptor chain. The *b* ion series (b_5 to b_2) locates the cross-link to K16 on the acceptor chain, providing strong evidence that at all time points the dominant underlying β-sheet structure is antiparallel and in-register.

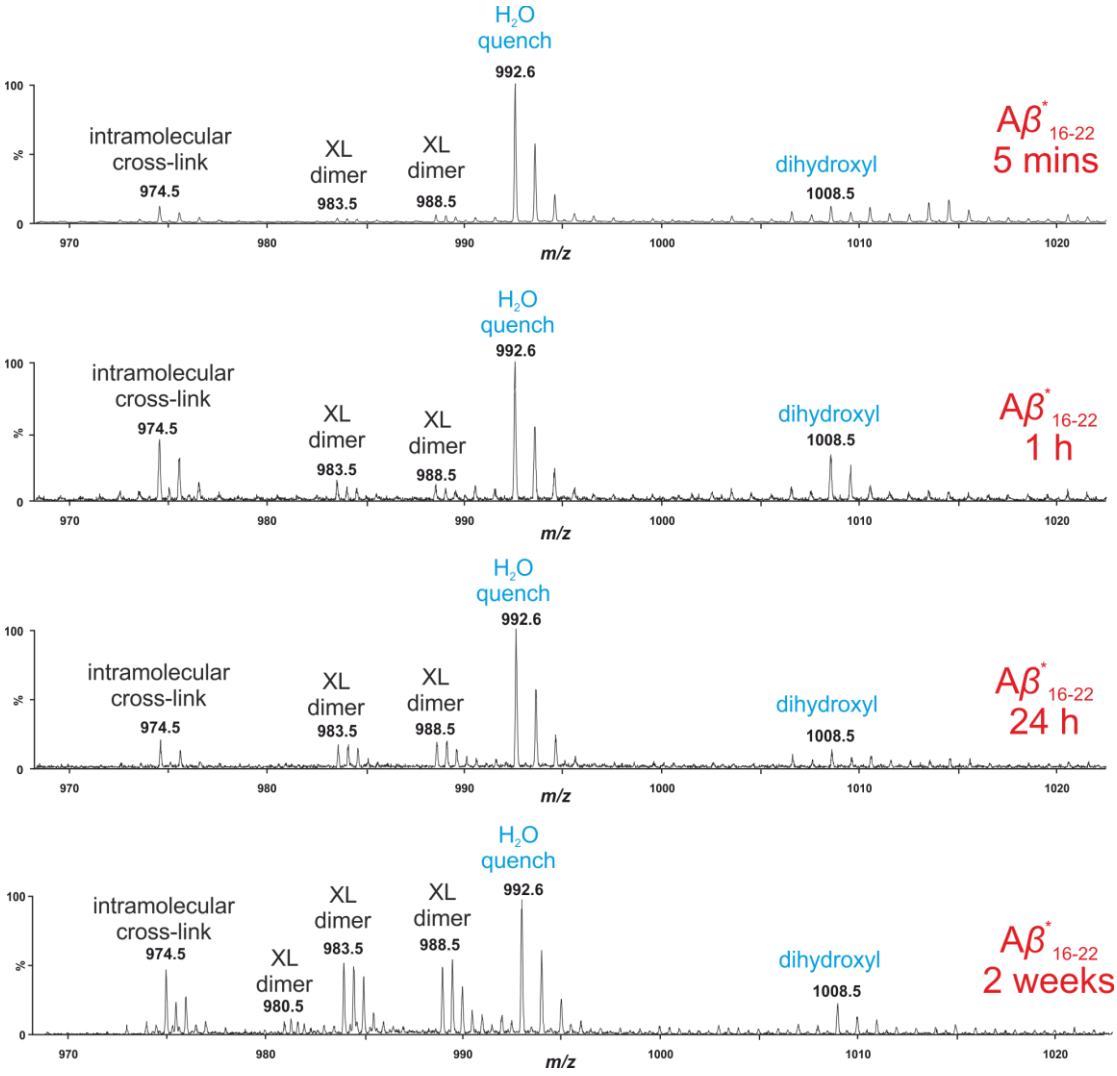

Figure 46. Full scan, ESI mass spectra of Aβ*$_{16-22}$ showing precursor monomer ions at m/z 992.6 (1^+; mass 991.6 Da) and cross-linked dimer ions in the region 800 – 900. At all time points, Aβ*$_{16-22}$ forms both intra – and intermolecular peptide cross-links. Products from the reaction between the carbene and water are labelled in blue and peptide cross-links are labelled in black.

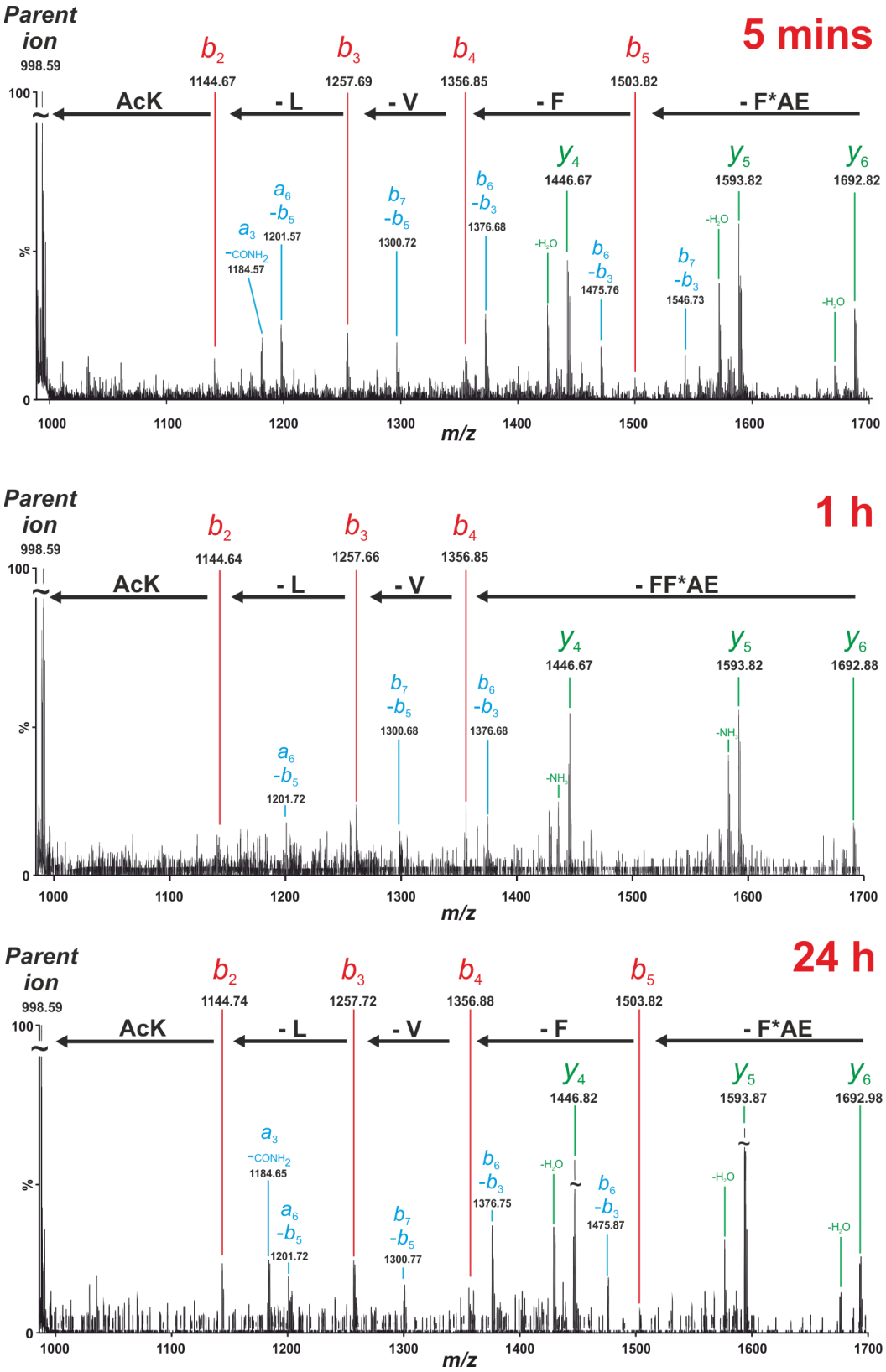

Figure 47. Annotated tandem MS/MS spectra demonstrating that at all time points (5 mins, 1 h and 24 h), Aβ*$_{16-22}$ forms antiparallel, in-register β-sheets. In the spectra, *b* ions are highlighted in red, *y* ions in green and any double fragmentation products in blue. The parent ion is 988.59 (2^+, mass 1975.16 Da) and F* on the acceptor chain is a linear diazoisomer.

2.19 Side chain contacts formed during DMD simulations of $A\beta_{16-22}$ self-assembly

The nature of the ESI-IMS-MS/MS analysis (in which there are many different isomeric and oligomeric products that can have the same m/z) means that positively identifying the presence of amorphous aggregates can be difficult. This is due to the fact that only some fragments containing structurally useful information can be assigned unambiguously (e.g. the b_2 ion that indicates the presence of antiparallel, in-register β-sheets) and, as such, the likelihood of being able to distinguish an amorphous aggregate is low (due to the random distribution of the cross-links). The DMD approach used in this study can also be used to measure the distance between specific side chains as the simulation progresses and may be able to identify structures that the PIC studies may have missed. To measure this, a side chain contact was given a value of 1 if the distance (d) between the side chains was within 1 – 3 Å, with the results for F19 and F20 seen in Figure 48.

At the simulation end point, both F19 and F20 are making the most contact with the residues that are directly opposite these side chains in an antiparallel, in-register orientation (F19 and V18 respectively, Figure 48c and d). This is in good agreement with the experimental data, which also observes cross-links consistent with an antiparallel, in-register orientation. Within the data, roughly three phases can be seen: 0 – 1500, 1500 – 3000, 3000 – 12000 ns. As can be seen in Figure 48a, the residue that F19 contacts the second most during the simulation is F19-V18. These contacts increase steadily until ~1000 ns at which point no further increase in the number of contacts is made. Contacts between F19 and V18 are possible in both antiparallel, out-of-register and parallel out-of-register conformations. Interestingly, Lynn and co-workers observed that at neutral pH $A\beta_{16-22}$ forms an intermediary antiparallel out-of-register alignment prior to transitioning into the final in-register alignment.[13] When looking at the contacts F20 forms during this initial period, two major contacts (other than F20-V18) can be observed: F20-L17 and F20-F20. The F20-L17 contact is possible in both an antiparallel, out-of-register or parallel, out-of-register conformation and again continues to increase until ~1500 ns at which point the number of contacts remains stable for the rest of the simulation. The F20-F20 contact can be observed in an antiparallel, in-register alignment and increases at a slightly slower rate than the F20-L17 contact in the first phase. However, rather than stopping at 1500 ns it continues to increase until it plateaus at ~3000 ns. Taken together, these results would suggest that as the simulation progresses both antiparallel in-register and antiparallel out-of-register structures are present (and some disordered aggregates, given the

range of contacts formed at early time points). After 1500 ns, however, the antiparallel, in-register alignment starts to dominate whilst the contacts for an antiparallel, out-of-register alignment plateau, indicating that this structure is now no longer growing and may interconvert to the in-register alignment, in agreement with the experimental observations made by Lynn and co-workers.[13] These series of simulations clearly demonstrate the power of combining simulations and experimental data to gain a full picture of peptide self-assembly at an atomistic level.

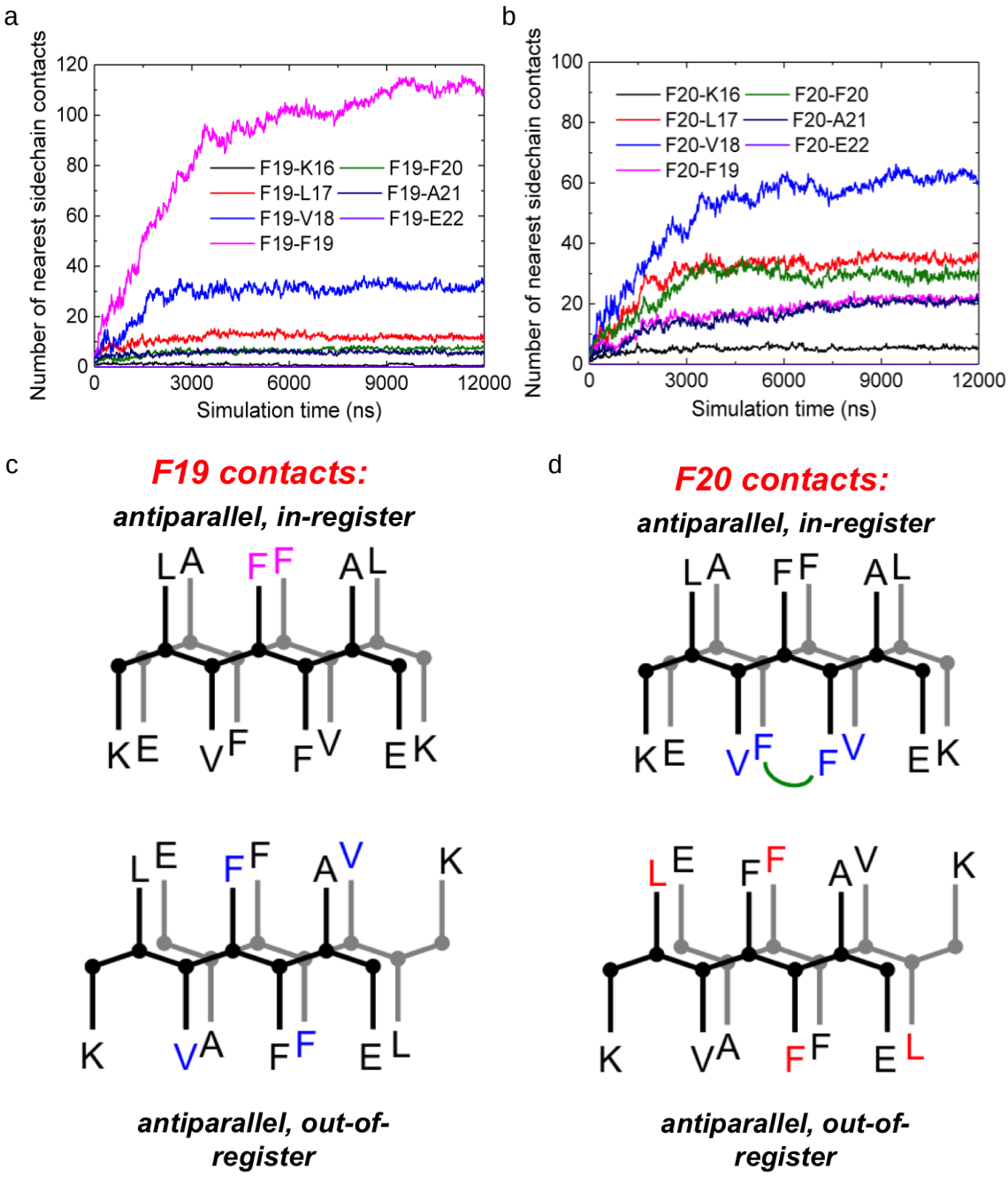

Figure 48. Analysis of the side chain contacts formed by $A\beta_{16-22}$ during the self-assembly process in the DMD simulations. The side chain contacts formed by F19 (a) and F20 (b) are shown, with schematics demonstrating how this relates to the different underlying β-sheets shown below (c and d respectively).

2.20 Proposed mechanism by which $A\beta_{16-22}$ self-assembles

According to the experimental data, the following mechanism for $A\beta_{16-22}$ self-assembly is tentatively proposed (Figure 49). $A\beta_{16-22}$ aggregates quickly, forming both fibrils and small amounts of amorphous aggregates (the initial decrease in fluorescence intensity, ~ 5 mins). These amorphous aggregates then form fibrils, with most of the self-assembly reaction complete within 1 - 2 hours (as evidenced by the plateau in the fluorescence quenching data). The fibrils formed at these time points tend to be isolated and unbundled. As the self-assembly reaction proceeds, the fibrils start to bundle together and coalesce, forming dense mats of fibrils structures (after 2 weeks). These large mats (partly) exclude water, forming a series of dry interfaces, in turn reducing the opportunity for water to quench the carbene and promoting the formation of interpeptide cross-links.

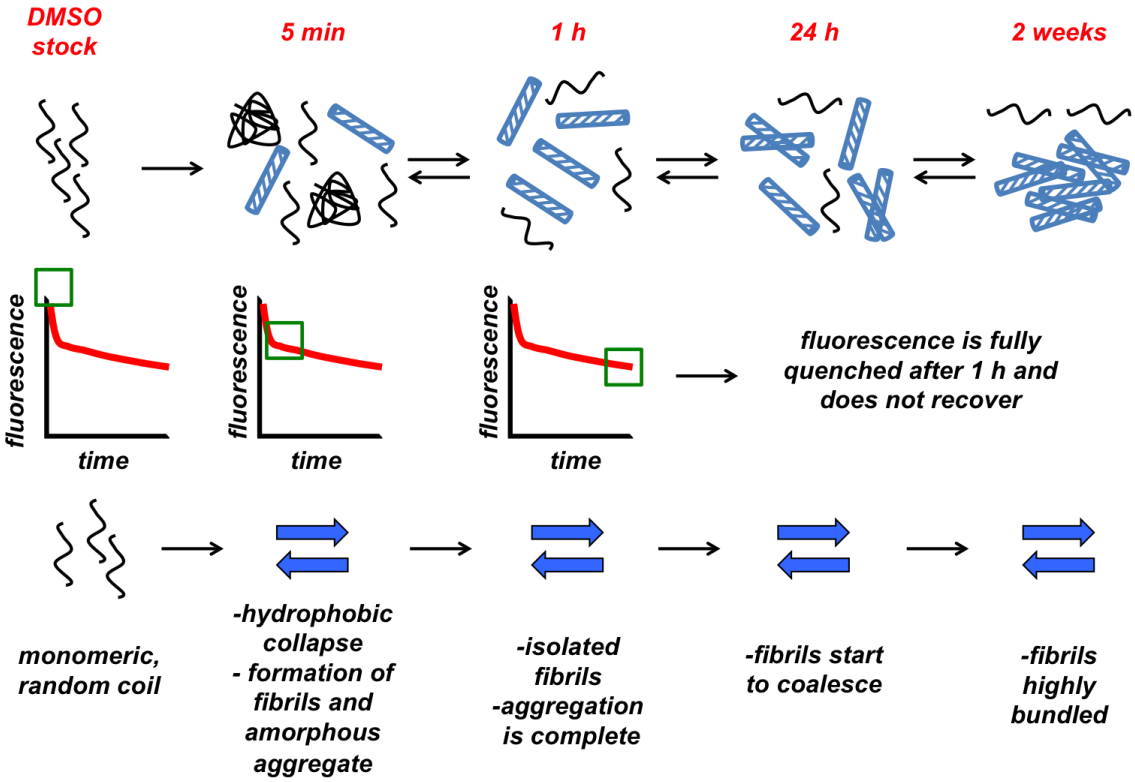

Figure 49. The experimentally proposed mechanism for $A\beta_{16-22}$ self-assembly. In the DMSO stock, $A\beta_{16-22}$ is monomeric and in a random coil. Upon solvation, antiparallel, in register fibrils and amorphous aggregates form with an initial decrease in fluorescence (5 mins). After 1 h, no amorphous aggregates can be seen and the fluorescence has fully quenched. As time continues, the aggregates bundle together, forming dense mats of fibrils that exclude water, forming dry interfaces that increase the cross-linking yield.

As described in Section 2.2.2, Lynn and co-workers observed a transition from out-of-register, antiparallel β-sheets before $A\beta_{16-22}$ assembled into the final in-register alignment.[13] No such transition was observed in the cross-linking data. There could be a number of reasons for this:

- the out-of-register alignment may be lowly populated compared with the in-register alignment and as such may not be captured by the cross-linking experiments at early time points;
- Lynn and co-workers performed their studies in water and acetonitrile with no added salt (i.e. at very low ionic strength), given that in the study presented here an 100 mM ammonium bicarbonate buffer at pH 7 was used the increase in ionic strength may increase the aggregation reaction such that the out-of-register alignment is bypassed/only briefly accessed

2.21 Conclusions

In this chapter, both $A\beta_{16-22}$ and a TAMRA-labelled peptide variant were synthesized and used in a fluorescence quenching assay. This assay demonstrated that $A\beta_{16-22}$ aggregates in two distinct phases. Within the first phase the fluorescence decreases rapidly (~10 mins) which is then followed by a slower, second phase that plateaus after 1 – 2 hours. A TEM time course confirms that fibrils are present after 5 mins. As time progresses these fibrils bundle together significantly. To characterise the β-sheet structures at a number of different time points, the PIC reagent Fmoc-TFMD-Phe was synthesized and incorporated into $A\beta_{16-22}$. PIC with ESI-IMS-MS/MS at different time points confirmed that $A\beta_{16-22}$ forms antiparallel, in-register β-sheets assembly at all time points, allowing a molecular mechanism to be proposed for $A\beta_{16-22}$ under the conditions used in this study. These experimental results were then compared with a series of detailed DMD simulations that were in agreement with the experimental data and also highlighted the presence of an antiparallel, out-of-register intermediary structure that could not be identified (due to the random nature of the cross-links formed) by PIC.

2.22 Future Work

After using PIC and ESI-IMS-MS to study the underlying structural changes that $A\beta_{16-22}$ undergoes as it self-assembles at pH 7 (in buffer), one of the next tasks would be to repeat the cross-linking analysis on $A\beta_{16-22}$ under low ionic strength conditions (such as those used by Lynn and co-workers).[13] Low ionic strength conditions should slow the self-assembly process enough such that the intermediary, out-of-register β-sheet structure can be captured and characterised. Confirming that $A\beta_{16-22}$ forms a random

coil structure when dissolved in solution (using NMR) would also complete the characterisation of the self-assembly process. Dynamic Light Scattering (DLS) measurements could also be used to further understand the initial transitions that occur upon solvation (such as whether oligomeric species that cannot be identified by fluorescence quenching or ESI-MS form). Future work could also include repeating the fluorescence quenching assays and PIC on $A\beta_{16-22}$ as it self-assembles at pH 2. Assembly at pH 2 should occur more slowly than at pH 7, providing an opportunity to capture any transitions using PIC. EPR measurements could also be made in order to further confirm that side chain contacts that were observed in the DMD simulation.

Now that PIC has been used on a short model peptide, such as $A\beta_{16-22}$, the next step would be to extend this methodology to the full-length sequence. The difficult nature of SPPS for sequences such as $A\beta_{40/42}$ requires the use of automated microwave synthesisers, which may present problems with diazirine stability during iterative rounds of synthesis. An important consideration when moving on to longer peptides is the placement of the cross-linker within the sequence. For example, placing the cross-linking reagent in the N-terminal region of $A\beta_{40}$ may not provide significant structural information as this region tends to be flexible in the final fibril structure.[83–85] A particular focus for the longer sequences would be to characterise the structures of the soluble, oligomeric intermediates that are implicated in the progression of Alzheimer's Disease.[86–88] The fundamental principles of the PIC strategy however would remain the same.

References:

1 J. J. Balbach, Y. Ishii, O. N. Antzutkin, R. D. Leapman, N. W. Rizzo, F. Dyda, J. Reed and R. Tycko, *Biochemistry*, 2000, **39**, 13748–13759.

2 M. Balbirnie, R. Grothe and D. S. Eisenberg, *Proc. Natl. Acad. Sci. U. S. A.*, 2001, **98**, 2375–2380.

3 R. Nelson, M. R. Sawaya, M. Balbirnie, A. Madsen, C. Riekel, R. Grothe and D. Eisenberg, *Nature*, 2005, **435**, 773–778.

4 M. R. Sawaya, S. Sambashivan, R. Nelson, M. I. Ivanova, S. A. Sievers, M. I. Apostol, M. J. Thompson, M. Balbirnie, J. J. W. Wiltzius, H. T. McFarlane, A. Ø. Madsen, C. Riekel and D. Eisenberg, *Nature*, 2007, **447**, 453–457.

5 P. M. Seidler, D. R. Boyer, J. A. Rodriguez, M. R. Sawaya, D. Cascio, K. Murray, T. Gonen and D. S. Eisenberg, *Nat. Chem.*, 2018, **10**, 170–176.

6 D. P. Smith, J. Anderson, J. Plante, A. E. Ashcroft, S. E. Radford, A. J. Wilson and M. J. Parker, *Chem. Commun.*, 2008, 5728–5730.

7 G. W. Preston, S. E. Radford, A. E. Ashcroft and A. J. Wilson, *Anal. Chem.*, 2012, **84**, 6790–6797.

8 M. Cheon, I. Chang and C. K. Hall, *Biophys. J.*, 2011, **101**, 2493–2501.

9 C. Hilbich, B. Kisters-Woike, J. Reed, C. L. Masters and K. Beyreuther, *J. Mol. Biol.*, 1992, **228**, 460–473.

10 G. Bitan, S. S. Vollers and D. B. Teplow, *J. Biol. Chem.*, 2003, **278**, 34882–34889.

11 C. Wurth, N. K. Guimard and M. H. Hecht, *J. Mol. Biol.*, 2002, **319**, 1279–1290.

12 K. Lu, J. Jacob, P. Thiyagarajan, V. P. Conticello and D. G. Lynn, *J. Am. Chem. Soc.*, 2003, **125**, 6391–6393.

13 M. C. Hsieh, C. Liang, A. K. Mehta, D. G. Lynn and M. A. Grover, *J. Am. Chem. Soc.*, 2017, **139**, 17007–17010.

14 A. K. Mehta, K. Lu, W. S. Childers, Y. Liang, S. N. Dublin, J. Dong, J. P. Snyder, S. V. Pingali, P. Thiyagarajan and D. G. Lynn, *J. Am. Chem. Soc.*, 2008, **130**, 9829–9835.

15 K. Tao, J. Wang, P. Zhou, C. Wang, H. Xu, X. Zhao and J. R. Lu, *Langmuir*, 2011, **27**, 2723–2730.

16 F. T. Senguen, N. R. Lee, X. Gu, D. M. Ryan, T. M. Doran, E. A. Anderson and B. L. Nilsson, *Mol. Biosyst.*, 2011, **7**, 486–496.

17 F. T. Senguen, T. M. Doran, E. A. Anderson and B. L. Nilsson, *Mol. Biosyst.*, 2011, **7**, 497–510.

18 S. A. Petty and S. M. Decatur, *J. Am. Chem. Soc.*, 2005, **127**, 13488–13489.

19 W. S. Childers, N. R. Anthony, A. K. Mehta, K. M. Berland and D. G. Lynn, *Langmuir*, 2012, **28**, 6386–6395.

20 N. R. Anthony, A. K. Mehta, D. G. Lynn and K. M. Berland, *Soft Matter*, 2014, **10**, 4162–72.

21 D. K. Klimov and D. Thirumalai, *Structure*, 2003, **11**, 295–307.

22 S. Santini, G. Wei, N. Mousseau and P. Derreumaux, *Structure*, 2004, **12**, 1245–1255.

23 U. F. Röhrig, A. Laio, N. Tantalo, M. Parrinello and R. Petronzio, *Biophys. J.*, 2006, **91**, 3217–3229.

24 H. D. Nguyen and C. K. Hall, *Proc. Natl. Acad. Sci. U. S. A.*, 2004, **101**, 16180–16185.

25 I. C. and C. K. H. M. Cheon, *Proteins*, 2010, **78**, 2950–2960.

26 B. J. Alder and T. E. Wainwright, *J. Chem. Phys.*, 1959, **31**, 459–466.

27 S. W. Smith, C. K. Hall and B. D. Freeman, *J. Comput. Phys.*, 1997, **134**, 16–30.

28 M. Cheon, I. Chang and C. K. Hall, *Protein Sci.*, 2012, **21**, 1514–1527.

29 M. Cheon, C. K. Hall and I. Chang, *PLoS Comput. Biol.*, 2015, **11**, 1–23.

30 Y. Wang, D. C. Latshaw and C. K. Hall, *J. Mol. Biol.*, 2017, **429**, 3893–3908.

31 T. Eichner and S. E. Radford, *FEBS J.*, 2011, **278**, 3868–3883.

32 G. Bitan and D. B. Teplow, *Acc. Chem. Res.*, 2004, **37**, 357–364.

33 G. W. Preston and A. J. Wilson, *Chem. Soc. Rev.*, 2013, **42**, 3289–301.

34 D. A. Fancy and T. Kodadek, *Proc. Natl. Acad. Sci. U. S. A.*, 1999, **96**, 6020–6024.

35 M. Suchanek, A. Radzikowska and C. Thiele, *Nat. Methods*, 2005, **2**, 261–7.

36 A. N. Calabrese and S. E. Radford, *Methods*, 2018.

37 G. W. Preston, S. E. Radford, A. E. Ashcroft and A. J. Wilson, *ACS Chem. Biol.*, 2014, **44**, 761–768.

38 A. Blencowe and W. Hayes, *Soft Matter*, 2005, **1**, 178–205.

39 L. Dubinsky, B. P. Krom and M. M. Meijler, *Bioorganic Med. Chem.*, 2012, **20**, 554–570.

40 R. A. Moss, *J. Org. Chem.*, 2017, **82**, 2307–2318.

41 P. L. Muller-remmers and K. Jug, *J. Am. Chem. Soc.*, 1985, **107**, 7275–7284.

42 F. Bernardi, A. Bottoni, M. Olivucci, M. a Robb, S. Wilseyg and N. Yamamoto, *J. Am. Chem. Soc.*, 1994, 2064–2074.

43 J. Das, *Chem. Rev.*, 2011, **111**, 4405–4417.

44 N. Kanoh, T. Nakamura, K. Honda, H. Yamakoshi, Y. Iwabuchi and H. Osada, *Tetrahedron*, 2008, **64**, 5692–5698.

45 J. Brunner, H. Senn and F. M. Richards, *J. Biol. Chem.*, 1980, **255**, 3313–3318.

46 C. W. G. Fishwick, J. M. Sanderson and J. B. C. Findlay, *Tetrahedron Lett.*, 1994, **35**, 4611–4614.

47 K. Biemann, *Annu. Rev. Biochem.*, 1992, **61**, 977–1010.

48 J. T. S. Hopper and C. V. Robinson, *Angew. Chemie - Int. Ed.*, 2014, **53**, 14002–14015.

49 L. Konermann, E. Ahadi, A. D. Rodriguez and S. Vahidi, *Anal. Chem.*, 2013, **85**, 2–9.

50 M. Wilm, *Mol. Cell. Proteomics*, 2011, **10**, M111.009407.

51 L. M. Young, L.-H. Tu, D. P. Raleigh, A. E. Ashcroft and S. E. Radford, *Chem. Sci.*, 2017, **00**, 1–11.

52 C. Seyler, C. Capello, S. Hellweg, C. Bruder, D. Bayne, A. Huwiler and K. Hungerbühler, *Ind. Eng. Chem. Res.*, 2006, **45**, 7700–7709.

53 D. M. Williams and T. L. Pukala, *Mass Spectrom. Rev.*, 2013, 169–187.

54 C. Uetrecht, R. J. Rose, E. van Duijn, K. Lorenzen and A. J. R. Heck, *Chem. Soc. Rev.*, 2010, **39**, 1633–1655.

55 B. C. Bohrer, S. I. Merenbloom, S. L. Koeniger, A. E. Hilderbrand and D. E. Clemmer, *Annu. Rev. Anal. Chem.*, 2008, **1**, 293–327.

56 D. P. Smith, T. W. Knapman, I. Campuzano, R. W. Malham, J. T. Berryman, S. E. Radford and A. E. Ashcroft, *Eur. J. Mass Spectrom.*, 2009, **15**, 113.

57 S. L. Bernstein, N. F. Dupuis, N. D. Lazo, T. Wyttenbach, M. M. Condron, G. Bitan, D. B. Teplow, J.-E. Shea, B. T. Ruotolo, C. V Robinson and M. T. Bowers, *Nat. Chem.*, 2009, **1**, 326–331.

58 L. M. Young, P. Cao, D. P. Raleigh, A. E. Ashcroft and S. E. Radford, 2014.

59 J. S. Cottrell, *J. Proteomics*, 2011, **74**, 1842–1851.

60 J. Madine, H. a. Davies, C. Shaw, I. W. Hamley and D. A. Middleton, *Chem. Commun.*, 2012, **48**, 2976–2978.

61 P. Ricchiuto, A. V. Brukhno and S. Auer, *J. Phys. Chem. B*, 2012, **116**, 5384–5390.

62 M. R. Nilsson, *Methods*, 2004, **34**, 151–160.

63 K. P. R. Nilsson, *FEBS Lett.*, 2009, **583**, 2593–2599.

64 S. I. A. Cohen, S. Linse, L. M. Luheshi, E. Hellstrand, D. A. White, L. Rajah, D. E. Otzen, M. Vendruscolo, C. M. Dobson and T. P. J. Knowles, *Proc. Natl. Acad. Sci. U. S. A.*, 2013, **110**, 9758–63.

65 C. Xue, D. Chang, T. Y. Lin and Z. Guo, *R. Soc. Open. Sci.*, 2017, **4**, 160696.

66 E. Hellstrand, B. Boland, D. M. Walsh and S. Linse, *ACS Chem. Neurosci.*, 2010, **1**, 13–18.

67 S. Biancalana, M. Koide, *Biochim. Biophys. Acta*, 2010, **7**, 1405–1412.

68 L. O. Tjernberg, D. J. Callaway, a Tjernberg, S. Hahne, C. Lilliehöök, L. Terenius, J. Thyberg and C. Nordstedt, *J. Biol. Chem.*, 1999, **274**, 12619–12625.

69 W. S. Childers, A. K. Mehta, K. Lu and D. G. Lynn, *J. Am. Chem. Soc.*, 2009, **131**, 10165–10172.

70 B. Bolognesi, J. R. Kumita, T. P. Barros, E. K. Esbjorner, L. M. Luheshi, D. C. Crowther, M. R. Wilson, C. M. Dobson, G. Favrin and J. J. Yerbury, *ACS Chem. Biol.*, 2010, **5**, 735–740.

71 C. W. Bertoncini and M. S. Celej, *Curr. Protein Pept. Sci.*, 2011, **12**, 205–20.

72 E. Brandenburg, H. von Berlepsch and B. Koksch, *Mol. Biosyst.*, 2012, **8**, 557–64.

73 F. Kundel, L. Tosatto, D. R. Whiten, D. C. Wirthensohn, M. H. Horrocks and D. Klenerman, *FEBS J.*, 2018, 1–27.

74 K. Garai and C. Frieden, *Proc. Natl. Acad. Sci. U. S. A.*, 2013, **110**, 3321–3326.

75 K. Chattopadhyay, E. L. Elson and C. Frieden, *Proc. Natl. Acad. Sci. U. S. A.*, 2005, **102**, 2385–2389.

76 T. J. van Ham, A. Esposito, J. R. Kumita, S. T. D. Hsu, G. S. Kaminski Schierle, C. F. Kaminski, C. M. Dobson, E. A. A. Nollen and C. W. Bertoncini, *J. Mol. Biol.*, 2010, **395**, 627–642.

77 W. Chen, L. J. Young, M. Lu, A. Zaccone, F. Strohl, N. Yu, G. S. K. Schierle and C. F. Kaminski, *Nano Lett.*, 2017, **17**, 143–149.

78 E. K. Esbjörner, F. Chan, E. Rees, M. Erdelyi, L. M. Luheshi, C. W. Bertoncini, C. F. Kaminski, C. M. Dobson and G. S. Kaminski Schierle, *Chem. Biol.*, 2014, **21**, 732–742.

79 J. R. Lakowicz, *Principles of Fluorescence Spectroscopy*, 2006.

80 C. F. Kaminski and G. S. Kaminski Schierle, *Neurophotonics*, 2016, **3**, 041807.

81 B. Palzs and S. Suhal, *Mass Spectrom. Rev.*, 2005, **24**, 508–548.

82 R. J. Medzihradszky, K. F., and Chalkley, *Mass Spectrom. Rev.*, 2015, **34**, 43–46.

83 I. Kheterpal, A. Williams, C. Murphy, B. Bledsoe and R. Wetzel, *Biochemistry*, 2001, **40**, 11757–11767.

84 I. Kheterpal, S. Zhou, K. D. Cook and R. Wetzel, *Proc. Natl. Acad. Sci. U. S. A.*, 2000, **97**, 13597–13601.

85 R. Tycko, *Cold Spring Harb. Perspect. Med.*, 2016, **6**, a024083.

86 C. G. Glabe, *J. Biol. Chem.*, 2008, **283**, 29639–29643.

87 C. Haass and D. J. Selkoe, *Nat. Rev. Mol. Cell Biol.*, 2007, **8**, 101–12.

88 T. P. J. Knowles, M. Vendruscolo and C. M. Dobson, *Nat. Rev. Mol. Cell Biol.*,

2014, **15**, 384–96.

Chapter 3:
Understanding the mechanism by which two amyloidogenic peptides interact

3.1 Heterogeneous amyloid aggregation *in vivo*

Despite often being studied *in vitro* as a single highly pure peptide sequence, *in vivo* amyloid aggregation can involve the interaction (and even co-assembly) of distinct and/or related sequences.[1–4] The Aβ sequence (as described in Chapter 1, Section 1.8) comprises a number of peptides with differing lengths that can interact during the aggregation process and become deposited in the extracellular plaques associated with AD.[5–7] Aβ has also been shown to interact with distinct sequences, such as transthyretin, *in vivo*.[8] The deposition of β_2-Microglobulin (β_2M) in the joints of patients undergoing kidney dialysis occurs in conjunction with an N-terminally truncated variant missing the first six amino acid residues (ΔN6), a peptide that has been shown to dramatically affect the rate of β_2M aggregation *in vitro* (Figure 50).[9,10] In order to further our understanding of these complex systems it is vital to unravel how systems containing more than one amyloidogenic peptide assemble and the interactions that take place. When considering mixed aggregation systems, a number of final fibril structures can occur and, as such, in the following sections, the term “co-assembly” will be used to indicate two amyloidogenic peptides that form fibrils containing both peptides (i.e. a true co-polymer), whereas the term “co-aggregation” will refer to amyloidogenic peptides that can interact during the self-assembly process but do not go on to form mixed fibrils. Given the acknowledgement that amyloidogenic peptides can interact and influence other sequences (that are either related or distinct) *in vivo*, a mechanistic understanding of how this can occur needs to be developed in order to fully appreciate the complexity of this pathological state.

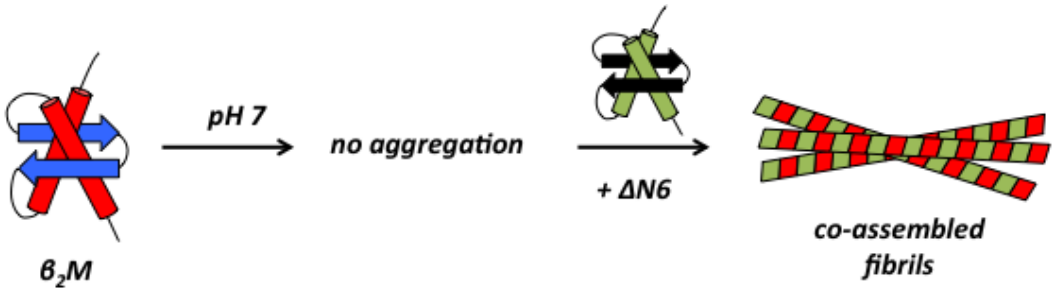

Figure 50. The co-assembly of β_2M and its N-terminally truncated variant ΔN6. At neutral pH, β_2m is resistant to aggregation, however, upon the introduction of ΔN6, self-assembly occurs forming co-assembled fibrils at the end of the self-assembly reaction.

3.2 Sequence similarity and heterogeneous amyloid aggregation

A key determinant of whether two amyloidogenic sequences can co-aggregate or co-assemble is the similarity of their amino acid sequences.[3,11,12] This is due to the significant role that side chain packing can have on fibrillar structure, as well as the statistical unlikelihood of two distinct peptides forming a single fibril.[3,13] The requirement for sequence similarity may be particularly apparent for cross-seeding (i.e. the ability of pre-formed fibrils of one peptide to increase the aggregation rate of another peptide), as can be seen in the aggregation behaviour of islet amyloid polypeptide (IAPP, the peptide implicated in type II diabetes) and $A\beta_{40}$ when incubated as a mixture.[12,14,15] IAPP and $A\beta_{40}$ have 25% sequence identity and 47% sequence similarity, with the core amyloidogenic regions sharing 39% sequence identity and 65% sequence similarity (Figure 51a).[3,12,14] When $A\beta_{40}$ fibrils are introduced into a pool of IAPP monomers, they can seed the aggregation of IAPP (Figure 51b); however, when IAPP fibrils are introduced into a pool of $A\beta_{40}$, the IAPP seeds have less than 2% of the seeding efficiency of $A\beta_{40}$ fibrils (Figure 51c).[12] This study also examined the ability of other amyloidogenic (including β_2M, polyglutamine and Ure2P) and non-amyloidogenic (including collagen and ovalbumin) peptides/proteins to influence the aggregation rate of $A\beta_{40}$. None of the peptides could seed the aggregation of $A\beta_{40}$, confirming that the sequence similarity plays a significant role in the ability of amyloidogenic peptides to co-aggregate. Interestingly, a study performed by Ashcroft, Radford and co-workers demonstrated that IAPP and $A\beta_{40}$ could form mixed oligomers (a dimer (1:1 ratio) or trimers (2:1 ratio of IAPP:$A\beta_{40}$ and *vice versa*).[14] When mixed together as monomeric peptides, the rate of aggregation (measured via ThT fluorescence) was found to be inbetween the two homomolecular aggregation rates of each peptide (Figure 2d). Sedimentation assays indicated that mixed fibrils had formed at the end of the self-assembly reaction.[14] These results demonstrate that the amino acid sequence plays a significant role in the ability of peptides to co-assemble, and that the sequence determinants for co-assembly and cross-seeding are not identical.

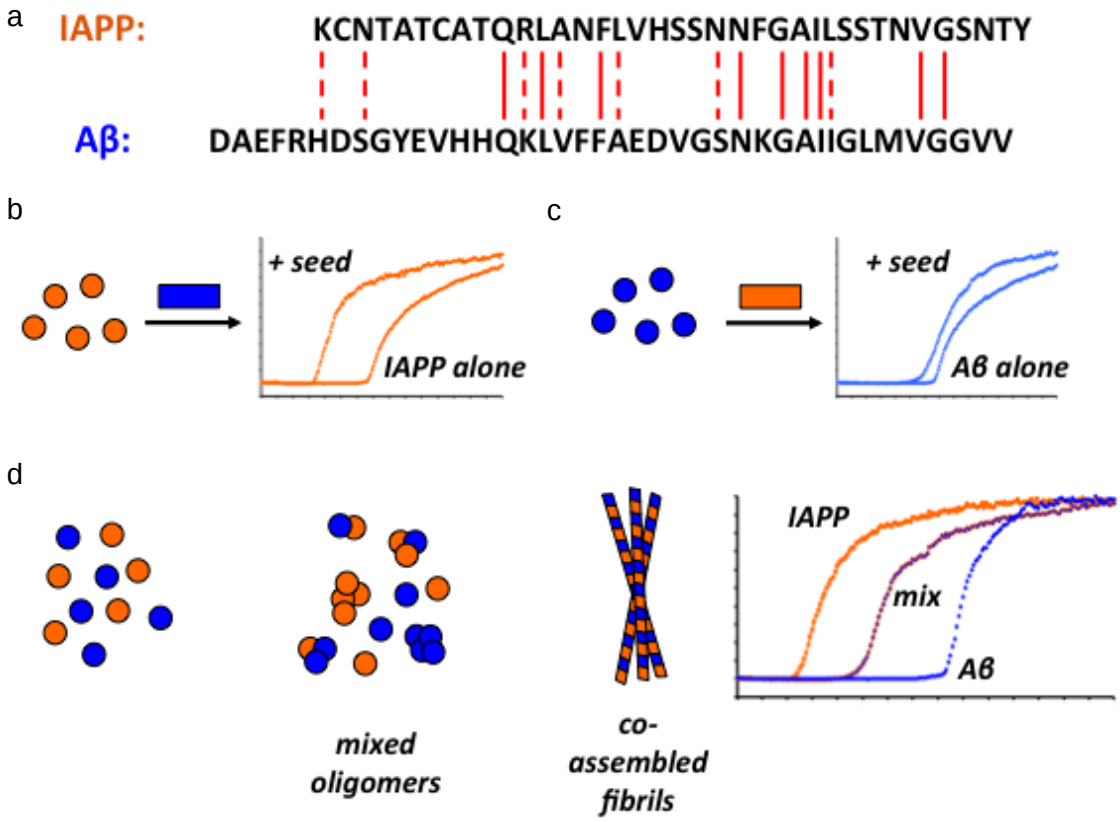

Figure 51. The importance of sequence similarity in mixed aggregation systems. IAPP (orange) and $A\beta_{40}$ (blue) have some sequence similarity (dashed lines are chemically similar, solid lines are identical amino acids, a). When $A\beta_{40}$ seeds (blue rectangle) are introduced into a pool of IAPP monomers (orange circles), they increase the aggregation rate of IAPP (b), however, IAPP seeds (orange rectangle) do not have a dramatic effect on the rate of $A\beta_{40}$ aggregation (blue rectangle, c). Mixing the peptides as monomers allows mixed oligomers and co-assembled fibrils to be formed, with a 1:1 mixture of the peptide producing a rate of aggregation that is between the two homogeneous rates (d).

3.3 Mixed aggregation kinetics

As described in Chapter 1 Section 1.12, the underlying microscopic mechanisms of amyloid self-assembly have been elucidated in a series of studies by Knowles, Linse, Dobson and co-workers.[16–19] The underlying processes in mixed aggregation systems can be considered to be more complex, due to the fact there are two peptides which can influence each stage of the self-assembly process.[20] The following section will describe each of these processes (primary nucleation, elongation, secondary nucleation and fragmentation) and their relation to systems containing two amyloidogenic peptides (Peptide A and Peptide B).

3.3.1 Primary nucleation

Primary nucleation involves the self-assembly of monomers in the absence of any preformed aggregates.[19] If the monomers of two amyloidogenic peptides can interact, there are three possible fates for these mixed oligomers: dissociation back into the constituent monomers (if unstable), formation of co-nuclei, and the formation of off-pathway oligomers (Figure 52). The unstable oligomers that dissociate back into their constituent monomers will slow the overall reaction rate of both peptides, as the monomers are not available for either primary nucleation or other secondary processes. The formation of off-pathway mixed oligomers will also retard the overall rate of aggregation of each peptide as they cannot return to the pool of monomers, reducing the concentration of monomers available for self-assembly. If, however, the mixed oligomers are stable and also provide a surface capable of recruiting monomers then they can be considered co-nuclei. These nuclei will increase the overall rate of reaction for each peptide and, as more peptide monomers are added, will eventually approach the homogeneous rate of self-assembly. Eventually the co-nuclei being incorporated into the fibrils at the end of the reaction. Depending on the sequence similarity of the peptides, these fibrils will either be co-assemblies or majority homomolecular fibrils with small, experimentally undetectable amounts of the other peptide located within their structure.

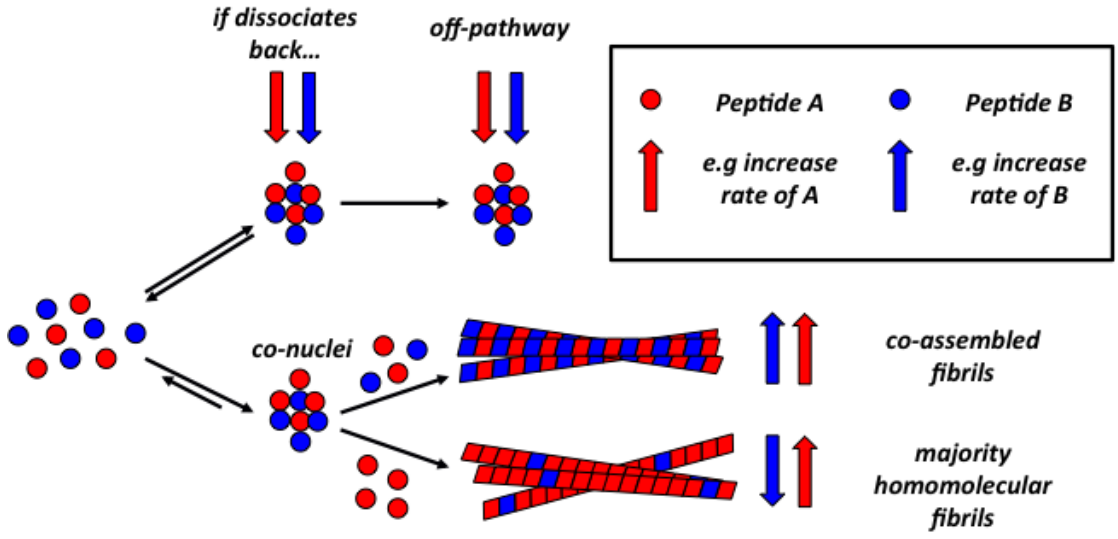

Figure 52. The different pathways available after primary nucleation in mixed aggregation systems, including the predicted effect on the overall aggregation rate of the peptide.

3.3.2 Elongation

If monomers of Peptide B are able to bind the fibril ends of Peptide A, three different effects on the overall rate of aggregation can be imagined (Figure 53).[20] The overall rate of Peptide A aggregation will decrease, as the fibril ends are now blocked by Peptide B, reducing the number of sites to which Peptide A can bind. For Peptide B, if a truly co-assembled fibril is formed, the overall aggregation rate will increase as the concentration of elongation competent monomers is increased. However, if this is not the case, then the overall rate of Peptide B aggregation will decrease, as the pool of monomers available for self-assembly has been decreased. A true co-assembly of Peptide's A and B will increase the aggregation rate of both peptides through elongation of the co-assembled fibrils.

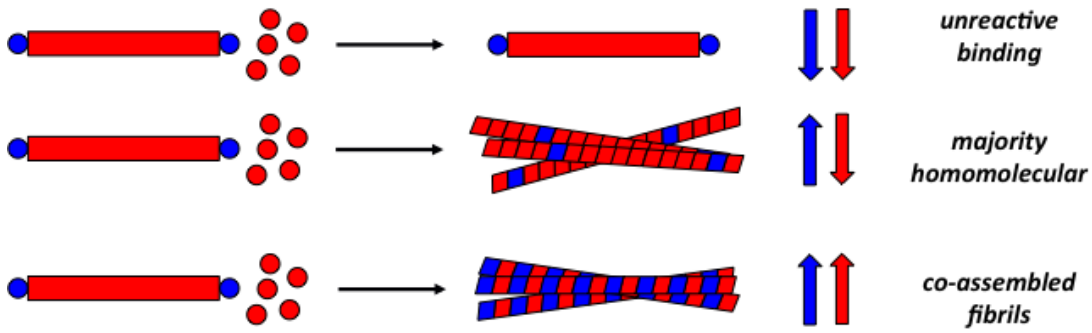

Figure 53. The different mechanisms of elongation and their associated impact on the rate of aggregation.

3.3.3 Surface catalysed secondary nucleation

There are three different secondary nucleation mechanisms that can occur in mixed aggregation systems (Figure 54). Firstly, if the surface of fibrils of Peptide A are not capable of nucleating Peptide B, then they may bind in a non-reactive manner, reducing the overall aggregation rate of both peptides (as fewer sites are available for Peptide A surface nucleation and the monomer concentration of Peptide B has been reduced). If the surface of Peptide A is capable of nucleating Peptide B then the overall rate of aggregation will increase for Peptide B (increased number of nuclei) but will be reduced for Peptide A (reduction in the number of sites available for Peptide A to bind to). If the two peptides can form co-nuclei then the overall rate of aggregation will be dependent on the fate of those co-nuclei (see above).

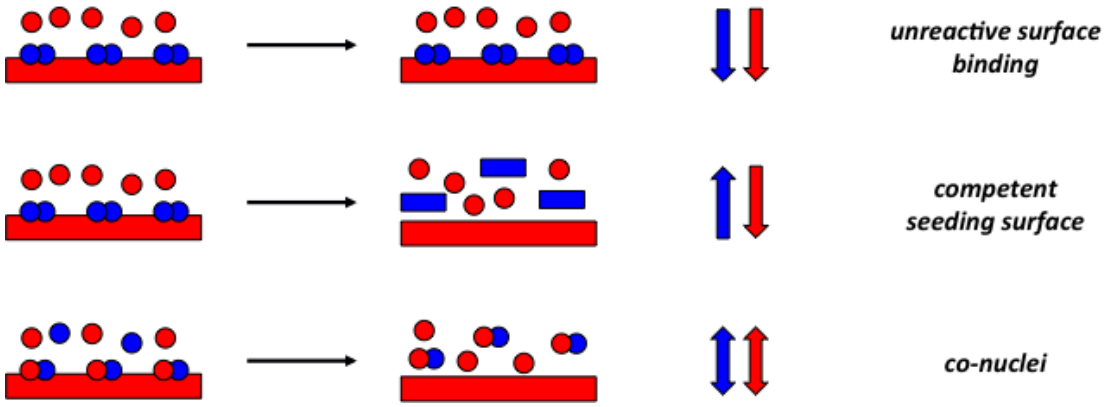

Figure 54. The different mechanisms of surface catalysed secondary nucleation within mixed aggregation systems and their associated impact on the rate of aggregation.

3.3.4 Fragmentation

The fragmentation of fibrils into smaller fibril fragments would (in a single peptide system) increase the aggregation rate of that peptide exponentially.[16,21] The effect of fragmentation on the rate of aggregation in a mixed peptide system will depend on the ability of those fibril fragments to increase the rate through the mechanisms described above (i.e. elongation and secondary nucleation). As such, and given the rate of fragmentation for Aβ is negligible under quiescent conditions, this mechanism can be considered to be a minor mechanistic possibility for the work performed in this chapter.

3.4 The aggregation of two variants of Aβ: $A\beta_{40}$ and $A\beta_{42}$

The identification of multiple variants of Aβ in the extracellular plaques of patients with AD has led to a number of studies being performed on how the two major proteinaceous components of the plaques, $A\beta_{40}$ and $A\beta_{42}$, interact.[20,22–30] These studies have used a wide range of conditions and peptide concentrations, with both synthetic and recombinant Aβ peptides. Generally, it has been shown that $A\beta_{40}$ interacts with $A\beta_{42}$, and slows the overall rate of $A\beta_{42}$ aggregation in a concentration dependent manner, with the ratio of $A\beta_{40}/A\beta_{42}$ thought to be important in how neurotoxic the Aβ peptide is.[23–27] Some studies have demonstrated that $A\beta_{42}$ increases the aggregation rate of $A\beta_{40}$ (both as a monomer and as fibrils); however, other studies have disputed this, limiting the seeding ability of $A\beta_{42}$ to the oligomeric intermediates formed by $A\beta_{42}$ or even showing that $A\beta_{42}$ slows the growth of $A\beta_{40}$.[22–24,27] It has also been reported that $A\beta_{40/42}$ can form mixed fibrils.[24,28]

In the face of these diverse, and sometimes contradictory, results, Knowles, Linse and co-workers performed a well-designed series of experiments using highly pure, recombinant $A\beta_{40/42}$ in order to establish the underlying mechanism of Aβ co-aggregation (Figure 55).[20] In this study, two different transitions were observed (as measured by ThT fluorescence), with circular dichroism (CD), isotope edited MS experiments and NMR spectroscopy establishing that the first transition was due to the aggregation of $A\beta_{42}$ and the second transition due to the aggregation of $A\beta_{40}$. Cryo-electron microscopy (cryo-EM) analysis confirmed that at the end of the self-assembly reaction, homomolecular fibrils had been formed. Seeding experiments demonstrated that $A\beta_{40}$ seeds had little/no effect on $A\beta_{42}$ (except at very high seed concentrations), whereas $A\beta_{42}$ seeds did have an impact on $A\beta_{40}$ aggregation (although it was not significant when compared with a self-seeded reaction. Monomeric $A\beta_{42}$ had a larger impact on the rate of $A\beta_{40}$ aggregation when compared to fibrillar $A\beta_{42}$ indicating that the primary mechanism of interaction was through cooperative primary nucleation. Baldasarre and co-workers used isotope-edited IR to probe the structure of these mixed oligomers and revealed that each peptide is largely randomly distributed within the oligomer, with both peptides contributing to the β-sheet content of the oligomer.[30]

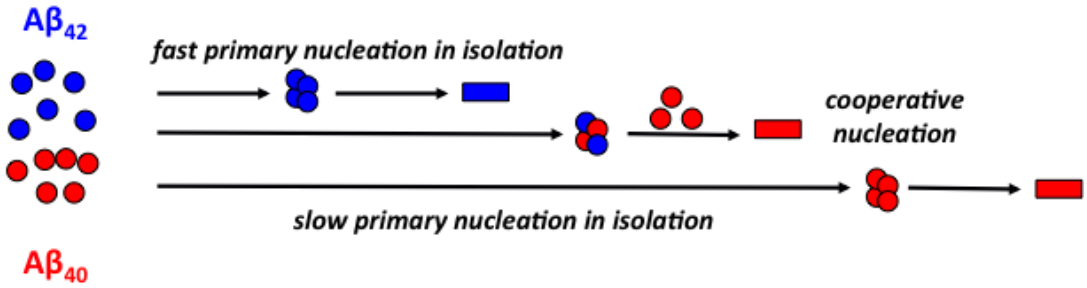

Figure 55. The mechanism by which $A\beta_{40}$ (red) and $A\beta_{42}$ (blue) interact. $A\beta_{42}$ monomers interact with $A\beta_{40}$ during primary nucleation, increasing the rate of primary nucleation for $A\beta_{40}$, which is slow in isolation.

3.5 The impact of peptide fragments on Aβ aggregation: the importance of the KLVFF motif

The search for inhibitors of Aβ aggregation has led to the investigation of shorter peptide fragments from the Aβ sequence to be examined for their inhibitory properties.[31–36] This search was based on the hypothesis that, given amyloid assembly

requires highly specific molecular recognition processes, sections of the same sequence would be more likely to recognise and bind full-length Aβ, than other peptide sequences or small molecules. The identification by Tjernberg and co-workers that the KLVFF region from the central hydrophobic core region of Aβ (residues 16 – 20) can bind to $Aβ_{40}$ and prevent the formation of fibrillar aggregates served as a starting point for the design of a number of different inhibitors.[32] A study by Okuno and co-workers broke down the Aβ peptide into a series of 5-mer peptides that were attached to solid-supports and incubated them with a fluorescently labelled KLVFF peptide, confirming that this motif binds to itself preferentially i.e. it is a "self-recognition motif".[37] A number of $Aβ_{40/42}$ inhibitors that incorporate that KLVFF motif have been designed, including those that use D-amino acids and N-terminal modifications, such as ferrocence or extended lysine chains.[33–36,38] Interestingly, longer peptide fragments from the Aβ sequence (such $Aβ_{11-40/42}$ and $Aβ_{20-40}$) have been shown to influence the aggregation rate of $Aβ_{40/42}$, as well as co-assemble into mixed fibrils.[22,39] These results would seem to indicate that the inherent propensity of the peptide fragment to form fibrils is a key determinant as to whether the fragment in question will inhibit or increase the aggregation rate of Aβ.

3.6 The use of Molecular Dynamics (MD) simulations to understand Aβ aggregation

The dynamic transitions that occur early during Aβ self-assembly can be difficult to characterise experimentally. However, advances in MD simulations have allowed this technique to be successfully applied to this problem.[40–42] A wide range of simulation procedures can be used, each with their own advantages and disadvantages. Atomistic MD simulations can provide detailed information at the atomic level, however, due to the high level of detail generated they are often limited to smaller systems and short timescales (up to microsecond timescales).[41] When used in combination with techniques, such as replica exchange (REMD), that allow simulations to sample multiple ensembles at different temperatures (in order to reduce the energy barriers in the energy landscape), atomistic simulations can be a powerful tool with which to explore the conformations of the early aggregates formed in amyloid self-assembly.[40,41] The simulation parameters (i.e. whether the solvent is explicit or implicit) can have a significant impact on the structures formed in the simulations.[43] As amyloid fibrils have remarkably similar characteristics, despite having a wide range of amino acid sequences, the use of coarse-grained models (in which amino acids are simplified into

bead-like structures) can allow longer timescales and larger systems to be accessed and explored.[44–46] The following sections will briefly describe some key examples of how MD simulations have been used to provide insight into both the initial (i.e. monomer and dimer formation) and the later stages of Aβ self-assembly (i.e. oligomerisation and secondary processes).

3.7 Insights into Aβ monomers and dimers from MD simulations

A number of studies have been undertaken to establish the secondary structure content of $A\beta_{40/42}$ monomers, both in isolation and when in complex with ions such as Cu^{2+}.[43,47–50] These studies have produced different results, depending on the conditions under which they have been performed. For example, Ball and co-workers used both NMR and MD simulations to probe the initial conformations of both $A\beta_{40}$ and $A\beta_{42}$, demonstrating that they both sampled a diverse range of secondary structures including β-strands, random coils and α-helices.[49] In this simulation, $A\beta_{42}$ formed a well-populated (34% of the ensemble) antiparallel β-hairpin structure that consisted of residues 16 – 21 and 29 – 36, whereas $A\beta_{40}$ formed a less-populated (10%) antiparallel β-hairpin consisting of residues 9 – 13 and 35 – 37. These observations contrast with the structures observed by Garcia and co-workers, in which both $A\beta_{40}$ and $A\beta_{42}$ adopt largely random coils, with a short 3_{10} helix in the N-terminus of $A\beta_{40}$ and a single β-turn for $A\beta_{42}$ around residue 12 – 15.[48] Generally, simulations on Aβ monomers tend to agree that they are largely disordered structures with a tendency to form a β-hairpin around residues 22 - 27.[43,47–49] Simulations focusing on Aβ dimers have often explored the effect that inhibitors (such as epigallocatechin gallate, EGCG) or familial mutants have on the dimer structure.[51–53] The Aβ dimers seen in these simulations are often unstructured with some amount of β-strand content and significant hydrophobic contacts, highlighting the dynamic nature of these early aggregation steps.

3.8 Insights into Aβ oligomerisation MD simulations

Strodel and co-workers performed atomistic simulations with REMD to probe the oligomersation of both $A\beta_{40}$ and $A\beta_{42}$, developing a novel method of analysing the datasets based on a transition network analysis.[54,55] This analysis breaks down the structure of the oligomers formed into a number of different factors, including oligomer size, number of interpeptide hydrophobic/salt bridge contacts and oligomer shape (spherical or elliptical).[55] In the simulations, extended oligomers were shown to be

more likely to go on and form higher order oligomers, whereas more compact oligomers were less likely to form higher order structures. Interestingly, the average oligomer mass distribution for the compact oligomers closely matched the oligomer distributions observed experimentally, indicating that these may be metastable structures.[55–57] The mass distribution also highlighted that $A\beta_{42}$ dimers and tetramers were substantially populated and went on to form higher order oligomers, whereas $A\beta_{40}$ largely formed higher order oligomers through monomer addition. The $A\beta_{42}$ dimers had more hydrophobic surface area exposed to the solvent and few strong interpeptide contacts allowing them to easily interact with other peptides. $A\beta_{40}$, however, formed strong C-terminal contacts within the dimer and had a lower surface area that was solvent exposed, reducing its ability to oligomerise further.

The self-assembly of $A\beta_{40}$ was further explored by Wolynes and co-workers using a coarse grained MD simulation that followed the different pathways taken by twelve $A\beta_{40}$ monomers to from oligomeric species.[46] The overall energy landscape was shown to be downhill, with an oligomer containing parallel β-sheets, referred to as a “fibrillar” oligomer based on the structure reported by Petkova and co-workers, as the energy minima.[58] Monomeric $A\beta_{40}$ sampled two different monomeric conformations, one with an α-helix formed by L17 and D23 and another with two β-strands in residues 17 – 23 and 30 – 36. The hairpin structure was stabilised upon dimer formation via intermolecular hydrogen bonding, with the higher order oligomers (trimers and tetramers) forming cylinders. The hexamer structures had two different conformations (antiparallel β-sheets, termed “pre-fibrillar” and the fibrillar oligomer described above) that was shown to interconvert by “back-tracking”. In this back-tracking step, the antiparallel structure dissociated with two strong self-recognising regions holding the oligomer together whilst the rest of the peptide underwent a conformational rearrangement to form the fully parallel, fibrillar oligomer. When examining two familial AD mutants (Arctic, E22G and Dutch E22Q), it was shown that increasing hydrophobicity at the 22 position increased the downhill nature of the energy landscape, possibility explaining why these mutants are associated with Aβ deposition early in life.[59]

3.9 Insights into Aβ secondary pathways from MD simulations

Visual insights into the molecular mechanism(s) of the secondary pathways involved in amyloid growth can provide detailed information about the intermolecular contacts

formed during the initial stages of elongation and surface catalysed secondary nucleation.[60–64] Stultz and Gurry used an atomistic simulation with which to observe the process of fibril elongation of a preformed, fixed fibril core ($A\beta_{9-40}$ or $A\beta_{17-42}$) by monomeric $A\beta_{40}$ and $A\beta_{42}$ respectively (Figure 56).[60] The fibril cores consisted of two in-register, parallel β-sheets and the contacts formed between the monomer and fibril core were measured using the average heavy atom distance (i.e a measure of hydrogen bonding between the fibril core and the monomeric peptide) and the fraction of residues forming β-strand secondary structure in the monomer. This study demonstrated that elongation occurred through a "dock and lock" mechanism, in which the monomer first associated to the N-terminal β-strand of the fibril core via intermolecular hydrogen bonding.[60] The initial association is then followed by the formation of an intermediate hairpin structure, which is stabilised by both intra- and intermolecular hydrogen bonds, prior to a final rearrangement step during which the intramoleuclar hydrogen bonds are broken and replaced with intermolecular hydrogen bonds to the second β-strand of the fibril core. Both $A\beta_{40}$ and $A\beta_{42}$ displayed similar mechanisms of fibril elongation, however, $A\beta_{42}$ was observed to "roll" along the fibril surface prior to docking at the fibril end.

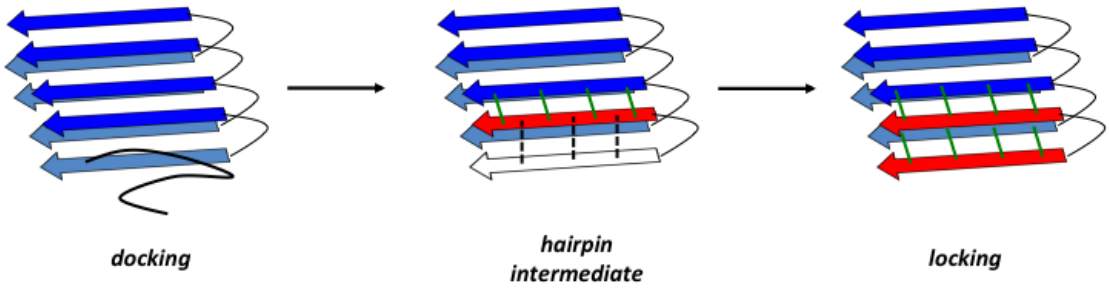

Figure 56. The "dock and lock" mechanism proposed by Stultz and Gurry for the elongation of Aβ fibrils (60). Monomeric Aβ (black line) is initially disordered when it binds to the fibril end (blue arrows), after which it forms one strand with intermolecular hydrogen bonds (green) and intramolecular hydrogen bonds holding the second strand (black lines) in a hairpin intermediate. The locking step follows a rearrangement of the hydrogen bonding so that all are intermolecular and the monomer is now attached to the fibril core (red arrows).

Another atomistic simulation examining the elongation of an $A\beta_{42}$ pentamer did not observe the hairpin-like intermediate.[61] Instead this simulation proposed that elongation occurred mainly through hydrophobic contacts, with the ends of the fibril being more

disordered than the fibril core, thus allowing peptides at the fibril ends to form more hydrophobic contacts. This disordered region at the end of fibril formed a “cap” that was stabilised through monomer addition, with the rate-determining step in this mechanism identified as the rearrangement of intra- to intermolecular hydrophobic contacts. The “dock and lock” mechanism was further supported by atomistic simulations performed by Zacharias and co-workers, who demonstrated that the addition of a monomer to the ends of a preformed $A\beta_{9-40}$ fibril core proceeded via the initial formation of non-native hydrogen bonds.[64] This initial “locking” phase was then followed by a slower rearrangement step in which the formation of native hydrogen bonds occurred. The driving force of fibril elongation was found to be entropic, with the expulsion of water from the fibril end by the incoming monomer compensating for the loss of entropy as the monomer forms ordered β-strands in complex with the fibril core.

Zacahrias and co-workers extended this analysis by applying the same methodology to exploring the association of monomers and structured oligomers onto the surface of a preformed $A\beta_{9-40}$ fibril (i.e. key events in surface catalysed secondary nucleation).[63] In this work, the authors demonstrated that the association of both monomers and oligomers (up to tetramer) was energetically favourable, with the association of a monomer onto the fibril surface being comparable that observed in their earlier work for fibril elongation (see above).[64] The lateral association of oligomers was much more favourable than that of the monomer. Monomer addition to the fibril surface also occurred via a “dock and lock” mechanism, whereby in solution the monomer exists largely as a disordered peptide with little secondary structure, prior to attachment to the fibril surface (fast “docking” process). Upon attachment, the monomer unfolds with key hydrophobic contacts being made between the hydrophobic C-terminus of the monomer to the same C-terminal region of the fibril core. This is then followed by a collapse of the monomeric peptide into a compact structure on the fibril surface (the slower “locking” process). The higher order oligomers (trimers and tetramers) did not undergo any significant structural change upon binding to the fibril surface, whereas the dimer underwent some unfolding upon attachment (similar to the monomer). As with the fibril elongation simulation, the expulsion of water from the fibril surface was once again noted to be a key driving force for the association of the monomer/oligomers to the fibril surface.

The molecular mechanism of surface catalysed nucleation was further explored by Strodel and co-workers in an atomistic simulation using a preformed $A\beta_{17-42}$ fibril and monomeric $A\beta_{42}$.[62] In this model, significant unfolding of $A\beta_{42}$ was observed upon

attachment to the fibril surface, resulting in an elongated monomer structure, with hydrophobic contacts being formed between residues K28 – I41 of the monomer and residues A30 – L34 of the fibril seed (Figure 57a). The interaction was primarily driven through hydrophobic contacts, however, the charged N-terminus of the monomer was key for the initial binding of the peptide to the surface. The β-sheet content was observed to increase after binding of the monomer to the fibril surface (1.2 ± 3.4% to 22.0 ± 9.6%), indicating that surface catalysed nucleation may play a role in the formation of β-sheets within nuclei. Simulations using dimeric $A\beta_{42}$ also demonstrated the same mechanism, in which binding of the oligomer to the fibril surface was followed by unfolding. The monomers were also observed to "slide" across the fibril surface, leading to dimer and eventually trimer formation (Figure 57b).

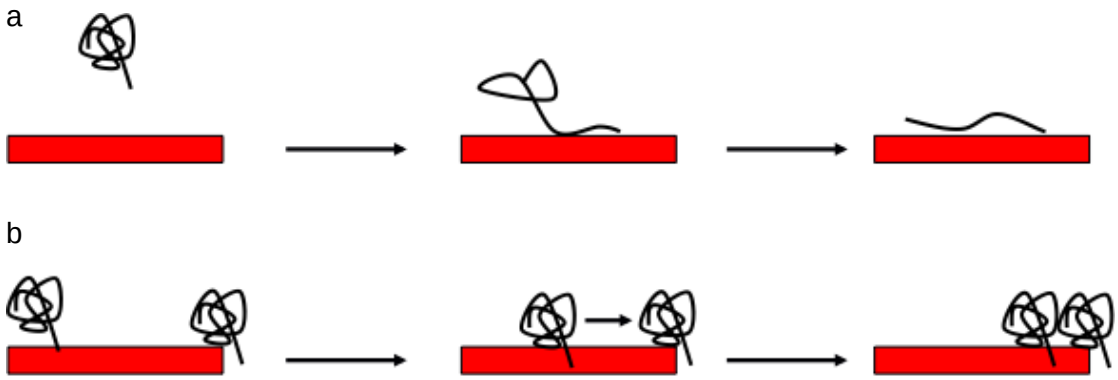

Figure 57. The surface mediated secondary nucleation mechanism observed by Strodel and co-workers (62). The monomeric $A\beta_{42}$ (black line) binds to the surface of the fibril (red) via hydrophobic contacts and start to unfold, eventually ending as an elongated peptide on the fibril surface (a). In the simulation, monomers were also observed to slide along the fibril surface and form dimers (b).

Aims and Objectives

In this chapter, the mechanism by which $A\beta_{16-22}$ increases the aggregation rate of $A\beta_{40}$ was elucidated and (in collaboration with Professor Carol Hall and Yiming Wang, North Carolina State University) the same system was analysed using discontinuous molecular dynamics (DMD) simulations. Combining thorough and detailed experimental analyses of complex amyloid systems with the visual insights provided by simulations can reveal details of the underlying mechanism that would have remained unseen, if either the experiments or simulations were used in isolation. As the KLVFF sequence (contained within $A\beta_{16-22}$) has been shown to bind and inhibit $A\beta_{40}$ understanding the mechanism by which they interact may provide valuable information to be used in the future design of Aβ inhibitors and confirming the site of interaction in solution with diazirine labelled $A\beta_{16-22}$ would also help this endeavour.

To achieve these aims, the understanding of the structure and kinetics of $A\beta_{16-22}$ and its diazirine labelled counterpart, developed in the previous chapter was used to inform the experimental design in this chapter. $A\beta_{40}$ was made via a recombinant method (kindly provided by Dr. Katie Stewart, University of Leeds) and initial characterisation of the interaction involved using Thioflavin-T (ThT), a commonly used amyloid binding dye that does not fluorescence significantly in the presence of $A\beta_{16-22}$ fibrils. After confirming the general effect of $A\beta_{16-22}$ on the aggregation rate of $A\beta_{40}$ (i.e. does it increase/decrease aggregation rate), seeding experiments were performed using preformed $A\beta_{16-22}$ fibrils in order to distinguish between primary and secondary pathways. The presence of any mixed oligomers was assessed using ion mobility-mass spectrometry (IMS-MS) and the composition of the fibrils formed at the end of the self-assembly reaction were assessed using a combination of electron microscopy (EM, with assistance provided Dr Matt Iadanza, University of Leeds) and photoinduced cross-linking (PIC). Once the mechanism of interaction between the two peptides was established experimentally, the same system was simulated under a variety of different conditions to thoroughly interrogate the proposed mechanism. The outcome was an atomistic view of how $A\beta_{16-22}$ fibrils catalyse $A\beta_{40}$ aggregation via surface catalysed secondary nucleation.

Results and Discussion

3.10 $A\beta_{16-22}$ increases the aggregation rate of $A\beta_{40}$

$A\beta_{16-22}$ was synthesized according to the procedure outlined in the Materials and Methods Section 4.1 and $A\beta_{40}$ was obtained via recombinant expression in *e. Coli* (kindly provided by Dr. Katie Stewart).[65–67] The $A\beta_{40}$ used in this study contains an N-terminal methionine residue, that has been shown to have no impact on either the final fibril structure or the aggregation rate of the peptide, and had also undergone a second purification step to ensure that is a single peak prior to use in any kinetic assays (Appendix 1)[65,68]. A common method for characterising the growth of amyloidogenic peptides is to use the fluorescent dye ThT, however, as outlined in Chapter 2, Section 2.10, in the presence of $A\beta_{16-22}$ fibrils, ThT did not significantly fluoresce.[18,69,70] As such, in the following sections any fluorescence assays using ThT will only report on the aggregation of $A\beta_{40}$ and the protocol for the ThT assays can be found in Materials and Methods 4.15. Each trace in the main body of the text is representative of three repeats (which can be found in Appendix 9). To initially characterise how $A\beta_{16-22}$ influences the aggregation rate of $A\beta_{40}$, the two peptides were mixed together at different molar ratios, whilst the total peptide concentration was held constant (40 μM, Figure 58). As the molar ratio of $A\beta_{16-22}$ to $A\beta_{40}$ increased, the aggregation rate of $A\beta_{40}$ was observed to increase, with the maximal effect seen at a 1:1 ratio of the two peptides (Figure 58). In order to characterise to what extent $A\beta_{40}$ aggregation accelerates in the presence of $A\beta_{16-22}$, the normalised reduction in $A\beta_{40}$ half-time ($t_{1/2}$, the time at which the growth

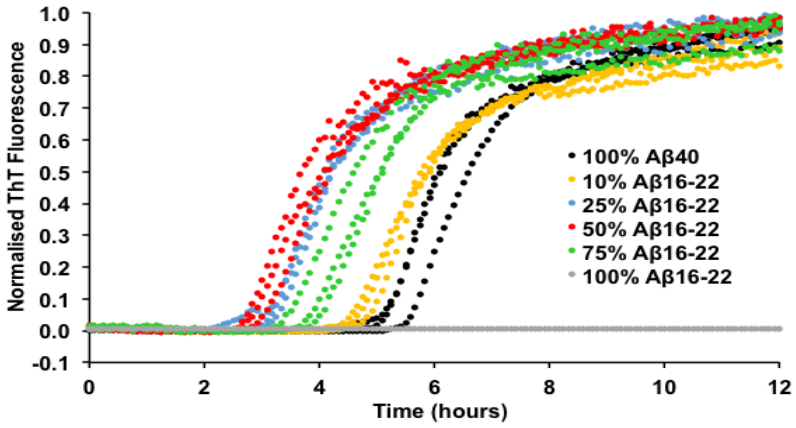

Figure 58. $A\beta_{16-22}$ increases the aggregation rate of $A\beta_{40}$, with the maximum increase in rate observed at a 1:1 ratio. The total peptide concentration was held at 40 μM, pH 7, 100 mM ammonium bicarbonate buffer, ThT 10 μM with a final DMSO concentration of 1%

curve reaches 50% amplitude) was calculated (Figure 59). The result demonstrates that $A\beta_{16-22}$ has a dramatic effect on the aggregation rate of $A\beta_{40}$.

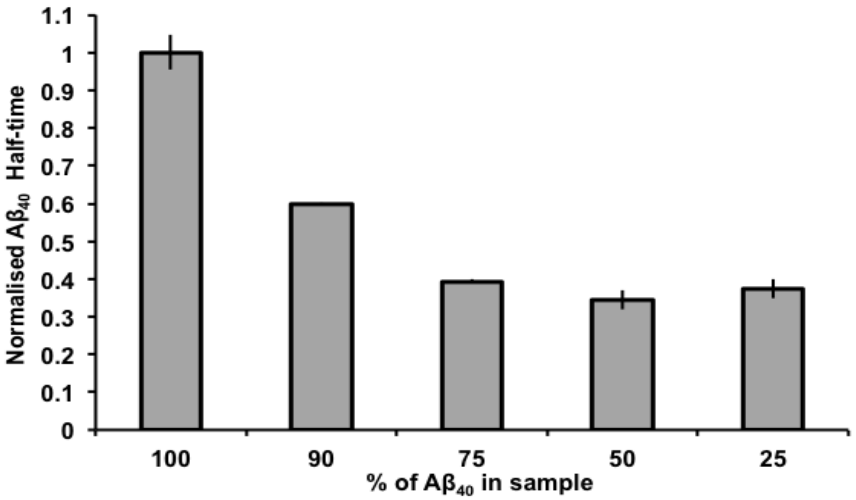

Figure 59. The acceleration in the rate of $A\beta_{40}$ aggregation in the presence of $A\beta_{16-22}$, measured via the effect on the half-time ($t_{1/2}$) of $A\beta_{40}$ aggregation. In the figure, the $t_{1/2}$ of $A\beta_{40}$ in the presence of $A\beta_{16-22}$ has been normalised against the $t_{1/2}$ of the equivalent concentration of $A\beta_{40}$ in isolation (the $A\beta_{40}$ concentration series used to calculate these half-times can be found in Appendix 9). The total peptide concentration was held at 40 μM, pH 7, 100 mM ammonium bicarbonate buffer, ThT 10 μM with a final DMSO concentration of 1% (v:v).

In order to confirm that the PRIME20 model and DMD approach used in the previous chapter could accurately model $A\beta_{40}$ self-assembly, simulations were performed on six monomeric $A\beta_{40}$ peptides (Figure 60, performed by Professor Carol Hall and Yiming Wang, see Chapter 2, Section 2.9 for a description of how the simulations are performed). At the start of the simulation (t = 0 μs), six $A\beta_{40}$ monomers were in random coil conformations. By t = 104 μs, a metastable oligomer structure was observed comprising both parallel β-sheets and β-hairpin structures. As the simulation proceeded (t = 230 μs), this oligomer underwent structural rearrangement, losing some β-sheet content. At the end of the simulation (t = 621 μs) a stable, parallel in-register amyloid-like fibril structure was observed. Each $A\beta_{40}$ peptide contains three β-strands (N-termini, central hydrophobic core and C-termini) within the structure, forming two β-sheets in total. Unlike other studies exploring the aggregation of $A\beta_{40}$, no anti-parallel oligomeric structures were observed in this study, with the final parallel hexameric oligomer resembling the fibrillar structure observed by Zheng et al.[46]

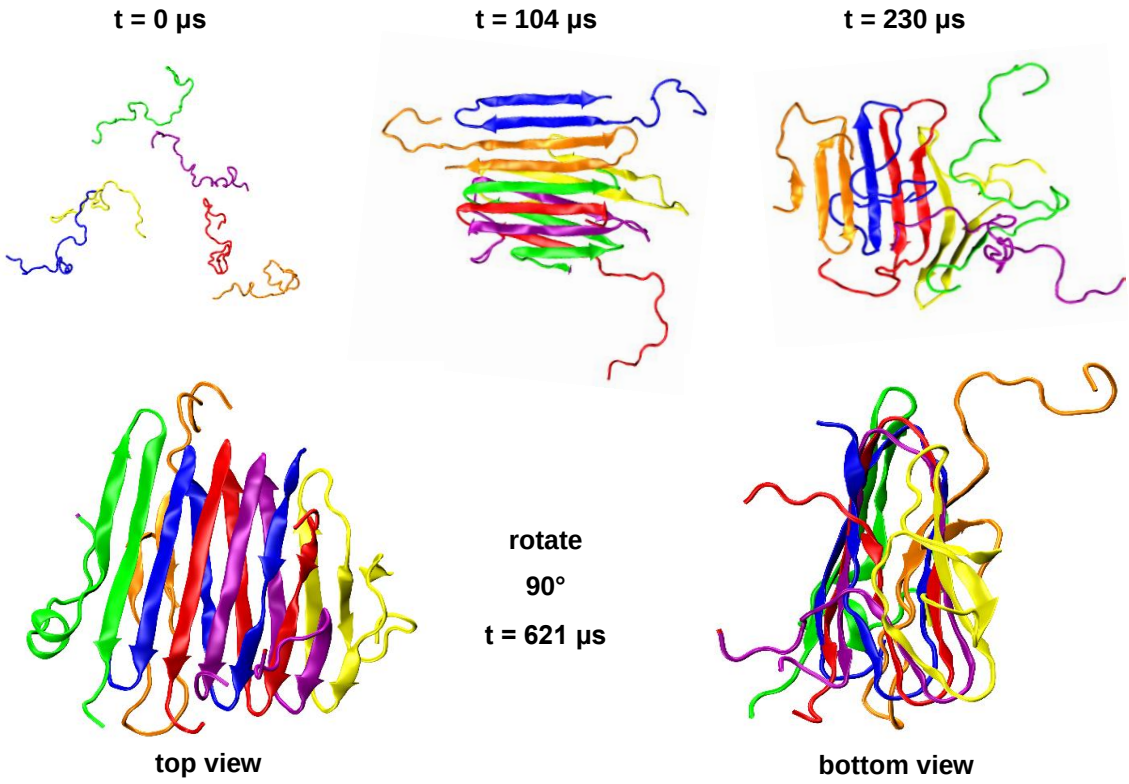

Figure 60. The self-assembly pathway of $A\beta_{40}$ in DMD simulations. At t = 0 µs, $A\beta_{40}$ exists as random coil monomers, that progresses through a variety of oligomeric states (t = 104 and 230 µs), prior to finally forming a parallel, in-register β-sheet oligomer.

3.11 $A\beta_{16-22}$ aggregates at a faster rate than $A\beta_{40}$ and is unaffected by the presence of $A\beta_{40}$

In order to characterise the effect that $A\beta_{40}$ has on the aggregation rate of $A\beta_{16-22}$ the fluorescence quenching assay developed in Chapter 2, Section 2.11 was employed. As demonstrated in Chapter 2, when incubated in isolation, when $A\beta_{16-22}$ is spiked with 5% TAMRA-Ahx-$A\beta_{16-22}$ a rapid decrease in fluorescence followed by a slower phase that plateaued after 1 h was observed (Figure 61a and Chapter 2, Section 2.11). In the presence of $A\beta_{40}$ (1:1 mol:mol ratio, 40 µM total peptide concentration, 2% (v/v) DMSO, Materials and Methods 4.16) no difference in the rate of fluorescence quenching was observed, indicating that $A\beta_{40}$ had no effect on $A\beta_{16-22}$ aggregation (Figure 61b). Sedimentation of the mixed system, via centrifugation, after 1 h demonstrated that $A\beta_{40}$ was present only in the supernatant fraction (Figure 61c), whilst only small amounts of the peptide were observed in the pellet fraction (Figure 61d, Materials and Methods 4.17). This confirmed that $A\beta_{16-22}$ was present as fibrils at the same time as $A\beta_{40}$ was present as soluble monomers/oligomers, indicating limited/no co-assembly occurred

between the two peptides. As demonstrated via a TEM time course in Chapter 2, Section 2.11, at these concentrations, $A\beta_{16-22}$ forms fibrils quickly (Figure 36c). Taken together these results demonstrate that $A\beta_{16-22}$ aggregates faster than $A\beta_{40}$ and that its rate of aggregation is unaffected by the presence of $A\beta_{40}$.

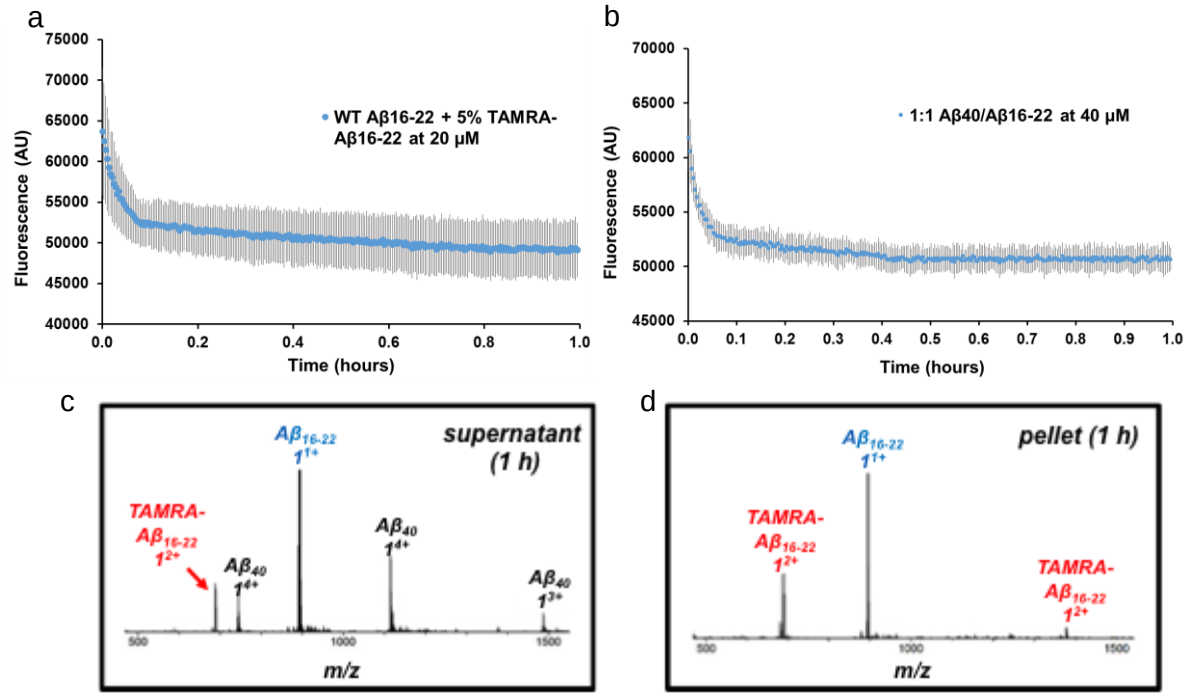

Figure 61. The aggregation rate of $A\beta_{16-22}$ is unaffected by the presence of $A\beta_{40}$. In fluorescence quenching experiments $A\beta_{16-22}$ has the same rate of aggregation when incubated in isolation (a) or in a 1:1 ratio with $A\beta_{40}$ (TAMRA-Ahx-$A\beta_{16-22}$ is held at 5% in both assays, 2% final DMSO concentration, v:v). When the samples are centrifuged and separated into supernatant (c) and pellet fractions (d), $A\beta_{16-22}$ (and its TAMRA-labelled counterpart) can be found in the pellet fractions, whereas momomeric/oligomeric $A\beta_{40}$ can be found in the supernatant.

3.12 Monomeric $A\beta_{16-22}$ can interact with monomeric and oligomeric $A\beta_{40}$ through the self-recognition motif KLVFF

The non-covalent and transient nature of the early stages of peptide self-assembly renders experimental analyses challenging. ESI is a soft ionization technique that can transfer non-covalent interactions, such as those that hold peptide oligomers together, into the gas phase.[71,72] When combined with native IMS-MS, which separates ions by both mass to charge ratio (m/z) and shape, this can be a powerful technique with which

to explore peptide self-assembly and differentiate small oligomer populations.[56,73] Under the conditions used in this study, ESI-IMS-MS analysis demonstrated that $A\beta_{40}$ forms a range of oligomeric structures (white, Figure 62a), ranging from monomers to pentamers. When incubated with $A\beta_{16-22}$, a number of heteromeric oligomers were observed (green, Figure 62b) along with oligomeric $A\beta_{40}$ (white) and nascent $A\beta_{16-22}$ (yellow). It should be noted that under these conditions $A\beta_{16-22}$ oligomers were not observed. The heteromeric oligomers correspond to multiple $A\beta_{16-22}$ monomers bound to either an $A\beta_{40}$ monomer or dimer. Their presence demonstrates that the two peptides can interact as monomers or as oligomers. Collision cross-section (CCS, Materials and Methods 4.18) analysis of the $A\beta_{40}$ species in the presence and absence of $A\beta_{16-22}$ indicated no significant difference in the gas phase conformation of $A\beta_{40}$, implying a conformational change in monomer or oligomer structure is unlikely to be the key factor for the increase of the rate of aggregation of $A\beta_{40}$ in the presence of $A\beta_{16-22}$ (Figure 62c – f).

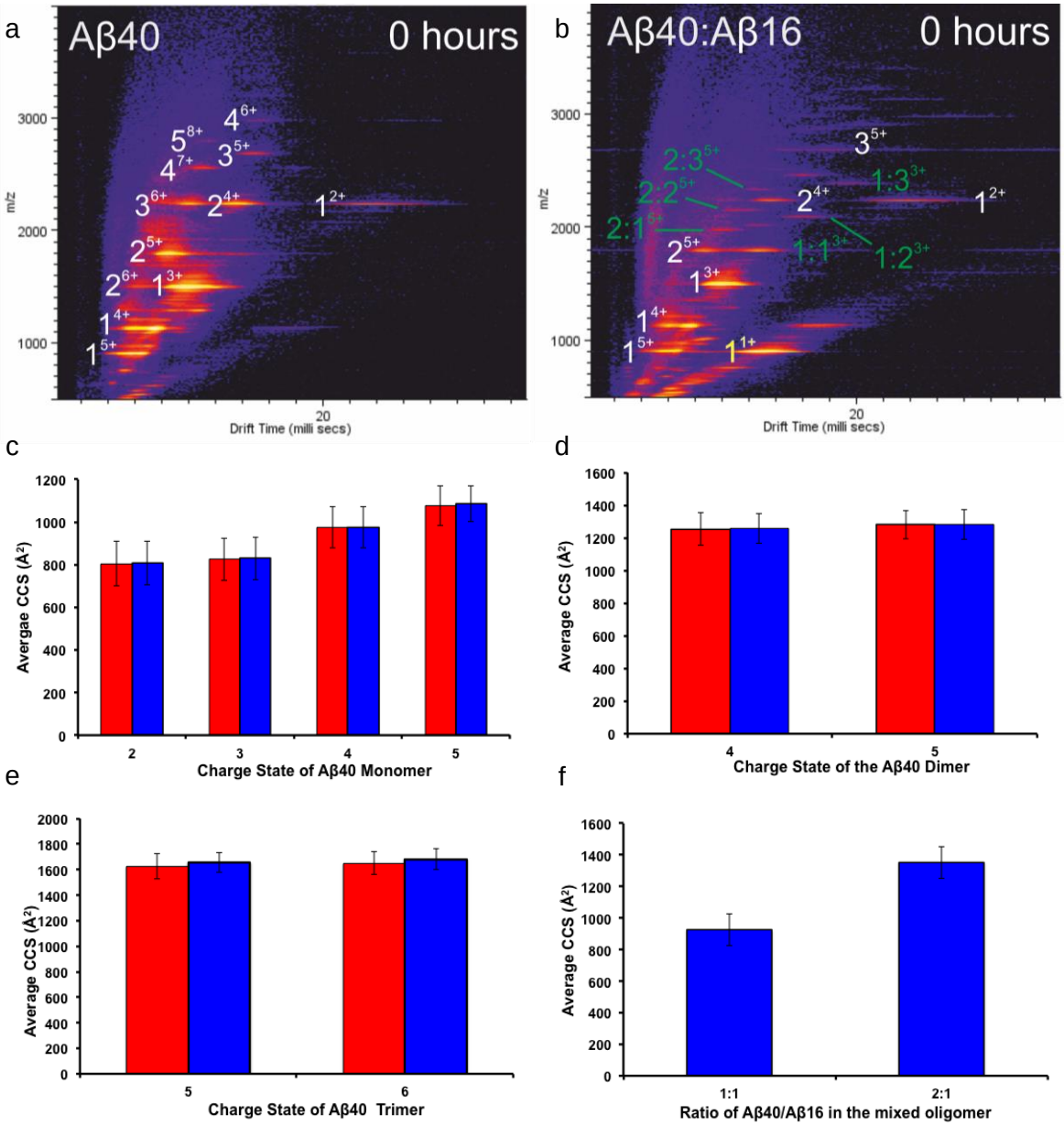

Figure 62. $A\beta_{16-22}$ and $A\beta_{40}$ can interact with each other at the monomer level. IMS measurements when $A\beta_{40}$ is either in isolation (a, white) or in the presence of $A\beta_{16-22}$ (b, yellow) demonstrate the presence of heterooligomeric species (green). The CCS areas of $A\beta_{40}$ monomers/oligomers are identical in the absence (red) and presence (blue) of $A\beta_{16-22}$ (c – e), whilst the CCS area of the mixed oligomers are as predicted for a 1:1 and 2:1 ratio of $A\beta_{40}$:$A\beta_{16-22}$ respectively (f).

In co-aggregation simulations in which both peptides begin in random coil structures, no apparent accelerating effect on the aggregation rate of $A\beta_{40}$ in the presence of $A\beta_{16-22}$ was observed (Figure 63a). The simulation generated energy contact map between the monomeric $A\beta_{16-22}$ and $A\beta_{40}$ peptides (Figure 63b) indicates $A\beta_{16-22}$, residues 18-20 (VFF) interact strongly with both β-sheet forming sections of $A\beta_{40}$ (residues 19-21 and

31-35, FFA and IGLM respectively). These results agree well with experimental data previously reported in the literature that indicates KLVFF is a “self-recognition element”. Despite attempts to capture the interaction experimentally using a diazirine labelled $A\beta_{16-22}$ ($A\beta^*_{16-22}$), the site of interaction could not be verified, likely due to the low percentage of any heterodimers present (as assessed by total ion count, 1.0 ± 0.5%) and the lower solution concentration of $A\beta_{16-22}$ arising as a consequence of its rapid aggregation (Figure 63c). The cross-links observed were homomolecular $A\beta^*_{16-22}$ cross-links, consistent with an in-register antiparallel, β-sheet structure and the pattern of cross-links observed in Chapter 2 (the MS/MS spectra can be found in Appendix 11).

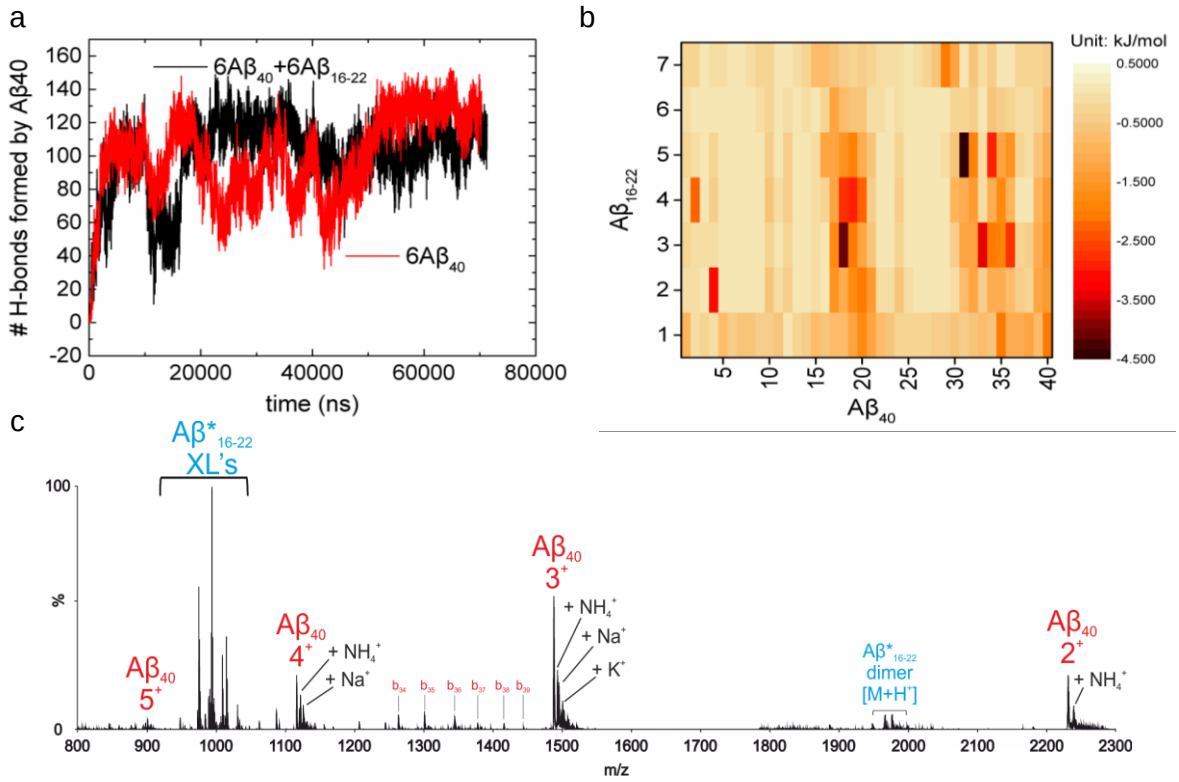

Figure 63. $A\beta_{16-22}$ monomers do not accelerate the rate of $A\beta_{40}$ aggregation, although they interact through the KLVFF motif. In DMD simulations in which both peptides start in random coil monomers, no apparent increase in the rate of $A\beta_{40}$ aggregation can be observed (a). The energy contact map demonstrates that the most significant contacts are via the KLVFF motif (b). When cross-linking experiments are performed at 5 mins with diazirine labelled $A\beta^*_{16-22}$, no heteromeric cross-links can be observed, with only homomeric $A\beta^*_{16-22}$ being observed (blue). $A\beta_{40}$ peaks corresponding to both monomer and dimer, as well as fragmentation products can also be observed (red).

3.13 $A\beta_{16-22}$ fibrils have a larger effect on the aggregation rate of $A\beta_{40}$ than $A\beta_{16-22}$ monomer

To further explore the effect of $A\beta_{16-22}$ on $A\beta_{40}$ aggregation, the effect of pre-formed $A\beta_{16-22}$ fibrils on $A\beta_{40}$ monomer aggregation was assessed. Self-seeding (where pre-formed fibrils are introduced to monomeric peptides) has been shown to abolish (or severely reduce) the lag phase, bypassing 1° nucleation.[16,74] Under all regimes, $A\beta_{16-22}$ fibrils increased the rate of aggregation of $A\beta_{40}$ (Figure 64). Higher $A\beta_{16-22}$ fibril concentrations (20%) increased the rate of $A\beta_{40}$ aggregation more than lower fibril concentrations (1%, Figure 64a). A direct comparison between “monomeric” (i.e. taken straight from a DMSO stock) and fibrillar $A\beta_{16-22}$ demonstrated that addition of $A\beta_{16-22}$ fibrils had the larger effect on the $A\beta_{40}$ aggregation rate (Figure 64b). These results indicate that it is through secondary pathways, such as surface catalysed nucleation and elongation, that $A\beta_{16-22}$ increases the aggregation rate of $A\beta_{40}$. However, as these assays (Figures 64a and b) used sonicated $A\beta_{16-22}$ fibrils, a direct comparison on the effect of sonication was also required; sonication of amyloid fibrils can increase the number of fibril ends within a sample, making the overall rate of aggregation more sensitive to elongation at the fibril ends. By introducing non-sonicated $A\beta_{16-22}$ fibrils (i.e. fewer fibril ends), a decrease in the rate of $A\beta_{40}$ aggregation would indicate elongation to be the dominant pathway by which the peptides interact. Side-by-side comparisons indicated that this was not the case (Figure 15c); in three independent assays the average half-time for sonicated fibrils = 6.2 ± 1.0 h; whereas for non-sonicated fibrils, the average half-time = 7.2 ± 0.7 h, indicating that elongation of $A\beta_{40}$ on the ends of $A\beta_{16-22}$ fibrils is unlikely to be the dominant contributor to accelerated $A\beta_{40}$ aggregation. Simulations of the aggregation of six $A\beta_{40}$ peptides were then performed in the presence of pre-formed $A\beta_{16-22}$ fibrils of different sizes (2, 3 and 4 β-sheets respectively). In these simulations, the presence of pre-formed $A\beta_{16-22}$ fibrils increased the rate of $A\beta_{40}$ aggregation, with the largest $A\beta_{16-22}$ fibril (i.e. 4 β-sheets) having biggest impact on the rate of β-sheet content formed by $A\beta_{40}$ (Figure 64d). Given the outcome of simulations with monomeric $A\beta_{16-22}$ (Figure 63a) which imply no apparent effect on the aggregation rate of $A\beta_{40}$, these simulations with $A\beta_{16-22}$ fibrils are in agreement with the experimental findings that the fibrillar structure of $A\beta_{16-22}$ is the dominant species influencing the aggregation rate of $A\beta_{40}$

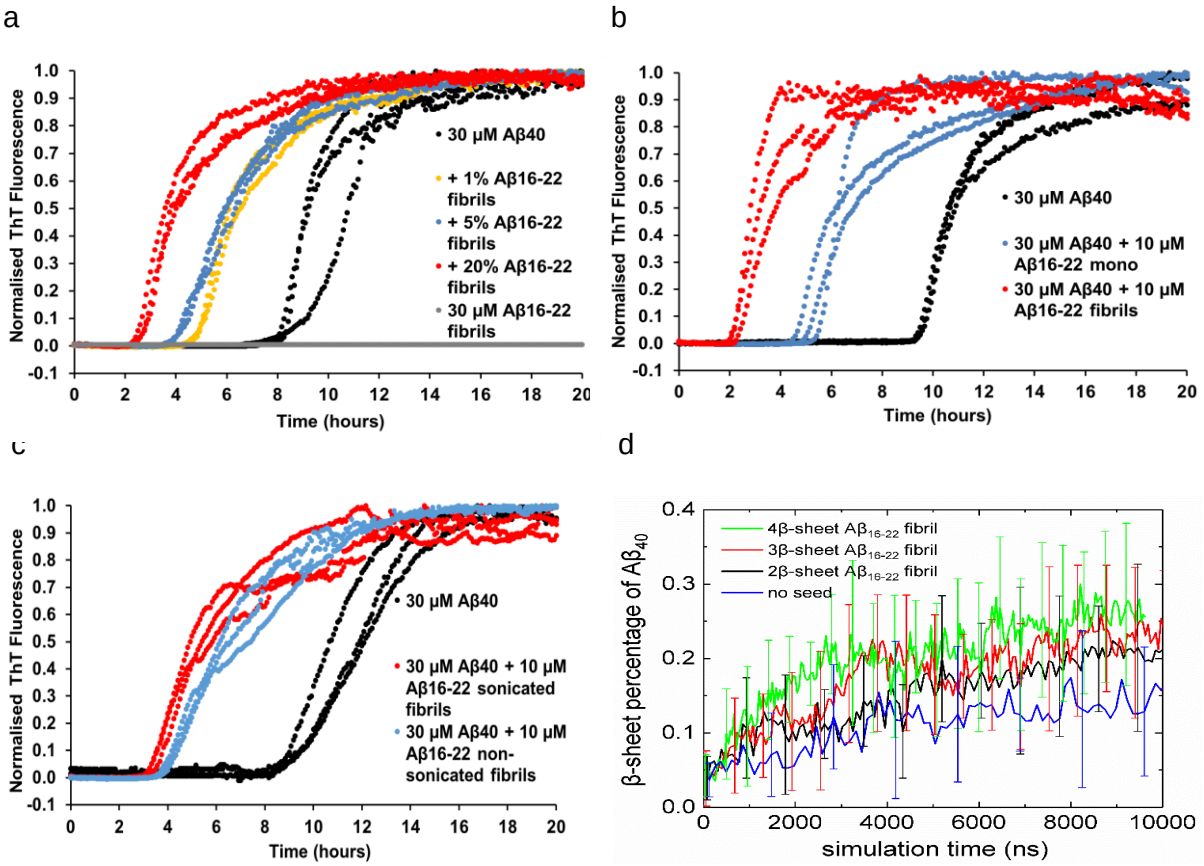

Figure 64. $A\beta_{16-22}$ fibrils increase the aggregation rate of $A\beta_{40}$. As increasing amounts of preformed fibrils are introduced into a pool of $A\beta_{40}$ monomers, the aggregation rate of $A\beta_{40}$ increases (a). When preformed fibrils are tested against the same concentration of $A\beta_{16-22}$ taken straight from a DMSO stock (i.e. should be monomeric), the fibrils have a bigger impact on the rate of $A\beta_{40}$ aggregation (b). When assessing the impact of sonication of the fibrils (i.e. whether the number of fibrils is important), no significant impact on the rate of $A\beta_{40}$ is seen, indicating that the rate of aggregation has limited sensitivity to elongation (c). When a preformed $A\beta_{16-22}$ fibrils with differing amounts of β-sheet layers (black = 2 layers, red = 3 layers and green = 4 layers) is placed in a simulation with random coil $A\beta_{40}$ monomers, the aggregation rate of $A\beta_{40}$ increases, compared to when in isolation (blue), with the number of β-sheet layers (d).

Taken together the ThT, native ESI-IMS-MS and fluorescence quenching experiments clearly point to a secondary nucleation mechanism in which $A\beta_{16-22}$ forms fibrils, prior to $A\beta_{40}$ interacting with these fibrils, which in turn affects the aggregation rate of $A\beta_{40}$. Direct comparisons between the addition of fibrillar $A\beta_{16-22}$ and "monomer" $A\beta_{16-22}$ to $A\beta_{40}$ emphasize that the fibril structure of $A\beta_{16-22}$ has the larger effect on $A\beta_{40}$ aggregation, despite the presence of small amounts of mixed oligomers (as demonstrated by the MS experiments). An increase in the presence of fibril ends does not appear to have a significant impact on the rate of $A\beta_{40}$ aggregation (Figure 64c,

implicating a surface catalysed nucleation mechanism, but not excluding a contribution to the rate acceleration from elongation.

3.14 $A\beta_{40}$ and $A\beta_{16-22}$ appear to form distinct homomolecular fibrils

The composition of the final fibril structure(s) represents a means to further discern the difference between the two different secondary pathways (surface catalysed and elongation). An elongation mechanism, in which $A\beta_{40}$ monomers add onto the ends of $A\beta_{16-22}$ fibrils would presumably form mixed fibrils, in which sections of each peptide can be found. Likewise, a surface catalysed mechanism would more likely produce homomolecular fibrils, as once formed on the $A\beta_{16-22}$ fibril surface the $A\beta_{40}$ nuclei could dissociate and form pure $A\beta_{40}$ fibrils. TEM images taken at the end of the aggregation reaction appeared to show that $A\beta_{40}$ fibrils display similar supramolecular fibril morphologies when incubated in isolation or co-aggregated with $A\beta_{16-22}$ (Figure 65, taken with the aid of Dr Matt Iadanza). It should be noted that this is a qualitative measure of fibril morphology/composition. Given that ThT only fluoresces significantly in the presence of $A\beta_{40}$ fibrils and not in the presence of $A\beta_{16-22}$ fibrils, the end-point fluorescence may provide an indication as to whether the final $A\beta_{40}$ fibril structures in the mixed system are similar to those of pure homomolecular $A\beta_{40}$. In all ThT assays performed, the end-point fluorescence values were within error of the value expected from pure $A\beta_{40}$ fibrils (Figure 66). Although both methods provide indirect evidence, they support the hypothesis that homomolecular $A\beta_{40}$ fibrils are formed at the end of the assembly reaction.

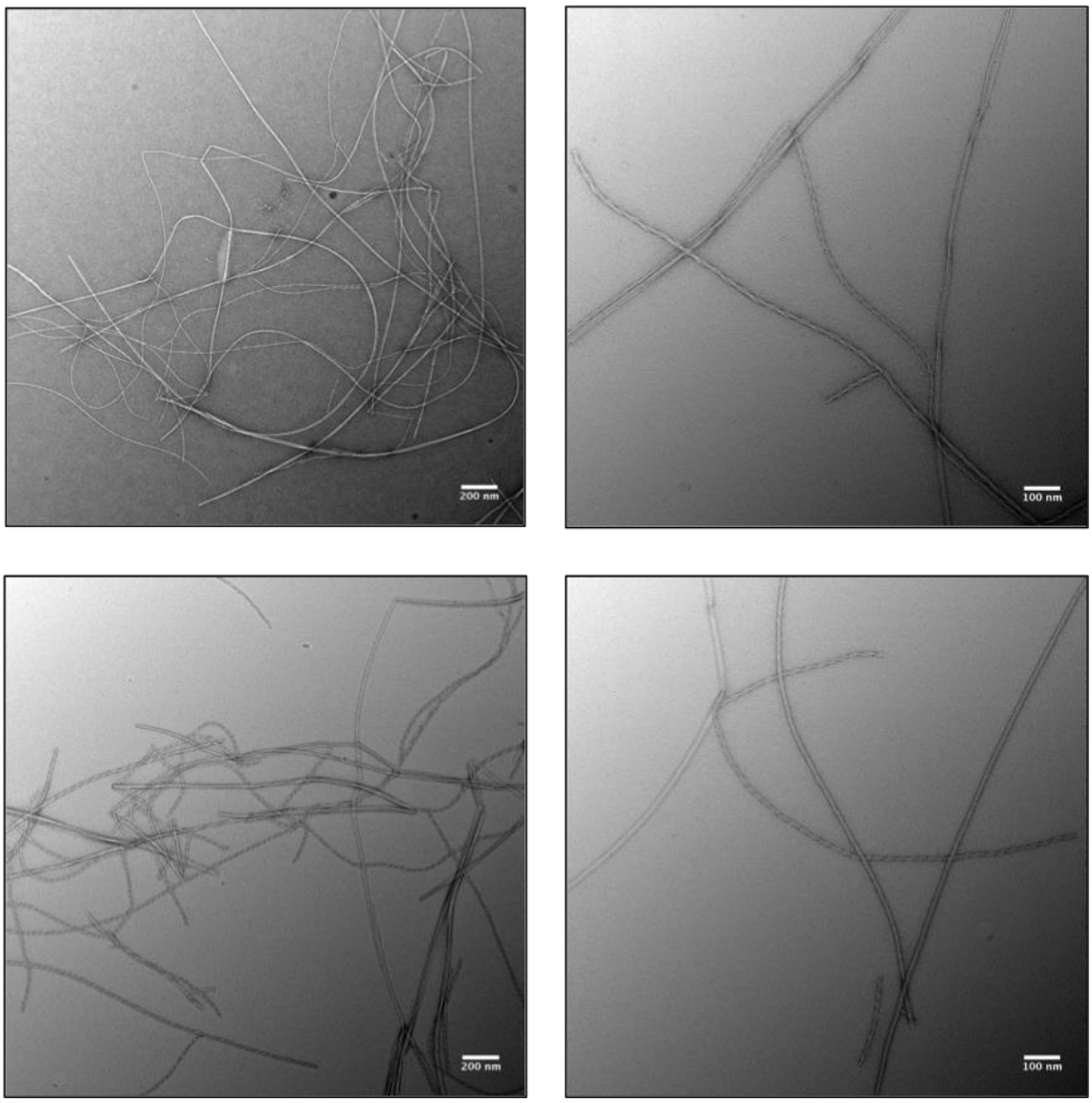

Figure 65. $A\beta_{40}$ fibrils have the same morphology when they are incubated in isolation (top) or in a 1:1 mixture of $A\beta_{40}/A\beta_{16-22}$ (bottom). The images on the right hand side are zoomed in images of the left hand image and were taken with the aid of Dr Matt Iadanza. Scale bars are 200 and 100 nm respectively and are shown in white for clarity.

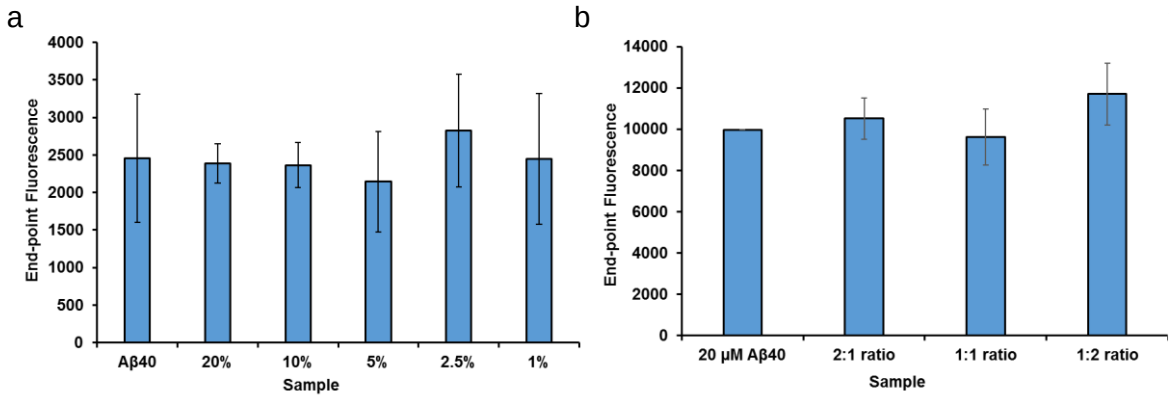

Figure 66. ThT end-points demonstrate that $A\beta_{40}$ fibrils produce the same amount of fluorescence in the presence of increasing amounts of seeds (a) or increasing amounts $A\beta_{16-22}$ monomers as when in isolation indicating that majority homomolecular fibrils are formed.

A further direct method to confirm the presence of homomolecular fibrils is to use PIC experiments, as described in detail in Chapter 2.[75] To perform the PIC experiments, a diazirine label was placed on F20 of $A\beta_{16-22}$ ($A\beta^*_{16-22}$). Prior to the PIC experiments, it was established (using a ThT fluorescence assay) that $A\beta^*_{16-22}$ has a similar effect on $A\beta_{40}$ aggregation kinetics (Figure 67a). PIC experiments performed at 5 mins and 24 hours indicate that no hetero-crosslinks form between $A\beta^*_{16-22}$ and $A\beta_{40}$ (Figures. 63c for 5 mins sample, 67b for 24 h sample). If co-assembled heteromolecular fibrils were present at the end of the aggregation reaction, upon irradiation at 365 nm, the carbene generated by the diazirine should form hetero-crosslinks between $A\beta_{40}$ and the labelled $A\beta^*_{16-22}$. All identifiable cross-links were consistent with inter/intramolecular $A\beta^*_{16-22}$ or solvent adducts previously identified by in the previous chapter, indicating that co-assembly does not occur (Figure 67b).

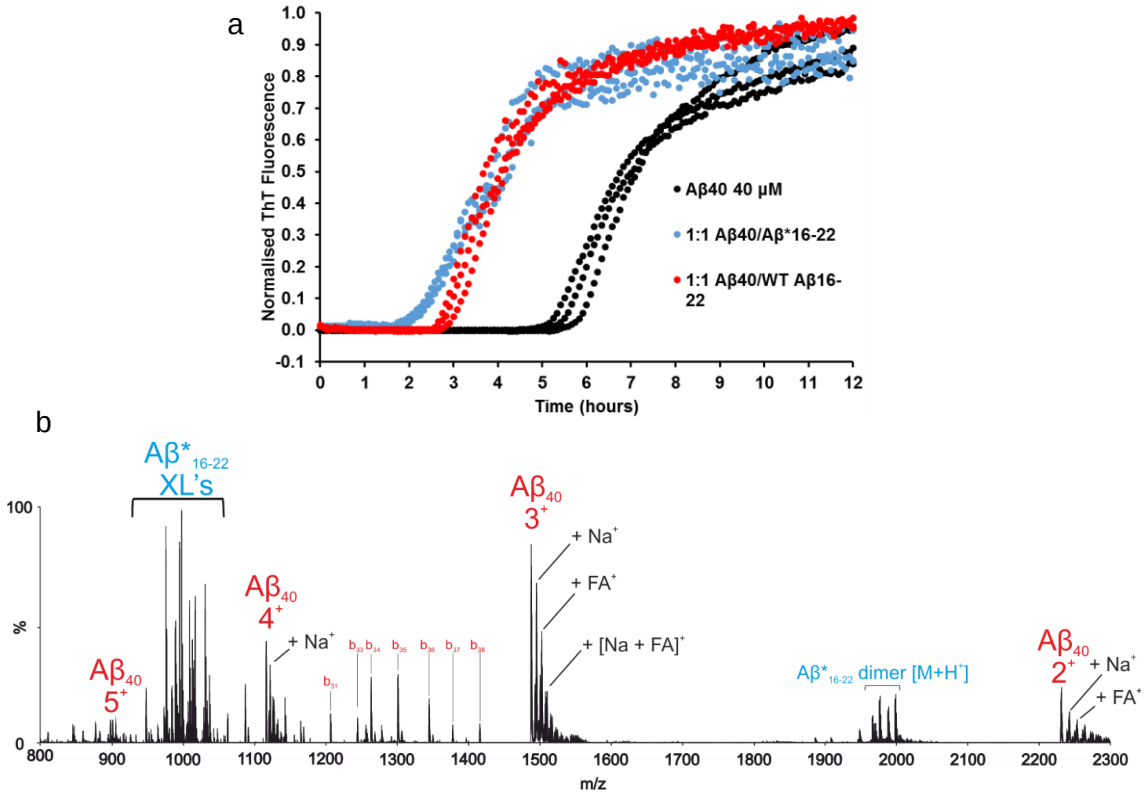

Figure 67. Aβ*$_{16-22}$ has the same effect on the rate of Aβ$_{40}$ as Aβ$_{16-22}$ (a) and at the end of the self-assembly reaction they form homomolecular fibrils (b).

To further support these conclusions, simulations following the co-aggregation reactions were performed; at the early stage (Figure 68, t = 0 μs) a mixture of monomeric and oligomeric Aβ$_{40}$ was present and as the simulation progressed (t = 57 μs), all Aβ$_{40}$ peptides coalesced into one β-sheet rich oligomer, with Aβ$_{16-22}$ intercalated within the structure. Throughout the simulation, monomeric Aβ$_{16-22}$ was observed to bind to other monomeric Aβ$_{16-22}$ peptides or the KLVFF motif of Aβ$_{40}$ in an unstable manner. In accordance with experimental data, at the end of the aggregation (t = 202 μs) the peptides did not formed a co-assembled aggregate but instead form distinct fibril-like structures (parallel for Aβ$_{40}$ and antiparallel for Aβ$_{16-22}$).

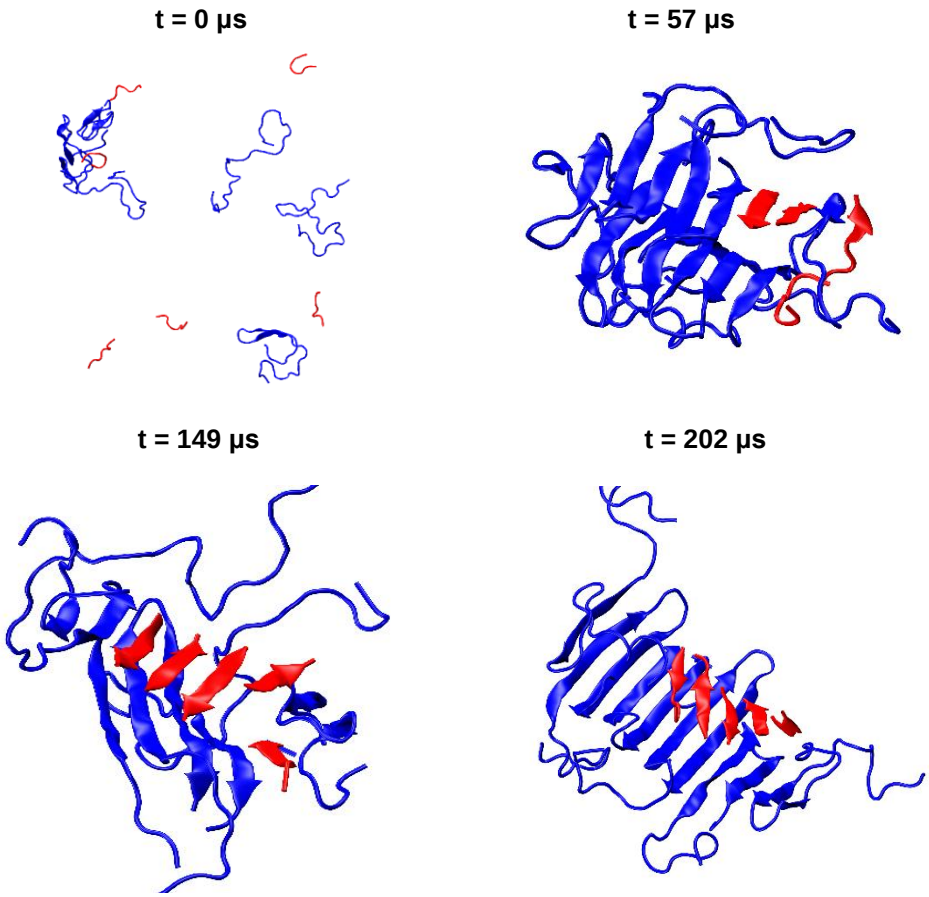

Figure 68. In DMD simulations, $A\beta_{40}$ and $A\beta_{16-22}$ form separate homomolecular structures. At the start of the simulation a mixture of both monomeric and oligomeric $A\beta_{40}$ is present (t = 0 µs, red) and as the simulation progress all $A\beta_{40}$ peptides coalesce into a single oligomeric structure, with $A\beta_{16-22}$ (blue) intercalated within the structure (t = 57 µs). At the simulation end point, $A\beta_{16-22}$ has formed a homomolecular β-sheet on the surface of the $A\beta_{40}$ oligomer, primarily interacting with the KLVFF motif within $A\beta_{40}$ (t = 202 µs).

3.15 $A\beta_{16-22}$ forms fibrils that provide a competent surface to nucleate $A\beta_{40}$, increasing its aggregation rate

A series of simulation snapshots (Figure 69), demonstrate the surface catalysed nucleation of $A\beta_{40}$ by a preformed $A\beta_{16-22}$ fibril. At the early stage of the simulation (t = 0 µs), three $A\beta_{40}$ peptides are present in an oligomer, either associated at the end of the fibril or elongated across the fibril surface. The $A\beta_{40}$ peptides predominantly adopt a random coil conformation, with small amounts of β-sheet structure. An elongated monomeric structure was also observed in simulations exploring the secondary nucleation of $A\beta_{42}$ on the surface of $A\beta_{11-42}$ performed by Barz et al.[62] As the simulation progressed (t = 1.16 µs), the $A\beta_{40}$ peptides remaining in solution were recruited by

those on the fibril surface. Once the oligomer became fully associated to the fibril surface, parallel β-sheets started to form. These β-sheets templated peptides present in a random coil conformation, pulling the oligomer more fully to the fibril surface (t = 1.93 μs). The amount of β-sheet structure in the surface-associated oligomer increased as the simulation progressed (t = 7.7 μs) until finally all four surface associated $A\beta_{40}$ peptides were found as a highly ordered oligomer (t = 29 and μs). $A\beta_{40}$ peptides attached to both the lateral surface and the end of the $A\beta_{16-22}$ fibril during the simulation (Figure 70) with the $A\beta_{40}$ C-terminal region attaching more frequently to the lateral surface of the fibril than to the fibril ends.

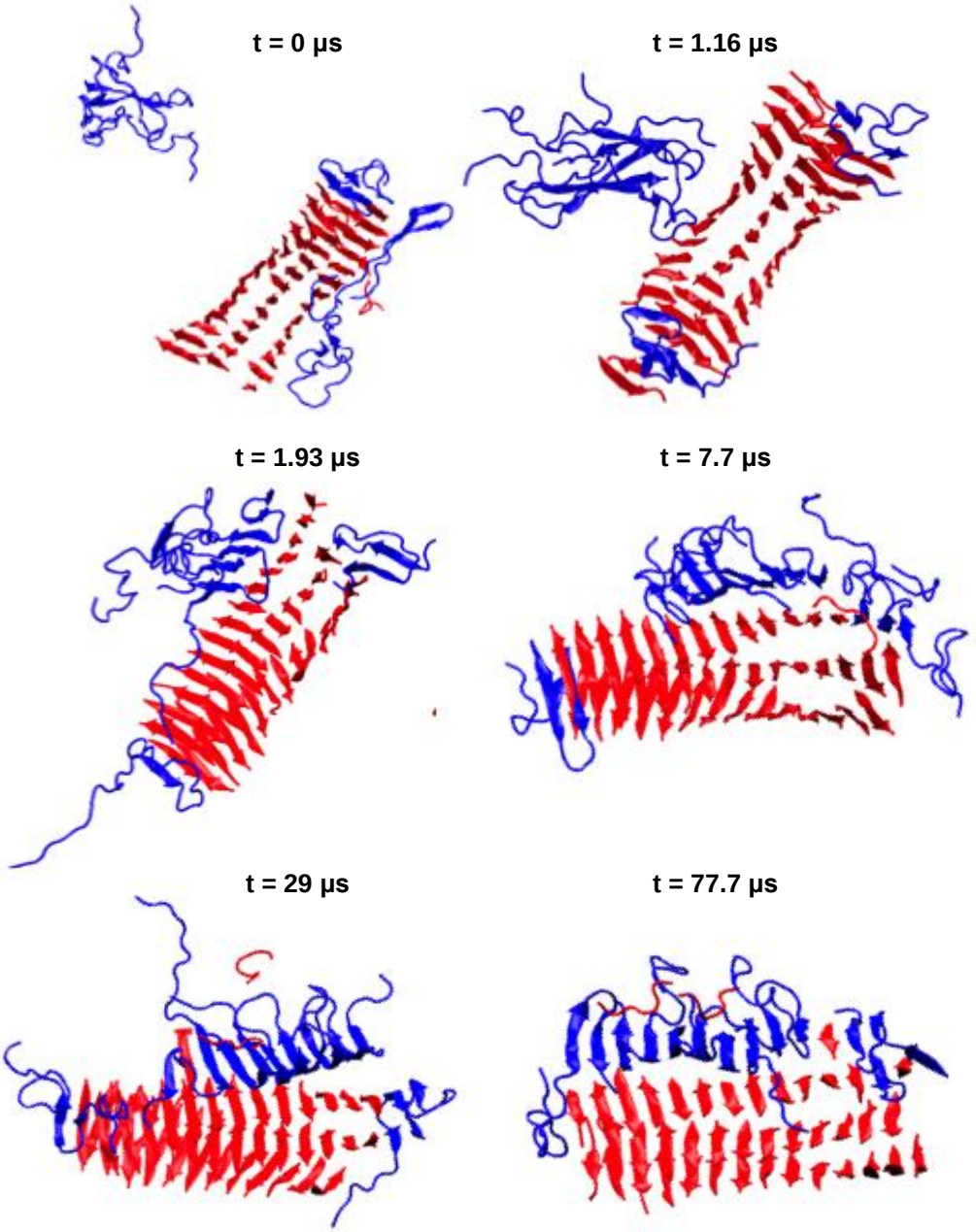

Figure 69. $A\beta_{16-22}$ (red) has a surface that is competent to nucleate the formation of β-sheet containing oligomers of $A\beta_{40}$ (blue), starting from a random coil $A\beta_{40}$ oligomer. A detailed description of how this occurs can be found in the main body of the text.

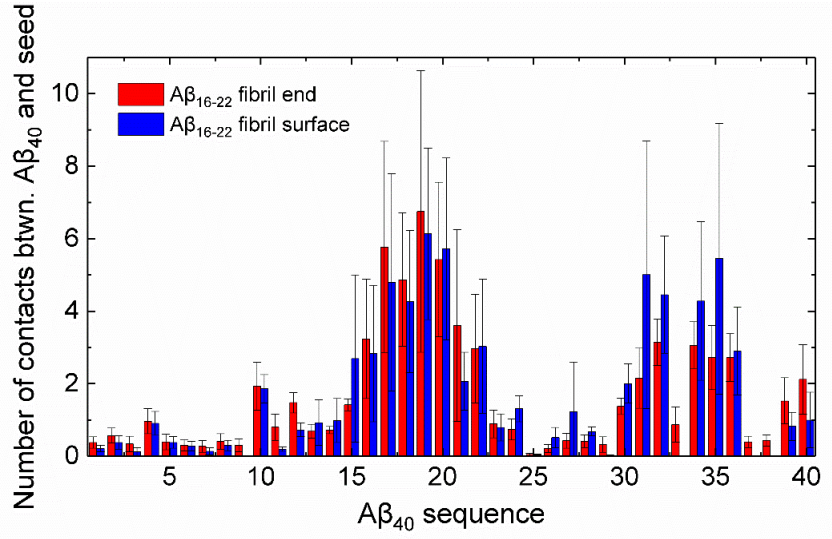

Figure 70. Plot of the average number of hydrogen bonding and side chain-side chain contacts between six $A\beta_{40}$ monomers and a 3-β-sheet $A\beta_{16-22}$ fibril during the simulation. As shown in Figure 21, $A\beta_{40}$ monomers attach to both the lateral surface and the end of the $A\beta_{16-22}$ fibril with its C-terminal part attaching more frequently to the lateral surface of the fibril than its two ends.

3.16 The proposed mechanism by which $A\beta_{16-22}$ and $A\beta_{40}$ interact

The proposed mechanism by which the two peptides interact (see schematic in Figure 71), proceeds with the majority of monomeric $A\beta_{16-22}$ aggregating relatively quickly, forming homomolecular fibrils. A small percentage (1.0 ± 0.5% from total ion count) of monomeric $A\beta_{16-22}$ forms mixed oligomers with $A\beta_{40}$ monomers and dimers. The mixed $A\beta_{16-22}/A\beta_{40}$ oligomers can have a number of different fates: If the mixed oligomers are fundamentally unstable, they may dissociate back into the constituent monomers, slowing the overall aggregation rate of each peptide. If the structure of the mixed oligomers is such that monomeric $A\beta_{16-22}$ and/or $A\beta_{40}$ cannot bind to the oligomer, then the mixed oligomers will not take any further part in the aggregation reaction. These oligomers can be referred to as “off-pathway”. However, if the structure of the mixed oligomers is such that monomeric $A\beta_{16-22}/A\beta_{40}$ peptides can bind, the rate of aggregation will eventually approach the homogenous rate. These mixed oligomers will be incorporated into majority homomolecular fibrils at a level that is not experimentally verifiable. The majority of $A\beta_{16-22}$ monomers go on to form homomolecular fibrils relatively quickly, providing a surface upon which $A\beta_{40}$ can nucleat. The aggregation rate of $A\beta_{40}$ is dominated by secondary nucleation processes, requiring the presence of $A\beta_{40}$ aggregates, the formation of which is (initially) reliant on the slow primary

nucleation rate. The increase in the rate of $A\beta_{40}$ aggregation in the presence of $A\beta_{16-22}$ is therefore due to the quick formation of the $A\beta_{16-22}$ fibril, in turn bypassing $A\beta_{40}$ primary nucleation.

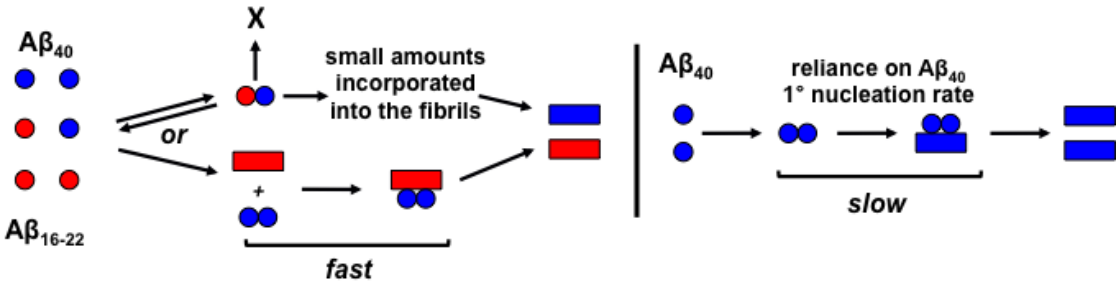

Figure 71. The proposed surface catalysed secondary nucleation mechanism by which $A\beta_{16-22}$ increases the aggregation rate of $A\beta_{40}$.

It might be expected that the aggregation of $A\beta_{40}$ would be inhibited in the presence of $A\beta_{16-22}$, as the $A\beta_{16-22}$ peptide contains the KLVFF motif. However, the results presented here conclusively demonstrate that $A\beta_{16-22}$ increases the aggregation rate of $A\beta_{40}$. The KLVFF motif has been described both as a "self-recognition element", in that it has been shown to recognise and bind to itself.[32,77] A number of modifications (such as C-terminal extensions with multiple K residues, N-terminal ferrocene extensions and N-methyl peptides) have been used to develop inhibitors that delay the aggregation of both $A\beta_{40}$ and $A\beta_{42}$.[32,34,36,38] Attempts to identify the binding site between $A\beta_{40}$ and the KLVFF motif have often used solid phase supports with short radiolabeled peptide fragments. Tjernberg and co-workers observed that the KLVFF peptide does not form fibrils (at a concentration of 200 μM).[78] However later studies, using cryo-TEM, showed that this fragment could form fibrils when placed in a phosphate buffer (at higher concentrations, 3 wt% or ~46 mM).[79] $A\beta_{16-22}$ however forms fibril structures at concentrations below those for KLVFF (20 – 40 μM). A computational search of all possible tripeptides (8,000) looking for sequences with a high aggregation propensity demonstrated that at the N-terminus positively charged residues such as K, R, S and T promote self-assembly, along with hydrophobic residues at the 2 or 3 position.[80] Interestingly, both D and E were highlighted as being favourable residues to have at the 3 position (C-termini). As this pattern of residues is mirrored within $A\beta_{16-22}$ (i.e. positively charged N-termini, hydrophobic core and negatively charged/hydrogen bond forming C-termini) it could be that the addition of the extra two residues, in particular E, give $A\beta_{16-22}$ a higher propensity towards forming antiparallel β-sheets, compared with amphiphilic KLVFF. As KLVFF does not form homomolecular fibrils until it reaches a

high enough concentration, it may bind to $A\beta_{40}$, reducing the ability of $A\beta_{40}$ to form nuclei and so slowing down the rate of aggregation. In comparison, $A\beta_{16-22}$, with its high propensity to self-associate into β-sheets, forms homomolecular fibrils quickly without binding to $A\beta_{40}$.

3.17 Conclusions

In conclusion, the co-aggregation of two amyloidogenic peptides has been analysed, $A\beta_{16-22}$ and $A\beta_{40}$, and it has been demonstrated that $A\beta_{16-22}$ forms fibrils relatively quickly and is unaffected by the presence of $A\beta_{40}$. Any hetero-oligomeric $A\beta_{16-22}$-$A\beta_{40}$ appear to play a minor role in the co-aggregation reaction. Once $A\beta_{16-22}$ forms fibrils, these species provide a surface that can interact with and nucleate the aggregation of $A\beta_{40}$, increasing its aggregation rate. All of these processes can be observed in DMD simulations, highlighting the power of the approach in observing, at the molecular level, how $A\beta_{40}$ first associates with fibril surface overtime.

3.18 Future Work

Although the mechanism by which the two peptides interact has been elucidated there are still some outstanding questions, namely whether the $A\beta_{40}$ oligomers formed on the surface of $A\beta_{16-22}$ are in a parallel (as suggested by the simulations) or an antiparallel orientation. As $A\beta_{16-22}$ forms antiparallel β-sheets, it may be expected that that if the fibril surface is truly templating the $A\beta_{40}$ oligomers then they would in an antiparallel orientation. In order to do this, the diazirine labelled cross-linker would need to be placed within the $A\beta_{40}$ monomers and cross-linked. The longer amino acid sequence of $A\beta_{40}$ may more challenging to analysing via MS/MS sequencing, requiring the development of new analysis methodologies. Other techniques, such as CD or IR, may find it difficult to separate out the two peptides without resorting to isotope editing techniques.

References:

1 G. G. Glenner and C. W. Wong, *Biochem. Biophys. Res. Commun.*, 1984, **120**, 885–890.

2 V. Bellotti, M. Stoppini, P. Mangione, M. Sunde, C. Robinson, L. Asti, D. Brancaccio and G. Ferri, *Eur. J. Biochem.*, 1998, **67**, 61–67.

3 C. J. Sarell, P. G. Stockley and S. E. Radford, *Prion*, 2013, **7**, 359–368.

4 M. Jucker and L. C. Walker, *Nature*, 2013, **501**, 45–51.

5 H. Mori, K. Takio, M. Ogawara and D. J. Selkoe, *J. Biol. Chem.*, 1992, **267**, 17082–17086.

6 J. Wiltfang, H. Esselmann, M. Bibl, A. Smirnov, M. Otto, S. Paul, B. Schmidt, H. Klafki, M. Maler, T. Dyrks, M. Bienert, M. Beyermann and E. Ru, *J. Neurochem.*, 2002, **81**, 481–496.

7 D. Scheuner, C. Eckman, M. Jensen, X. Song, M. Citron, N. Suzuki, T. D. Bird, J. Hardy, M. Hutton, W. Kukull, E. Larson, E. Levy-Lahad, M. Viitanen, E. Peskind, P. Poorkaj, G. Schellenberg, R. Tanzi, W. Wasco, L. Lannfelt, D. Selkoe and S. Younkin, *Nature*, 1996, **2**, 874–870.

8 X. Li, E. Masliah, N. Reixach and J. N. Buxbaum, *J. Neurosci.*, 2011, **31**, 12483–90.

9 T. Eichner and S. E. Radford, *Mol. Cell*, 2011, 43, 8–18.

10 T. K. Karamanos, A. P. Kalverda, G. S. Thompson and S. E. Radford, *Mol. Cell*, 2014, **55**, 214–226.

11 M. R. H. Krebs, L. a Morozova-Roche, K. Daniel, C. V Robinson and C. M. Dobson, *Protein Sci.*, 2004, **13**, 1933–1938.

12 B. O'Nuallain, A. D. Williams, P. Westermark and R. Wetzel, *J. Biol. Chem.*, 2004, **279**, 17490–17499.

13 M. R. Sawaya, S. Sambashivan, R. Nelson, M. I. Ivanova, S. a Sievers, M. I. Apostol, M. J. Thompson, M. Balbirnie, J. J. W. Wiltzius, H. T. McFarlane, A. Ø. Madsen, C. Riekel and D. Eisenberg, *Nature*, 2007, **447**, 453–457.

14 L. M. Young, R. A. Mahood, J. C. Saunders, T. Ling-Hsien, D. P. Raleigh, S. E. Radford and A. E. Ashcroft, *Analyst*, 2015, **20**, 6990–6999.

15 P. Westermark, A. Andersson and G. T. Westermark, *Physiol. Rev.*, 2011, **91**, 795–826.

16 S. I. A. Cohen, M. Vendruscolo, C. M. Dobson and T. P. J. Knowles, *J. Mol. Biol.*, 2012, **421**, 160–171.

17 G. Meisl, X. Yang, E. Hellstrand, B. Frohm, J. B. Kirkegaard, S. I. A. Cohen, C.

M. Dobson, S. Linse and T. P. J. Knowles, *Proc. Natl. Acad. Sci. U. S. A.*, 2014, **111**, 9384–9.

18 S. I. A. Cohen, S. Linse, L. M. Luheshi, E. Hellstrand, D. A. White, L. Rajah, D. E. Otzen, M. Vendruscolo, C. M. Dobson and T. P. J. Knowles, *Proc. Natl. Acad. Sci. U. S. A.*, 2013, **110**, 9758–63.

19 M. Tö, T. C. T. Michaels, K. Sanagavarapu, X. Yang, G. Meisl, S. I. A. Cohen, T. P. J. Knowles Bd and S. Linse, *Chem. Commun.*, 2018.

20 R. Cukalevski, X. Yang, G. Meisl, U. Weininger, K. Bernfur, B. Frohm, T. P. J. Knowles and S. Linse, *Chem. Sci.*, 2015, **6**, 4215–4233.

21 T. P. J. Knowles, C. A. Waudby, G. L. Devlin, S. I. A. Cohen, A. Aguzzi, M. Vendruscolo, E. M. Terentjev, M. E. Welland and C. M. Dobson, *Science.*, 2009, **326**, 1533–1538.

22 J. T. Jarrett, E. P. Berger and P. T. Lansbury, *Biochemistry*, 1993, **32**, 4693–4697.

23 S. W. Snyder, U. S. Ladror, W. S. Wade, G. T. Wang, L. W. Barrett, E. D. Matayoshi, H. J. Huffaker, G. A. Krafft and T. F. Holzman, *Biophys. J.*, 1994, **67**, 1216–1228.

24 K. Hasegawa, I. Yamaguchi, S. Omata, F. Gejyo and H. Naiki, *Biochemistry*, 1999, **38**, 15514–15521.

25 Y. Yan and C. Wang, *J. Mol. Biol.*, 2007, **369**, 909–916.

26 A. Jan, O. Gokce, R. Luthi-Carter and H. A. Lashuel, *J. Biol. Chem.*, 2008, **283**, 28176–28189.

27 K. Pauwels, T. L. Williams, K. L. Morris, W. Jonckheere, A. Vandersteen, G. Kelly, J. Schymkowitz, F. Rousseau, A. Pastore, L. C. Serpell and K. Broersen, *J. Biol. Chem.*, 2012, **287**, 5650–5660.

28 M. Török, S. Milton, R. Kayed, P. Wu, T. McIntire, C. G. Glabe and R. Langen, *J. Biol. Chem.*, 2002, **277**, 40810–40815.

29 M. Iljina, G. A. Garcia, A. J. Dear, J. Flint, P. Narayan, T. C. T. Michaels, C. M. Dobson, D. Frenkel, T. P. J. Knowles and D. Klenerman, *Sci. Rep.*, 2016, **6**, 1–8.

30 M. Baldassarre, C. M. Baronio, L. A. A. Morozova-Roche and A. Barth, *Chem. Sci.*, 2017, **00**, 1–8.

31 I. W. Hamley, *Chem. Rev. Am. Chem. Soc.*, 2012, **112**, 5147–5192.

32 L. O. Tjernberg, J. Naslund, F. Lindqvist, J. Johansson, A. R. Karlstrom, J. Thyberg, L. Terenius and C. Nordstedt, *J. Biol. Chem.*, 1996, **271**, 8545–8549.

33 L. O. Tjernberg, C. Lilliehöök, D. J. Callaway, J. Näslund, S. Hahne, J. Thyberg, L. Terenius and C. Nordstedt, *J. Biol. Chem.*, 1997, **272**, 12601–12605.

34 J. Ghanta, C. L. Shen, L. L. Kiessling and R. M. Murphy, *J. Biol. Chem.*, 1996, **271**, 29525–29528.

35 D. J. Gordon, R. Tappe and S. C. Meredith, *J. Pept. Res.*, 2002, **60**, 37–55.

36 L. Zhang, G. Yagnik, Y. Peng, J. Wang, H. Xu, Y. Hao, Y.-N. Liu and F. Zhou, *Anal. Biochem.*, 2013, **2**, 292–299.

37 K. Watanabe, T. Segawa, K. Nakamura, M. Kodaka, T. Konakahara and H. Okuno, *J. Pept. Res.*, 2001, **58**, 342–346.

38 D. J. Gordon, K. L. Sciarretta and S. C. Meredith, *Biochemistry*, 2001, 8237–8245.

39 J. D. Barritt, N. D. Younan and J. H. Viles, *Angew. Chemie - Int. Ed.*, 2017, **56**, 9816–9819.

40 J. Nasica-Labouze, P. H. Nguyen, F. Sterpone, O. Berthoumieu, N. V. Buchete, S. Coté, A. De Simone, A. J. Doig, P. Faller, A. Garcia, A. Laio, M. S. Li, S. Melchionna, N. Mousseau, Y. Mu, A. Paravastu, S. Pasquali, D. J. Rosenman, B. Strodel, B. Tarus, J. H. Viles, T. Zhang, C. Wang and P. Derreumaux, *Chem. Rev.*, 2015, **115**, 3518–3563.

41 A. Morriss-Andrews and J.-E. Shea, *Annu. Rev. Phys. Chem.*, 2015, **66**, 643–666.

42 J. E. Straub and D. Thirumalai, *Annu. Rev. Phys. Chem.*, 2011, **62**, 437–463.

43 O. O. Olubiyi and B. Strodel, *J. Phys. Chem. B*, 2012, **116**, 3280–3291.

44 C. Wu and J.-E. Shea, *Curr. Opin. Struct. Biol.*, 2011, **21**, 209–220.

45 I. C. and C. K. H. M. Cheon, *Proteins*, 2010, **78**, 2950–2960.

46 W. Zheng, M.-Y. Tsai, M. Chen and P. G. Wolynes, *Proc. Natl. Acad. Sci. U. S. A.*, 2016, **113**, 11835–11840.

47 N. G. Sgourakis, Y. Yan, S. A. McCallum, C. Wang and A. E. Garcia, *J. Mol. Biol.*, 2007, **368**, 1448–1457.

48 D. J. Rosenman, C. Connors, W. Chen, C. Wang and A. E. Garcia, *J. Mol*, 2013, **8**, 3338–3359.

49 K. A. Ball, A. H. Phillips, D. E. Wemmer and T. Head-Gordon, *Biophys. J.*, 2013, **104**, 2714–2724.

50 Q. Liao, M. C. Owen, O. O. Olubiyi, B. Barz and B. Strodel, *Isr. J. Chem.*, 2017, **57**, 771–784.

51 P. Das, A. R. Chacko and G. Belfort, *ACS Chem. Neurosci.*, 2017, **8**, 606–618.

52 T. Zhang, J. Zhang, P. Derreumaux and Y. Mu, *J. Phys. Chem. B*, 2013, **117**, 3993–4002.

53 V. H. Man, P. H. Nguyen and P. Derreumaux, *J. Phys. Chem. B*, 2017, **121**, 2434–2442.

54 B. Barz, O. O. Olubiyi and B. Strodel, *Chem. Commun.*, 2014, **50**, 5373–5375.

55 B. Barz, Q. Liao and B. Strodel, *J. Am. Chem. Soc.*, 2018, **140**, 319–327.

56 S. L. Bernstein, N. F. Dupuis, N. D. Lazo, T. Wyttenbach, M. M. Condron, G. Bitan, D. B. Teplow, J.-E. Shea, B. T. Ruotolo, C. V Robinson and M. T. Bowers, *Nat. Chem.*, 2009, **1**, 326–331.

57 C. Denison and T. Kodadek, *J. Proteome Res.*, 2004, **3**, 417–425.

58 A. T. Petkova, R. D. Leapman, Z. Guo, W.-M. Yau, M. P. Mattson and R. Tycko, *Science*, 2005, **307**, 262–265.

59 K. Irie, K. Murakami, Y. Masuda, A. Morimoto, H. Ohigashi, R. Ohashi, K. Takegoshi, M. Nagao, T. Shimizu and T. Shirasawa, *J. Biosci. Bioeng.*, 2005, **99**, 437–447.

60 T. Gurry and C. M. Stultz, *Biochemistry*, 2014, **53**, 6981–6991.

61 M. Bacci, J. Vymětal, M. Mihajlovic, A. Caflisch and A. Vitalis, *J. Chem. Theory Comput.*, 2017, **13**, 5117–5130.

62 B. Barz and B. Strodel, *Chem. - A Eur. J.*, 2016, **22**, 8768–8772.

63 N. Schwierz, C. V. Frost, P. L. Geissler and M. Zacharias, *J. Phys. Chem. B*, 2017, **121**, 671–682.

64 N. Schwierz, C. V. Frost, P. L. Geissler and M. Zacharias, *J. Am. Chem. Soc.*, 2016, **138**, 527–539.

65 D. M. Walsh, E. Thulin, A. M. Minogue, N. Gustavsson, E. Pang, D. B. Teplow and S. Linse, *FEBS J.*, 2009, **276**, 1266–1281.

66 K. L. Stewart, E. Hughes, E. A. Yates, G. R. Akien, T. Y. Huang, M. A. Lima, T. R. Rudd, M. Guerrini, S. C. Hung, S. E. Radford and D. A. Middleton, *J. Am. Chem. Soc.*, 2016, **138**, 8328–8331.

67 K. L. Stewart, E. Hughes, E. A. Yates, D. A. Middleton and S. E. Radford, *J. Mol. Biol.*, 2017.

68 R. Silvers, M. T. Colvin, K. K. Frederick, A. C. Jacavone, S. L. Lindquist, S. Linse and R. G. Griffin, *Biochemistry*, 2017, acs.biochem.7b00729.

69 M. R. Nilsson, *Methods*, 2004, **34**, 151–160.

70 F. Kundel, L. Tosatto, D. R. Whiten, D. C. Wirthensohn, M. H. Horrocks and D. Klenerman, *FEBS J.*, 2018, 1–27.

71 D. M. Williams and T. L. Pukala, *Mass Spectrom. Rev.*, 2013, 169–187.

72 J. T. S. Hopper, A. Rawlings, J. P. Afonso, D. Channing, R. Layfield and N. J. Oldham, *J. Am. Soc. Mass Spectrom.*, 2012, **23**, 1757–1767.

73 L. M. Young, L.-H. Tu, D. P. Raleigh, A. E. Ashcroft and S. E. Radford, *Chem. Sci.*, 2017, **00**, 1–11.

74 G. Meisl, J. B. Kirkegaard, P. Arosio, T. C. T. Michaels, M. Vendruscolo, C. M.

Dobson, S. Linse and T. P. J. Knowles, *Nat. Protoc.*, 2016, **11**, 252–272.

75 G. W. Preston and A. J. Wilson, *Chem. Soc. Rev.*, 2013, **42**, 3289–301.

76 G. W. Preston, S. E. Radford, A. E. Ashcroft and A. J. Wilson, *Anal. Chem.*, 2012, **84**, 6790–6797.

77 K. Watanabe, T. Segawa, K. Nakamura, M. Kodaka, T. Konakahara and H. Okuno, *J. Pept. Res.*, 2001, **58**, 342–346.

78 L. O. Tjernberg, D. J. E. Callaway, A. Tjernberg, S. Hahne, C. Lilliehöök, L. Terenius, J. Thyberg and C. Nordstedt, *J. Biol. Chem.*, 1999, **274**, 12619–12625.

79 M. J. Krysmann, V. Castelletto, A. Kelarakis, I. W. Hamley, R. a Hule and D. J. Pochan, *Screening*, 2008, 4597–4605.

80 P. W. J. M. Frederix, G. G. Scott, Y. M. Abul-Haija, D. Kalafatovic, C. G. Pappas, N. Javid, N. T. Hunt, R. V Ulijn and T. Tuttle, *Nat. Chem.*, 2014, **7**, 30–37.

Materials and Methods

4.1. General materials for peptide synthesis

All amino acids, coupling reagents and resins were purchased from Novasyn (Merck), Fluorochem or Sigma-Aldrich. All amino acids were *N*-Fmoc protected and side chains were protected with Boc (Lys) or OtBu (Glu). $A\beta_{16-22}$ (**9**), TAMRA-Ahx-$A\beta_{16-22}$ (**18**) and $A\beta^*_{16-22}$ (**19**) were synthesized using standard SPPS conditions on an automated solid-phase peptide synthesiser (CEM LibertyBlue) for $A\beta_{16-22}$ and TAMRA-Ahx-$A\beta_{16-22}$ or manually for $A\beta^*_{16-22}$. Manual peptide synthesis was performed in 4 mL vaculate reservoirs and PTFE taps with draining from a water aspirator. General methods for automated SPPS can be found in Section 4.3. DMF, dichloromethane (DCM) and diethyl ether (Et_2O) used in peptide synthesis was of ACS grade from Sigma-Aldrich. DMSO used for peptide stock solutions was purchased from Sigma-Aldrich and used without further purification. Peptide identify was confirmed by liquid chromatography and mass spectrometry (LCMS) was performed using an Agilent Technologies 1200 series LC and a Bruker HCT ultra ion-trap MS. High Performance Liquid Chromatography (HPLC) purification and analysis was performed as described in Section 4.4.

4.2. General methods for manual peptide synthesis

Method 1: Resin swelling

Low-loading (0.33 mmol/g) rink amide-MHBA resin (0.2 mM) was weighed out, placed in a vacuum reservoir with DMF (3 mL) and agitated for 2 h on a mechanical spinner (Bibby Scientific) at ambient temperature to swell the resin prior to use in the coupling steps.

Method 2: Deprotection of *N*-Fmoc-protected amino acid residues

N-terminal protecting groups were removed using 25% piperidine in DMF solution (5 x 2 mL x 2 min) and subsequent washing with DMF (5 x 2 mL x 2 min). Successful deprotection was checked using the Kaiser Test.

Method 3: Kaiser Test[1]

The Kaiser Test was used to check for successful deprotection and/or coupling for all residues. A small number of resin beads were removed from the vacuum reservoir and treated with a few drops of the following solutions (in the stated order):

1. Ninhydrin (5% w/v) in EtOH;
2. Phenol (80% w/v) in EtOH;
3. 1 mM $KCN_{(aq)}$ in pyridine (2% v/v).

The solution was heated to ca. 150 °C for 1 min. Successful coupling will produce no colour change, whereas a successful deprotection (in which the amino acid's *N*-terminal primary amine is revealed) will produce a bright blue colour.

Method 4: Amino acid coupling

For each step, 5 equivalents of the desired *N*-Fmoc-protected amino acid (e.g 1 mM based on 0.2 mM of resin) were coupled using oxyma (5 equivalents) and DIPEA (5 equivalents) in DMF (2 mL) for 2h. The first coupling onto the resin was performed using the same procedure. Due to the hydrophobic nature of the peptides, all amino acid residues were coupled twice to limit any amino acid deletions.

Method 5: *N*-terminal acetyl capping ($A\beta_{16-22}$ and $A\beta^*_{16-22}$)

The deprotected resin was washed with DMF (5 x 2 min x 2 mL), DCM (5 x 2 min x 2 mL) and Et_2O (5 x 2 min x 2 mL). Acetic anhydride (10 equivalents) and DIPEA (10 equivalents) were then added to the resin, which was agitated overnight on a mechanical spinner at room temperature.

Method 6: *N*-terminal TAMRA capping (TAMRA-Ahx-$A\beta_{16-22}$)

Prior to coupling of the fluorescent label a 6-aminohexanoic acid (6-Ahx) linker would be coupled using Method 4. For fluorescent labelling, TAMRA-COOH (5 equivalents) was dissolved in a solution of DMF (2 mL) containing oxyma (5 equivalents) and DIC (5 equivalents) then stirred for 10 mins. The pre-activated TAMRA solution was added to resin, which was agitated in the dark overnight on a mechanical spinner at room temperature.

Method 7: Cleavage

After elongation and subsequent *N*-terminal acetylation/TAMRA-Ahx labeling was complete, the resin would be washed with DMF (5 x 2 min x 2 mL), DCM (5 x 2 min x 2mL) and Et_2O (5 x 2 min x 2 mL). The resin was then treated with TFA:TIPS:H_2O (98:1:1, 2 mL x 2 h). The resulting solution was concentrated *in vacuo* and the crude product precipitated from ice-cold Et_2O (40 mL) and pelleted in a centrifuge (3000 x 2 min). The supernatants were removed and the crude product purified using preparative HPLC (with UV detection).

N.B- The methods outlined above were also used for “test” cleavages after the coupling of 3-4 amino acids residues to confirm, via LC-MS analysis, that the SPPS was proceeding as expected.

4.3. General methods for automated peptide synthesis

Automated solid-phase peptide synthesis was carried out on a LibertyBlue CEM Peptide synthesizer.[2] Peptides that were built using the synthesizer follow the same sequence of cycles as for manual SPPS, however, the introduction of coupling reagents, washing steps and each amino acid is controlled by a pre-programmed sequence designated by the user. To ensure successful coupling to the resin the first coupling step was always performed twice. The resin was placed into a clean 50 mL falcon tube and manually swelled in 50:50 DMF/DCM for 1 hour after which it was placed onto the synthesizer. The synthesis then continued by automated cycles of deprotection and coupling as follows:

- Deprotection: Resin is washed with DMF (15 mL) followed by deprotection with 20% piperidine in DMF solution (2 x 7 mL) at 75 °C and a final wash with DMF (15 mL).
- Coupling: The desired *N*-Fmoc-protected amino acid (5 equivalents), Oxyma (5 equivalents) and DIPEA (5 equivalents) in DMF (1.5 mL) were introduced to the reaction chamber for 4 mins at 75 °C.

After the SPPS had been completed (with a final *N*-Fmoc-deprotection) the resin would be removed from the synthesizer, placed in a 4 mL reservoir and washed with DMF (3 x 2 min x 2 mL), DCM (3 x 2 min x 2 mL) and Et_2O (3 x 2 min x 2 mL). *N*-terminal acetylation or TAMRA-labeling and subsequent cleavage from the resin would be carried out manually according the respective methods in Section 4.2.

4.4. General materials and methods for HPLC purification and analysis

Peptides were purified by preparative scale HPLC using an X-bridge C18 preparative column (reversed phase) on an increasing gradient of MeCN to H_2O (length = 100 mm, diameter = 19 mm, particle size = 5 µM) from Phenomenex; the pump, autosampler and fixed-wavelength UV detector were from Gilson. Crude peptides were dissolved in DMSO at an approximate concentration of 15 – 20 mg/mL^{-1} and injected into the column in 300 µL aquilots. The solvent gradient (either 5 – 95% or 5 – 50%, MeCN in

H_2O) was increased linearly over a 15 min run time at a flow rate of 10 mL/min^{-1}. The fixed-wavelength detector was set to scan the eluent at either 220, 254 or 270 nm with peak-based collection for 30 s after the diode was triggered. Fractions were analyzed by LC-MS (high mass method, as described in Section 4.1) and fractions containing the desired peptide were combined, concentrated under reduced pressure and lyophilized. The purity of the peptide samples was determined by the School of Chemistry HPLC service using an Ascentis Express C18 column (length = 10 mm, diameter = 2.1 mm, particle size = 2.7 µm; Supelco) with pump, autosampler and diode array detector all from Agilent.

4.5. General materials and methods for organic synthesis

Non-aqueous reactions were carried out in washed and oven-dried glassware. Solvents and reagents were used as received from major suppliers without prior purification unless stated. Anhydrous tetrahydrofuran (THF), ethanol (EtOH), acetonitrile (MeCN), dichloromethane (DCM) and diethyl ether (Et_2O) were obtained from the in-house solvent purification system from Innovative Technology Inc. PureSolv®. Anhydrous dimethyl formamide (DMF), methanol (MeOH) and chloroform ($CHCl_3$) were obtained from major chemical suppliers equipped with a SureSeal™ (or equivalent). For reactions under non-anhydrous conditions, the solvents used were of HPLC quality and provided by Fisher or Sigma-Aldrich. Water in aqueous solutions and used for quenching was deionised, and water used for buffers and HPLC was ultra-pure 18 MΩ from an ELGA Purelab system. Mixtures of solvents are quoted as ratios and correspond to a volume:volume ratio. Drying of organic extracts was performed using magnesium sulphate. Thin layer chromatography was performed on Merck Kieselgel 60 F254 0.25 mm precoated aluminium plates. Product spots were visualized under UV light (λ_{max} = 254 nm) and/or by staining with basic potassium permanganate. If any other TLC dip was used, it is stated under the specific experimental procedure. Flash chromatography was performed using silica gel 60 (0.043 – 0.063 mm VWR) using pressure by means of head bellows. ^{1}H NMR spectra were recorded on Bruker DPX 300 (300 MHz) or Avance 500 (500 MHz) spectrometers and referenced to either residual non-deuterated solvent peaks or tetramethylsilane. ^{1}H spectra are reported as follows: δ_H (spectrometer frequency, solvent): ppm to two decimal places (number of protons, multiplicity, *J* coupling constant in hertz, assignment). Chemical shifts are quoted in ppm with signal splitting recorded as singlet (s), doublet (d), triplet (t), quartet (q), quintet (quin.) multiplet (m), broad (br) and apparent (app.). Coupling constants, *J*, are measured to the nearest 0.1 Hz. Similarly, ^{13}C spectra are reported as follows: δ_C

(spectrometer frequency, solvent): ppm to one decimal place (assignment). Liquid Chromatography and Mass Spectrometry (LC-MS) was performed using an Agilent Technologies 1200 series LC and a Bruker HCT ultra ion-trap MS.

4.6 Synthesis of *N*-Fmoc protected TFMD-Phe

The synthesis of *N*-Fmoc protected TFMD-Phe was carried out according to the literature procedure originally developed by Fishwick and co-workers and improved upon by Smith and co-workers.[3,4] It should be noted that a change in protecting group has been implemented. All synthetic products were characterised using ^{1}H NMR and, if necessary to confirm the identity of the product, ^{13}C NMR, ESI-LC-MS (ESI-MS) or ESI-HRMS.

4-Bromobenzyl alcohol *O*-(tert-butyldiphenylsilyl) ether (21)[4]

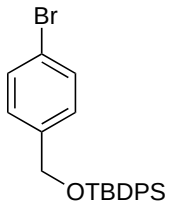

At ambient temperature and under an atmosphere of N_2, *tert*-butyldiphenylsilyl chloride (31 g, 166 mmol) was added to a stirred solution of 4-bromobenzyl alcohol (**17**, 44 g, 170 mmol) and imidazole (11.8 g, 173 mmol) in anhydrous DMF (100 mL). Stirring was continued for 18 h after which the reaction mixture was poured into H_2O (200 mL) and the crude product extracted with hexane (2 x 200 mL). The combined extracts were concentrated under reduced pressure and purified using column chromatography on silica gel (DCM) to afford the title compound as a white crystalline compound (61 g, 143 mmol, 87%). R_f: 0.6 (hexane); δ_H (500 MHz, $CDCl_3$) 7.55 (d, 2H, 2 x ArCH, J = 7.5 Hz), 7.29 (m, 5H, Ar), 7.23 (m, 5H, Ar), 7.07 (d, 2H, 2 x ArCH, J = 7.5 Hz), 4.57 (s, 2H, CH_2), 0.96 (s, 9H, ^{t}Bu); δ_c (125 MHz, $CDCl_3$) 140.1 (Ar*C*), 135.6 (Ar*C*), 133.4 (Ar*C*), 131.4 (Ar*C*), 129.9 (Ar*C*), 127.9 (Ar*C*), 120.7 (Ar*C*), 65.0 (Ar*C*H_2), 26.9 (^{t}Bu *C*H_3), 19.4 (^{t}Bu q. *C*).

_N,N_-diethyltrifluoroacetamide (22)[5]

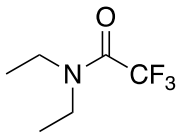

At 0 °C (iced water) and under an atmosphere of N_2, trifluoroacetic acid (7 mL, 45 mmol) in DCM (50 mL) was added slowly to a stirred solution of diethylamine (13 mL, 125 mmol). Stirring was continued for 18 h, during which time the reaction was allowed to warm to ambient temperature. The crude product was poured into DCM (200 mL), washed with saturated $NaHCO_3$ (2 x 200 mL), dried over $MgSO_4$ and concentrated under reduced pressure. The title compound was afforded without further purification (7.5 g, 44.3 mmol, 95%) as a yellow oil. R_f: 0.63 (DCM); δ_H (500 MHz, $CDCl_3$) 3.44 (m, 4H, 2 x CH_2), 1.24 (m, 6H, 2 x CH_3). δ_c (125 MHz, $CDCl_3$) 156.2 (q, J = 35 Hz, $COCF_3$), 116.6 (q, J = 286 Hz, CF_3), 41.8 (ethyl *C*), 41.4 (ethyl *C*), 13.8 (ethyl *C*), 11.9 (ethyl *C*); v_{max}/cm^{-1} (liquid film): 2983 (m), 1683 (s; amide I) and 1455 (m).

4-[*tert*-Butyldiphenylsiloxy)methyl]-2,2,2-trifluoroacetophenone (23)[4]

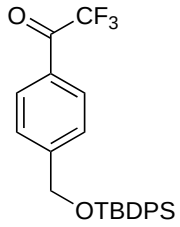

Under an atmosphere of N_2, a stirred solution of **21** (19.5 g, 46 mmol) in anhydrous THF (250 mL) was cooled to -78 °C (dry ice-acetone). *n*-Butyl lithium (1.6 M in hexane, 56.0 mL, 49 mmol) was added slowly and left to stir for 1 h. *N,N*-trifluoroacetamide (**22**, 11.7 g, 69 mmol) in anhydrous THF (50 mL) was added dropwise and the temperature maintained at -78 °C whilst the reaction stirred for a further 2 h. The reaction mixture was quenched by the dropwise addition of saturated aqueous NH_4Cl and poured into Et_2O (200 mL). The crude product was washed with saturated aqueous NH_4Cl (2 x 200 mL), H_2O (200 mL) and brine (200 mL), and dried over $MgSO_4$. The organic solvents were removed under reduced pressured to afford the title compound as an orange oil (19.1 g, 43 mmol, 94%). R_f: 0.5 (5:95 EtOAC:hexane); δ_H (500 MHz, $CDCl_3$) 7.99 (d, 2H, 2 x ArCH, J = 8.5 Hz), 7.63 (m, 5H, Ar), 7.46 (d, 2H, 2 x ArCH, J = 8.3 Hz), 7.31 (m, 5H, Ar), 4.78 (s, 2H, CH_2), 1.07 (s, 9H, ^{t}Bu). δ_c (125 MHz, $CDCl_3$) 171.5 ($COCF_3$), 149.7 (Ar*C*), 135.8 (Ar*C*), 132.9 (Ar*C*), 130.0 (Ar*C*), 129.9 (Ar*C*), 127.9 (Ar*C*), 118.7

(Ar*C*), 65.0 (Ar*C*H_2), 26.9 (^{t}Bu *C*H_3), 19.4 (^{t}Bu q. *C*). The *C*F_3 carbon and *C*OCF3 coupling were not observed.

4-[*tert*-Butyldiphenylsiloxy)methyl]-2,2,2-trifluoroacetophenone oxime (24)[4]

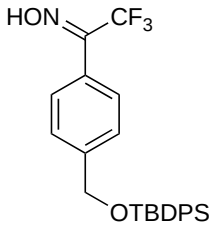

At 60 °C and under an atmosphere of N_2, hydroxylamine hydrochloride (6.0 g, 86 mmol) was added to a stirred solution of crude **23** (19.1 g, 43 mmol) in anhydrous EtOH (150 mL) and anhydrous pyridine (40 mL). Stirring was continued for 18 h under an atmosphere of N_2 at 60 °C, after which the organic solvents were removed under reduced pressure. The residue was dissolved in Et_2O (150 mL), washed with H_2O (2 x 100 mL), dried over $MgSO_4$ and concentrated under reduced pressure. The crude product was purified by column chromatography (2:1, DCM-hexane) to afford the title compound as an orange oil (15.9 g, 34 mmol, 80%). R_f: 0.65 (2:1 DCM:hexane); δ_H (300 MHz, $CDCl_3$) 8.48 (app. d, 1H, NOH, J_{app} = 6.0 Hz), 7.59 (m, 4H, ArCH), 7.30 (m, 10H, ArCH), 4.69 (app. d, 2H, CH_2, J_{app} = 6.0 Hz), 0.99 (s, 9H, ^{t}Bu). ESI-MS found: 456.7, $C_{25}H_{25}F_3NO_2Si$ requires 456.2 (negative ion mode).

4-[*tert*-Butyldiphenylsiloxy)methyl]-2,2,2-trifluoroacetophenone-*O*-(4-toluenesulphonyl) oxime (25)[4]

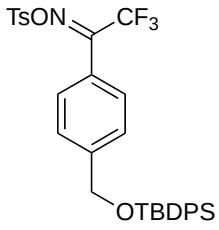

At 0 °C and under an atmosphere of N_2, *p*-toluenesulphonyl chloride (3.2 g, 17 mmol) was added to a stirred solution of **24** (5.5 g, 12 mmol), 4-(dimethylamino)pyridine (146 mg, 0.1 mmol) and anhydrous triethylamine (1.7 mL, 12 mmol) in anhydrous DCM (100 mL). The mixture was stirred for 3 h over which time the reaction was allowed to warm to room temperature. The crude product was washed with water (2 x 200 mL), dried over $MgSO_4$ and concentrated under reduced pressure. The product was purified using column chromatography on silica gel (10:90, EtOAc:hexane) to afford the title

compound (6.0 g, 9 mmol, 80%) as a orange oil. R_f: 0.7 (10:90, EtOAc:hexane); δ_H (500 MHz, $CDCl_3$) 7.94 (d, 2H, ArCH, J = 8.3 Hz), 7.71 (m, 4H, ArCH), 7.41 (m, 12H, ArCH), 4.84 and 4.82 (2 x s, 2H, 2 x CH_2), 2.51 and 2.49 (2 x s, 3H, 2 x $ArCH_3$), 1.14 and 1.11 (2 x s, 9H, 2 x ^{t}Bu).

3-[α-(*tert*-Butyldiphenylsiloxy)-4-tolyl]-3-trifluromethyl diaziridine (26)[4]

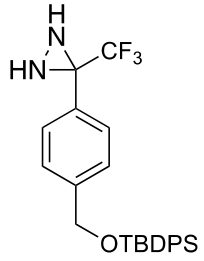

Under a N_2 atmosphere, gaseous NH_3 was condensed at -78 °C (dry ice-acetone) into a solution of **25** (6 g, 10 mmol) in anhydrous THF (50 mL) at -78 °C (dry ice-acetone). The total volume of NH_3 added was approximately 50 mL during the course of the reaction. Stirring was continued for 3 h after which it was allowed to warm to ambient temperature for 18 h, during which any residual NH_3 evaporated. The resulting mixture was filtered to remove a colourless precipitate and poured into Et_2O (150 mL), washed with H_2O (2 x 200 mL), dried over $MgSO_4$ and concentrated under reduced pressure. The product was purified using column chromatography on silica gel (DCM) to afford the title compound as a colourless oil (2.6 g, 5.7 mmol, 58%). R_f: 0.5 (9:1, DCM:hexane); δ_H (500 MHz, $CDCl_3$) 7.82 (d, 2H, ArCH, J = 8.2 Hz), 7.70 (m, 5H, ArCH), 7.40 (m, 5H, ArCH), 7.31 (d, 2H, ArCH, J = 8.2 Hz), 4.82 (s, 2H, CH_2), 2.82 (d, 1H, NH, J = 9.1 Hz), 2.25 (d, 1H, NH', J = 9.1 Hz), 1.1 (s, 9H, ^{t}Bu).

3-[α-(*tert*-Butyldiphenylsiloxy)-4-tolyl]-3-trifluromethyl diazirine (27)[4]

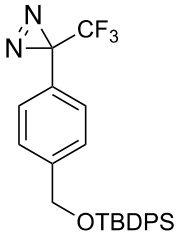

In a darkened fume hood and at ambient temperature, small portions of I_2 (3.1 g, 12 mmol) were added to a stirred solution of **26** (5.5 g, 12 mmol) and triethylamine (1.02 mL, 15 mmol) in MeOH (10 mL) until a deep red colour persisted. After stirring for a

further 30 mins the reaction mixture was neutralized with 10% (w/v) aqueous citric acid solution (checked with indicator paper) and quenched with 5% (w/v) aqueous sodium metabisulphite. The organic solvents were removed under reduced pressure and the residue was dissolved in Et_2O (100 mL), washed with H_2O (2 x 200mL), dried over $MgSO_4$ and concentrated under reduced pressure. The crude product was purified using column chromatography on silica gel (2:1, hexane:DCM) to afford the title compound as a colourless oil (4.7 g, 10 mmol, 86%). R_f: 0.3 (2:1, hexane:DCM); δ_H (500 MHz, $CDCl_3$) 7.81 (d, 2H, 2 x ArCH, J = 8.2 Hz), 7.51 (m, 5H, ArCH), 7.45 (m, 5H, ArCH), 7.24 (d, 2H, 2 x ArCH, J = 8.2 Hz), 4.73 (s, 2H, CH_2), 1.1 (s, 9H, ^{t}Bu); δ_c (125 MHz, $CDCl_3$) 142.9 (Ar*C*), 135.8 (Ar*C*), 132.9 (Ar*C*), 130.0 (Ar*C*), 129.9 (Ar*C*), 127.9 (Ar*C*), 121.1 (*C*F_3), 118.7 (Ar*C*), 64.9 (Ar*C*H_2), 28.3 (diazirine *C*), 26.9 (^{t}Bu *C*H_3), 19.4 (^{t}Bu q. *C*). *C*F_3 coupling and *C*O*C*F_3 were not observed.

4-[3-Triflouromethyl-3*H*-diazirine-3-yl)benzyl alcohol (28)[4]

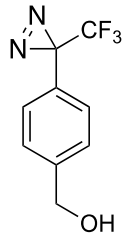

In a darkened fume hood, at ambient temperature and under a N_2 atmosphere, **27** (4.5 g, 9 mmol) was treated with 1M tetra-*n*-butylammonium fluoride in 95:5 THF-H_2O (13 mL, 11 mmol) in anhydrous THF (10 mL). The reaction was stirred at ambient temperature for 5 h, then poured into Et_2O (100 mL), washed with H_2O (2 x 200 mL), dried over $MgSO_4$ and concentrated under reduced pressure. The crude product was purified using column chromatography on silica gel (gradient elution, hexane in Et_2O, 0-80%) to afford the desired product as a colourless oil (720 mg, 3 mmol, 33%). R_f: 0.2 (2:1 hexane:Et_2O); δ_H (300 MHz, $CDCl_3$) 7.42 (d, 2H, 2 x ArCH, J = 8.4 Hz), 7.21 (d, 2H, 2 x ArCH, J = 8.4 Hz), 4.73 (s, 2H, CH_2).

3-[α-(iodo-4-tolyl]-3-trifluromethyl)-3H-diazirine (29)[4]

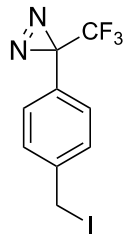

In a darkened fume hood, at ambient temperature and under a N_2, methyltriphenoxyphosphonium iodide (1.36 g, 3.4 mmol) was added to a stirred solution of **28** (370 mg, 1.7 mmol) in anhydrous MeCN (5 mL). The reaction was stirred at ambient temperature for 20 h, before being diluted with Et_2O (30 mL) and washed with NaOH (1 M, 2 x 20 mL) and H_2O (2 x 25 mL), dried over $MgSO_4$ and concentrated under reduced pressure. The crude product was purified using column chromatography on silica gel (2:1, hexane:Et_2O) to afford the desired product as a red solid (478 mg, 1.5 mmol, 88%). R_f: 0.67 (2:1, hexane:Et_2O); δ_H (500 MHz, $CDCl_3$) 7.44 (d, 2H, 2 x ArCH, J = 8.5 Hz), 7.13 (d, 2H, 2 x ArCH, J = 8.5 Hz), 4.43 (s, 2H, CH_2). δ_c (125 MHz, $CDCl_3$) 141.1 (Ar*C*), 129.2 (Ar*C*), 128.7 (Ar*C*), 126.9 (Ar*C*), 121.7 (q, J = 273 Hz, *C*F_3), 28.3 (q, J = 40 Hz, diazirine *C*), 3.69 (*C*H_2).

Nickel complexation of (S)-2-[*N*-(*N*'-benzylprolyl)amino]-benzophenone and glycine (30)[6]

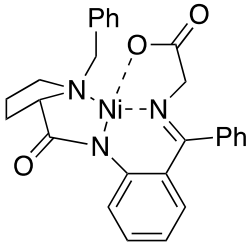

(S)-2-[*N*-(*N*'-benzylprolyl)amino]-benzophenone (2 g, 5 mmol), glycine (2 g, 26 mmol) and Ni (II) nitrate hexahydrate (3.1 g, 11 mmol) were dissolved in MeOH (30 mL). The reaction mixture was then warmed to 55 °C and stirred for 10 mins, followed by the addition of 25% (w/w) NaOMe in MeOH (10.1 mL, 44 mmol) with stirring continued for 1 h. AcOH (3.6 mL, 57 mmol) was added and the mixture refrigerated at 4 °C for 48 h (during which time excess Ni and any starting material precipitated). The resulting dark red solution was filtered and the filtrate concentrated under reduced pressure to afford the crude product as a dark red crystalline material. The crude product was purified using column chromatography on silica gel (5:1, $CHCl_3$:acetone) to afford the desired product as a dark red crystals (2.2 g, 4.5 mmol, 90%). R_f: 0.18 (5:1, $CHCl_3$:acetone); δ_H

(500 MHz, $CDCl_3$) 8.29 (app. d, 1H, 2 x ArCH, *J* = 10 Hz), 8.08 (app. d, 2H, 2 x ArCH, J_{app} = 10 Hz), 7.52 (m, 3H, ArCH), 7.44 (m, 2H, ArCH), 7.34 (m, 1H, ArCH), 7.22 (m, 1H, ArCH), 7.10 (app. d, 1H, ArCH, J_{app} = 10 Hz), 6.92 (m, 1H, ArCH), 6.81 (d, 1H, ArCH, *J* = 10 Hz), 6.70 (m, 1H, ArCH), 4.50 (d, 1H, benzylic CHH', *J* = 10.0 Hz), 3.81 (s, 1H, benzylic CHH', *J* = 10.0 Hz), 3.77 (s, 1H, NCHPh), 3.71 (s, 2H, 2x Gly αH), 3.67 (m, 1H, Pro δHH'), 3.48 (m, 1H, Pro αH), 3.37 (m, 1H Pro γHH'), 2.58 (m, 1H, Pro βHH'), 2.45 (m, 1H, Pro βHH'), 2.17 (m, 1H, Pro δHH'), 2.08 (m, 1H Pro γHH'). ESI-MS found: m/z 498.1 [$M+H^+$], $C_{27}H_{26}N_3NiO_3$ requires 498.1.

Alkylation of Ni-complex with 3-[α-(iodo-4-tolyl]-3-trifluromethyl)-3H-diazirine (31)[4]

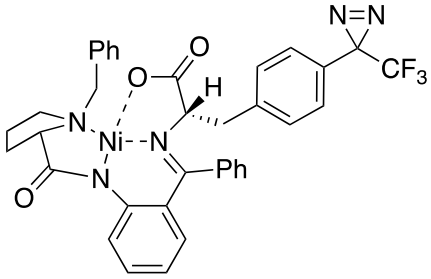

In a darkened fume hood and under a N_2 atmosphere, Ni-complex **30** (350 mg, 1.1 mmol) and vacuum dried, powdered NaOH (141 mg, 3.5 mmol) were dissolved in anhydrous MeCN (5 mL) at -22 °C (MeOH:ice). To this mixture, **29** (350 mg, 1.1 mmol) was added and the reaction stirred for 18 h, during which time the reaction mixture was allowed to warm to ambient temperature. Et_2O (20 mL) was added and the crude product washed with 1 M NaOH (2 x 20 mL) and H_2O (2 x 20 mL), dried over $MgSO_4$ and concentrated under reduced pressure. The crude product was purified using column chromatography on silica gel (9:1, $CHCl_3$:acetone) to afford the desired product as a glassy red solid (700 mg, 1.0 mmol, 94%). R_f: 0.6 (9:1, $CHCl_3$:acetone); δ_H (500 MHz, $CDCl_3$) 8.27 (app. d, 1H, 2 x ArCH, *J* = 5 Hz), 8.02 (app. d, 2H, 2 x ArCH, J_{app} = 10 Hz), 7.73 (m, 2H, Phe ArCH), 7.58 (m, 3H, ArCH), 7.45 (m, 2H, ArCH), 7.33 (m, 1H, ArCH), 7.22 (m, 1H, ArCH), 7.19 (m, 2H, Phe ArCH), 7.09 (app. d, 1H, ArCH, J_{app} = 10 Hz), 6.92 (m, 1H, ArCH), 6.69 (d, 1H, ArCH, *J* = 10 Hz), 6.70 (m, 1H, ArCH), 4.38 (d, 1H, benzylic CHH', *J* = 10 Hz), 4.26 (s, 1H, Phe αH), 3.51 (s, 1H, benzylic CHH', *J* = 10 Hz), 3.77 (s, 1H, NCHPh), 3.67 (m, 1H, Pro δHH'), 3.48 (m, 1H, Pro αH), 3.37 (m, 1H Pro γHH'), 3.08 (m, 1H, Phe βHH'), 2.87 (m, 1H, Phe βHH'), 2.58 (m, 1H, Pro βHH'), 2.27 (m, 1H, Pro βHH'), 1.91 (m, 1H, Pro δHH'), 1.71 (m, 1H Pro γHH'). ESI-HRMS found: m/z 696.1747 [$M+H^+$], $C_{36}H_{31}N_5NiO_3F_3$ requires 696.1732.

(*S*)-3-[4-[3-(trifluoromethyl)-3H-diazrinin-3-yl]phenyl]alanine (15)[4]

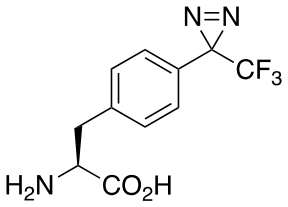

In a darkened fume hood, a stirred solution of **31** (700 mg, 1.0 mmol) and 1.2 M HCl (aq, 16 mL, 19.2 mmol) in MeOH (30 mL) was heated at reflux until a complete colour change (from red to yellow) was observed. The reaction mixture was allowed to cool to ambient temperature at which point the MeOH was removed under reduced pressure. The aqueous residue was washed with $CHCl_3$ (2 x 50 mL) and the combined washings extracted with H_2O (3 x 25 mL) and then combined. The aqueous fractions were then adsorbed onto Dowex 50WX2-110 H^+ resin exchange resin (15 g). The resin was washed with H_2O (100 mL), MeOH (100 mL) and the desired compound eluted with saturated NH_3 in MeOH (150 mL). Fractions that were positive against ninhydrin were combined and concentrated under reduced pressure to afford the desired product as an off-white solid (215 mg, 0.8 mmol, 78%). R_f: 0.7 (5:3:1, $CHCl_3$:MeOH:AcOH); δ_H (500 MHz, CF_3COOD) 7.41 (d, 2H, 2 x ArH, J = 8.1 Hz), 7.31 (d, 2H, 2 x ArH, J = 8.1 Hz), 4.82 (m, 1H, Phe αH), 3.66 (dd, 1H, Phe βHH', J = 14.5 and 4.7 Hz), 3.44 (dd, 1H, Phe βHH', J = 15.8 and 9.6 Hz). ESI-MS found 274.2, $C_{11}H_{11}F_3N_3O_2$ requires 274.1.

(*S*)-*N*-(9-Fluorenylmethoxycarbonyly)-[4-[3-(trifluoromethyl)-3H-diazrinin-3-yl]phenyl]alanine (32)[4]

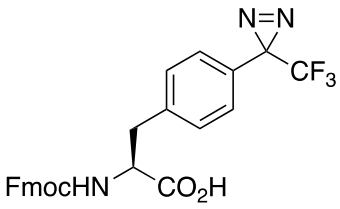

In a darkened fume hood, *N*-(9-Fluorenylmethoxycarbonyloxy) succinimide (137 mg, 0.4 mmol) was added slowly to a stirred suspension of **15** (100 mg, 0.36 mmol) and $NaHCO_3$ (93 mg, 1.1 mmol) at 0 °C in H_2O (4 mL) and acetone (1 mL). The reaction mixture was left to stir for 48 h after which it was poured into 1 M HCl (aq, 30 mL) and the crude product was extracted with $CHCl_3$ (3 x 25 mL) and concentrated under reduced pressure. The residue was then redissolved in EtOAc (20 mL), washed with 1 M HCl (aq, 100 mL), H_2O (100 mL), brine (100 mL), dried over $MgSO_4$ and concentrated under reduced pressure. The crude product was purified using column

chromatography on silica gel (gradient elution, MeOH in $CHCl_3$, 0-10%) to afford the desired product as an off-white solid (75 mg, 0.2 mmol, 50%). R_f: 0.2 (9:1, DCM:MeOH); δ_H (500 MHz, $CDCl_3$) 7.79 (d, 2H, ArCH, *J* = 7.5 Hz), 7.64 (d, 2H, ArCH, *J* = 7.5 Hz), 7.39 (m, 8H, ArCH), 5.20 (d, 2H, NH_2, *J* = 7.0 Hz), 4.60 (m, 1H, Phe αH), 4.38 (m, 1H, Fmoc C<u>H</u>H'), 4.25 (m, 1H, Fmoc CH<u>H</u>'), 4.17 (t, 1H, Fmoc CH, *J* = 6.5 Hz), 3.26 (dd, 1H, Phe β<u>H</u>H', *J* = 9.0 and 14.0 Hz), 3.15 (dd, 1H, Phe βH<u>H</u>', *J* = 6.5 and 14.5 Hz).

4.7 Materials for self-assembly experiments

All peptides were synthesised and purified as described above. HFIP was purchased from AlfaAesar. Ammonium bicarbonate was of mass spectrometry grade and purchased from Sigma-Aldrich. Buffers were made using 18 MΩ H_2O from the system described in Section 4.17 and sterile filtered (0.22 μm) prior to use in any self-assembly reaction. All eppendorfs and pipette tips (Gilson) were autoclaved (Prestige Benchtop Medical Autocalve) to prevent bacterial contamination. Carbon-formvar coated copper grids for TEM were purchased from Agar Scientific and activated at 254 nm for 30 mins prior to use.

4.8. Aggregation protocol for $A\beta_{16\text{-}22}$ phase diagram

$A\beta_{16\text{-}22}$ was diluted from a DMSO stock solution (1 – 30 mM) to the required concentration (10 – 300 μM) in 100 mM ammonium bicarbonate buffer (pH 7). Final DMSO concentration was kept at 1% (v/v) in all assays. After a week, aliquots were taken for TEM analysis (Section 4.9). If no fibrils were observed, the samples were left to incubate for another week. Conditions under which $A\beta_{16\text{-}22}$ did not form visible fibrils (using extensive TEM analysis) after two weeks were counted as those under which fibrils do not form.

4.9. General method for TEM analysis

TEM images were taken at the end of each experiment by removing 5 μL from the necessary well/eppendorf and incubated on carbon-formvar grids for 30 s prior to staining with 2% (w/v) uranyl acetate solution for an additional 30s. Images were taken on a JEM-1400 (JEOL Ltd., Toyko, Japan) or an Tecnai T12 (FEI, Oregon, USA)

transmission electron microscopes. Images were taken using either a ATM CCD camera or a Gatan Ultrascan 1000 XP (994) CCD camera (JEM-1400) or an Ultrascan 100XP (994) CCD camera (Tecnai F12). Once taken, images were processed using ImageJ (NIH).

4.10. General method for fluorescence quenching assays

Wild type $A\beta_{16-22}$ was spiked with TAMRA-Ahx-$A\beta_{16-22}$ at different percentages (100 – 1% for end-point assays, 5% for kinetic quenching assays) and incubated in 100 mM ammonium bicarbonate, pH 7 with a final concentration of 2% DMSO (v/v). The total peptide concentration was 40 μM. Samples were placed in quartz cuvettes (Helma QS Quartz, 1 cm path length) and analysed using a temperature controlled (Quantum Northwest PC425 Peltier controller) Quantamaster fluorimeter (Photon Technical Industries, Canada) at 37 °C. Kinetic measurements were taken every 30 s for the duration of the experiment (in triplicate) and TEM images were taken at the end of each experiment to ensure the presence of fibrils. The TAMRA fluorophore was excited at 520 nm and emission recorded at 600 nm to reduce the inner filter effect. Slit widths were 0.3 nm for excitation and 5 nm for emission

4.11. General protocol for PIC experiments

$A\beta^*_{16-22}$ (40 μM) was incubated in eppendorf tubes at 37 °C in 100 mM ammonium bicarbonate with a final volume of 1% DMSO (v/v) for either 5 mins, 1 h, 24 h or 2 weeks in the dark (as described in Section 4.7). Samples were then irradiated for 1 min using a home built LED lamp (see Appendix 4) at 365 nm, lyophilized overnight, taken up in hexafluoroisopropanol (HFIP, 100 μL) and left overnight to ensure any aggregates were disrupted. HFIP was then removed under a gentle stream of N_2 and the cross-linked products taken up in 50:50 H_2O/MeCN + 0.1% formic acid to a final concentration of ~40 μM and analysed using ESI-IMS-MS/MS.

4.12 Materials for ESI-IMS-MS

All organic solvents and mass spec grade H_2O were purchased from Fisher Scientific. Sodium Iodide was purchased from Sigma-Aldrich.

4.13. ESI-IMS-MS Instrumentation

All samples were prepared as described above (Section 4.11). A Synapt HDMS quadrupole time-of-flight mass spectrometer (Micromass UK Ltd., Waters Corporation, Manchester, UK), equipped with a Triversa NanoMate (Advion Biosciences, Ithaca, NY, USA) automated nano-ESI interface was used for all cross-linking and IMS experiments. The NanoMate contains both an autosampler and nano-electrospray source through which the sample is delivered into the mass spectrometer. The instrument has a travelling-wave IMS device situated in-between the quadrupole and the time-of-flight analysers. The ion-mobility cell contains three sections connected in series: a trap ion guide, the drift-tube and a transfer ion guide. Samples were analysed by positive ionisation nanoESI (nESI) with a capillary voltage of 1.7 kV and a N_2 nebulising gas pressure of 0.8 psi. The following instrument parameters were used: cone voltage 60 °C; source temperature 60 °C; backing pressure 4.7 mbar, ramped travelling speed 7 – 20 V; travelling wave speed 400 ms^{-1}; IMS N_2 gas flow 20 mL min^{-1}; IMS cell pressure 0.55 mbar. The m/z scale was calibrated with aq. NaI cluster ions. Data were processed by use of MassLynx v4.1 and Driftscope software supplied with the mass spectrometer.

4.14. Protocol for ESI-IMS-MS/MS analysis of cross-linked products

To perform the MS/MS sequencing, the quadrupole was operated in resolving mode. The required ion was isolated based on m/z ratio in the quadrupole. After the ions had passed through the trap ion guide and IMS cells, the transfer ion guide voltage would be increased from 2 V to 40 V, causing the ions to fragment prior to entering the time-of-flight mass analyser. By fragmenting the ions in this manner, doubly charged dimers and singly charged monomers with the same m/z ratio can be isolated and analysed.

4.15 Protocol for ThT fluorescence assays

Samples were prepared in a 96-well non-binding plate (Corning Costar 3881, Corning Life Sciences, Amsterdam, The Netherlands) sealed with clear sealing film (BMG Labtech, Aylesbury, Bucks, UK) and were incubated in a FLUOstar OPTIMA plate reader (BMG Labtech, Aylesbury, Bucks, UK) for 20 hours at 37 °C without agitation. Samples had a volume of 95 µL containing 10 µM ThT in 100 mM ammonium bicarbonate, pH 7, and a final concentration of 1% (v/v) DMSO. $A\beta_{16-22}$ was taken from

a DMSO stock and lyophilised $A\beta_{40}$ (kindly provided by Dr Katie Stewart) was dissolved in 100 mM ammonium bicarbonate buffer and kept on ice prior to use (to limit aggregation). For seeding experiments, $A\beta_{16-22}$ was incubated at 50 μM for at least 24 hours in the same buffer as described above with the presence of fibrils confirmed by Transmission Electron Microscopy (TEM, described above). Prior to the assay, the fibrils were probe sonicated for 5 s at 22% amplitude to generate “seeds”. For assays that compared the effect of sonication and non-sonication, fibril samples were treated incubated in the manner described above, however, one sample of preformed $A\beta_{16-22}$ fibrils would be sonicated (using the settings described above) and the other would be introduced into the assay without sonication. The ThT experiments used excitation and emission filters of 430 and 485 nm. Each ThT experiment shown was repeated in independent assays on three different occasions with the traces shown in the main body of the text representative of all repeats (which can be found in Appendix 8).

4.16 Protocol for fluorescence quenching assays with a 1:1 (mol:mol) ratio of $A\beta_{16-22}/A\beta_{40}$

Wild type $A\beta_{16-22}$ was spiked with 5% TAMRA-Ahx-$A\beta_{16-22}$ and mixed with $A\beta_{40}$ at a 1:1 (mol:mol) ratio and incubated in 100 mM ammonium bicarbonate, pH 7 with a final concentration of 2% DMSO (v/v). The total peptide concentration was 40 μM. Samples were placed in quartz cuvettes (Helma QS Quartz, 1 cm path length) and analysed using a temperature controlled (Quantum Northwest PC425 Peltier controller) Quantamaster fluorimeter (Photon Technical Industries, Canada) at 37 °C. Kinetic measurements were taken every 30 s for the duration of the experiment (in triplicate) and TEM images were taken at the end of each experiment to ensure the presence of fibrils. The TAMRA fluorophore was excited at 520 nm and emission recorded at 600 nm to reduce the inner filter effect. Slit widths were 0.3 nm for excitation and 5 nm for emission.

4.17 General sedimentation protocol

Samples were taken at the desired time point and centrifuged (20 mins, 14,000 g, 4 °C). Each sample was then separated into pellet and supernatant fractions, lyophilised overnight and disaggregated in hexafluoroisopropanol (HFIP) for at least 2 hours. The HFIP was removed under a stream of N_2 and the peptides were taken up in DMSO prior to analysis by high-resolution mass spectrometry (Bruker HCT ion-trap MS).

4.18 Method for collision cross-section (CCS) calibration

For all native ESI-IMS-MS experiments, the instrumentation and setting described in section 4.13 were used. Collision cross-section (CCS, Ω) measurements were estimated by use of a calibration obtained by analysis of denatured proteins (cytochrome c, ubiquitin and alcohol dehydrogenase) and peptides (tryptic digests of alcohol dehydrogenase and cytochrome C) with known CCSs obtained elsewhere from drift tube ion mobility measurements.[7,8] The proteins were denatured in 50:50 H_2O:MeCN + 0.1% formic acid prior to introduction to the mass spectrometer. The CCS (Ω) of the peptide monomers/oligomers was then calculated according to equation below:

$$\Omega\left(\text{Å}^2\right) = \text{A} \times (t_D)^B \times z \times \sqrt{\frac{1}{m_{ion}} + \frac{1}{m_{gas}}}$$

where A is the determined calibration constant, *z* is the charge state of the ion, *B* is the exponential factor (determined experimentally), t_D is the corrected absolute drift time, m_{ion} is the mass of the ion and m_{gas} is the mass of the gas used in the ion-mobility cell (N_2). Data were processed by use of MassLynx v4.1 and Driftscope softwave supplied with the mass spectrometer.

4.19 General protocol for PIC experiments with a 1:1 (mol:mol) ratio of Aβ*$_{16-22}$/Aβ$_{40}$

Aβ*$_{16-22}$ (20 μM) and Aβ$_{40}$ (20 μM) were incubated in eppendorf tubes at 37 °C in 100 mM ammonium bicarbonate with a final volume of 1% DMSO (v/v) for either 5 mins or 24 h, in the dark (as described in Section 4.7). Samples were then irradiated for 1 min using a home built LED lamp (see Appendix 4) at 365 nm, lyophilized overnight, taken up in hexafluoroisopropanol (HFIP, 100 μL) and left overnight to ensure any aggregates were disrupted. HFIP was then removed under a gentle stream of N_2 and the cross-linked products taken up in 50:50 H_2O:MeCN + 0.1% formic acid to a final concentration of ~40 μM and analysed using ESI-IMS-MS/MS (described in Section 4.14).

References:

1 E. Kaiser, R. L. Colescott, C. D. Bossinger and P. I. Cook, *Anal. Biochem.*, 1970, **34**, 595–598.

2 J. M. Collins, K. A. Porter, S. K. Singh and G. S. Vanier, *Org. Lett.*, 2014, **16**, 940–943.

3 C. W. G. Fishwick, J. M. Sanderson and J. B. C. Findlay, *Tetrahedron Lett.*, 1994, **35**, 4611–4614.

4 D. P. Smith, J. Anderson, J. Plante, A. E. Ashcroft, S. E. Radford, A. J. Wilson and M. J. Parker, *Chem. Commun.*, 2008, 5728–5730.

5 J. Robson and J. Reinhart, *J. Am. Chem. Soc.*, 1955, **77**, 245.

6 Y. N. Belokon, A. G. Bulychev, S. V. Vitt, Y. T. Struchkov, A. S. Batsanov, T. V. Timofeeva, V. A. Tsyryapkin, M. G. Ryzhov, L. A. Lysova, V. I. Bakhmutov and V. M. Belikov, *J. Am. Chem. Soc.*, 1985, **107**, 4252–4259.

7 D. P. Smith, T. W. Knapman, I. Campuzano, R. W. Malham, J. T. Berryman, S. E. Radford and A. E. Ashcroft, *Eur. J. Mass Spectrom.*, 2009, **15**, 113.

8 S. J. Valentine, A. E. Counterman and D. E. Clemmer, *J. Am. Soc. Mass Spectrom.*, 1999, **10**, 1188–1211.

Appendix 1- Supplementary HPLC and HRMS data

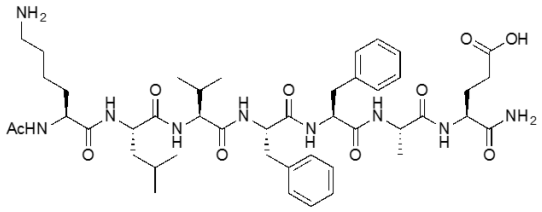

Exact mass: 893.50 Da
Molecular Formula: $C_{45}H_{67}N_9O_{10}$

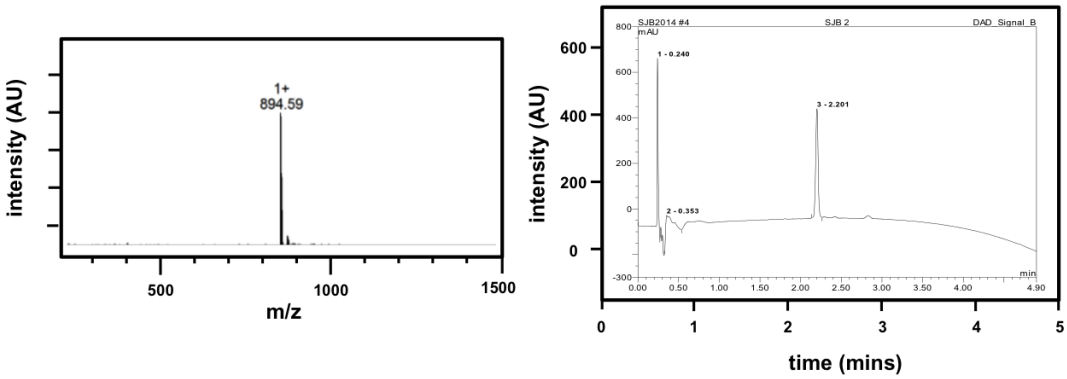

Figure 72. HRMS and HPLC of WT $A\beta_{16\text{-}22}$.

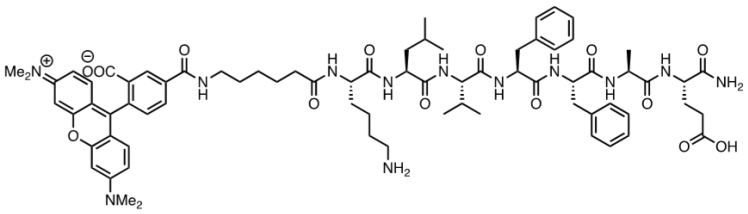

Exact mass: 1376.72 Da
Molecular Formula: $C_{74}H_{96}N_{12}O_{14}$

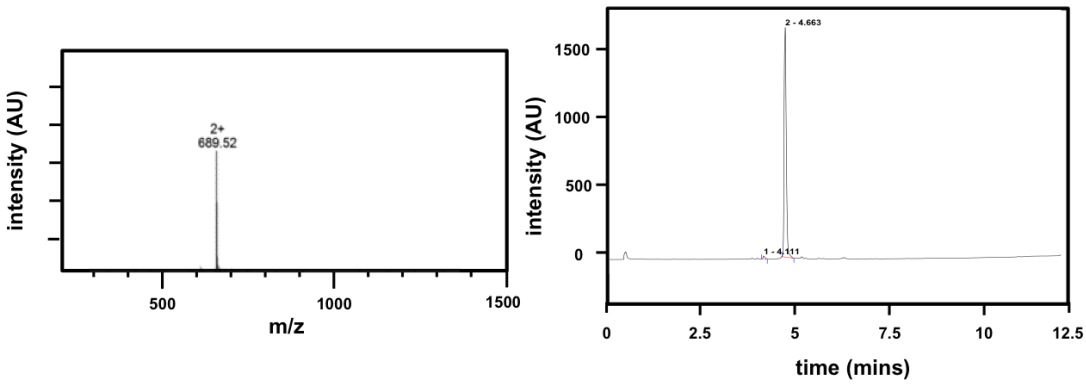

Figure 73. HRMS and HPLC of TAMRA-Ahx-$A\beta_{16\text{-}22}$.

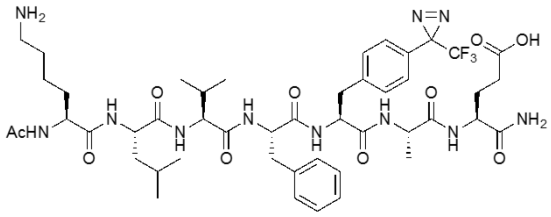

Exact mass: 1001.49 Da
Molecular Formula: $C_{47}H_{66}F_3N_{11}O_{10}$

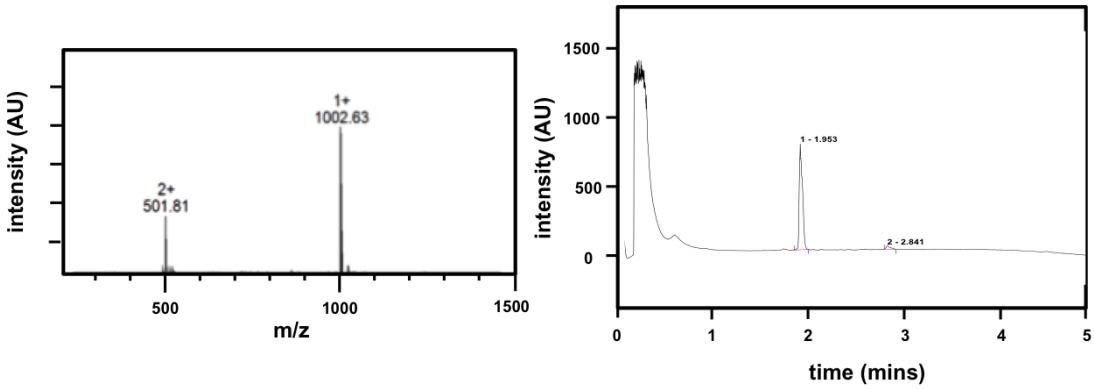

Figure 74. HRMS and HPLC of Aβ*$_{16-22}$.

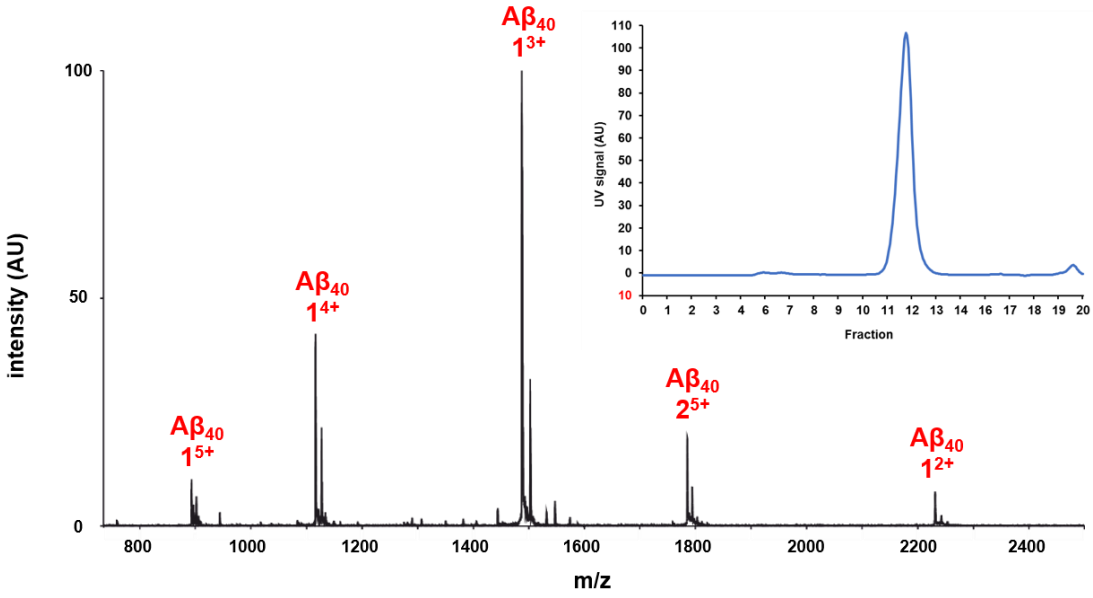

Peak	m/z expected	m/z observed
1^{2+}	2230.60	2230.84
1^{3+}	1487.40	1487.42
1^{4+}	1115.80	1115.81
1^{5+}	892.84	892.85
2^{5+}	1784.68	1784.92

Figure 75. HRMS and size exclusion chromatography of $A\beta_{40}$, indicating that it is a single peak prior to introduction into any kinetic assays.

Appendix 2- Supplementary tandem MS/MS spectra

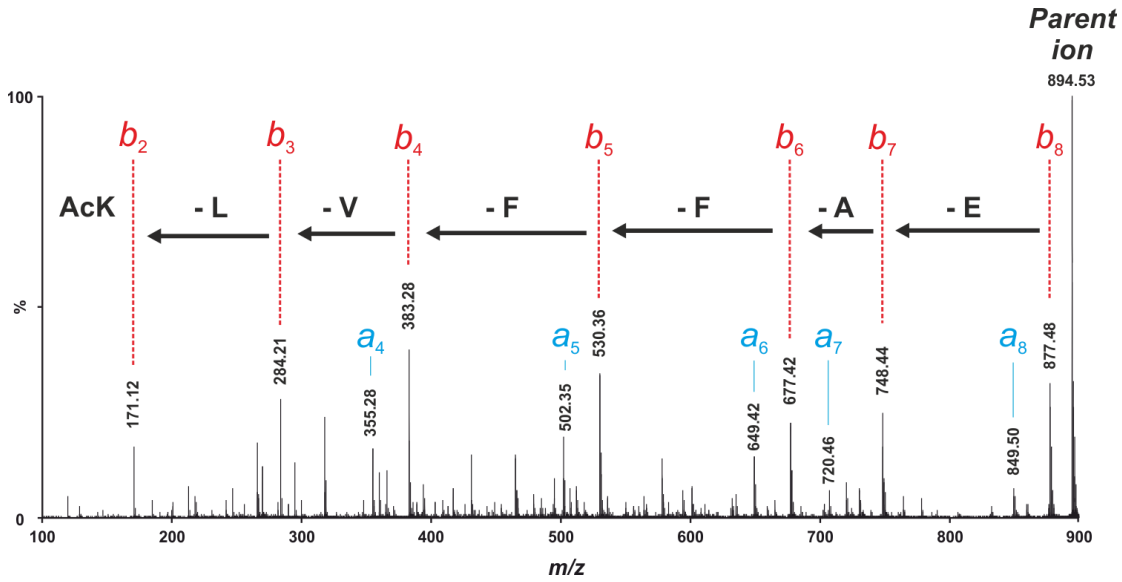

Figure 76. Tandem MS/MS spectra of WT $A\beta_{16\text{-}22}$.

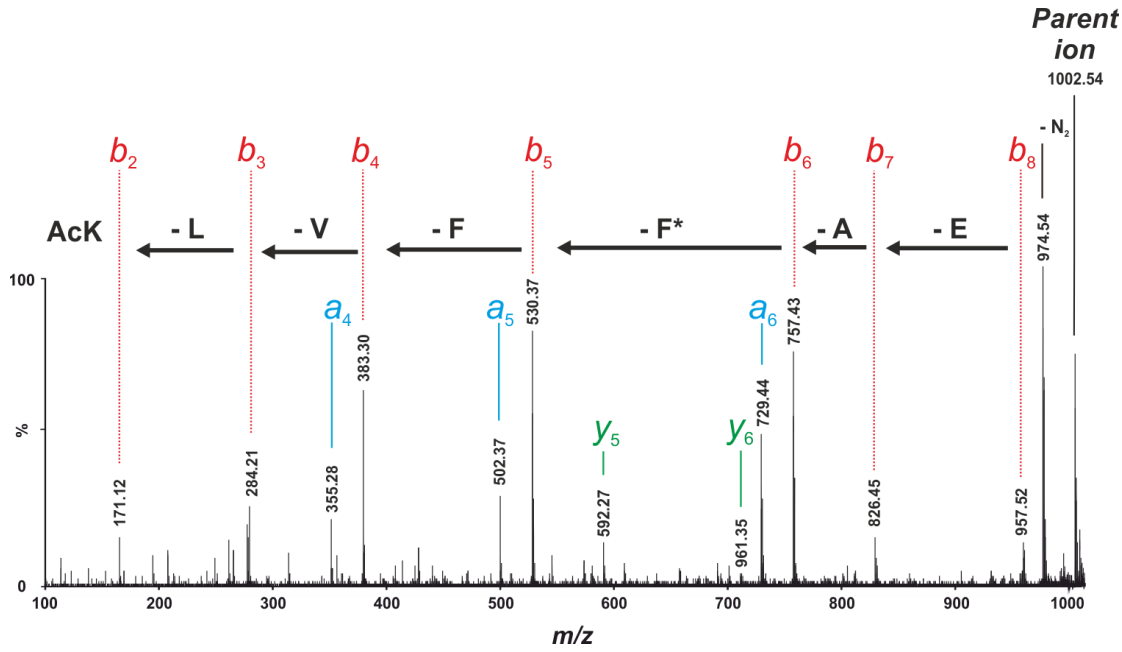

Figure 77. Tandem MS/MS spectra of $A\beta^*_{16\text{-}22}$.

Appendix 3- Supplementary fluorescence quenching data

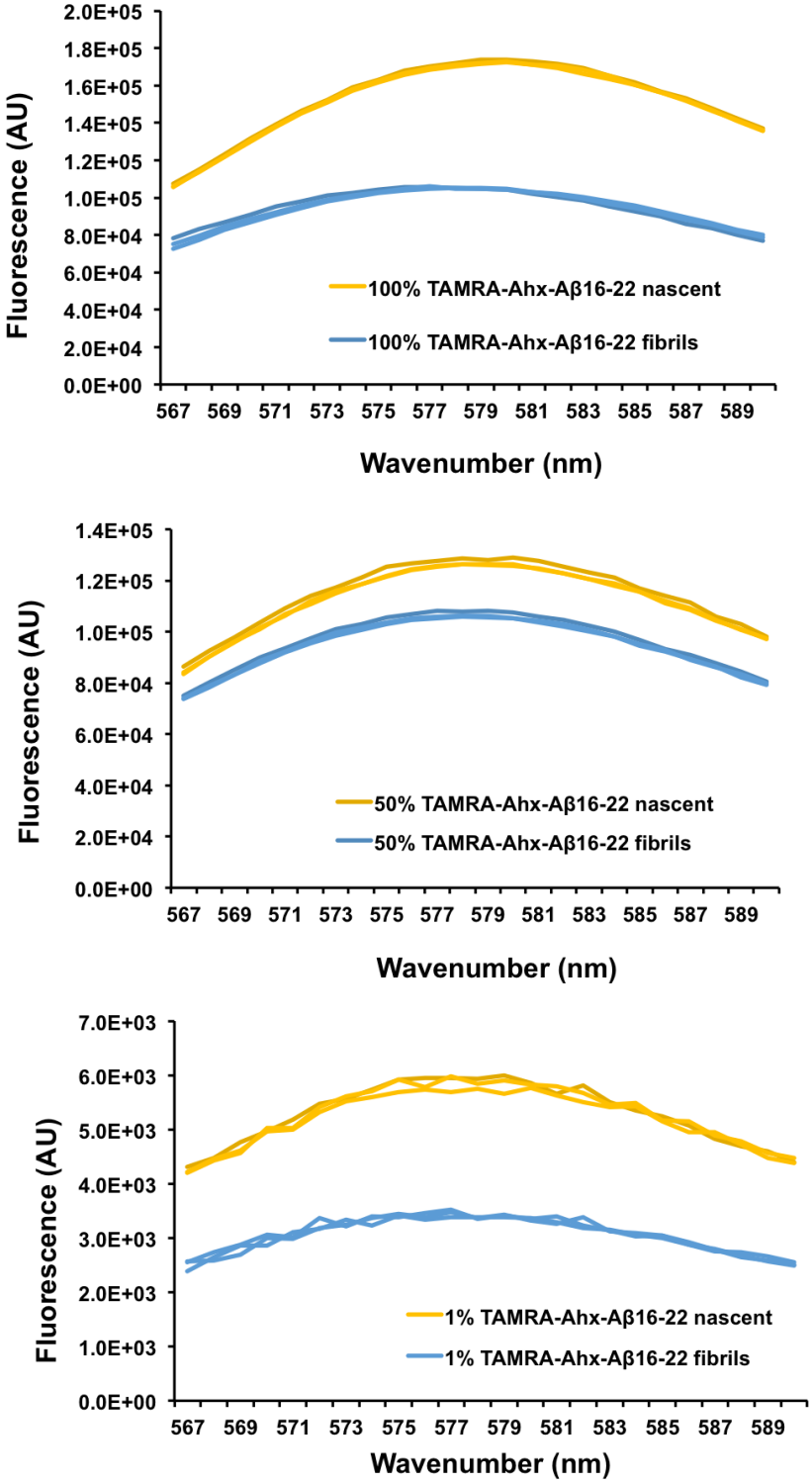

Figure 78. Fluorescence quenching end-points with either 100% (top), 50% (middle) and 1% (bottom) TAMRA-Ahx-$A\beta_{16-22}$ spiked in to WT $A\beta_{16-22}$.

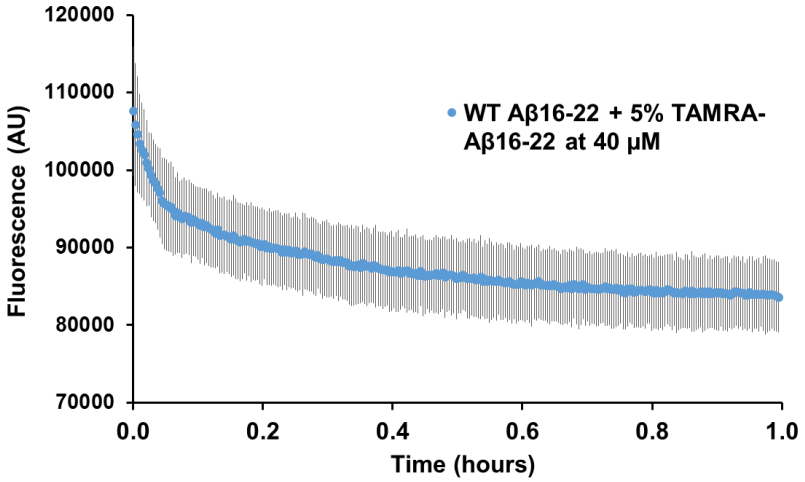

Figure 79. Supplementary fluorescence quenching data for TAMRA-Ahx-$A\beta_{16-22}$ spiked in to WT $A\beta_{16-22}$.(5%, total peptide concentration 40 μM).

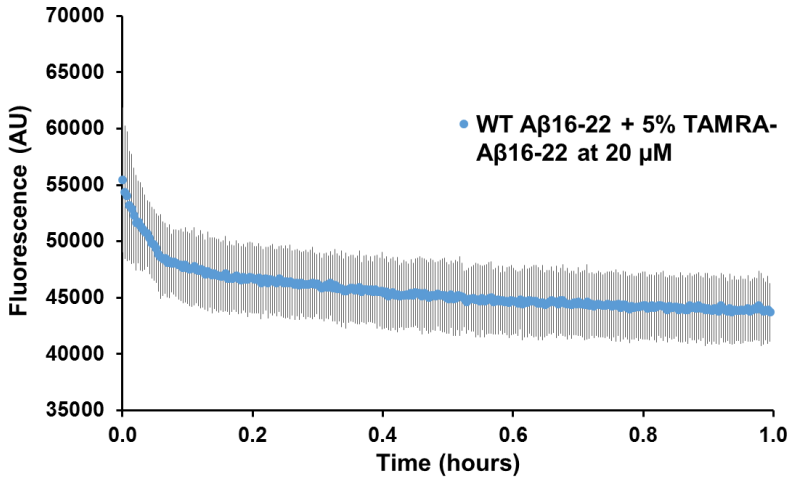

Figure 80. Supplementary fluorescence quenching data for TAMRA-Ahx-$A\beta_{16-22}$ spiked in to WT $A\beta_{16-22}$.(5%, total peptide concentration 20 μM).

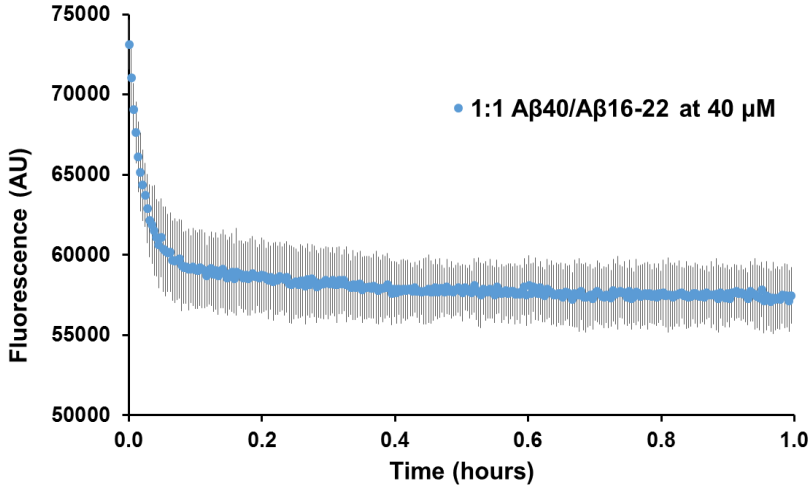

Figure 81. Supplementary fluorescence quenching data for TAMRA-Ahx-$A\beta_{16-22}$ spiked in to WT $A\beta_{16-22}$ (5%) with a 1:1 ratio of $A\beta_{40}$ (total peptide concentration 40 μM).

Appendix 4- Description of LED crosslinking lamp

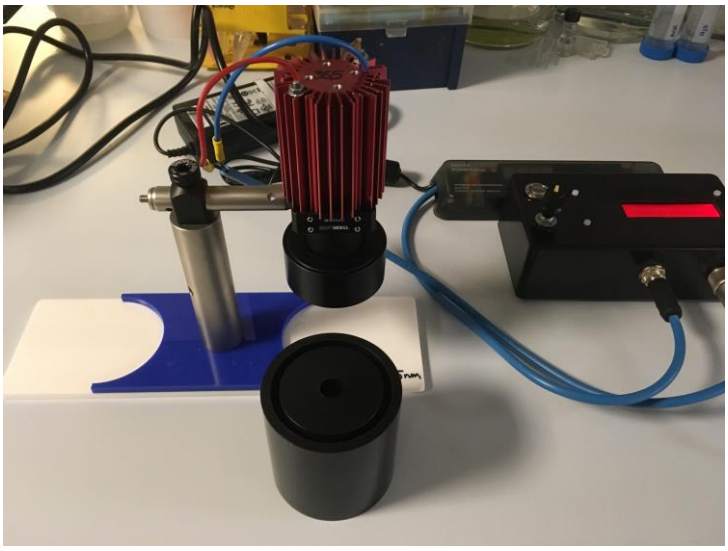

Figure 82. The LED cross-linking set-up used in this work. The lamp was home built (Professor Nik Kapur and Mark Levenstein, University of Leeds) and the image was taken by Jim Horne (University of Leeds).

The UV lamp consisted of a 4 UV LED array that was mounted on a standard star circuit board (Led Engin, part LZ4-44UV00-0000, peak wavelength 365 nm, radiant flux 4.1 W, viewing angle 110°). This was attached to a heat sink (DragonStar part ILA-HSINK-STAR-50X60MM-BLK-K) to dissipate heat from the LED array. A lens was attached to the front of the lamp (Thorlabs CP02T/M) and attached to the heatsink with two threaded bars (M3 thread), to which a lens tube (Thorlabs SM1L20) was attached. A condenser lens (Thorlabs ACL2520U-A, Ø25 mm, f = 20.1 mm, NA = 0.60), located within this lens tube, was used to focus the light to a 6 mm spot. As a guide, the centre of the lens was positioned ~20 mm from the LED and ~25 mm from the sample. Power was provided by a dedicated constant current LED controller (eldoLED PWR180D1) regulated to 1000 mA output current. In turn this was powered from a standard desktop power supply with an output of 19 V. The duration of illumination was controlled by a timer-box which controlled a relay that made or broke the circuit between the controller and LED. The sample was held in an Eppendorf tube that was located in a block below the LED lamp. The lamp was built by Professor Nik Kapur and Mark Levenstein (University of Leeds).

Appendix 5- Notation for MS/MS sequencing

Figure 83. Nomenclature for tandem MS/MS sequencing for $A\beta_{16-22}$, based on the Roepstroff-Fohlman-Biemann convention (see references in Chapter 2).

Appendix 6- Fragmentation calculator

The possibility of double fragmentation required the building of a generic fragment calculator in Microsoft Excel 2007 (built by George W Preston). This calculator is built for $A\beta_{16-22}$ and allows the user to enter the identity of the moiety on the relevant F residue (in this case F20). All other residues are treated as constants and as fragments were isolated as $[fragment + 2H]^{2+}$ or $[fragment + H]^{+}$ ions, only these products were calculated. The calculator takes the mass of the dimer and sequentially removes amino acids residues (and losses of ammonia and water), generating the predicted masses for the fragment ions (a, b, c, x, y and z, see Appendix 5 for an explanation of the notation).The output from the calculator is given in 8 x 8 tables and also calculates the possible fragmentation products based on pairwise combinations of N-C_α, C_α-O and other amide backbone fragmentations.

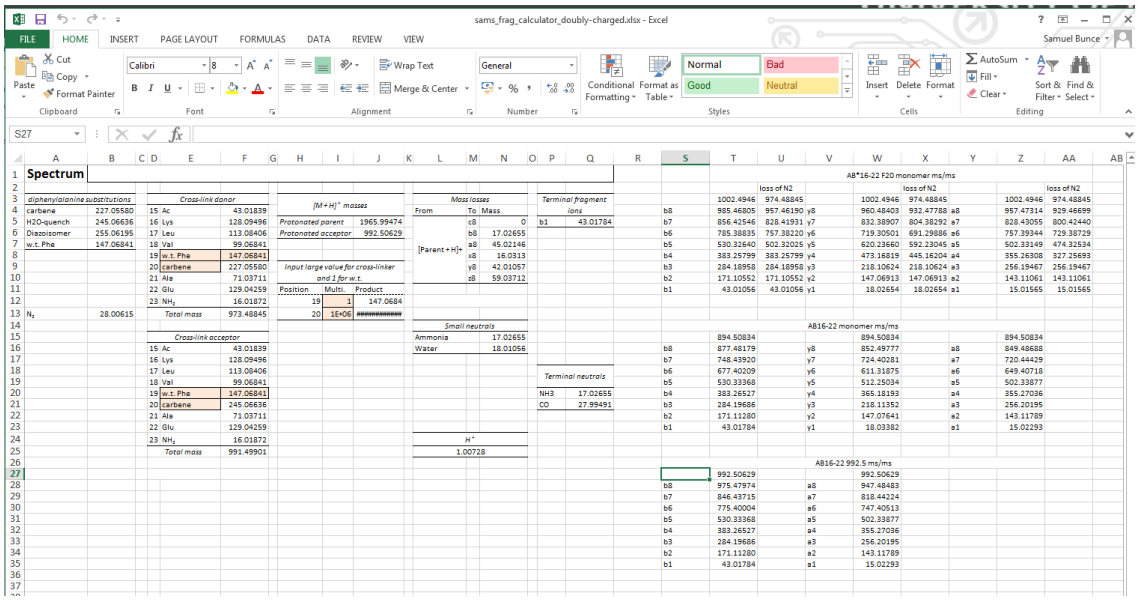

Figure 84. The interface of the fragmentation calculator built by George W Preston for assessing the presence of double fragmentation products in the MS/MS experiments.

Appendix 7- Supplementary MS/MS spectra

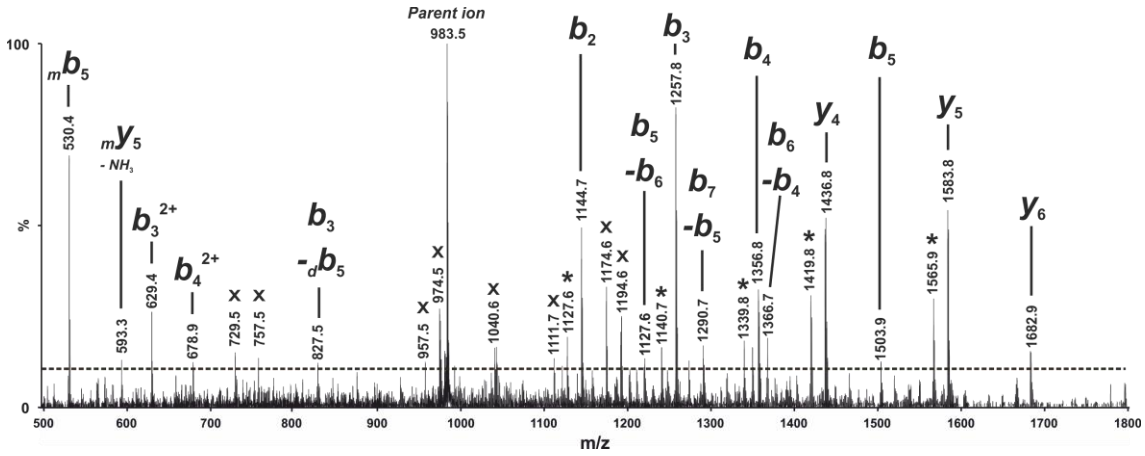

Figure 85. Fully assigned and annotated tandem MS/MS spectra for peak at m/z 983.6 (2^+; mass: 1965.2 Da) after 2 weeks. Key: subscript m = fragment comes from the monomer; subscript d = fragment ion has been lost from donor chain; x = unassignable; * = loss of NH_3 from proceeding fragment ion.

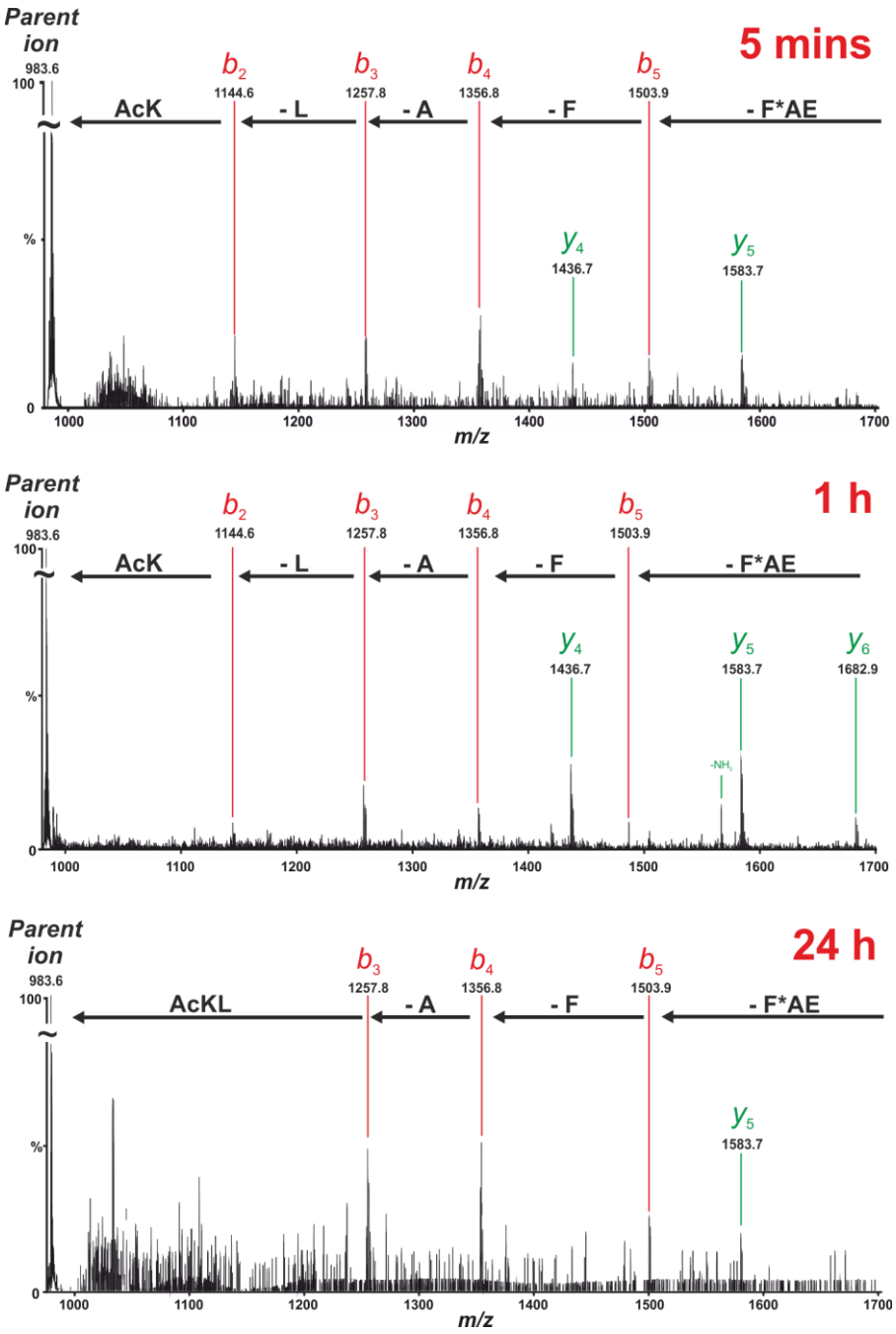

Figure 86. Annotated tandem MS/MS spectra for peak at m/z 983.6 (2^+; mass: 1965.2 Da) after 5 mins, 1 h and 24h incubation demonstrating that at all time points $A\beta^*_{16\text{-}22}$ forms in-register, antiparallel β-sheets.

Appendix 8- Supplementary ThT data

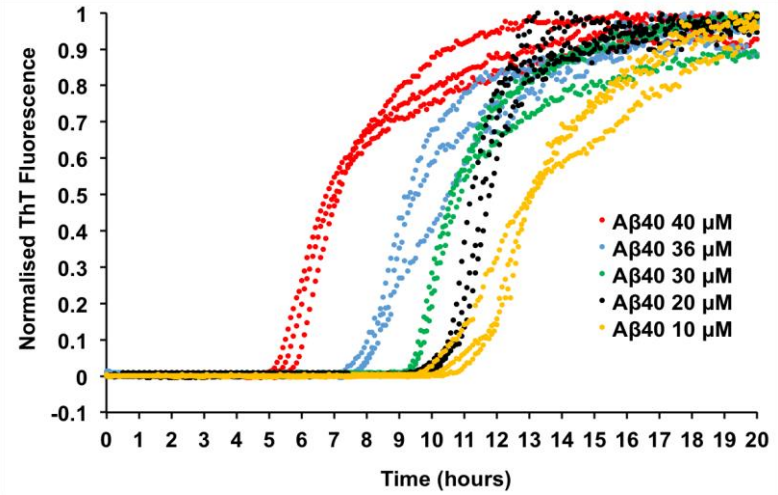

Figure 87. $A\beta_{40}$ concentration series used to normalise the half-times in Figure 59 (Section 3.10).

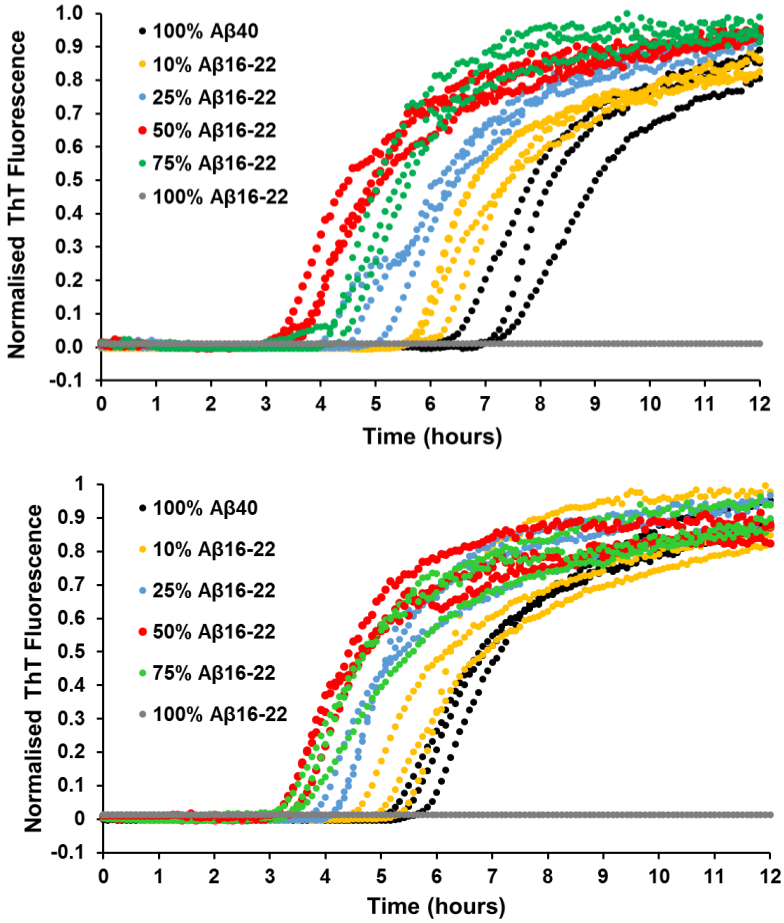

Figure 88. Repeats of the ThT assays outlined in Figure 58 (in which the molar ratio of $A\beta_{16-22}$ to $A\beta_{40}$ is increased whilst holding the total peptide concentration constant at 40 μM).

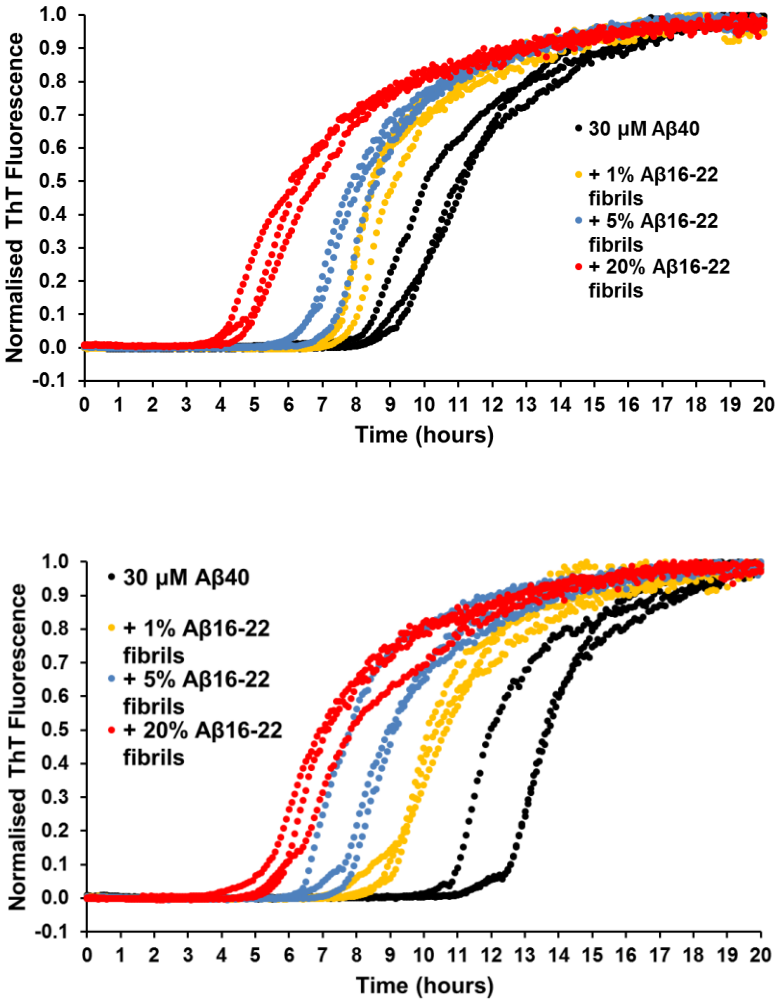

Figure 89. Repeats of the ThT assays outlined in Figure 64a (in which the effect of introducing increasing amounts of preformed $A\beta_{16-22}$ fibrils on the rate of $A\beta_{40}$ aggregation was assessed.).

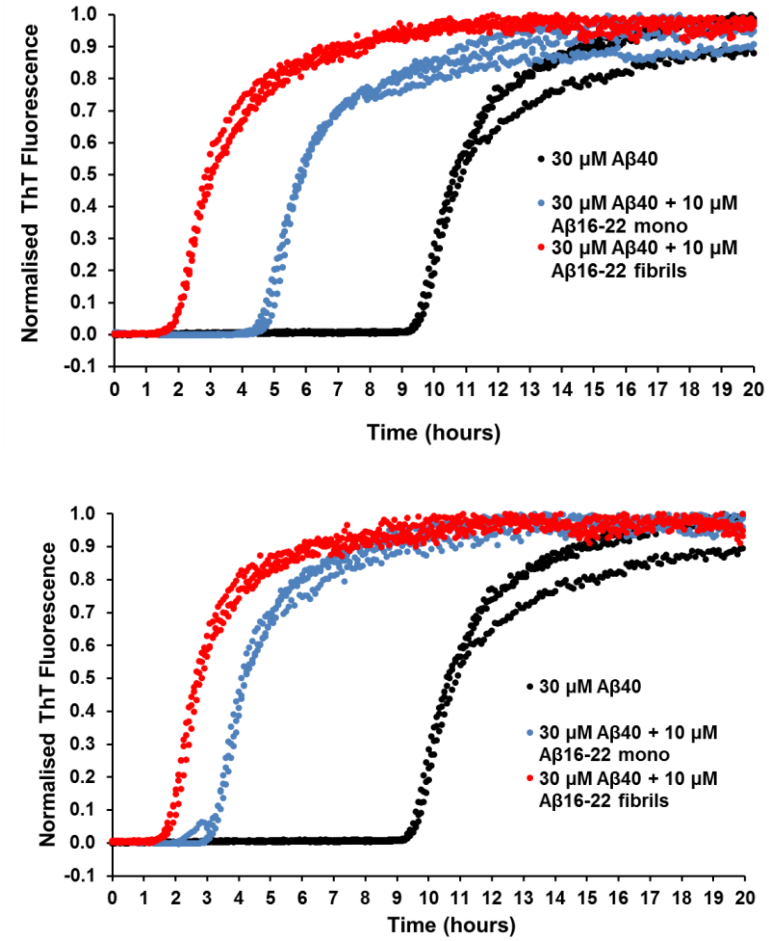

Figure 90. Repeats of the ThT assays outlined in Figure 64b (in which the effect of introducing either preformed $A\beta_{16-22}$ fibrils or $A\beta_{16-22}$ taken from a DMSO on the aggregation rate of $A\beta_{40}$ is assessed).

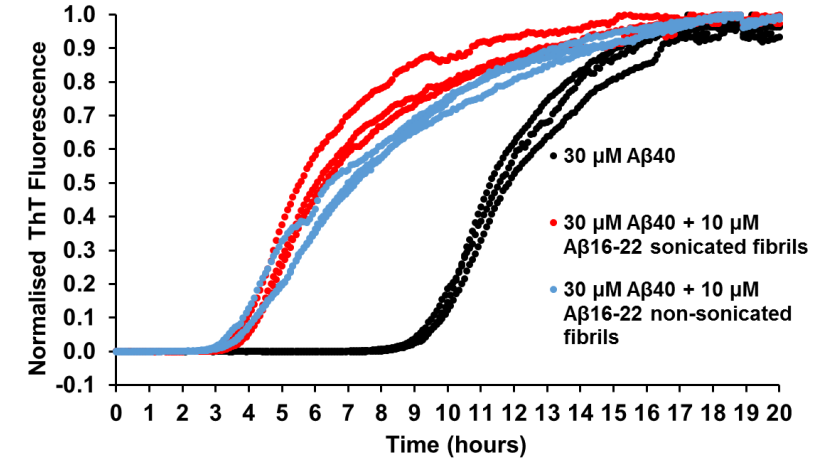

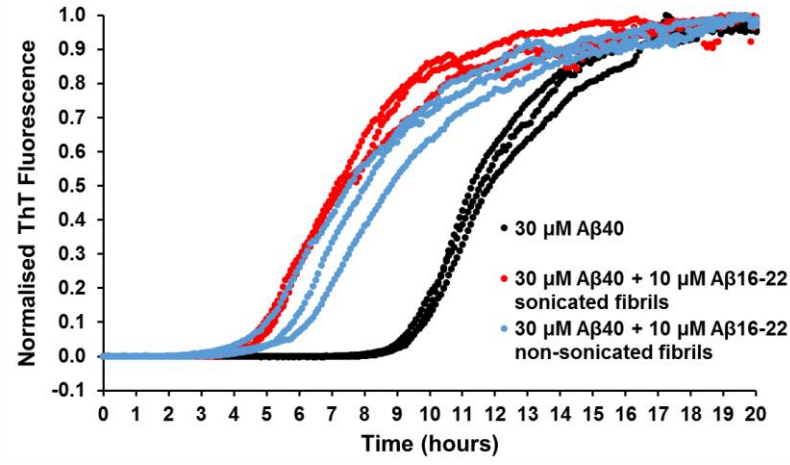

Figure 91. Repeats of the ThT assays outlined in Figure 64c (in which the effect of sonicating the preformed $A\beta_{16-22}$ fibrils on the aggregation rate of $A\beta_{40}$ was assessed).

Appendix 9- Supplementary MS/MS spectra for 1:1 ratio of Aβ*$_{16-22}$ and Aβ$_{40}$ after 5 mins and 1 h incubation

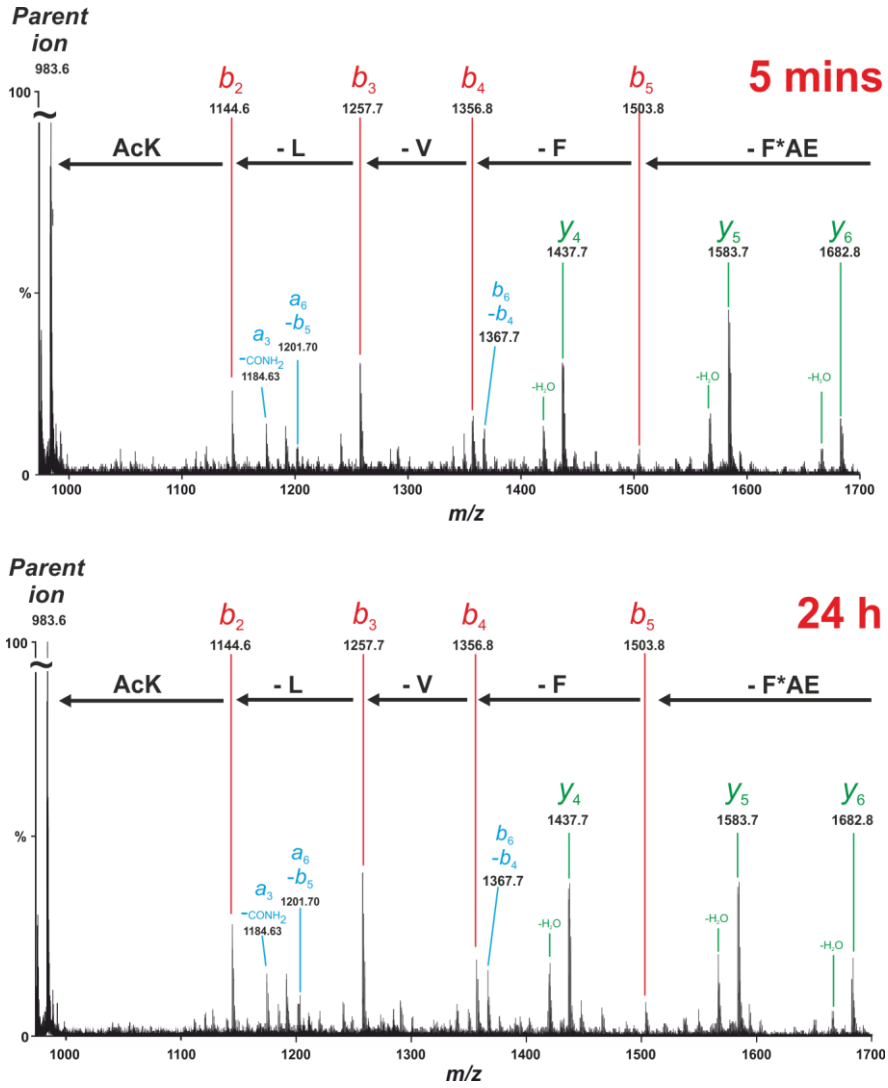

Figure 92. Annotated tandem MS/MS spectra for peak at m/z 983.6 (2^{+}; mass: 1965.2 Da) after 5 mins and 24 h incubation of a 1:1 ratio of Aβ*$_{16-22}$ and Aβ$_{40}$ demonstrating that at both time points Aβ*$_{16-22}$ forms in-register, antiparallel β-sheets.